Technical University of Denmark

DTU

Active Site Engineering in Electrocatalysis

Verdaguer Casadevall, Arnau; Stephens, Ifan; Chorkendorff, Ib

Publication date:
2015

Document Version
Publisher's PDF, also known as Version of record

Link back to DTU Orbit

DTU Library
Technical Information Center of Denmark

Active Site Engineering in Electrocatalysis

Arnau Verdaguer Casadevall

Active Site Engineering in Electrocatalysis

A Ph.D. thesis by

Arnau Verdaguer Casadevall

Supervisors: Ifan Stephens and Ib Chorkendorff

January 2015

Center for Individual Nanoparticle Functionality

Department of Physics

Technical University of Denmark

Cover page: Illustration of a PtHg$_4$(110) surface folding into a core-shell nanoparticle.

Table of Contents

Preface

This thesis is submitted in partial fulfillment of the candidacy for the Ph.D. degree from the Technical University of Denmark (DTU). The work presented here has mainly taken place at the Technical University of Denmark, Department of Physics, at the Center for Individual Nanoparticle Functionality (CINF) through the Catalysis for Sustainable Energy (CASE) initiative. CINF is funded by the Danish National Research Foundation, which is greatly acknowledged for its support to this project. The work was carried out from February 2012 to January 2015 with Professors Ib Chorkendorff and Ifan Stephens as supervisors. Part of the work has taken place at Stanford University, Department of Chemistry, with Professor Matthew Kanan as advisor. I thank the Otto Mønsted's foundation for funding part of my work at Stanford University.

If I had to choose three words to describe my Ph.D. these would be:
- Fun
- Intense
- Enlightening

Undoubtedly I've had a very positive experience, first and foremost thanks to the people I've been so privileged to work with. The passion, energy and helpfulness of everyone have been a beacon of strength guiding me during both good and difficult times. In particular, I would like to thank all my coauthors at CINF: Patricia, Søren, María, Paolo, Brian, Björn, Elisa, Rasmus, Tobias, Soren, Ib and Ifan; at CAMD, Ulrik, Samira, Reza and Jan; at CEN, Davide and Thomas and at Stanford Christina and Matt.

A special word goes to my advisors, Ib and Ifan, for general guidance as well as giving me freedom and trust to pursue fun but often unsuccessful experiments.

I am also very grateful to Patricia, Björn and María for teaching me so much, especially in the beginning of the project. Also to our small lunch team: Elisa, Brian and Rasmus and to my flatmate for most of this period, Tobias (and Elias).

Finally, I wish the reader a pleasant lecture, as much as I enjoyed writing this thesis.

Kgs. Lyngby, January 31st 2015

Arnau Verdaguer

Abstract

The overall goal of this thesis has been to design better catalysts for electrochemical reactions through a fundamental understanding of the materials at atomic scale. This has been achieved by combining electrochemical measurements with a variety of characterization techniques, often in ultra high vacuum, as well as theory calculations. The thesis falls in three different parts: firstly, study of model systems for oxygen reduction to water; secondly, oxygen reduction to hydrogen peroxide on both model systems and commercially relevant nanoparticles and thirdly CO_2 and CO electroreduction studies on nanostructured electrodes.

- Oxygen reduction to water has been carried out on Pt-rare earth alloys, which outperformed the activity of Pt by as much as a factor of five while showing promising stability. The increase in activity can be attributed to compressive strain of the Pt overlayer formed under reaction conditions, which is ultimately controlled by the crystal structure of the underlying alloy.

- Oxygen reduction to hydrogen peroxide has been investigated on single site catalysts, mainly alloys of noble metals with Hg. This resulted in a very special structure with isolated atoms of Pt or Pd surrounded by Hg, which greatly enhanced selectivity to H_2O_2 during oxygen reduction. Compared to state-of-the-art Au-based catalysts, Pt-Hg and Pd-Hg alloys present over 20 and 100 times increase in mass activity respectively. It was proven that activity for this reaction is controlled by the binding energy of the sole reaction intermediate.

- CO_2 and CO electroreduction studies have attempted to understand the unprecedented activity of oxide-derived Cu recently reported in the literature. Temperature programmed desorption measurements reveal very strong CO binding at these surfaces, inexistent in other forms of Cu. The presence of strong CO binding sites correlates well with electrochemical activity, which paves the way for the rational development of even better electrocatalysts.

Dansk resume

Det overordnede mål med denne afhandling har været at designe bedre katalysatorer til elektrokemiske reaktioner gennem brug af fundamental forståelse af materialer på atomarskala. Dette er blevet opnået ved at kombinere elektrokemiske målinger med et væld af karakteriseringsmetoder, ofte under ultra-højt vakuum, samt teoretiske beregninger. Afhandling tæller tre dele: først et studie af modelsystemer for oxygen reduktion til vand; dernæst oxygen reduktion til hydrogen peroxid, både på modelsystemer og kommercielt relevante nanopartikler og den sidste del vedrører studier af CO_2- og CO-reduktion på nano-strukturerede elektroder.

- Oxygen reduktion til vand er blevet udført på Pt-sjældne jordarter legeringer, som udviser aktiviteter på op mod fem gange den for Pt samtidig med, at udvise lovende stabilitet. Den øgede aktivitet kan tilskrives kompressionen af det overlag af ren Pt der bliver dannet under reaktionsbetingelserne. Mængden af kompression er ultimativt set styret af den krystalstruktur der er i den underliggende legering.

- Oxygen reduktion til hydrogen peroxid er blevet undersøgt på katalysatorer hvor det aktive sted er enkelt-atomer, hovedsageligt legeringer af ædle metaller med Hg. Disse legeringer resulterer i unikke strukturer hvor der findes isolerede atomer af enten Pt eller Pd omgivet af Hg, dette øger selektiviteten for H_2O_2 produktionen substantielt under oxygen reduktionen. Sammenlignet med state-of-the-art Au-baserede katalysatorer udviser henholdsvis Pt-Hg og Pd-Hg over 20 og 100 gange disses masseaktivitet. Denne høje aktivitet fremkommer af den nær-optimale bindingsenergi for reaktionens ene mellemstof som beregnet med density functional theory.

- CO_2- og CO-elektroreduktion studier har været brugt til at undersøge den fornylige publicerede høje aktivitet oxid-afledt Cu udviser som samtidig er uden fortilfælde. Temperatur programmeret desorptions målinger har påvist tilstedeværelsen af meget underkoordinerede steder på overfladensom ikke er at finde på andre former af Cu. Der er en god korrelation mellem mængden af disse steder og den målte elektrokemiske aktivitet, dette åbner op for en rute til rationelt design af endnu bedre elektrokatalysatorer.

List of Publications

Appended

Oxygen reduction to water

Paper I

Pt$_5$Gd as a highly active and stable catalyst for oxygen electroreduction.

María Escudero-Escribano, <u>Arnau Verdaguer-Casadeval</u>l, Paolo Malacrida, Ulrik Grønbjerg, Brian P. Knudsen, Anders K. Jepsen, Jan Rossmeisl, Ifan E. L. Stephens, Ib Chorkendorff.

*Journal of the American Chemical Society, 2012, **134**, 16476-16479 –*

http://pubs.acs.org/doi/abs/10.1021/ja306348d

Paper II

Enhanced activity and stability of Pt-La and Pt-Ce alloys for oxygen electroreduction: the elucidation of the active surface phase.

Paolo Malacrida, María Escudero-Escribano, <u>Arnau Verdaguer-Casadevall</u>, Ifan E. L. Stephens, Ib Chorkendorff.

*Journal of Materials Chemistry A, 2014, **2**, 4234-4243 –*

http://dx.doi.org/10.1039/C3TA14574C

Oxygen reduction to hydrogen peroxide

Paper III

Enabling direct H$_2$O$_2$ production via rational electrocatalyst design.

Samira Siahrostami[*], <u>Arnau Verdaguer-Casadevall</u>[*], Mohammadreza Karamad, Davide Deiana, Paolo Malacrida, Björn Wickman, María Escudero-Escribano, Elisa A. Paoli, Rasmus Frydendal, Thomas W. Hansen, Ib Chorkendorff, Ifan E. L. Stephens, Jan Rossmeisl.

*Nature Materials, 2013, **13**, 1137-1143 –*

http://www.nature.com/nmat/journal/v12/n12/full/nmat3795.html *Equal contributions.*

Paper IV

Trends in the electrochemical synthesis of H_2O_2: enhancing activity and selectivity by electrocatalytic site engineering.

Arnau Verdaguer-Casadevall, Davide Deiana, Mohammadreza Karamad, Samira Siahrostami, Paolo Malacrida, Thomas Hansen, Jan Rossmeisl, Ib Chorkendorff, Ifan E. L. Stephens.

Nano Letters, 2014, **14***, 1603-1608 –* http://pubs.acs.org/doi/abs/10.1021/nl500037x

Paper V

Alkaline oxygen reduction on single site electrocatalysts: tuning selectivity

Arnau Verdaguer-Casadevall, Ib Chorkendorff, Ifan E. L. Stephens.

In preparation, 2015 – based on section 4.5 of this thesis.

CO and CO_2 electroreduction

Paper VI

Probing the active site for CO reduction on oxide-derived Cu electrocatalysts.

In preparation, 2015 – based on section 5 of this thesis.

Other publications

Paper VII

The effect of ammonia upon the electrocatalysis of hydrogen oxidation and oxygen reduction on polycrystalline platinum.

Arnau Verdaguer-Casadevall, Patricia Hernandez-Fernandez, Ifan E. L. Stephens, Ib Chorkendorff, Søren Dahl.

Journal of Power Sources, *2012,* **220***, 205-210 –*
http://www.sciencedirect.com/science/article/pii/S0378775312012955

Paper VIII

Activity and selectivity for O_2 reduction to H_2O_2 on transition metal surfaces.

Samira Siahrostami, Arnau Verdaguer-Casadevall, Ib Chorkendorff, Ifan E. L. Stephens, Jan Rossmeisl.

ECS Transactions, 2013, **58***, 53-62 –* http://ecst.ecsdl.org/content/58/2/53.abstract

List of Patents

Patent I

Platinum and palladium alloys suitable as fuel cell electrodes.
Ifan Stephens, Jan Rossmeisl, María Escudero Escribano, Arnau Verdaguer Casadevall, Paolo Malacrida, Ulrik Grønbjerg, Brian Knudsen, Anders Jepsen, Ib Chorkendorff.
EP 12175450.1 (filed July 6, 2012).

Patent II

Platinum and palladium alloys suitable as fuel cell electrodes.
Ifan Stephens, María Escudero Escribano, Arnau Verdaguer Casadevall, Paolo Malacrida, Ulrik Grønbjerg, Jakob Schiøtz, Jan Rossmeisl, Ib Chorkendorff.
EP 12193574.6 (filed November 21, 2012).

Patent III

Catalysts for electrochemical synthesis of hydrogen peroxide.
Ifan Stephens, Arnau Verdaguer Casadevall, Björn Wickman, Jan Rossmeisl, Paolo Malacrida, Ib Chorkendorff, Samira Siahrostami, María Escudero Escribano, Mohammedreza Karamad.
EP 13165265.3 (filed April 25, 2013).

List of Abbreviations

CV	Cyclic voltammetry
EDS	Energy-dispersive X-ray spectroscopy
DFT	Density functional theory
EXAFS	Extended X-ray absorption fine structure
GC	Gas chromatography
HAADF	High-angle annular dark field
NMR	Nuclear magnetic resonance
OD	Oxide-derived
RRDE	Rotating ring-disk electrode
SEM	Scanning electron microscopy
STM	Scanning tunneling microscopy
(S)TEM	(Scanning) Transmission electron microscopy
TPD	Temperature programmed desorption
UHV	Ultra-high vacuum
(AR)XPS	(Angle-resolved) X-ray photoelectron spectroscopy
XRD	X-ray diffraction

1 Introduction

This introduction is meant to give an overview of some of the main challenges humanity is facing in the 21st century and to put the role of catalysis, and in particular that of my research, in perspective. Any reader not interested in my subjective view on the matter can skip directly to chapter 2. More detailed motivations for each project are given in the beginning of the respective sections.

Technological and societal advancement have fuelled an unprecedented growth in human population and development. In Figure 1.1 I show the evolution of human population during the past 300 years together with a projection for the next 35. There were 1 billion people in 1800, and this number grew by 600 % to reach 7 billion people in 2012. Human population is expected to grow to 10 billion by 2050. Every year about 135 M people are born and 60 M die, adding 75 M to Earth, or 6 M people every month. By 2050, more than half of the population will be concentrated in the African continent, China and India.
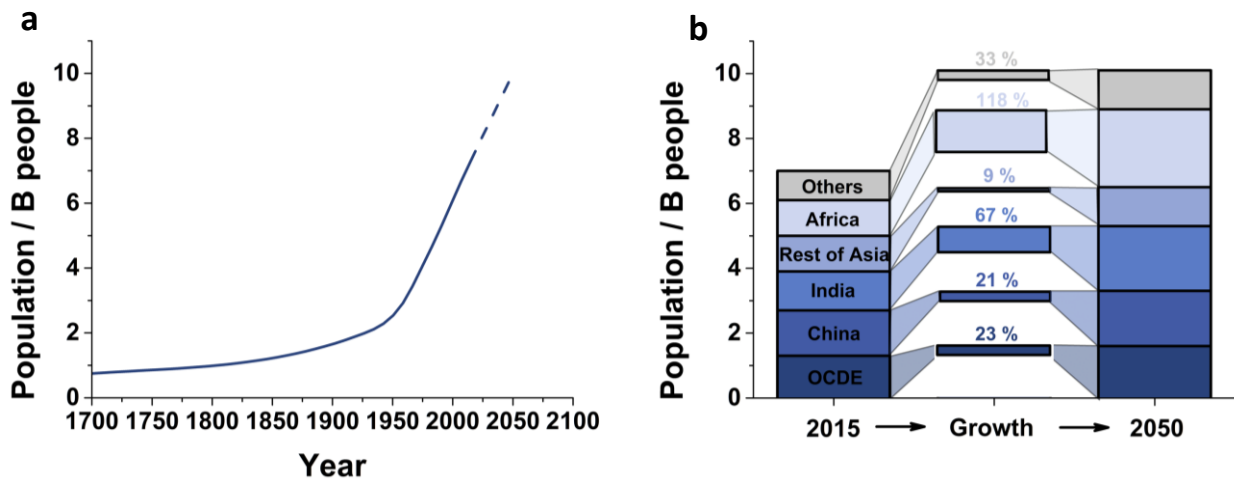
Figure 1.1: Human population based on OCDE data[1]. a) Evolution of world's human population over the last 300 years (solid line) and projection until 2050 (dashed line), with the y-axis representing billion people. b) Distribution of population by region in 2015, expected growth and projection for 2050.

As a result of both population growth and increased standards of living, Earth's natural resources are under stress. One way to measure the sustainability of any given resource

is the biological footprint, a measure of how much physical land is needed to supply such resources. Biological footprint is often measured in global hectares. A global hectare represents the average productivity of all biologically active areas (measured in hectares) any given year[2]. This includes forests, croplands, fishing waters etc, but not deserts, glaciers and other biologically inert areas. In total, there are 12.6 B global ha on Earth (and 14.8 B metric ha)[3]. Averaging the total number of global hectares over the 7 B people living today results in roughly 1.8 global ha per person, value at which resources are consumed at the same speed as they replenish. In reality, on average every person uses 2.52 global ha, which is a 40 % higher than what is sustainable, and it is only possible because resources have been accumulated over the years. Very large differences exist depending on each person's lifestyle, with income being the most important parameter in determining personal footprint[4].

Data on an income basis is notoriously hard to find (I was only able to find it for Canada[5]). Instead, data segmented by country is readily available[3]. In Figure 1.2 I show the footprint per capita (in global hectare units) as a function of GDP per capita for various countries. The trend confirms that people in rich countries, with a higher GDP per capita, utilize more global hectares –and consequently resources– than people in poor countries. This is exemplified by the red line, which is a linear fit of all points in the plot. In rich countries such as Denmark or the US people use four times more global ha than what is sustainable, while for instance in India, a poorer country, that value is only half.
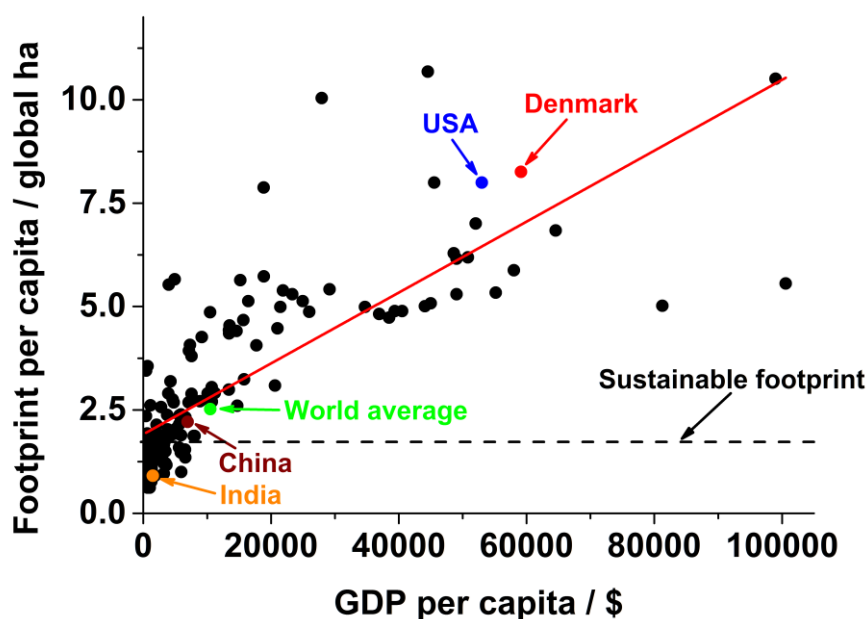

Figure 1.2: Footprint vs GDP per capita for different countries. Selected countries are colored and the world average is marked in green. The value for sustainable footprint is the horizontal dashed

line, and is based on population in 2015 and the number of global ha available. Data on footprint from Global Footprint Network [3]; data on GDP from United Nations (in 2013 \$)[6], not normalized to purchasing power parity.

This puts data on population growth in perspective; while OECD countries will add only 300 M people by 2050, these people alone will use more resources than the 2.4 B people added in Africa and India combined.

Independently from that, people want to increase their standards of living, which has traditionally required using more resources. A very genuine example on that is access to adequate water sanitation, which undoubtedly satisfies basic human needs. According to the United Nations, 2.5 B people (1/3 of the total population) at present lack access to adequate water sanitation (Figure 1.3). This includes safe water for drinking, cleaning and other basic uses. Treating water requires resources (energy, materials etc.), whose production inevitably needs global hectares. Other examples in that area are expected increases in agricultural output, which is predicted to be of 70 % by 2050 due to population growth and shifts in dietary preferences[7], or adoption of smartphones, growing from 2 B in 2015 to 6 B by 2020[8].
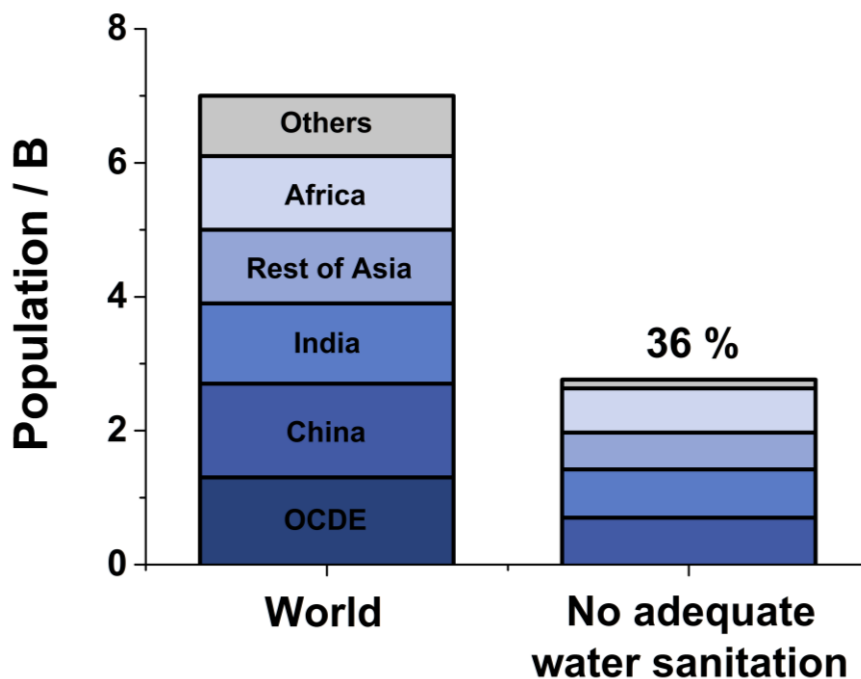

Figure 1.3: Total world population (in billion people) by region and fraction without access to adequate water sanitation, which accounts for 36 % of the total. Data from United Nations[9].

These two trends of increasing population and simultaneously increasing resources used per capita can be combined in a (perhaps oversimplified) mathematical equation:

$$\text{Total resources used} = \text{Population} \times \frac{\text{Resources used}}{\text{Person}}$$

Essentially, the total amount of resources used grows linearly with population and resources used/person (tightly linked with standard of living). Given that these two variables are growing, the total number of resources used will grow as well. That would be fine if there were such resources available (in the long term, if they were unlimited), as has been the case for the whole of human history. However, at present the rate of consumption of resources is higher than that of replenishment, as exemplified by data on global ha, which creates a new challenge for mankind.

Tackling this problem will require changes on humanity at both social and technological levels. Changes at a social level include access of women to education and careers, pacification of war zones etc. On a technological level, the saying 'doing more with less' has a particular relevance. It summarizes the need to achieve higher outputs using fewer resources. This requires substantial improvements in either a) efficiency of current technologies or b) development of disruptive technologies minimizing resource utilization.

One of the areas where such disruptive improvements are heavily sought after is in improving processes associated to energy or chemicals production, the topics of research of this Ph.D. thesis. Both energy and chemicals are cornerstones of modern civilization. They are commodities used by consumers and industry, and have an impact in practically all areas of society, from agriculture to electronics. To assess their importance it is relevant to look at their relative weight in the world's GDP, which totaled $63 trillion in 2010[10]. Energy accounted for $6.4 trillion, more than a 10 % of the world's GDP[11], while chemicals were worth $3.1 trillion −5 % of the GDP[12]. Thus, energy and chemicals combined account for roughly 15 % of the global GDP and are basic for the functioning of modern societies.

Today, both energy and chemicals are produced in a centralized infrastructure, with only a handful of plants to meet demand[13]. Most large scale processes were developed decades ago and require significant upfront capital investments. In addition, transportation to end users adds to the total cost. In contrast, a decentralized infrastructure to produce energy and chemicals would be more secure (being less subject to natural disasters or geopolitical situation), minimize transportation costs and depending on the processes used it can make a more efficient use of resources. Other very different industries have experienced or are experiencing a similar trend to decentralization, for instance communication with the rise of internet or more recently financial transactions with the invention of the block chain.

Electrochemical methods are a promising means to achieve a decentralized chemicals and energy infrastructure. They typically require little plant as they operate under mild conditions (low temperature and low pressure) and can be readily switched on and off, enabling their coupling to intermittent sources of energy. These factors encourage their development and eventual deployment. However, to date such efficiencies have not been possible, mostly due to difficulties in catalyzing reactions under mild conditions. This is one of the pillars to establish a more efficient decentralized energy and chemicals production infrastructure.

In this thesis I will present three examples where improvements in electrochemistry can contribute to solve some of the challenges associated with scarcity of the world's natural resources. The three examples I will present are in the area of electrocatalysis, defined as the type of catalysis resulting in the modification of an electrochemical reaction occurring on an electrode surface[14].

I have focused on correlating the structure of catalysts to their electrochemical reactivity. This understanding is of crucial importance to build solid grounds on which improve catalyst design. Paramount to this is Sabatier's principle and the development of volcano plots.

In catalysis, the goal is to recombine interatomic bonds of reactants to form products as efficiently as possible. In heterogeneous catalysis a non-consumed surface is used to promote the rate of a reaction, with the surface actively binding to intermediate states of the molecules. Binding with the appropriate strength, neither too strongly nor too weakly, facilitates adsorption of reactant molecules while favoring their desorption[15]. Mathematically, this is represented by the Gibbs free energy (ΔG). At equilibrium, the ideal catalyst should present thermoneutral adsorption of intermediates (i.e. $\Delta G=0$). $\Delta G > 0$ will imply adsorption is too strong, and $\Delta G < 0$ will mean adsorption is too weak; in either case activity will decrease from the thermoneutral maximum. This gives rise to so called 'volcano plots', where activity is a function of adsorption energy to a surface as can be seen in Figure 1.4. Measuring adsorption energies experimentally is cumbersome; therefore other more accessible parameters are often used as a descriptor. Fundamentally these descriptors are in one way or another linked to intermediate adsorption energy[16, 17].
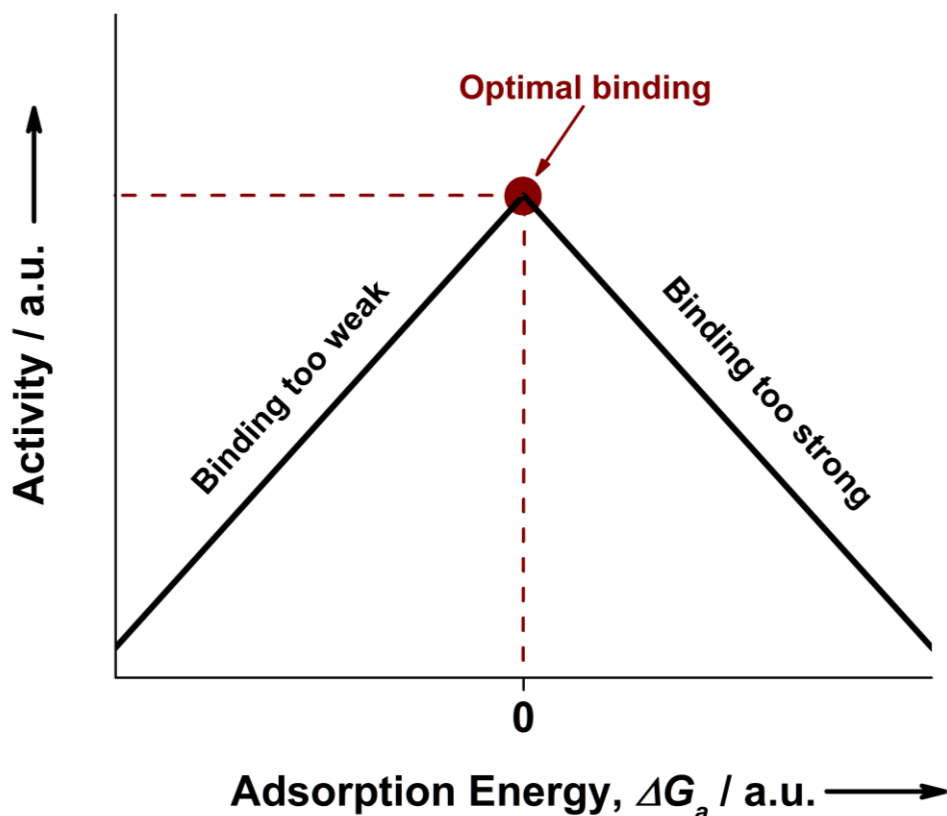
Figure 1.4: Schematic representation of a volcano plot, with the solid black lines representing the activity trends *vs*. adsorption energy, and the dashed lines showing the adsorption energy for optimal activity.

For intermediates binding through the same element, there is a linear relation between their binding energies to a given surface. This means that if intermediate *A* binds stronger to surface *a* and weaker to surface *β*, the trend will be the same for intermediate *B* and the relation will be linear. This is known as scaling relations, and it implies that it is not possible to independently change binding energy of several reaction intermediates. It also enables using a single descriptor to describe activity even if many intermediates exist. Examples have been reported for a variety of reactions, for instance catalysts for ammonia and methanol synthesis[16, 18]. With the development of supercomputers, binding strength can be calculated without experiments, and calculations are getting more and more accurate over time[16, 19]. Regardless of the approach used, binding energy is strongly influenced by the exact configuration of the atoms near the surface –what is known as active site. Understanding and improving the active site is primordial to realize improvements in catalyst reactivity, and ultimately enable more efficient processes.
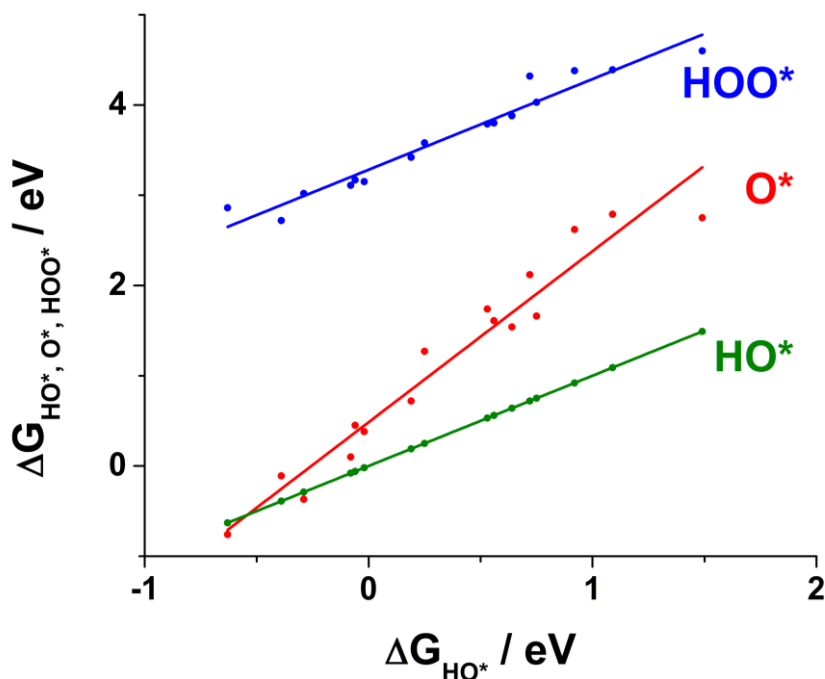
Figure 1.5: Theoretically calculated ΔG_{HO*}, ΔG_{O*} and ΔG_{HOO*} as a function of binding energy to ΔG_{HO*} on various metallic surfaces. Adapted from [20].

These principles are widely accepted by the heterogenous catalysis community, and they also apply to electrocatalysis. Pioneering work by Roger Parsons in the 1950s demonstrated the volcano principle held for the hydrogen evolution reaction[21]. Knowledge of the active sites responsible for a reaction was minimal at the time due to lack of adequate characterization techniques. Using modern equipment, a much better picture, even at the atomic level, of the catalyst structure is possible. Correlating that with electrochemical properties, such as activity and selectivity, greatly enhances catalyst development.

A pertinent example on electrocatalyst improvements based on understanding of the active sites is hydrogen evolution on MoS_2 surfaces. For years, MoS_2 was thought to be an inactive catalyst for that reaction[22]. Theoretical calculations showed that the binding energy of hydrogen to MoS_2 is very dependent on surface termination[23]. While bulk MoS_2 predicted to be inactive, the Mo edge in MoS_2 would have a nearly optimal binding energy. Later on it was experimentally demonstrated that this particular configuration of atoms is indeed a very active site for the reaction[24]. By nanostructuring it was possible to increase the density of these active sites, realizing even greater activity

improvements[25, 26, 27]. This emphasizes the value of having a detailed knowledge on the active site and how it can promote technological advancement.

Researchers have strived to develop rational models for a variety of reactions, aiming at finding readily accessible and accurate descriptors to accelerate catalyst discovery: hydrogen evolution[23, 28], oxygen evolution[29, 30], oxygen reduction[31, 32, 33, 34, 35] and CO_2 reduction[36] are some of the examples. Nevertheless, the inherent complexity of the reaction environment has made it challenging to establish a 'one size fits all' framework. pH dependency effects and product selectivity are two of the main areas most models fail to address[37, 38].

Building upon this knowledge, in this thesis I have tried to understand what are the fundamental parameters that make catalytically effective active sites. On the basis of this insight, I have strived to design new active sites with improved properties.

Outline of the thesis

I have attempted to structure the thesis in a coherent, easy to follow way. It is divided into four chapters; one for experimental techniques and three for each of the reactions I studied.

Chapter 2 is devoted to the experimental techniques I have used during the project, outlining briefly the fundamentals and explaining how and why they have been used in my research.

Chapter 3 describes the discovery of novel catalysts for oxygen reduction to water based on alloys of platinum and rare earths.

Chapter 4 is dedicated to oxygen reduction to hydrogen peroxide on single site catalysts.

Chapter 5 involves the search for the active site during CO reduction on oxide-derived Cu catalysts.

The aim has been to make each chapter independent and readable on its own, but keeping the active site motif as a common driver. In particular, I have aimed to give quantitative arguments motivating each of the lines of research in the beginning of each chapter. A summary of my own research in the context of recent work in the field follows; I recommend the reader interested in specific details to read the appended publications or references.

2 Experimental techniques

I have used several experimental techniques to perform the measurements, which I have divided into three parts. a) electrochemical techniques to measure activity and stability of catalysts; b) methods to identify and quantify the products of reactions; c) characterization tools to get insight into catalyst structure/composition.

2.1 Electrochemical techniques

Electrochemistry studies chemical reactions involving the transfer of charged species between an electrode and an electrolyte[39]. Its study requires using a variety of methods depending on the particularities of a reaction. I will first describe the basics of electrochemistry and then explain in more detail the different techniques I used.

All electrochemical measurements in this thesis have taken place in a three electrode cell configuration. In such a cell there are three electrodes, each with a specific function. A diagram of it is shown in Figure 2.1.

- Working electrode (WE): consists of the catalyst to be studied.
- Counter electrode (CE) / auxiliary electrode: to measure the current from the CE to the working electrode. It is usually a Platinum mesh or wire. If Pt contamination of the electrolyte is an issue it can be replaced by a carbon rod.
- Reference electrode (RE): provides a scale to which relate the potential of the working electrode.
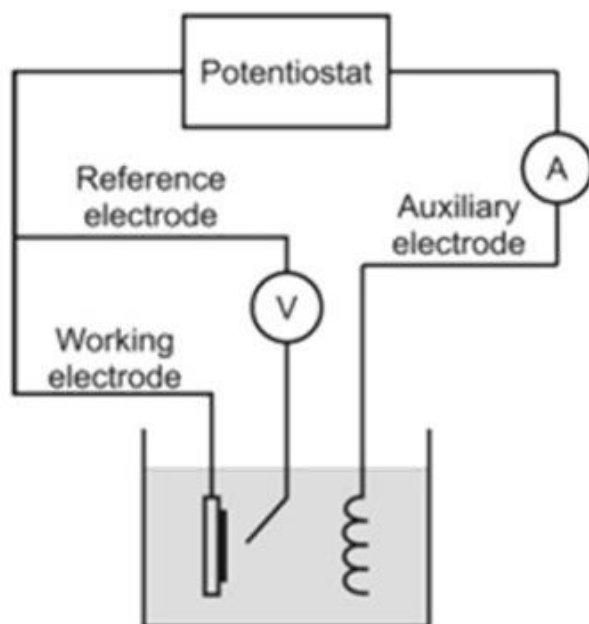
Figure 2.1: Schematic diagram of a three electrode setup. Voltage is measured between working and reference electrode, indicated by 'V' in the figure. Current flows between counter and working electrode, marked as 'A'. Adapted from [40].

The reference electrode deserves a few lines for itself given its particularities. Since it is not possible to measure the potential of a single electrode, a stable and consistent scale to which refer the potentials is requied. This scale is based on the standard Hydrogen electrode, a redox electrode where the potential has been set to zero for all temperatures. However, if the reaction takes place at a certain pH value, it is convenient to introduce the reversible hydrogen electrode (RHE). The RHE is a kind of standard hydrogen electrode (SHE) that enables comparison of potentials at different pH values. The relation between the two types of electrodes is given by the equation:

$$U(\text{RHE}) = U(\text{SHE}) - 0.059 \cdot \text{pH}$$

If the reference electrode is placed in the same electrolyte as the working electrode it enables determination of the potential difference between both while current runs from counter electrode to working electrode. In this thesis all the potentials are referred to the RHE scale.

Introducing a reference electrode adds an additional layer of complexity to the measurements. To understand why I show the equivalent electrical circuit for an electrochemical cell in Figure 2.2. The area close to the electrode can be seen as a capacitor, C_{dl}, and a resistance in parallel, R_F. This is because on the electrode surface there are two charge layers very close to each other, acting as a capacitor, and a resistance stemming from the charge transfer between electrode and reactant. The

resistance between points A and B in Figure 2.2 represents the solution resistance caused by ions moving in the electrolyte.
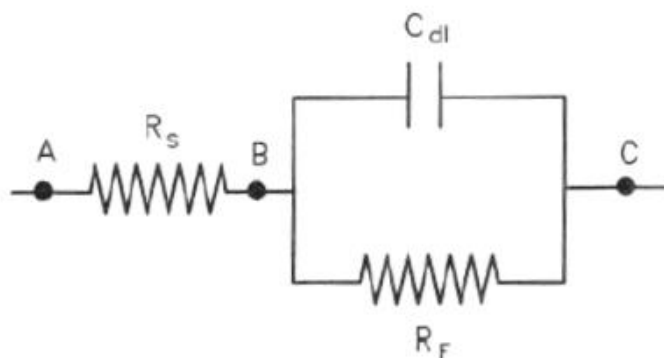
Figure 2.2: Schematic representation of an electrochemical cell. The potential is measured between A and C, while the current is monitored between B and C. The electrode surroundings can be seen as a capacitor and a resistance in parallel. Adapted from [41].

This resistance is called Ohmic drop, and the potential difference between A and B has to be subtracted from that measured in order to get the potential between B and C. This can be done by using Ohm's law ($V_{BC} = iR_s$):

$$V_{BC} = V_{AC} - iR_s$$

This permits expressing both potential and current between the same points, which enables for a more accurate determination of electrochemical activity.

2.1.1 Electrode and cell preparation for the electrochemical measurements

Prior to every electrochemical measurement in the three-electrode glass cell there are several steps to follow in order to ensure reproducibility. They can be divided into two parts: electrochemical cell cleaning and electrode preparation.

Firstly, the electrochemical cell is cleaned in a piranha solution (3:1 mixture of 96 % sulphuric acid and 30 % hydrogen peroxide solution) for 48 hours. Then the cell is rinsed several times with Millipore water to eliminate all sulfate traces and filled with the corresponding electrolyte, made of Millipore water (18 MΩcm of resistivity). In certain cases where trace amounts of Pt or Au were to be avoided fresh aqua regia was used, consisting of a solution of 3:1 concentrated HNO_3 and HCl.

I have also used a variety of chemicals for the solutions used in electrochemical experiments. In some cases their purity may impact on the results, therefore I would like to specify the supplier I obtained them from.

- $HClO_4$ – Merck Suprapur 70 % concentration.
- KOH – Sigma Aldrich 99.99 % (trace metal basis), semiconductor grade, hydrated.
- $Hg(ClO_4)_2$ – Sigma Aldrich 99.998 % (trace metal bases), hydrated.
- Gases – AGA 5N5 grade.

Regarding working electrode preparation, I used a variety of materials throughout the project, each of them requiring different preparation procedures. I mostly used a report by Ludwig A. Kibler[42], from Ulm University, as a guideline for the preparation of all pure metals. Other electrodes were prepared according to cited literature or through my own procedures. Below is a brief outline:

Oxygen reduction to water

- Polycrystalline Platinum: Polished and then flame annealed at a temperature of roughly 800 ºC for 2 minutes. Then I let it cool down under a stream of Argon and cover with a drop of hydrogenated water to prevent contamination before embedding it into the RRDE assembly.
- Pt_5X alloys: Purchased from Mateck GmbH at request. Polished and subsequently sputtered in UHV to ensure cleanliness and surface composition. Immediately after removal from UHV I covered them with a drop of hydrogenated water and embedded them in the RRDE assembly.

Oxygen reduction to H_2O_2

- Polycrystalline Palladium: Polished and then annealed by induction heating under Argon atmosphere at ~700 ºC. Let it cool down and covered with a drop of dearated water.
- Polycrystalline Copper: Electropolished for 2 min in a 1:3 solution of 85 % H_3PO_4 at 2.1 V *vs* a Pt mesh placed ~2 cm away from the electrode. The color visibly changes from 'orange' to almost white. Then I move it to a beaker with dearated water to remove Cu ions and ortophosphoric acid for ~30 s and transfer it to the cell[43].
- Polycrystalline Silver: Polished and then annealed by induction heating under 5 % Ar/H_2 atmosphere at ~700 ºC. Let it cool down and covered with a drop of hydrogenated water.
- Pt/C nanoparticles: Commercial sample from ETEK.

- Pd/C nanoparticles: Commercial sample from ETEK.

- Au/C nanoparticles: Commercial sample from ETEK.

- Hg alloys: I followed a paper from Wu and coworkers[44] where they prepare Pt-Hg. I used the same method for all Hg alloys. Essentially, it consists of Hg electrodeposition from 0.1 mM $Hg(ClO_4)_2$ solution in 0.1 M $HClO_4$ at 0.2 V for 2 min.

CO_2 and CO electroreduction

- Polycrystalline Copper: Electropolished for 2 min in a 1:3 solution of 85 % H_3PO_4 at 2.1 V *vs* a Pt mesh placed ~2 cm away from the electrode. The color visibly changes from 'orange' to almost white. Then I move it to a beaker with dearated water to remove Cu ions and ortophosphoric acid for ~30 s and transfer it to the cell.

- OD Cu 1 (oxide-derived Cu 1): Annealed in the muffle furnace at 500 ºC for 1 h, then reduced in the electrochemical cell at -0.5 V before starting the experiment.

- OD Cu 2: Annealed in the muffle furnace at 500 ºC for 1 h, then reduced thermally under 1 bar of H_2 at 130 ºC. The preparation procedure for both OD Cu electrodes was developed by Kanan and coworkers[45, 46].

- Bi doped OD Cu: Electrodeposition of Bi on polycrystalline copper at -0.4 V from 1 mM Bi^{3+} in 0.1 M $HClO_4$. Subsequently oxidized at 500 ºC for 1 h in the muffle furnace, and reduced at 130 ºC in the tube furnace under a H_2 stream.

2.1.2 Cyclic Voltammetry (CV)

Cyclic voltammetry is a widely used electrochemical technique due to its simplicity and reproducibility. In these experiments potential is swept back and forth across the desired range at a constant scan rate while measuring the current[39], as represented in Figure 2.3. This permits distinguishing different reactions occurring at the catalyst and it is a quick assessment tool of the state of the surface and its activity. Cycling the potential presents the advantage of cleaning the electrode from possible contamination[47], and this results in very reproducible data across experiments or even different labs.
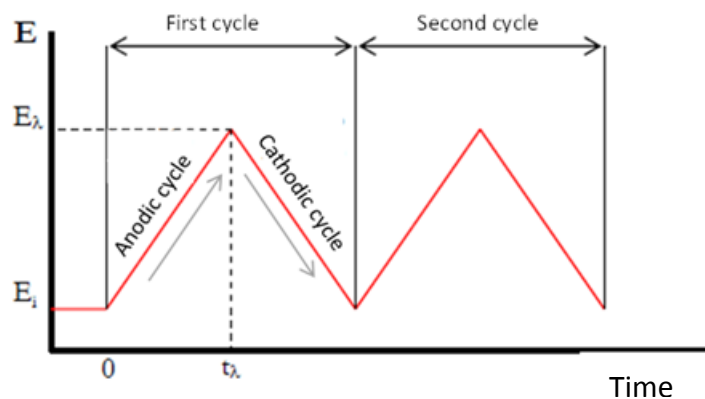
Figure 2.3: Potential variation over time in a cyclic voltammetry study. The potential is swept between the two values E_i and E_λ at a constant scan rate dE/dt. Adapted from [48].

CV is the technique of choice to measure oxygen reduction or to investigate changes in the oxidation state or surface of a catalyst induced by the applied potential. One very useful example in this regards is the CV of an electrode in inert gas saturated electrolyte (typically Argon or Nitrogen). In such a CV it is possible to check how clean the surface and the electrolyte are before carrying out additional experiments. In Figure 2.4 I show how it looks like for polycrystalline Pt, which has a few traits making it unique. The concepts used here can be applied to many of the materials studied in this thesis.
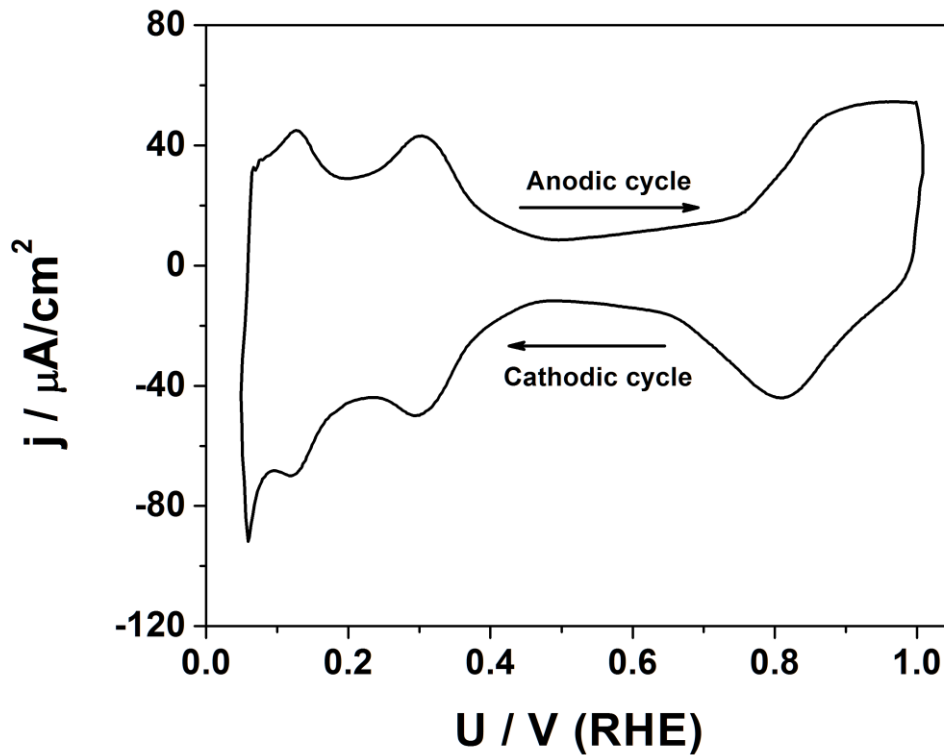
Figure 2.4: CV of a polycrystalline Platinum electrode in Argon saturated 0.1 M $HClO_4$. Both the anodic and cathodic cycles are shown. Measurement taken at 23 ºC and 50 mV/s with no rotation.

In the following, * denotes an active site on the surface.

- From 0 to 0.4 V the two characteristic peaks correspond to Hydrogen desorption from the Platinum surface through the reaction:

$$H^* \rightarrow Pt + H^+ + e^-$$
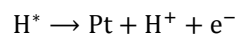
  With the released electron causing the recorded positive current.

- From 0.4 to 0.7 V there is the double layer region, where capacitance induces a positive current.
- From 0.7 to 1 V the hydroxyl ions from water are adsorbed on the Platinum surface:

$$* + H_2O \rightarrow OH^* + e^- + H^+$$
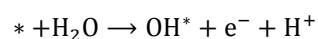
  Thus resulting in a positive current.

The reverse reactions take place in the backward scan, thus giving rise to the symmetry in the profile.

- Already in the cathodic cycle, the first feature, from 1 to 0.7 V, is a negative current caused by the desorption of hydroxyl ions

$$OH^* + e^- + H^+ \longrightarrow * + H_2O$$
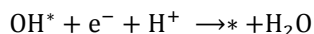
- The double layer capacitance also generates a negative current, from 0.7 to 0.4 V.
- Hydrogen adsorbs at the surface between 0.4 and 0 V, causing the two characteristic peaks because of the reaction

$$* + H^+ + e^- \longrightarrow H^*$$
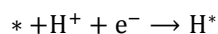
2.1.3 Chronoamperometry

In certain cases it can be interesting to measure the current as a function of time when keeping the electrode at a constant potential. Such experiments receive the name of chronoamperometry, and they are mainly used to accumulate products of a reaction at a given potential. CO/CO_2 reduction is typically measured using this method. Operating at a constant potential presents the disadvantage that contaminants may accumulate at the electrode surface[47].

2.1.4 Rotating Ring-Disk Electrode (RRDE)

The rotating ring-disk electrode is a hydrodynamic method widely used for reaction kinetics measurements[39, 49]. Its strong points are that steady state can be reached very fast and that mass transport can be controlled by rotation speed. In these measurements the working electrode consists of a disk embedded in an insulator rod which is connected to a rotator, enabling rotation speed control. I have used this setup for all oxygen reduction measurements.
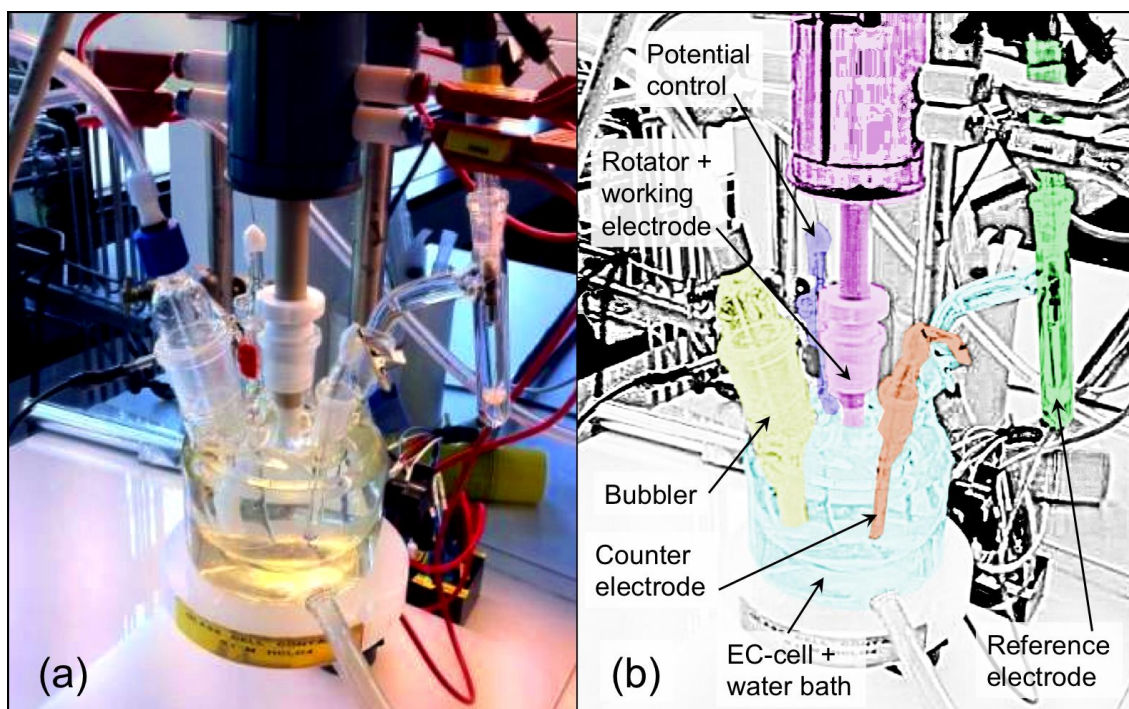
Figure 2.5: Rotating ring-disk electrode setup with a three-electrode cell used for the electrochemical measurements. Counter electrode, working electrode and reference electrode are clearly visible. a) Actual picture. b) Schematic representation. Adapted from [50].

Analytical equations can be useful to understand RRDE principles and extract valuable data from experiments. Mass transport of the reactant is convective until a very small diffusion layer, whose thickness δ is defined by:

$$\delta = 1.61 \cdot D^{1/3} v^{1/6} \omega^{-1/2}$$

Where D is the reactant diffusion coefficient in the electrolyte, v the electrolyte kinematic viscosity and ω the rotation speed of the disk. If the reaction rate at the electrode is very fast, it will reach a point where all the reactant that can be supplied is consumed immediately, creating a surface concentration of reactant which is virtually 0. Thus, the limiting factor in the current is the speed at which reactant can reach the surface. This current is called diffusion-limited current (j_l), and can be computed through the Koutecky-Levich equation:

$$j_l = nFc_o \frac{D}{\delta} = 0.62nFc_o D^{2/3} v^{-1/6} \omega^{1/2}$$

Where n is the number of electrons transferred in the reaction, F the Faraday constant and c_o the concentration of reactants. A useful check to see if the setup is working properly is to plot the inverse of the square root of the rotation speed against the

inverse of the current ($1/j_l$ vs $\omega^{-1/2}$) for different rotation speeds, which ideally should follow a linear relation. This plot is commonly known as a Koutecky-Levich plot.

Assuming that the reaction is of first order with respect to the reactant partial pressure the relation between measured current density and kinetic current density (j_k) (involving only catalysis effects) can be derived:

$$\frac{1}{j} = \frac{1}{j_k} + \frac{1}{j_l}$$

Which allows expressing the kinetic current density as a function of the measured current and the diffusion-limited current[39, 49].

$$j_k = \frac{j \cdot j_l}{j - j_l}$$

This last equation explains why RRDE is the method of choice to derive kinetic parameters for an electrode. In short, j_k is dependent on total current density and limiting current density; two immediately accessible parameters.

A useful tool that can be simultaneously used with the measurement at the disk is the ring. The ring, made of Platinum in my case, is separated from the electrode by a very small insulating gap. It can measure electrochemical reactions on the products from the working electrode, potentially giving useful information on them. A classical use of the RRDE is to measure the hydrogen peroxide yield during oxygen reduction. In such measurements the ring is set at a potential of 1.2 V. At this potential there is no current from oxygen reduction/evolution and all current measured will be from hydrogen peroxide oxidation[49], as represented in Figure 2.6.

The fraction of peroxide being formed can then be computed using

$$X_{H_2O_2} = \frac{2I_R/N}{I_D + I_R/N}$$

N being the collection efficiency (fraction of products collected at the ring coming from the disk), which was estimated for the setup used as a 20 % using the ferri-ferrocyanide redox couple[49], I_R the ring current and I_D the disk current.
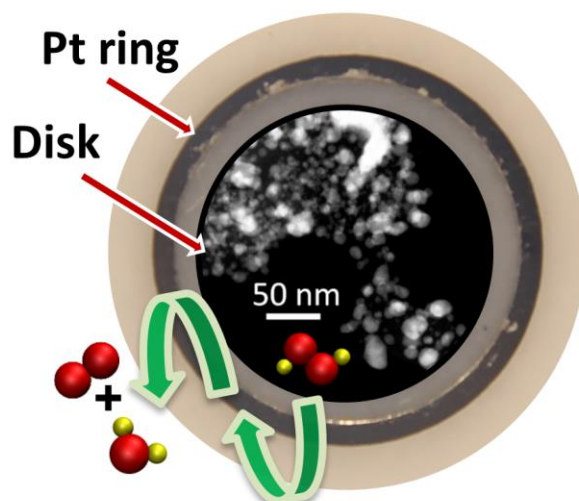
Figure 2.6: Picture of a rotating ring-disk electrode with a schematic representation of H_2O_2 oxidation at the ring. The disk has been modified to show a TEM overview with metallic nanoparticles. Oxygen is represented in red; hydrogen in yellow.

As an example, Figure 2.7 exhibits a RRDE measurement on polycrystalline platinum. The plot is divided into three parts, from bottom to top: disk data, ring data and H_2O_2 efficiency. In all plots the x-axis is the applied potential at the disk. The black line in the bottom plot represents the disk current density. Oxygen reduction occurs from 1 V, with an exponential increase in current characteristic of kinetic control. Soon mass transport of oxygen becomes the limiting factor in the current and it plateaus at -6 mA/cm^2, the characteristic value for four electron oxygen reduction to water at 1600 rpm. This limit will decrease at lower rotation speeds and increase at higher, proportionally to $\omega^{1/2}$. At low potentials (< 0.4 V) the surface of Pt becomes covered with hydrogen and selectivity changes to H_2O_2[49]. As oxygen reduction to H_2O_2 requires only two electrons and the reaction is already mass transport limited, current will decrease. At a rotation speed of 1600 rpm the mass transport limited current for 100 % H_2O_2 selectivity is 3 mA/cm^2. The actual value is close to -4 mA/cm^2 at ~0 V, implying a mixed selectivity to water and H_2O_2. These trends can be confirmed by the ring measurement, which shows no current until < 0.4 V. Below that value a positive current attributed to H_2O_2 oxidation appears. Based on this current and the RRDE equations it is trivial to derive how much hydrogen peroxide is produced at the disk, shown in red in the bottom plot, and the proportion of H_2O_2 with respect to water, shown in the top plot. Note that in these experiments the actual *product* distribution and not *electron* distribution (as in CO_2 reduction) is represented.
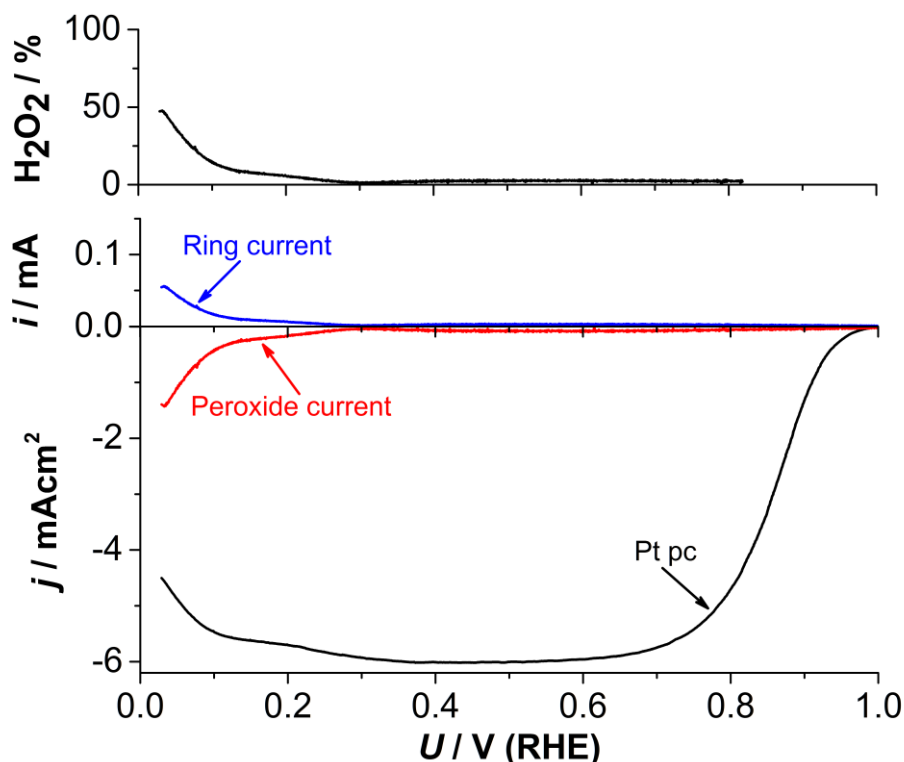
Figure 2.7: Oxygen reduction on polycrystalline platinum. Percentage of H_2O_2 over total product molecules as a function of the applied potential (top plot) and RRDE voltammograms (bottom plot) with the disk current (black), ring current (blue) and corresponding current to hydrogen peroxide (red), obtained from the ring current. Measurement taken at 1600 rpm in O_2-saturated 0.1 M $HClO_4$ and 50 mV/s at room temperature. Only the anodic cycle is shown.

2.1.5 CO$_2$ and CO electroreduction setup

In oxygen reduction there is only a reaction occuring and it is relatively simple to identify the products. In contrast, in CO_2 or CO reduction many processes can occur simultaneously. Typically there will be some hydrogen evolution from water in parallel to hydrocarbon and/or alcohol formation. An extra layer of complexity arises since products can be in gas (hydrogen, hydrocarbons) or liquid form (alcohols). In addition, in these experiments the counter electrode has to be separated from the working electrode, often using an alkaline exchange membrane (Selemion). This is done to avoid oxidation of the reduced compounds at the counter-electrode.

In the following I will write the main reactions I have observed during CO_2 or CO reduction. A more extensive overview including several other minor products can be found in the literature[43, 51].

- Hydrogen evolution

$$2H^+ + 2e^- \rightarrow H_{2(g)} \qquad\qquad U^0 = 0 \text{ V}$$

- CO_2 reduction

$$CO_{2(g)} + 2H^+ + 2e^- \rightarrow CO_{(g)} + H_2O_{(l)} \qquad\qquad U^0 = -0.103 \text{ V}$$

$$CO_{2(g)} + 2H^+ + 2e^- \rightarrow HCOOH_{(l)} \qquad\qquad U^0 = -0.171 \text{ V}$$

- CO reduction

$$2CO_{(g)} + 7H_2O_{(l)} + 8e^- \rightarrow CH_3CH_2OH_{(l)} + 8OH^- \qquad\qquad U^0 = 0.18 \text{ V}$$

$$2CO_{(g)} + 3H_2O_{(l)} + 4e^- \rightarrow CH_3CO_{2\ (l)}^- + 3OH^- \qquad\qquad U^0 = 0.5 \text{ V}$$
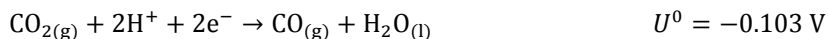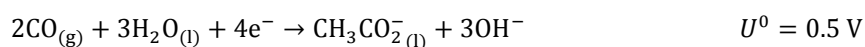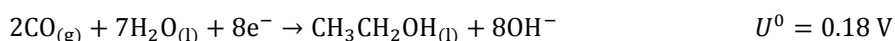
Note that CO_2 is itself acidic, and in bicarbonate solution where CO_2 reduction experiments are carried out the pH will be below 7. For that reason, in the equations for CO_2 reduction I have considered free protons directly as the proton source. This is different in CO reduction, where pH is set to alkaline ($\sim$13) and water acts as a proton source, which is reflected in the equations. Regardless of the proton source, both carbon source and final products will be the same, as well as the reversible potential for the reactions.

As seen in Figure 2.8, the $CO_{(2)}$ reduction setup consists of a leak-tight H-cell coupled to a gas chromatographer. Constant purging of the electrolyte pushes the gas to the gas chromatographer, which is run periodically. This permits detection of gas phase products, while liquid products have to be measured after the reaction using nuclear magnetic resonance. Linking current density to product quantification results in Faradaic efficiency. Faradaic efficiency tells what percentage of electrons is used to make each product and is usually regarded as a figure of merit in these experiments. It can be computed using the equation:

$$FE_i = \frac{n_i}{n_T}$$

Where *FE* is Faradaic efficiency, n_i number of electrons to product *i* and n_T total number of electrons. n_T is given by the total charge transferred during the reaction, and n_i relies on analytical techniques to quantify the different products and calculate how many electrons they required. Extensive details on these methods are given in the following section. In this case, opposite to hydrogen peroxide detection by RRDE, the *electron* distribution and not *product* distribution is represented.
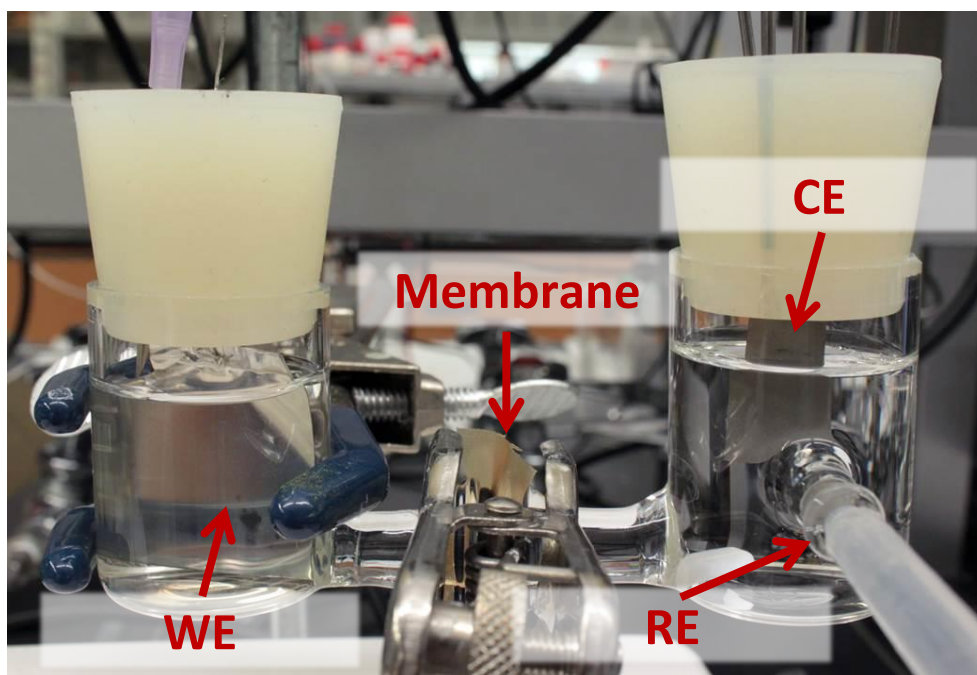
Figure 2.8: Picture of the electrochemical cell used for $CO_{(2)}$ reduction experiments. WE, CE and RE represent working, counter and reference electrode respectively.

2.2 Analytical Chemistry Techniques

Throughout the project it has been important to measure a variety of compounds from the reactions. This is particularly challenging for $CO_{(2)}$ reduction, where there exist a variety of products[43]. I have used complimentary techniques to quantify both liquid and gas products. To detect H_2O_2 I have used permanganate titration. For hydrogen, hydrocarbons and alcohols from $CO_{(2)}$ reduction I have used mainly gas chromatography (gas products) and nuclear magnetic resonance spectroscopy (liquid products).

2.2.1 Permanganate Titration

Permanganate titration is the method I used to quantify how much H_2O_2 was produced. H_2O_2 is a molecule that can be detected in a variety of ways, including spectroscopy (UV-vis, NMR), decomposition and subsequent oxygen detection or titration. Perhaps the most common method is permanganate titration, because it is a) simple, b) quantitative and c) cheap[52]. It is based on the following reaction:

$$5H_2O_2 + 2MnO_4^- + 6H^+ \rightarrow 2Mn^{2+} + 5O_2 + 8H_2O$$
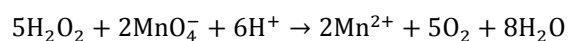
MnO_4^- has a very distinct reddish color, which disappears once it is converted into Mn^{2+}. For this to happen there has to be H_2O_2 present, therefore once all H_2O_2 has been consumed the solution will adopt the characteristic red color of unreacted MnO_4^-. This allows backtracking the original concentration of H_2O_2. This reaction also requires protons, therefore it only happens in acidic environment. On a practical note, addition of the MnO_4^- source should be slow enough to let the reaction happen and avoid MnO_2 formation. The latter is particularly critical as MnO_2 can catalyze decomposition of H_2O_2[52].

2.2.2 Gas Chromatography (GC)

In $CO_{(2)}$ reduction there are several possible gas products, mainly hydrogen, CO, methane and ethylene. The most commonly used method for their detection is gas chromatography[53] because it allows for both product identification and quantification with adequate sensitivity.

A schematic of a GC is shown in Figure 2.9. Briefly, a sample of the gas to be analyzed is injected into a column which slows down the movement of molecules. Each molecular species has a different retention time, permitting identification. At the end of the column there may be a methanizer (to convert oxidized carbon species into methane, easier to detect) and a detector. Each molecule has a different retention time through the column, which enables product identification. An independent calibration with a known concentration gas is required for quantification. I have used two kinds of detectors, always simultaneously:

1. Thermal conductivity Detector (TCD): measures changes in thermal conductivity of the gas phase. It is a non-destructive method and it is mainly used to detect H_2.

2. Flame Ionization Detector (FID): A hydrogen flame ionizes organic compounds in the gas, which are then detected. Preceded by a methanizer which converts carbon-containing species into CH_4, it enables very sensitive detection of hydrocarbons and alcohols as well as CO or CO_2.
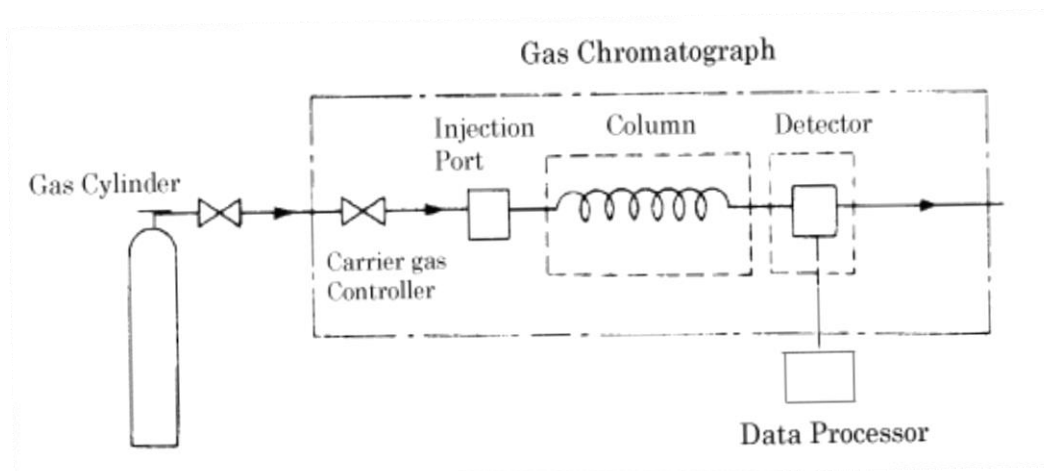
Figure 2.9: Schematic representation of a gas chromatograph. Adapted from [54].

The GC I used was from Stanford Research Instruments. Figure 2.10 shows a characteristic trace from CO_2 reduction on oxide-derived Cu. The signals for both TCD (black) and FID (red) detectors are given over time. In the TCD detector, only the negative peak at 60 s corresponds to a reaction product, in this case H_2. The positive peak next to it is an artifact associated with the sudden release of hydrogen, and the negative signal at 210 s arises from an internal valve switch. The peak at 280 s is due to CO_2 reactant, which is also detected.

In this case the FID detector was preceded by a methanizer, therefore all signals correspond to methane but the retention times are characteristic of the different compounds. The first peak at 160 s is CO, a product from CO_2 reduction; while the second peak is a valve switch. The last feature is CO_2 which has been converted to methane. The reason the peak is so large is that the electrolyte is CO_2 purged. Products are quantified by comparing the area under the peaks to an injection with a known composition.
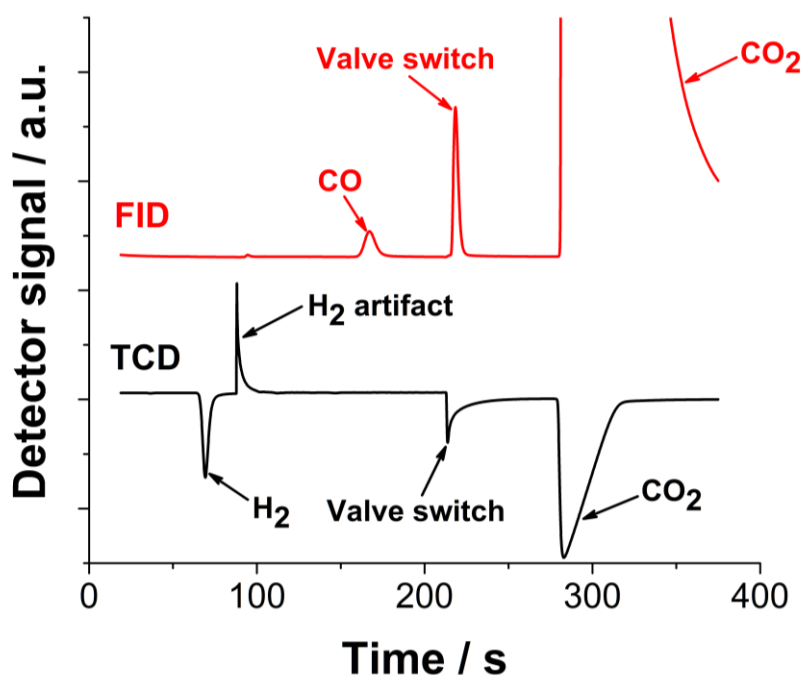
Figure 2.50: GC trace from a typical CO_2 reduction measurement on oxide-derived Cu at -0.5 V in CO_2-saturated 0.5 M $NaHCO_3$. Both FID (red) and TCD (black) traces are present with the various features identified.

2.2.3 Nuclear Magnetic Resonance Spectroscopy (NMR)

NMR spectroscopy is widely used in chemistry for identification of compounds. I used this technique for quantification of liquid products in the electrolyte after $CO_{(2)}$ reduction experiments[43]. The operating principles are fairly simple: nuclei in a magnetic field absorb and reemit electromagnetic radiation. The energy at which this radiation is reemitted depends on the properties of the nuclei and on the strength of the magnetic field. ^{1}H NMR allows for identification of the different types of protons present in a sample –by different meaning they are in a different chemical environment. The peaks are unique for each compound, and their magnitude can then be used to determine the concentration, particularly when related to an internal standard. The internal standard is helpful to obtain quantitative results because the magnitude of the peaks depends on several factors hard to control (status of the instrument, alignment of the sample…).

The NMR at Stanford University was from Oxford Instruments 700 MHz, and the recipe used to prepare the samples was:

- 0.5 mL electrolyte
- 0.1 mL D_2O
- 1.67 parts per million (on a mass basis) of dimethyl sulphoxide (DMSO)

Measurements are simple to conduct and fairly reproducible. When measuring samples in water it is important to suppress its ^{1}H signal (from protons in water). This is achieved by sending a pre-pulse at the water proton frequency. This pulse will saturate their resonance and reduce the intensity of the signal when sending the measurement pulse. Figure 2.11 illustrates an example for NMR spectroscopy on an ethanol standard. There are four main features: at 4.8 ppm there is the water peak, which is very prominent even after suppression. The peak at 3.6 ppm corresponds to ethanol, in particular to the CH_2 block, and is a double duplet. The internal standard, DMSO, appears at 2.68 ppm and the areas under the other peaks are related to it for quantification. Finally, at 1.1 ppm the CH_3 chain in ethanol has a triplet.
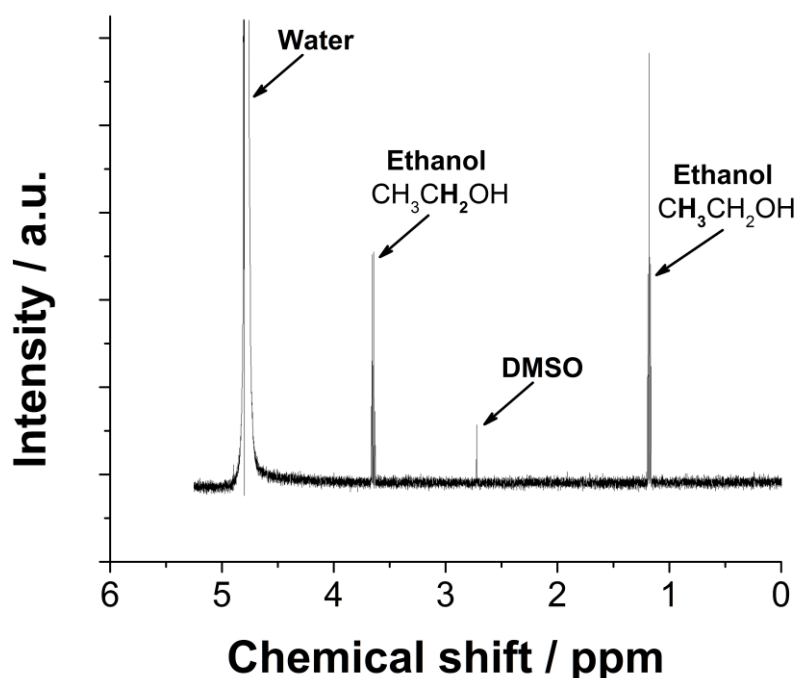
Figure 2.61: NMR spectrum for a standard containing 1 mM of ethanol in water. DMSO and D_2O were added before the measurement. The protons highlighted in bold in the chemical formulas are those responsible for the peak.

2.3 Catalyst Characterization Techniques

2.3.1 Electrochemical Surface Area Measurement

When doing electrochemistry, it is important to know the surface area of the samples. This allows for normalization of the current to exposed area of the material, critical to accurately quantify intrinsic catalytic activity. Depending on the material of the

electrode there are different ways to do that; most of them relying on charge transfer of species between electrode and electrolyte.

- **Hydrogen underpotential deposition (H-upd):** consists of hydrogen adsorption taking place before hydrogen evolution. Used mainly on Pt electrodes, every cm^2 of Pt gives 210 μC of current due to H-upd. The integration is performed as shown in figure 2.12. This method gives ambiguous results on Pt-alloy electrodes, and for that reason it should only be used on pure Pt[55, 56].
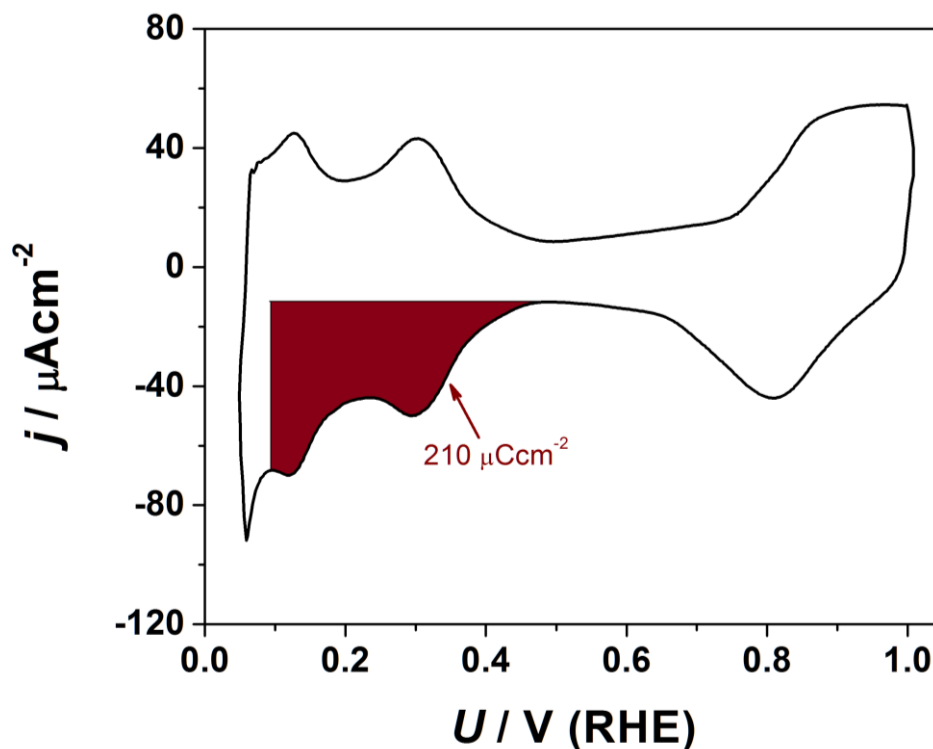
Figure 2.12: Cyclic voltammograms of polycrystalline Pt. The area highlighted in red is used for the H-upd measurement, corresponding to 210 μC/cm^2. Measurement taken in Argon saturated 0.1 M $HClO_4$ at 23 ºC and 50 mV/s with no rotation.

- **Surface oxide reduction:** Similar to H-upd, but in this case relying on reduction of surface oxide. This was my method of choice for Pd electrodes, as exemplified in Figure 2.13. Note that it is highly dependent on the upper potential limit as depth of the oxide layer increases with upper potential. According to Grdén et al[57], for an upper potential limit of 1.2 V, surface oxide coverage on Pd should be 0.5 and charge 210 μC/cm^2. As a reference point, a full oxide coverage is reached at 1.5 V, which would correspond to a charge of 420 μC/cm^2.
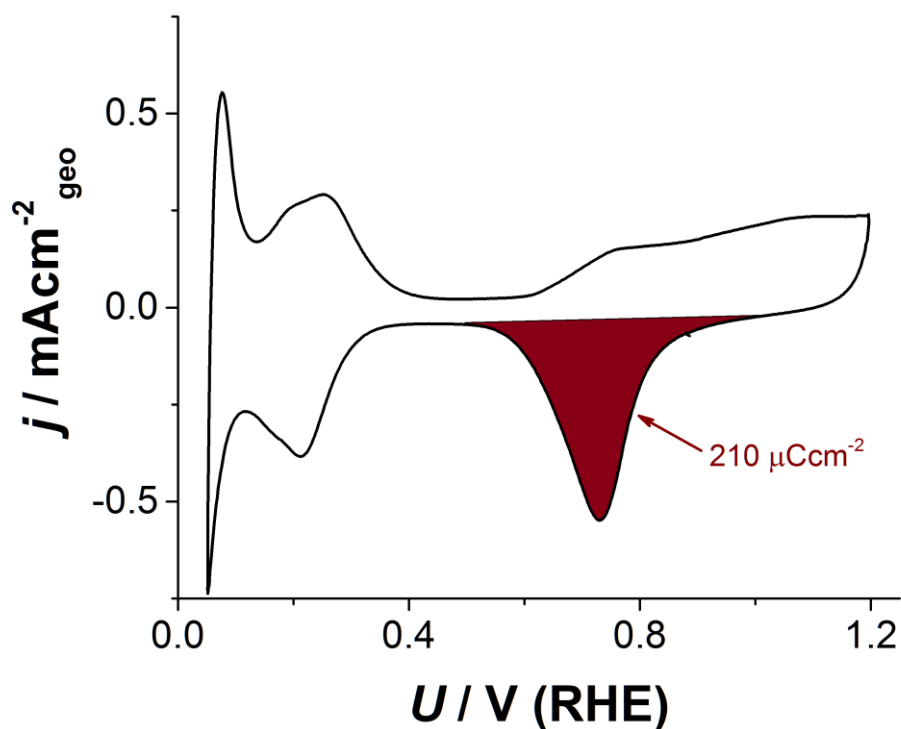
Figure 2.13: Cyclic voltammograms of Pd/C nanoparticles. The area highlighted in red is used for the surface area measurement, corresponding to 210 µC/cm². Measurement taken in Argon saturated 0.1 M $HClO_4$ at room temperature and 50 mV/s with no rotation.

- **CO stripping:** Adsorption of CO to the surface followed by subsequent desorption induced by CO electrooxidation. It is important to ascertain the solution is CO-free when performing CO oxidation. I used this method on Pt or Pt alloys, but it could be used on other electrodes such as Pd, Ir etc. On polycrystalline Pt, a value of ~340 µC/cm² is often used[58], owing to a CO coverage of 80 % (Figure 2.14).
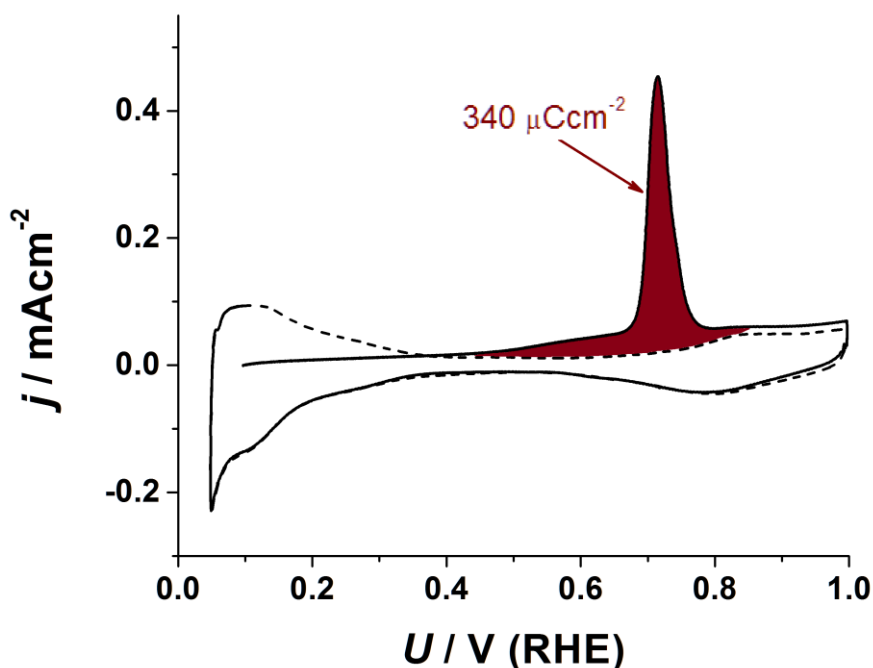
Figure 2.14: CO stripping voltammogram (solid line) for polycrystalline Pt and background CV in Argon saturated electrolyte (dashed line). The area highlighted in red is used for the surface area determination, with an equivalence of 340 µC/cm^2. Measurement taken in Argon saturated 0.1 M HClO$_4$ at 23ºC and 50 mV/s with no rotation. The electrolyte was saturated was CO for 10 min and purged with Ar for 30 min before recording the stripping curve. During all this time the electrode was kept at 0.1 V.

- **Metal upd:** Adsorption of metallic ions from an ion-containing solution and subsequent oxidation. In particular, I used Cu upd from a solution of 3 mM CuClO$_4$ in 0.1 M HClO$_4$. On Pt, the potential is held at 0.32 V for 2 minutes before ramping up the potential at 50 mV/s. For Cu upd on Pt, charge under the peak corresponds to 430 µC/cm^2. This is a very robust method that can be used on many electrodes and using many different probe ions[59, 60].

- **Capacitance:** When no reactions occur at the surface of electrode the latter acts as a capacitor. By comparing the current at this potential region against that of a sample with a known surface area (for instance an atomically flat sample), one can obtain an estimate for the surface area. This is the method I used for OD Cu electrodes, shown in Figure 2.15. These measurements can also be repeated at different scan rates to obtain several data points.
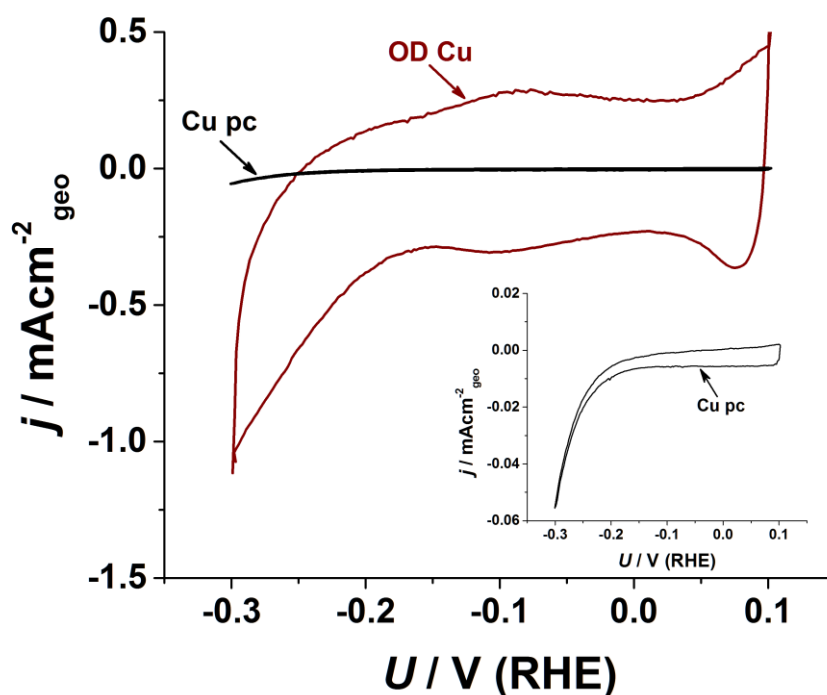
Figure 2.75: Cyclic voltammograms on OD Cu (red) and polycrystalline Cu (black). The inset zooms into the polycrystalline Cu curve. In this case, at 0 V the capacitance for OD Cu is a factor of ~100 higher than for Cu pc. Measurement taken in Argon saturated 0.1 M KHCO$_3$ at 20 mV/s.

2.3.2 X-ray Photoelectron Spectroscopy (XPS)

XPS is a technique used to detect chemical species at the sample surface, up to ~5 nm of depth[61]. This method was used to identify the composition of various catalysts, both in polycrystalline and nanoparticulate form. Paolo Malacrida performed all XPS measurements in this thesis.

XPS is based on the photoelectric effect, explained in Figure 2.16. A beam of X-rays (obtained from an Aluminum anode in the setup used, giving an energy of 1486.7 eV) is sent to the sample and this beam excites electrons in inner core levels of the atoms (the so called photoelectrons) with a kinetic energy of:

$$E_k = h\upsilon - E_b - \phi$$

Where $h\upsilon$ is the energy of the incident radiation, E_b the binding energy of the excited electron and Φ the work function of the analyzer. While the incident radiation can in theory be externally controlled (in practice this is only possible in synchrotron facilities), the binding energy and the work function are element-specific.
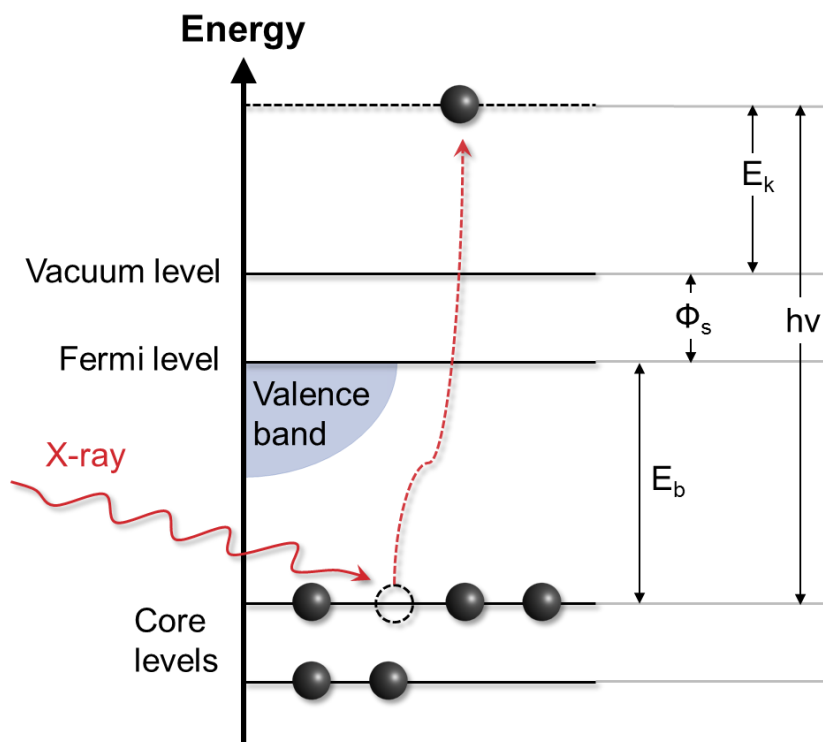
Figure 2.16: Schematic representation of an XPS measurement. The black circles represent electrons, and one of them is excited from a core level to vacuum by an X-ray. Adapted from [50].

The emitted photoelectrons are then collected and measuring their energy permits to determine the element they come from and its oxidation state. In practice only the electrons in the upper layers of the sample can escape and be detected, converting it into a useful tool to probe the surface region. Since emitted photoelectrons would get scattered by any molecules they encounter in their path to the collector, ultra-high vacuum conditions are required to let them reach it and measure their energies. In XPS spectra the number of counts (at a certain electron binding energy) is represented against the binding energy of the electrons.

I found as well particularly useful to look at data from angle-resolved XPS, which gives information on sample composition as a function of depth. This is achieved by simply tilting the sample with respect to the analyzer and taking multiple measurements at varying angles. As the tilting angle increases the emitted electrons will come from closer to the surface.

2.3.3 X-ray Diffraction (XRD)

XRD is a powerful technique to easily determine the crystalline structure of a solid sample[61]. I used it in various instances, but perhaps where it had most impact was on

the Pt-rare earth alloys. XRD is based on the Rayleigh scattering, the interaction between incoming electromagnetic radiation and the valence electrons of an atom. X-rays are elastically scattered by these electrons, and therefore if there is long range periodicity in the atomic arrangement a constructive interference pattern will occur at certain angles. If no constructive interference occurs, for instance in amorphous samples, the emitted radiation will be inexistent. By measuring the intensity of the scattered X-rays as a function of the detector angle it is possible to know the crystalline structure of a material, including phase, space group, lattice parameters etc.
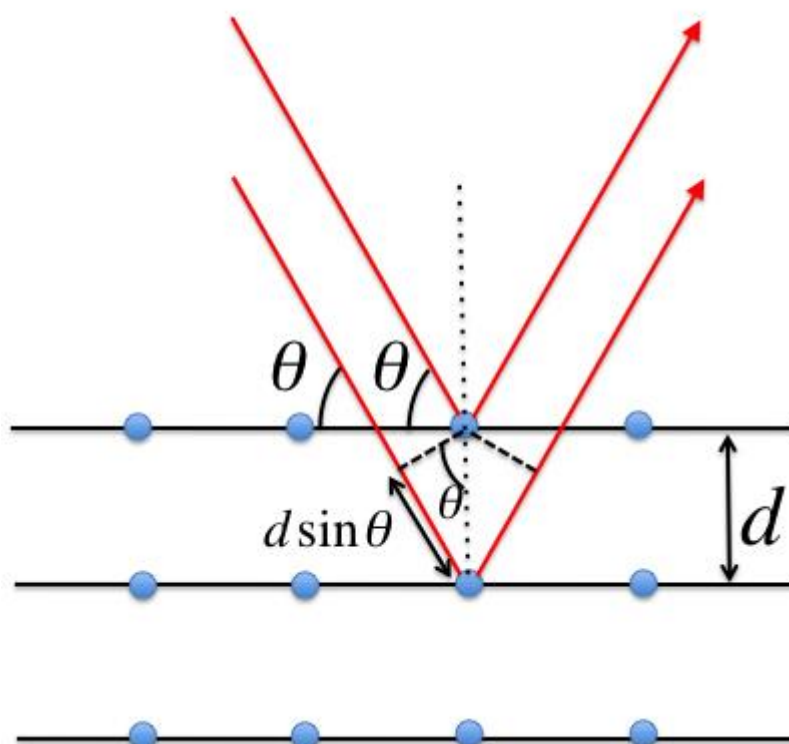
Figure 2.17: Schematic of XRD principle. X-rays are shown as red lines, atoms in the crystalline structure in blue. Adapted from [62].

Figure 2.17 shows a schematic diagram of XRD. In particular, Bragg's law gives the conditions for constructive interference:

$$n\lambda = 2dsin\theta$$

Where d is the distance between planes, λ the radiation wavelength and θ the angle of incidence of the radiation. Typically it is possible to get insight from a measurement by comparing it to a database or to similar materials. This is exemplified by Figure 2.18 with the XRD of polycrystalline Pt. Each of the different facets present gives rise to a distinct peak.
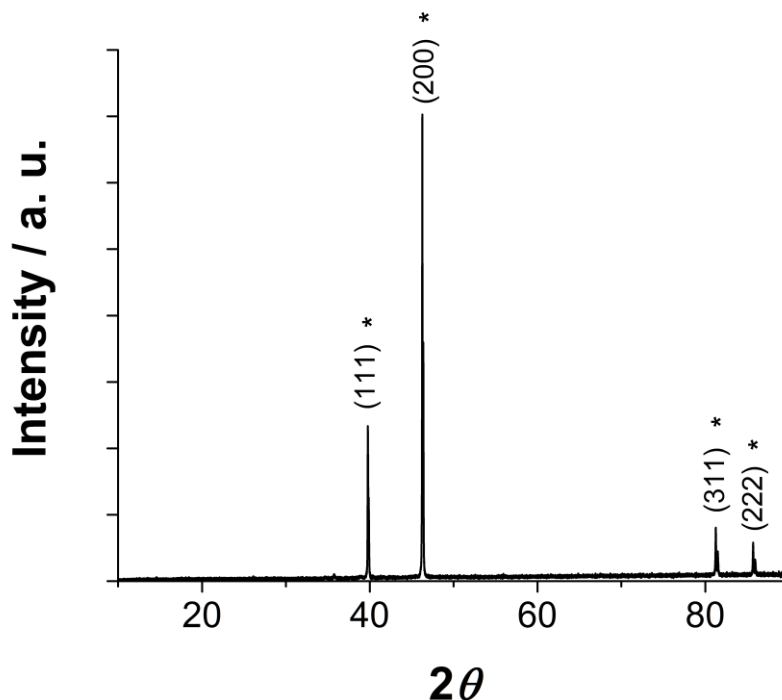
Figure 2.18: XRD on a Pt polycrystalline sample. The signal due to known facets has been indicated by specifying the facet in parentheses. * mark the positions according to literature[63]. Measurement performed by Ifan Stephens.

2.3.4 Transmission Electron Microscopy (TEM)

TEM is a UHV microscopy technique capable of providing atomic resolution images of materials[61]. In contrast to XRD or XPS which give average values on a wide area, TEM gives very local information, even at the atomic level. Thus, one has to be careful in the analysis of results and ensure phenomena occur over the whole sample and not on a particular location.

TEM relies on a beam of electrons crossing through a specimen and being subsequently detected, resulting in a 2D projection (Figure 2.19). Electrons are oriented via electromagnetic lenses, which permit easy focus and magnification of the images. Intensity in the 2D projection is dependent on the atomic number, and chemical composition of a particle can be derived on this basis. However, other positive chemical identification methods are often used in combination.

One of such methods is energy dispersive X-ray spectroscopy (EDS). It is based on inner shell electrons on a specimen absorbing enough energy to ionize an atom, resulting in subsequent relaxation phenomena which emit characteristic X-rays. Incident electrons may also scatter inelastically with other nuclei, with the lost energy giving rise to an X-ray background known as Bremsstrahlung radiation. Overall,

characteristic peaks from relaxation rise over the background signal, which allows for elemental identification. Since in TEM initial electrons can be directed accurately, EDS signal will arise from the image area.
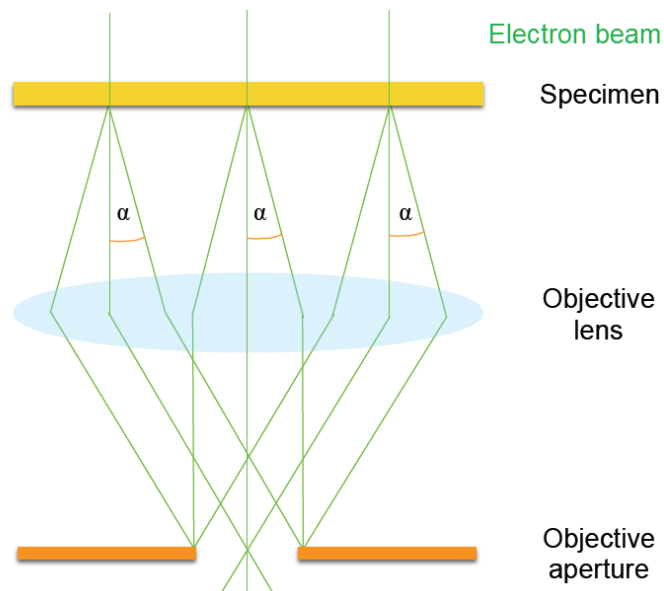
Figure 2.19: Schematic of the formation of a bright field image in TEM. The electron path is drawn in green lines, and the effects of specimen and lenses are clearly visible. Adapted from [64].

In my thesis, TEM in combination with EDS was used to determine the composition and atomic structure of Pt-Hg and Pd-Hg nanoparticles. All TEM measurements were performed by Davide Deiana, from DTU CEN/Danchip.

I personally find the technique very visual and capable of giving unique insight on a sample. Especially elemental mapping via EDS brings TEM to a whole new level, enabling chemical identification at atomic scale. Drawbacks are that it is ex-situ and it gives localized information.

2.3.5 Temperature Programmed Desorption (TPD)

Temperature programmed desorption is a UHV technique very useful to determine how strongly a probe molecule (in my case always CO) is bound to a sample[61]. The principle is simple: said probe molecule is dosed in the UHV chamber while the sample is kept at a temperature low enough so molecules adsorb to it. After the desired dose, temperature is ramped up in a linear manner while a mass spectrometer monitors the

desorption of molecules as a function of sample temperature. Analysis of the desorption peak shape and position gives information on binding energies, and since these depend on the facets present, it can also give information about the sites present at a surface. Accurate extraction of binding energies from a TPD analysis is challenging because temperature-dependent adsorbate coverage needs to be taken into account. In my case I was mostly interested in the facets present and a simple deconvolution of the peaks was sufficient.

I operated TPD myself at Stanford, but given the problems I had with that setup I will not show any of this data here. Instead, all results I show were obtained by Tobias Johansson in the setup at DTU. Unless otherwise stated, temperature ramp was of 2 K / s and CO doses were of ~200 L (equivalent to $2 \cdot 10^{-7}$ mbar for 17 min).

3 Oxygen reduction on Pt-rare earth alloys

3.1 Introduction

Fuel cells have been a very active subject of research in the recent times. Three of the main factors making them attractive are a) potentially higher efficiency (up to 60 %) compared to Diesel engines (which have 25 % of efficiency); b) enhanced energy security as their operation does not rely directly on oil or gas; c) silent operation and leaving only water as the main byproduct. The original concept dates back to 1828, when William Grove extracted electrical energy from the reaction of hydrogen and oxygen to form water:

$$H_2 + \frac{1}{2}O_2 \rightarrow H_2O \qquad\qquad U^0_{O_2/H_2O} = 1.23\,\text{V}$$

Fuel cells have since evolved and their concept has been expanded to include other reactants than hydrogen and oxygen, but regardless of that their principle of operation is very similar. A fuel (typically hydrogen but it could also be methanol, ethanol etc.) is oxidized at the anode producing protons and electrons. Protons cross a proton-conducting membrane while electrons are forced through an external circuit generating electricity. Protons and electrons recombine at the cathode with an oxidant, typically oxygen (in which case water is formed). Variations exist depending on the charged species crossing the membrane, but the core idea would remain to extract electricity from the chemical bonds of molecules.

A non-exhaustive common distinction classifies fuel cells according to operation temperatures[65].

- **Solid oxide fuel cells:** They operate at high temperatures (600-800 ºC), making them valid for stationary and/or long term operation. Perhaps the main issue they face is the lack of stable materials at such high temperatures. Research efforts focus on decreasing operating temperature or stabilizing materials[65, 66].

- **Intermediate temperature fuel cells:** Operating at a temperature of 150-400 ºC, materials are more stable than in solid oxide fuel cells. The core challenge is

to develop polymeric membranes able to conduct protons efficiently at such temperature[65].

- **Low temperature fuel cells:** Working below 100 ºC permits fast start/stop cycles and the use of highly efficient membranes, but the slow reactions at the catalyst layers limit their overall efficiency. They also suffer from poisoning from impure reactant streams as well as water management issues[65]. A possible subclassification is given by the membrane used, with possibilities including polymer electrolyte membrane, phosphoric acid or alkaline exchange membrane.

All the work in this section was carried out in relation to polymer electrolyte membrane (PEM) fuel cells; a particular subset of low temperature fuel cells using a polymeric membrane to separate anode and cathode. Acidic membranes, such as Nafion, are higher performing than their alkaline counterparts and readily available today[67]. A schematic of a PEM fuel cell is exhibited in Figure 3.1. Oxygen is often the oxidant at the cathode, and even when using expensive Pt-based catalysts oxygen reduction is the bottleneck in efficiency[20, 47, 65]. PEM fuel cells are promising for a variety of applications: stationary power generation, consumer electronics etc. I will focus the following analysis on automotive applications, but similar conclusions could be drawn for other usage cases. For transportation functions, fuel cells are interesting because they enable long driving ranges and low fuelling times very similar to internal combustion engines, but using (potentially) renewable and non-polluting fuels. For instance, for Toyota's commercially available vehicle, named Toyota Mirai, range is of 690 km and refueling takes 3 minutes[68]. To date official numbers on fuel consumption have not been released.
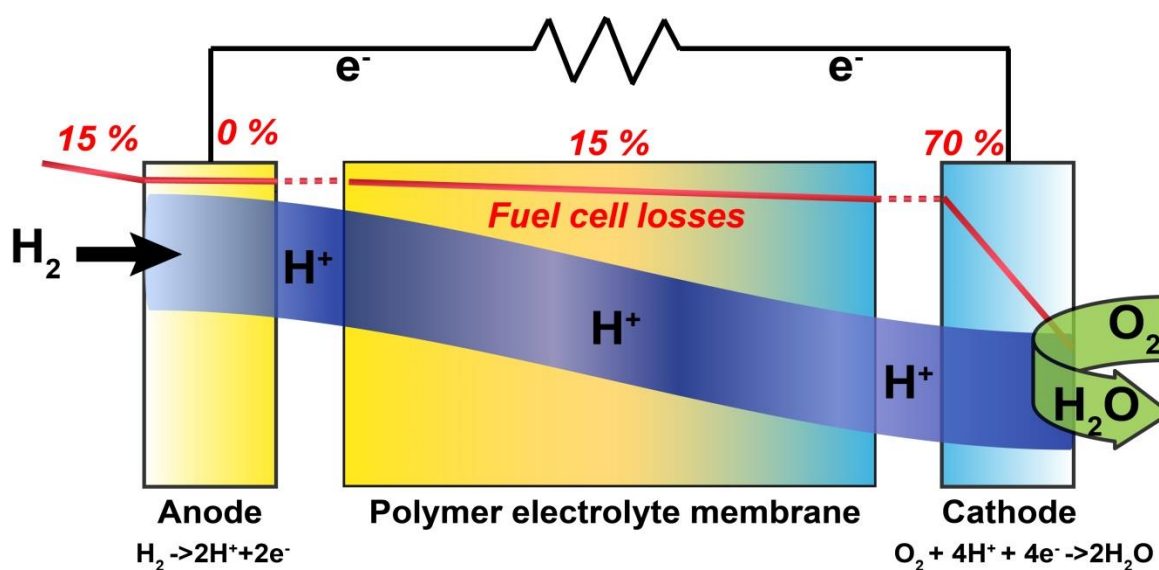
Figure 3.1: Schematic representation of a PEM fuel cell. The path of hydrogen is shown with a blue background and the corresponding reactions at anode and cathode are indicated below. The red line represents percentage of losses over the whole fuel cell (based on data from Gasteiger

and coworkers[65]). From left to right, efficiency losses are due to hydrogen transport through the gas diffusion layer, hydrogen oxidation, membrane resistance losses and oxygen reduction.

As of today, fuel cell cars are sold in the hundreds globally –out of 65 million cars sold per year–, owing mainly to their high prices and the lack of a suitable hydrogen infrastructure. Decreasing the cost of fuel cells is a high priority, after which hydrogen infrastructure could be deployed. In Figure 3.2 I show the cost of the engine for different automotive technologies; internal combustion engines, batteries and fuel cells. For simplicity, the data represents the cost of the engine exclusively; fuel costs, maintenance, infrastructure and other costs are excluded from this analysis. Clearly, internal combustion engines are the cheapest option, owing to decades of development and mass manufacturing. Batteries are three times as expensive on a per kW basis, and fuel cells are the most expensive option unless mass manufactured, in which case they are on par with batteries. This highlights the importance of economies of scale, enabling a five-fold cost reduction per kW from increasing production from 1.000 to 500.000 units. However, even with such mass production fuel cells would still remain twice as expensive as internal combustion engines.

To understand how to reduce cost further I have included a breakdown for fuel cell costs in the same graph. In light blue I show cost associated to stack (framing, membrane, gas diffusion layers etc), and in dark blue that related to balance of plant (pumps, blowers etc). In dark red is the cost of the platinum catalyst. As shown in the graph, ramping up production would reduce costs for stack and balance of plant by ~85 %. Instead, the cost for the Pt catalyst is only reduced by 40 % when increasing production volume –the high cost of Pt as a raw material being the cause[69]. Therefore, reducing the amount of Pt used would have a strong impact in fuel cell price.
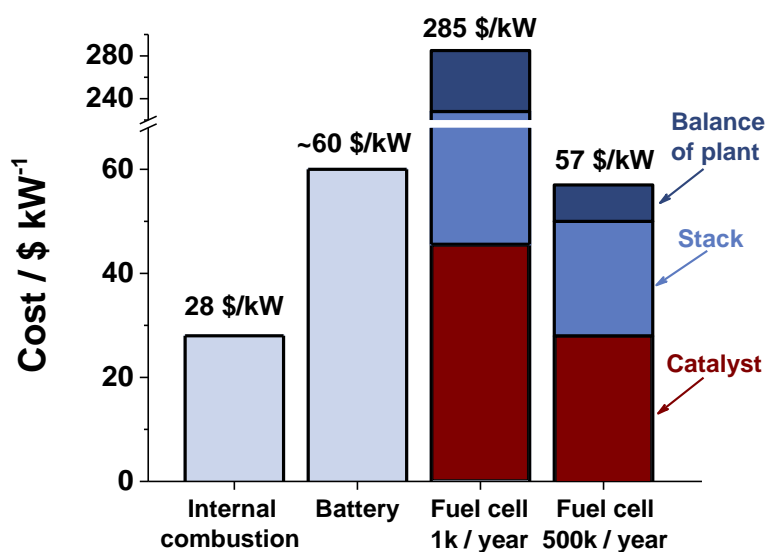
Figure 3.2: Cost per kW of several automotive engine technologies. Data for internal combustion is from Mercedes-Benz[70], battery from Tesla Motors[71] and H_2/O_2 PEM fuel cell from DOE[72]. A breakdown of fuel cell costs by part is also given. Note the strong dependency on economies of scale for fuel cells, as exemplified by production of 1.000 and 500.000 cars per year.

At the anode, hydrogen oxidation is highly efficient in acid conditions[73], and 90 % of the platinum catalyst is used at the cathode[65]. At present, even when using high loadings the efficiency of the cathodic oxygen reduction accounts for ~70 % of the total losses[20, 47] (Figure 3.3). Therefore, to reach equivalent performance cost reductions should come from catalyst improvements.
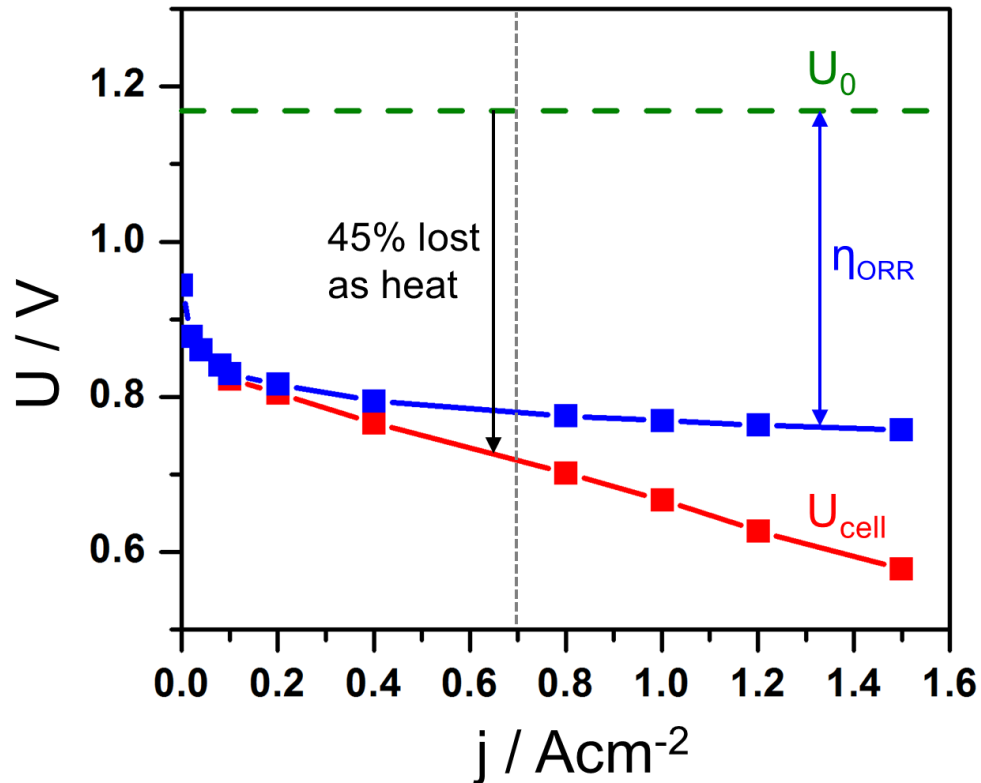
Figure 3.3: Polarization curve for a state-of-the-art fuel cell and impact of oxygen reduction on the performance. The thermodynamic ideal efficiency is shown as the green dashed line; the solid red line is the performance of a fuel cell and the blue line represents the losses attributed to ORR with a typical catalyst made of Pt/C nanoparticles. Adapted from[20, 47].

3.2 State-of-the-art

Traditionally, efforts have been oriented to a) lowering the amount of Pt; b) discovering active catalysts without Pt. Regardless of the approach, catalysts should be stable over extended operation. Up to date, the possibility of using non-Pt materials in acid environment has shown limited success despite recent advances[74, 75, 76]. First steps of technological implementation have mostly occurred through Pt materials, and avenues for lowering their costs are being explored on three main areas:

1. Catalyst-support interaction to increase Pt active surface area and stability[77, 78, 79, 80, 81].
2. Nanoparticle size and shape control[82, 83, 84, 85, 86, 87, 88].
3. Alloying Pt with other metals seeking an activity improvement[32, 33, 89, 90].

These are all areas worth of investigation. Fundamental research plays a bigger role in finding new materials with better performance than Pt, and that is also what I focused on. A widespread way to study the catalyst in relevant fuel cell conditions is by carrying out measurements in liquid electrolyte, typically perchloric acid[47], using rotating ring-

disk electrode setups. This allows measurements of the relevant reactions with a limited set of parameters involved, ruling out factors such as humidification, gas streams, architecture etc. which matter for fuel cells performance, but are less relevant when exclusively assessing different catalysts. For that reason, all measurements I refer to in this section were done using 0.1 M $HClO_4$.

My research builds up on earlier results obtained in our laboratory. Increasing activity by alloying Pt with late transition metals (Fe, Co, Ni and Cu) has been a well-known strategy for many years[91]. This is exemplified by the volcano plot in Figure 3.4, where the x-axis represents the theoretically calculated binding energy of OH to Pt-based surfaces and the y-axis is the experimentally measured activity (both relative to Pt). As shown in the volcano, Pt binds oxygen slightly too strongly for optimal activity. Alloying Pt with late transition metals weakens the Pt-O bond and results in higher activity. The most active surfaces are single crystals of $Pt_3Ni(111)$, which present a nearly optimal binding energy and are very close to the top of the volcano, resulting in almost an order of magnitude activity enhancement over Pt. However, under operating conditions the performance of these alloys tends to degrade due to dealloying of the late transition metal[92, 93, 94, 95]. Recent results have shown that suitable heat treatment can stabilize these alloys, at least in accelerated stability tests[86, 96, 97, 98]. The propensity of transition metal compounds to dealloying could be rationalized by the negligible enthalpy of formation these alloys (Figure 3.5). Instead, alloys of Pt and early transition metals (such as Y or La) present a much lower enthalpy of formation, which might stabilize them kinetically against dealloying[20, 33]. In particular, according to theory predictions Pt_3Y should be very active for the oxygen reduction[33] as shown in Figure 3.4.

For Pt_3Y, DFT calculations assumed yttrium would be present as close to the surface as the second layer, which turned out not to be the case in experiments. Y is so oxophilic that it leaches out leaving a thick Pt overlayer behind[99, 100]. This means theoretical predictions were done on a different surface than experiments. Having several monolayers of Pt on top of a Pt-Y alloy implies neither bifunctional nor ligand effects can play a role in the increased activity. Instead, strain effects, namely a Pt compression with respect to the pure metal, could be the main factor weakening the Pt-O binding energy[100]. Other possibilities are structural effects[101]. To date, accurate modelling of the surface has remained challenging, mostly owing to strain relaxation effects. Initial theory calculations were irrelevant in this case, but it shows how a shift in focus (by alloying Pt with early transition metals instead of late) can unveil interesting results.
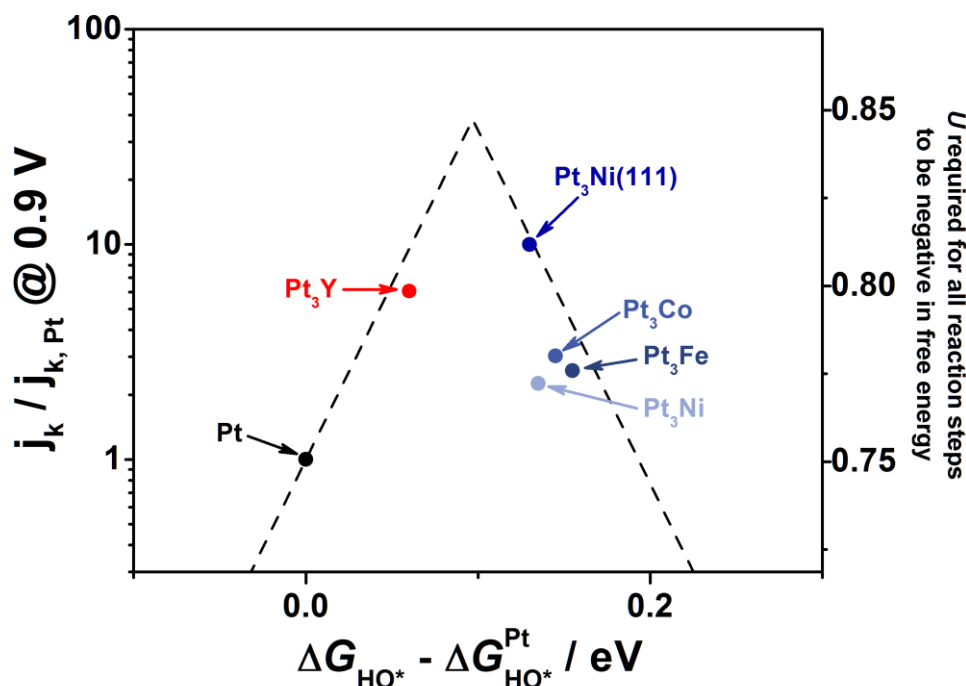
Figure 3.4: Volcano plot for different oxygen reduction catalysts. The x-axis is the difference in OH binding energy with respect to pure Pt. The left y-axis is the kinetic current density relative to polycrystalline Pt at 0.9 V, and the right y-axis is the computed onset potential at standard conditions. Plot adapted from [20], with points for Pt and Pt_3Y from [33], Pt_3Ni (111) from [89] and Pt_3Co, Pt_3Ni and Pt_3Fe from [31, 102]. All catalysts were tested in a RRDE setup in O_2-saturated 0.1 M $HClO_4$.

3.3 Oxygen reduction on Pt₅Gd

Based on earlier works on Pt_5La and Pt_5Y[20, 99] we chose to investigate two other polycrystalline alloys of platinum and rare-earth metals: Pt_5Gd and Pt_5Sm. The ratio 5:1 was chosen on the basis of the most stable phases thermodynamically[103]. The very negative heat of formation of such alloys may make them stable under reaction conditions, which could prevent dealloying occurring in other Pt alloys (traditionally Pt and late transition metals such as Fe, Cu, Co…). It is worth noting that, similar to the yttrium case, stabilization of rare earths by alloying is not enough to prevent dissolution of the rare earth element into the acidic electrolyte. Typically, for rare earths dissolution will occur above ~-2.5 V, and alloying would bring this to ca. above -1 V, which is still far from operating potentials at 0.7 V[104, 105]. It is also important to be aware of metal prices; for instance Gd is traded at $ 200 / kg, far below the $ 40.000 / kg of Pt[106].
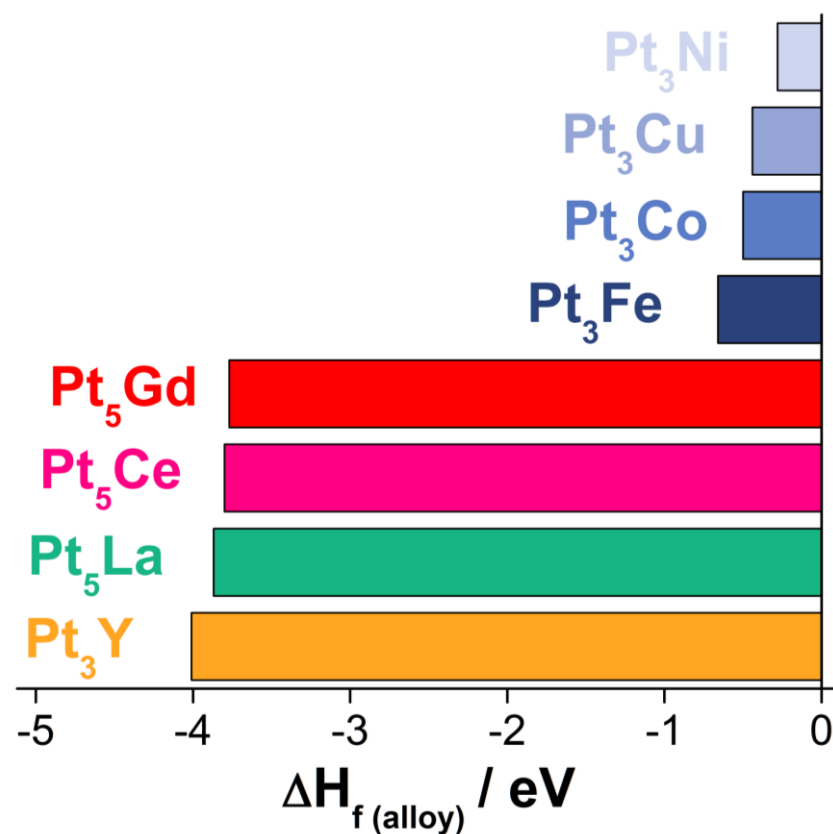
Figure 3.5: Experimental enthalpies of formation per formula unit. Values respectively taken from: Pt_3Ni[107], Pt_3Cu[108], Pt_3Co[109], Pt_3Fe[109], Pt_5Gd[104, 110], Pt_5Ce[104, 110], Pt_5La[104, 110], Pt_3Y[110].

Before performing electrochemical measurements, the samples were sputter-cleaned by Paolo Malacrida in UHV and their cleanliness was confirmed with XPS. Then María and I took them to the electrochemical cell and measured oxygen reduction. We started by measuring on Pt_5Gd samples. In Figure 3.6 I show oxygen reduction voltammetry on Pt_5Gd, Pt and Pt_3Y, the most active polycrystalline sample to date. For all samples, at high potentials there is an exponential increase in current, which plateaus at ~-6 mA/cm^2 as oxygen becomes mass transport limited. The closer the exponential curve is to the reversible potential of 1.23 V, the more active a sample is. Clearly, Pt_5Gd is closer to 1.23 V and therefore has a higher activity than Pt. To quantify how much we extracted the kinetic current density, shown in Figure 3.6 –that way we omit mass transport limitations. A widespread standard in the field is to measure the activity of a catalyst based on the kinetic current density at 0.9 V[47]. For instance, for Pt that value is of 2 mA/cm^2 [84]. For Pt_5Gd kinetic current density at 0.9 V reaches 10 mA/cm^2, which means it is five times more active than pure Pt. This is similar to the activity improvement reported in Pt_3Y. In addition, Pt_5Gd is resistant to extended cycling. After 10.000 cycles between 0.6 and 1 V the activity decreased only by a 14 %.
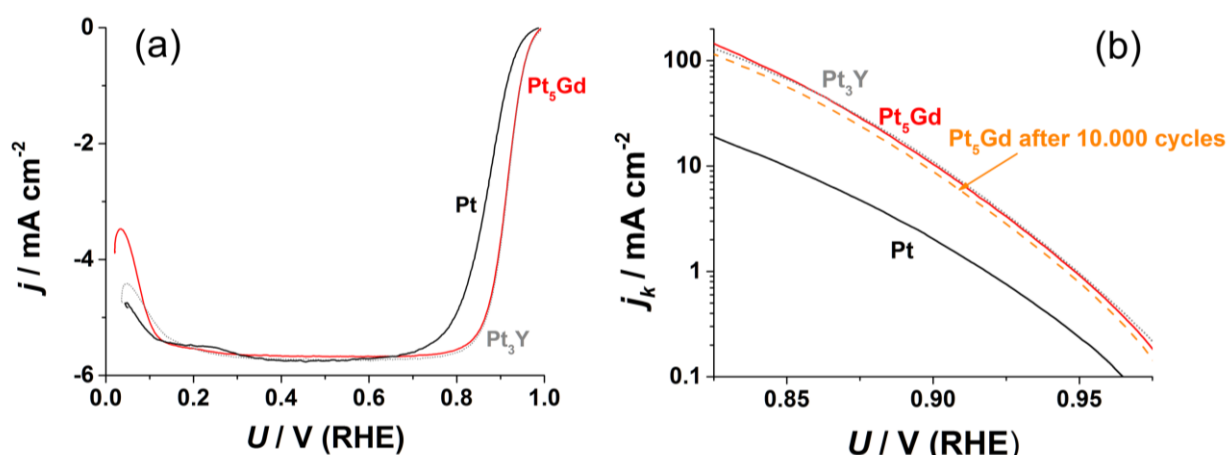
Figure 3.6: Oxygen reduction on Pt_5Gd (red) as compared to Pt (black) and Pt_3Y (grey). a) Disk voltammograms. b) Tafel plots showing the kinetic current density of the samples. A Pt_5Gd measurement after 10.000 cycles between 0.6 and 1 V is also included (orange). All measurements taken in O_2-saturated 0.1 M $HClO_4$ at 50 mV/s and normalized to geometric surface area.

The next step was to understand why Pt_5Gd was active. For that we took the sample out of the electrochemical cell and back to the XPS chamber, where Paolo characterized it by XPS. AR-XPS showed results very similar to those obtained on Pt-Y samples; a thick Pt overlayer on top of a Pt-Gd substrate (Figure 3.7). The overlayer is a result of the exposure to the electrolyte, where there is a significant driving force for Gd to leach out of the sample leaving Pt behind. These results discard electronic and bifunctional effects as the main causes behind the activity increase, given that they would require Gd near the surface of the sample. The simplest explanation for the enhancement in activity is a compressed Pt overlayer relative to Pt(111) (see Figure 3.7). As a result, the surface is less reactive and the activity enhanced[90, 111]. XRD experiments show the phase of the Pt_5Gd alloy is hexagonal. Using this phase as a substrate, DFT calculations (performed by Ulrik Grønbjerg) support a compressed Pt overlayer, but also show that strain relaxation on the topmost layer must play an important role as otherwise Pt would be too compressed. Determining how much strain relaxation there is has remained an elusive piece of data, both computationally and experimentally.

Another option for the activity enhancement would be that the Pt overlayer contains an increased amount of steps at the surface. These destabilize OH at adjacent terrace sites, resulting in enhanced activity. Such effects have been reported for stepped single crystals[101, 112].
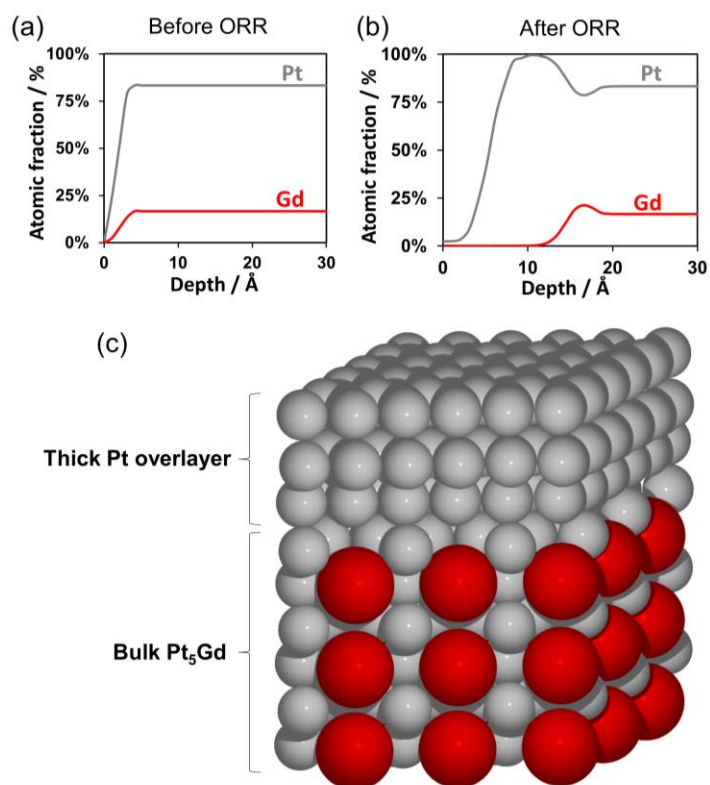
Figure 3.7: Pt_5Gd structural characterization. a) AR-XPS analysis after sputtering the sample and before introducing it into the electrochemical cell. b) AR-XPS after electrochemical measurements. Carbon and oxygen traces due to sample transfer have been omitted from the plots. c) Schematic representation of a compressed Pt overlayer on a Pt_5Gd alloy. XPS measurements performed by Paolo Malacrida; schematic designed by Ulrik Grønbjerg.

3.4 Trends in oxygen reduction on Pt-rare earth alloys

Encouraged by these results we also purchased and tested other alloys of Pt and rare earths with the same stoichiometry. XPS measurements showed a nearly identical behavior for all of them: during sputtering rare-earths were metallic, they became oxidized after air exposure and after electrochemistry all traces of oxide disappeared, with only metallic peaks present. In addition, a thick Pt overlayer was present only after electrochemistry, supporting the notion that rare earth atoms close to the surface dissolve in the electrolyte. The activity in all cases was at least three times that of Pt, and samples were in general stable.

While activity data has been successfully reproduced by other groups, there has been some controversy in the literature as to what is the origin of the enhancement. Bifunctional effects have been suggested by Yoo and coworkers[113], but they would require rare earths present at the surface. Thermodynamics considerations of the dissolution potential presented in the previous section as well as our own surface

characterization data suggest that is not the case, but in order to completely rule that hypothesis out in-situ measurements would be required.

XRD data showed that these Pt_5X alloys have an hexagonal Cu_5Ca type structure from La to Gd. The structure of alloys from Tb to Tm is mainly hexagonal, perhaps with a minor orthorhombic phase. At the point of writing this thesis results were not conclusive. However, the argumentation that follows holds for both hexagonal and orthorhombic phases. Lattice parameters derived from XRD are in good agreement with the literature[114]. In particular, Pt-Pt lateral spacing in the bulk, determined by the lattice parameter *a*, was used as a good descriptor of the activity. The parameter *b* could also be used as it is proportional to *a* (both in hexagonal and orthorhombic phases), but for simplicity all further analysis will be based on *a*. This particular lattice parameter impacts on the compression of the Pt overlayer. As *a* decreases, Pt-Pt distance is reduced both in the bulk and in the overlayer, which in turn weakens the Pt-O bond and enhances ORR activity. This is represented by the right leg of the volcano in Figure 3.8. After a certain degree of compression in the bulk has been achieved, activity decreases again, as shown by the left leg. This occurs right after Pt_5Tb, which opens room for three main hypotheses, all dependent on the precise structure of the Pt overlayer:

- The Pt overlayer is more and more compressed as *a* decreases. As a result, binding strength keeps on weakening with a maximum at Pt_5Tb, after which activity decreases.
- After Pt_5Tb, the level of compression is so high that the Pt overlayer collapses and finds a new equilibrium at a lower compression level. This would strengthen Pt binding relative to Pt_5Tb and lower activity.
- The crystalline structure might change slightly from Pt_5Tb to Pt_5Tm, which could lead to different overlayer thickness or faceting.
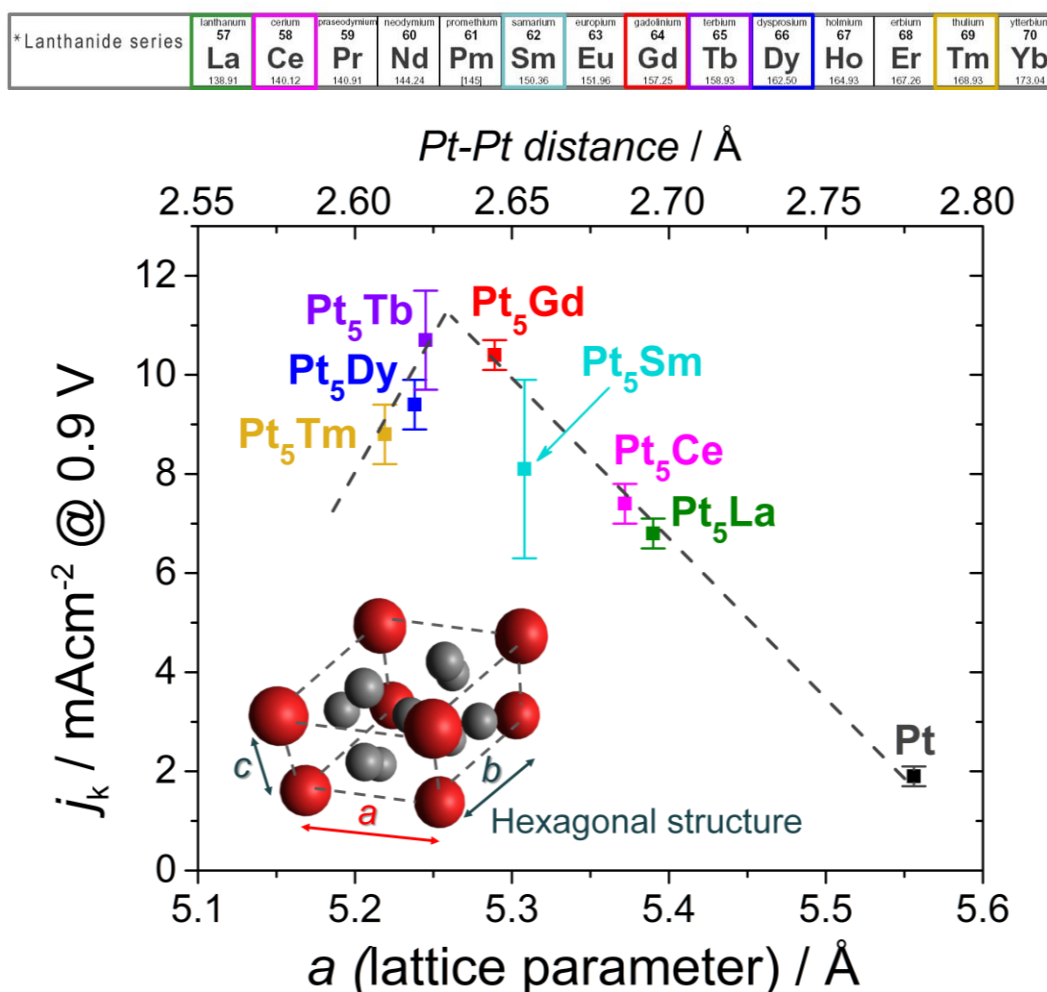
Figure 3.8: Trends in oxygen reduction on polycrystalline Pt-rare earth alloys. The top figure shows the fraction of the periodic table corresponding to rare earth elements, ordered by atomic number. The elements whose Pt alloys were measured are highlighted in colors. The bottom figure represents kinetic current density at 0.9 V *vs* lattice parameter *a*, calculated from XRD measurements. *a* is equivalent to Pt-Pt lattice distance in the bulk, as shown in the top X-axis. The dashed lines serve as a guide to the eye. The inset is a representation of a hexagonal structure, with lattice parameters *a*, *b* and *c* indicated. Rare earths are depicted in red; Pt in grey. Electrochemical measurements were done with a rotating ring-disk electrode setup in O_2-saturated 0.1 M $HClO_4$ at 50 mV/s and normalized to geometric surface area. Figure adapted from María Escudero-Escribano.

Knowing the exact properties of the overlayer is complex by itself, even more when only the top layer matters. Proving or discarding these hypotheses is very challenging. Using top layer sensitive experiments such as temperature programmed desorption may be a way forward, but there does not seem to be a simple method to test the hypotheses.

I would like to point out that this analysis is presumably only valid for samples with similar strain relaxation. Should a sample have different strain relaxation, for instance induced by a thinner Pt overlayer, the results would not be directly comparable to Pt-rare earth alloys.

3.5 Outlook

Alloys of Pt and rare earths hold promise as oxygen reduction electrocatalysts. In particular, Pt_5Gd and Pt_5Tb, exhibit a fivefold enhancement in activity over pure Pt in the polycrystalline form. Rare earth elements dissolve in the acidic electrolyte and leave behind a compressed Pt overlayer at the surface of the electrode responsible for the activity increase. Compression of the bulk is determined by the lattice parameter *a* in the structure of such alloys, which in turn is a good descriptor of the activity. The high enthalpy of formation of these materials might stabilize them against corrosion in operating conditions[100].

Based on these results, I would like to underline three additional points from this section:

- Special attention should be paid to characterizing catalysts under conditions as close as possible to operation. By definition a catalytic reaction is a dynamic environment and it can change the nature of the materials used[115, 116]. In the Pt-rare earth alloys case for oxygen reduction, understanding is only possible when analyzing the catalyst *after* the reaction (ideally it should be *during* the reaction, but for practical reasons that is not always possible).
- While the activity of Pt_5Gd and others is very high, $Pt_3Ni(111)$ is still the most active surface for ORR, being almost twice as active as Pt_5Gd. The rational for working on these rare-earth alloys is that they might be more stable than Pt-Ni under operating conditions, and that still remains to be proven (especially in the nanoparticulate form)[100].
- From the trends derived here and in other works there seems to be a fundamental limitation to the activity for oxygen reduction. Further increases in activity could come through alternative approaches than alloying, such as ionic liquid coatings[86, 117] or doping to break the scaling relations[118].

In the future, the main challenge for this project will be to find a method to synthesize these materials in a high surface area form and optimize their performance. This is particularly challenging given the very different oxidation energies of Pt and rare-earth metals. Nevertheless, a first proof of principle of the concept was achieved by making clusters in UHV[100]. From an application standpoint, the feasibility of the chemical synthesis method, the durability of the material and ultimately cost of competing alternatives will determine the viability of these catalysts.

4 H$_2$O$_2$ synthesis on single site electrocatalysts

4.1 Introduction

Today, hydrogen peroxide is a highly commoditized product used for a variety of applications including chemical synthesis, pulp and paper bleaching and environmental remediation[13]. Approximately 4 B kg of H$_2$O$_2$ are produced per year (Figure 4.1). To put this number in perspective I find useful to compare it to total human population, ~7 B people. This means that on average each person on Earth uses more than 0.5 kg of H$_2$O$_2$ every year. The use of H$_2$O$_2$ is increasing, mainly driven by higher demand from current applications, but also due to rising technologies. These include wastewater treatment, where H$_2$O$_2$ can be used to oxidize pollutants, and specialty uses in the dairy and mining industries. These novel uses rely on the benign properties of H$_2$O$_2$ as an oxidant, decomposing itself into harmless O$_2$ and H$_2$O and leaving no other chemicals in the process.

Pulp and Paper Bleaching - 1.7B Kg

Textile - 0.3B Kg

Treating Water - 0.1B Kg

Chemicals Synthesis - 1.7B Kg **Other - 0.1B Kg**
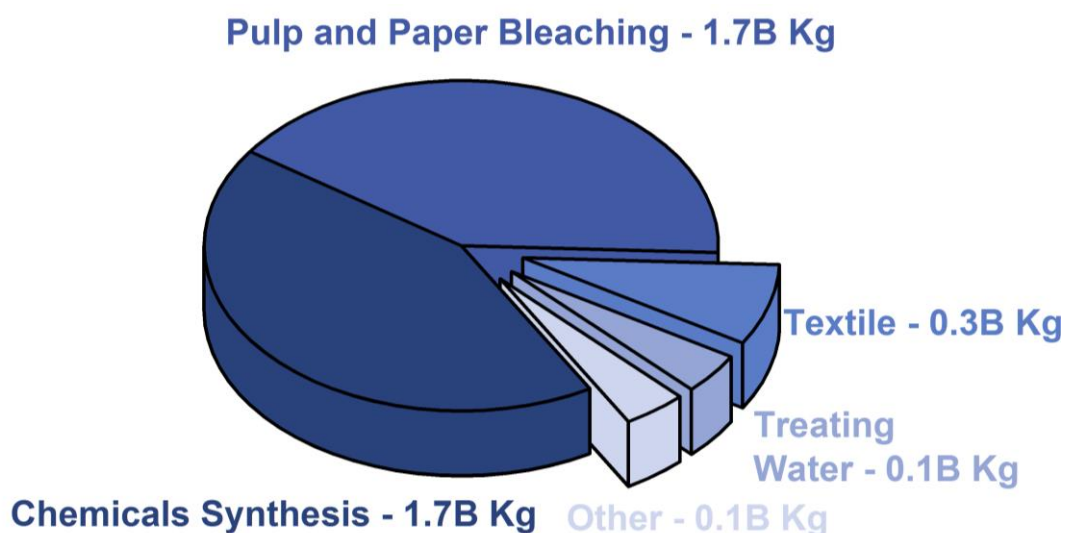
Figure 8: Annual H$_2$O$_2$ production by application. Global production totals ~4 B / year. Data adapted from Campos-Martin et al[119].

Hydrogen peroxide as a molecule was first discovered in 1818 by Louis Jacques Thénard. He produced it by treating barium peroxide with nitric acid[120]:

$$2HNO_3 + Ba(OH)_2 \rightarrow Ba(NO_3)_2 + H_2O_2$$
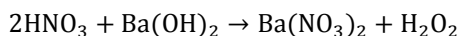
This process was actually used until the mid 20th century, when the anthraquinone process was first commercialized by BASF. Today, practically all H$_2$O$_2$ is produced via this route. The anthraquinone process is a batch synthesis method relying on the sequential oxidation and reduction of quinone molecules[13]. This process requires large economies of scale to be economically competitive, which forces production to be very centralized and far from the end point of use. In fact, there are only about 60 plants worldwide producing the 4 B kg of H$_2$O$_2$ consumed annually[119]. H$_2$O$_2$ is sold at a market prize of ~$1.5[121]. In Figure 4.2 I show a breakdown of the costs for the anthraquinone process. Plant and solvent take a major share of the cost, while raw materials and energy represent a minor share. Transportation adds a 20 % on average, but is highly variable and dependent on location and order size.
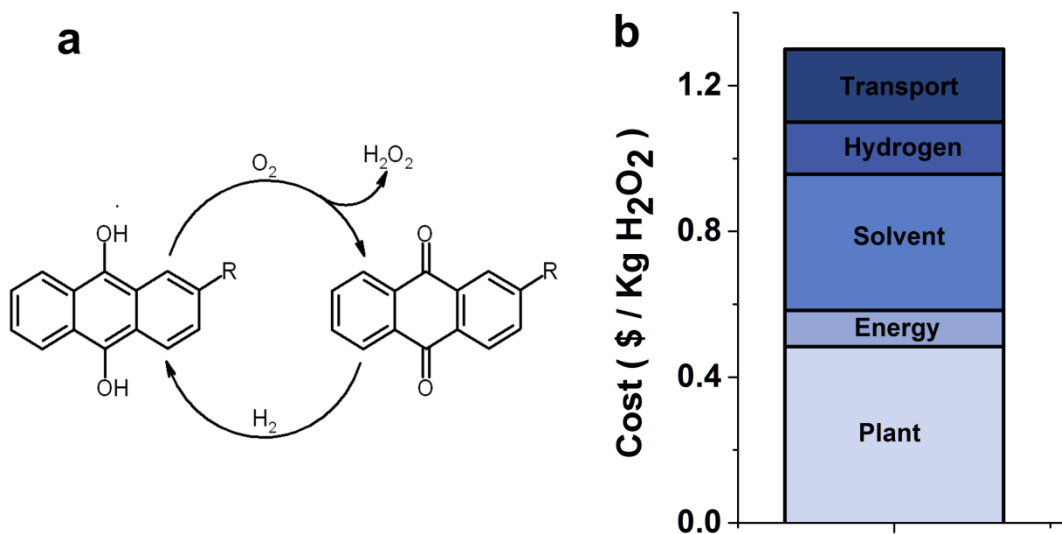
Figure 9: Anthraquinone process. a) Schematic diagram for the anthraquinone process; adapted from Wikipedia[122]. b) Breakdown of costs associated to production of H$_2$O$_2$, adapted from Hancu et al [123].

The pitfalls of the current production method have motivated the research of alternative production routes. One of them is direct synthesis of H$_2$O$_2$ on a heterogenous catalyst by reacting H$_2$ and O$_2$[119, 124].

$$H_2 + O_2 \rightarrow H_2O_2$$
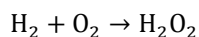
This would be a more efficient process, possible to carry out at a smaller scale and in a continuous mode as opposed to batch synthesis. In fact, it is categorized as one of the dream reactions in catalysis by Rostrup-Nielsen[125]. Implementation is facing a major fundamental challenge: H_2O_2 decomposes on most catalysts in the reactor right after being formed. This can be overcome using acid treated Au-Pd catalysts, where the back reaction is shut off[126, 127, 128]. Progress in that area has been steady in the past years, with several pilot plants in operation (the catalyst actually used in the plants remains a trade secret)[129].

On this landscape, electrochemical H_2O_2 production, mainly using as raw materials water and air, presents two key advantages:

1. On-site production, reducing transportation costs and enabling its use in remote locations.
2. Potentially there is a cost advantage on electrochemical production compared to the anthraquinone process as it is a continuous method and intrinsically more efficient.

Typically hydrogen peroxide production occurs via oxygen reduction at the cathode:

$$O_2 + 2H^+ + 2e^- \rightarrow H_2O_2 \qquad\qquad U^0_{O_2/H_2O_2} = 0.7\ \text{V}$$

Reactions at the anode must provide protons, for instance via water oxidation, either to oxygen[130, 131] or even more interestingly to hydrogen peroxide[132]:

$$2H_2O \rightarrow O_2 + 4H^+ + 4e^- \qquad\qquad U^0_{O_2/H_2O_2} = 1.23\ \text{V}$$

$$2H_2O \rightarrow H_2O_2 + 2H^+ + 2e^- \qquad\qquad U^0_{O_2/H_2O_2} = 1.76\ \text{V}$$

Water oxidation to hydrogen peroxide would be advantageous, but the study of this reaction is still in its infancy. Oxygen evolution is easier to implement. It is possible to calculate the cost of the energy required for the reaction. From a thermodynamic perspective, hydrogen peroxide production through oxygen reduction, with oxygen evolution at the cathode would require a potential difference of 0.53 V. This assumes ideal catalysts with no overpotential. Considering an electricity price of $ 0.085/kWh this translates into an electricity cost for hydrogen peroxide of $ 0.07/kg, well below H_2O_2 market price of $ 1.5/kg[121]. In reality, electricity costs will be inevitably higher due to overpotentials at the catalyst and costs associated to building and operating the plant.

Several researchers and companies have investigated H_2O_2 production at the cathode in the past years. Some of the approaches have focused on engineering a system leveraging on developments from fuel cells and electrolyzers[133, 134, 135, 136, 137, 138], some

have focused on discovering suitable membranes[139] and the majority have centered their attention to catalyst design. Finding a catalyst which is a) active, optimizing energy usage; b) selective, ensuring high yields of H$_2$O$_2$, and c) stable, permitting long-lasting devices has remained a challenge. Notable efforts in that direction occurred in the past years, where several novel materials such as Au-Pd or nitrogen doped carbon have been reported[140, 141, 142]. However, none of these catalysts reaches an optimal combination of activity, selectivity and stability.

4.2 Theoretical screening

Building on the theoretical understanding of oxygen reduction to water, Jan Rossmeisl (professor at DTU Physics) and Samira Siahrostami carried out a screening study searching for catalysts yielding hydrogen peroxide. They looked for materials with a very specific kind of active sites: single atoms of a reactive material, for instance Pt, Pd, Ir etc, surrounded by inert elements, namely Ag, Au and Hg. With the reactive atom acting as the active site, the O-O bond should remain intact during oxygen reduction and yield hydrogen peroxide very selectively (Figure 4.3). The calculations should reveal materials meeting the criteria of activity, selectivity and stability simultaneously.

$$O_2 + H^+ + e^- \rightarrow OOH^*$$

$$OH^* + H^+ + e^- \rightarrow H_2O$$

$$OOH^* + H^+ + e^- \rightarrow H_2O_2$$

$$OOH^* + H^+ + e^- \rightarrow OOH^* + O^*$$
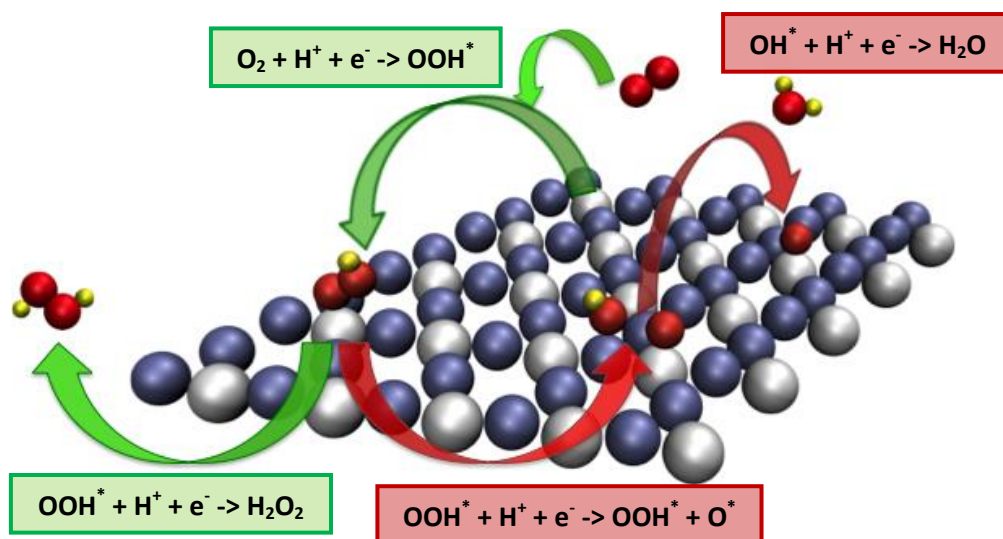
Figure 10: Schematic representation of oxygen reduction on a PtHg$_4$(110) surface. The green arrows represent the oxygen reduction path to H$_2$O$_2$; the red ones that to water. The reaction path has been indicated in the text boxes, with * representing an adsorbed molecule. Mercury is pictured in blue, platinum in white, oxygen in red and hydrogen in yellow.

Several materials with such structure are possible; nonetheless, it is important to bear in mind that these materials should be stable at the surface under acidic conditions at high

potentials (pH 1 and ~0.7 V), which turn out to be quite restrictive. The Pourbaix diagram[143] is used to see which elements meet this criterion. Figure 4.4 represents standard dissolution potentials for several elements. Standard dissolution potentials inform about when corrosion occurs with 1 M of ions in solution, which is hardly the case experimentally[144]. In practice dissolution will occur at a lower potential because concentration of the respective ions will be lower than 1 M. The higher the dissolution potential the more stable an element is. For instance, Au is the noblest metal and the most stable element, with a dissolution potential well above 1.5 V. Other noble metals, such as Pt, Ir, Pd and Hg should also be stable close to the O_2/H_2O_2 reversible potential of 0.7 V. Rh, Ru and Cu are more prone to dissolution but could be stabilized with the right alloy. Co, Ni and other metals are very reactive and their utilization would be seriously compromised by dissolution.

On this basis, alloys formed of Pt, Ir, Pd, Rh, Ru and Cu as reactive elements and Au, Hg and Ag as inert elements can be considered. There are various combinations possible; for instance Pd-Au alloys already studied by Jirkovsky and coworkers[141], surface alloys of different combinations and a few bulk alloys. Stability of the alloys will impact on how prone surfaces are to arrange themselves into an ordered isolated sites structure. This is given in Figure 4.4, with the formation energy of the different alloys. Most materials have negligible formation energy, close to 0 eV per formula unit. Only Ir/Au and $PtHg_4$ present significantly negative energies of formation and the isolated site structure should be stable.

Based on previous work for oxygen reduction to water[145, 146], an adequate activity descriptor would be the binding energy of the reaction intermediates (OH or OOH) to the surface. Only one of the stable candidates is close to the optimal activity, $PtHg_4$. This material had been studied in detail by Wu and coworkers, including in-situ STM images[44], and the isolated Pt atoms structure derived from their studies was used in the screening study.

This is summarized in the volcano plot in Figure 4.4. The x-axis shows the binding energy of OH and the y-axis the potential at which oxygen reduction becomes thermodynamically downhill. The solid red lines represent the volcano for oxygen reduction to water, and those in blue for oxygen reduction to H_2O_2. As reference points, I have included Pd and Pt –well known catalysts to produce water– as well as Au –well known to produce H_2O_2. Without taking ensemble effects such as isolated active sites into account, catalysts on the strong binding site of the blue volcano will thermodynamically reduce H_2O_2 further to water. Those close to the top will reduce oxygen to both H_2O_2 and water, and only those on the weak binding site, such as Au, will

produce H_2O_2. Ensemble effects ensure selectivity shifts to H_2O_2, preventing O-O bond breaking. Of all the initial candidates, only Pt-Hg is realistically promising showing adequate stability and activity. Another important aspect of the volcano is the minimum overpotential required for the reactions. In the case of oxygen reduction to water, scaling relations prevent an optimal binding of all intermediates to a surface, which translates in a minimum overpotential of ~0.3 V[145]. For oxygen reduction to H_2O_2 there is only one reaction intermediate whose binding energy to a surface should be possible to tune. Therefore, at the right catalyst very high current densities at a negligible overpotential should in principle be possible.
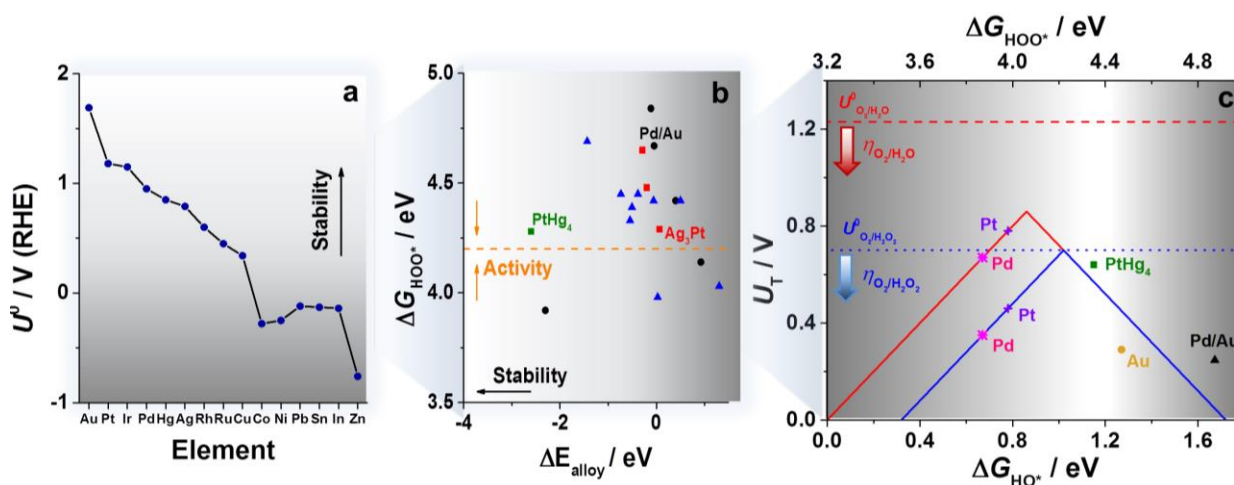
Figure 11: Theoretical screening of single site catalysts for selective oxygen reduction to H_2O_2. a) Dissolution potential of various elements under standard conditions based on Pourbaix diagrams[143]. The background color gradient scales with stability. b) Formation energy (per formula unit) of single site catalysts and binding to OOH. The optimal OOH binding is plotted as the orange dotted line. Bulk alloys are shown with red or green squares; surface alloys with Au substrate are shown as black circles and surface alloys with non-Au substrates as blue triangles. The background color gradient scales with stability. c) Theoretically calculated volcano plot for the two-electron (blue) and four-electron (red) reduction of O_2, with the limiting potential plotted as a function of ΔG_{OH} (lower x-axis) and ΔG_{OOH} (top x-axis). The equilibrium potential for the two-electron pathway is shown as the blue dotted line, while that for the four-electron path is a red line. The most promising range of OH binding energies is highlighted with a white gradient. Calculations performed by Samira Siahrostami and Mohammedreza Karamad.

Before proceeding, I would like to point out the differences between this screening study and other approaches. Previous works start with a large pool of materials and then narrow it down to a few interesting ones. For instance, Greeley and coworkers used calculations on more than 700 compounds to discover Pt-Bi for hydrogen evolution[28]. Here, we were looking for a very particular property on the structure of materials from the beginning: isolated sites. This reduced the number of materials considered to less than 50. Such a targeted screening is only possible if a robust framework is already in place, and it greatly accelerates development by reducing computing time and minimizing uncertainties.

4.3 H$_2$O$_2$ production on Pt–Hg

From the theoretical screening, PtHg$_4$, an alloy I had been working on for CO reduction, should be active and selective for the reaction. I used a procedure similar to that detailed by Wu and coworkers[44] for their synthesis. Briefly, Hg was electrodeposited on the Pt sample for two minutes at 0.2 V from a 0.1 mM Hg(ClO$_4$)$_2$ solution. This should yield a Pt-Hg alloy on the first layers without need for annealing or any additional treatment. I performed oxygen reduction on the electrode, shown in Figure 4.5. The substantial disk current indicates oxygen reduction does occur at the electrode. The current is always below the mass transport limit for four electron oxygen reduction, -6 mA/cm^2 at 1600 rpm of rotation speed. This indicates oxygen reduction may not happen through the four electron path. A mainly two electron reduction is confirmed by the significant ring current, showing H$_2$O$_2$ is present. In fact, most of the disk current accounts for H$_2$O$_2$ production. This is reflected on the very high selectivity to H$_2$O$_2$, nearing 100 % at most potentials. Paolo Malacrida performed XPS on the sample after oxygen reduction. Surface composition was close to PtHg$_4$, the most stable alloy thermodynamically and it showed Pt was alloyed. AR-XPS determined that there were about 7-8 monolayers of alloy before Pt composition increased (Figure 4.5). This indicated PtHg$_4$ was present at the surface, presumably containing isolated Pt sites. Voltammograms in N$_2$ confirm that, as there is a significant suppression of the hydrogen upd peaks (Figure 4.5). This has been shown in the past to happen on isolated sites of Pd on the Au-Pd system[147], and isolated Pt sites might behave similarly. Overall, these results were encouraging and in line with the theoretical calculations.

Figure 12: Experimental characterization of Pt-Hg on extended surfaces. a) H_2O_2 selectivity as a function of the applied potential and RRDE voltammograms at 1600 rpm in O_2-saturated electrolyte with the disk current (black), ring current (blue) and corresponding current to hydrogen peroxide (red) obtained from the ring current (only the anodic cycle is shown). b) AR-XPS depth profile of Pt-Hg, performed by Paolo Malacrida. Adventitious C and O traces have been omitted for clarity. c) Voltammograms in N_2-saturated electrolyte of Pt (black) and Pt-Hg (blue). All electrochemical measurements taken in 0.1 M $HClO_4$ and 50 mV/s at room temperature.

The next step I took was to test Pt-Hg/C nanoparticles to see if that material would also work in technologically relevant nanoparticulate form. I made an ink with commercial Pt/C, drop casted it on a glassy carbon and subsequently electrodeposited Hg the same way as for the polycrystalline sample[49]. Measurements were very promising, giving very high activity and stability similarly to the extended surfaces (Figure 4.6). I then compared the data to literature values to get a quantitative estimate for how much more active Pt-Hg was. The main reference was a work by Jakub Jirkovsky and others reporting Au and Au-Pd nanoparticles for oxygen reduction[141]. Pt-Hg showed a mass activity 20 times higher than Au or Au-Pd, which was the best metal catalyst reported for electrochemical H_2O_2 production in acid. In addition, samples were extremely stable, showing no degradation after 10.000 cycles between 0 and 0.8 V.

To understand better what was the structure of the nanoparticulate samples I focused mainly on two techniques: XPS and TEM. Based on Paolo Malacrida's XPS measurements, the Pt:Hg ratio was 1:1. Davide Deiana performed extensive TEM measurements on the samples (Figure 4.6). Essentially EDS showed both Pt and Hg at the particles, but the lattice parameters of the core corresponded to pure Pt. By putting these two pieces of information together we concluded that the nanoparticle had a core of Pt and a shell of Pt-Hg, represented schematically in Figure 4.6. The precise composition of the outermost layers of the nanoparticles remains an open question; for that a synchrotron-based technique such as X-ray absorbtion spectroscopy would be most useful. Nevertheless, the voltammograms in N_2 show a behavior very similar to that of the polycrystalline sample; I propose that a $PtHg_4$-like structure is formed at the surface, similar to that reported on Pt(111)[44].
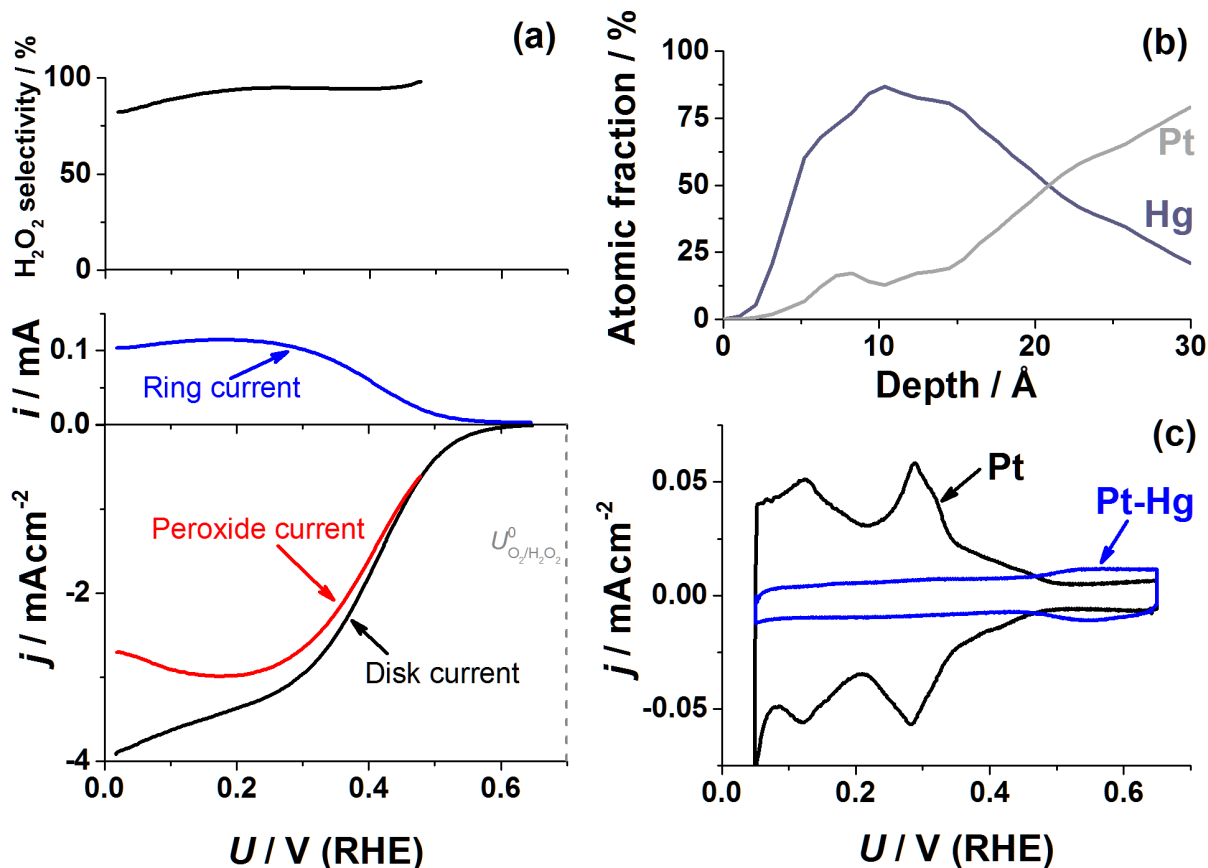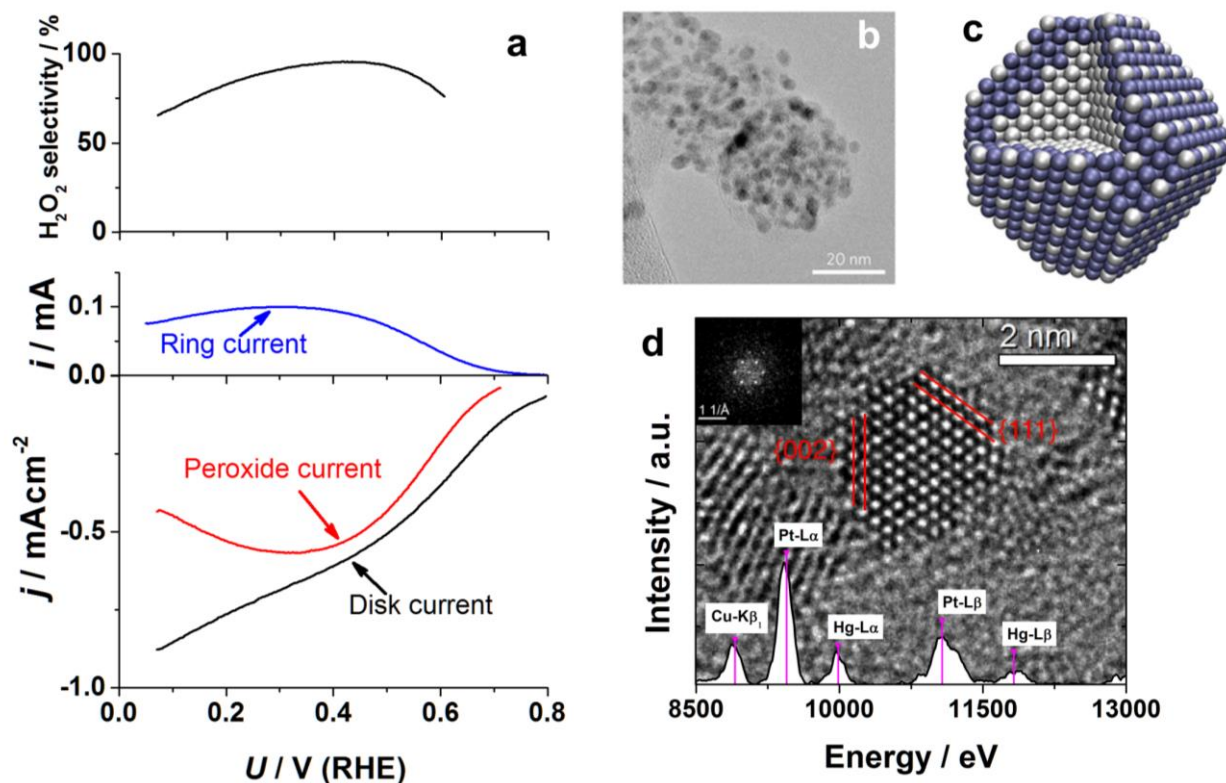

Figure 13: Experimental characterization of Pt-Hg/C nanoparticles. a) H_2O_2 selectivity as a function of the applied potential and RRDE voltammograms at 1600 rpm in O_2-saturated electrolyte with the disk current (black), ring current (blue) and corresponding current to hydrogen peroxide (red) obtained from the ring current (only the anodic cycle is shown). All electrochemical measurements taken in 0.1 M $HClO_4$ and 50 mV/s at room temperature. The disk current is normalized to the surface area of Pt nanoparticles (from H-upd) before deposition of Hg. b) TEM overview image of Pt-Hg/C nanoparticles. c) Schematic representation of a Pt-Hg/C nanoparticle with a Pt core and a Pt-Hg shell, done by Mohammedreza Karamad. d) HR-TEM image of a single Pt-Hg nanoparticle, with the corresponding EDS spectrum superimposed. The peaks correspond to Pt and Hg from the nanoparticle, and Cu, from the TEM grid; the (111) and (002) planes are shown in red; the corresponding diffractogram is shown in the inset. TEM measurements performed by Davide Deiana.

4.4 Trends in H$_2$O$_2$ production

The data on Pt-Hg was very promising, but given that the reduction of oxygen to H$_2$O$_2$ requires only two electrons it should, in theory, be possible to achieve much higher current densities at a very low overpotential. This is the case for other two electron reactions, such as hydrogen oxidation/evolution on Pt[148]. By looking at the volcano plot in Figure 4.4, Pt-Hg binds oxygen a little too weakly to be optimal. Knowing that Pd binds oxygen slightly stronger than Pt[145] I considered it might be possible to alloy Pd with Hg to weaken the metal-O bond and increase activity. I started by looking at the phase diagram, which showed various possible Pd-Hg alloys[103]. One of them was Pd$_2$Hg$_5$, which also has facets displaying isolated sites. I then used the same Hg electrodeposition method as before on a polycrystalline Pd sample. Electrochemical results showed an activity one order of magnitude higher than Pt-Hg and very high selectivity. From AR-XPS data it is unclear what the structure is at the surface, especially because of the depth-dependent composition. Nevertheless, the sample consists of a Hg-enriched topmost layer on a Pd-Hg alloy.

Based on the successful outcome of the experiments on Pt-Hg alloys, we set out to investigate other transition metal-Hg alloys that were stable in acid. This limited the choice to Cu and Ag, as the other few metals stable in acid (for instance Ir, Ru or Rh) do not alloy with Hg[149]. I tested polycrystalline samples of Cu-Hg and Ag-Hg prepared in the same manner as the other Hg alloys. They both showed 100 % selectivity to H$_2$O$_2$. The activity for Cu-Hg was comparable to Au, while that of Ag-Hg was an order of magnitude higher and comparable to Pt-Hg. Unfortunately we could not use any UHV technique on those alloys as Hg evaporated under vacuum. My hypothesis is that these alloys are not very stable and it is easy for Hg to evaporate. However, making use of the phase diagrams it was possible to understand that Cu-Hg should have a CuHg$_4$ phase with isolated Cu sites[150]. Ag-Hg has a variety of alloys in the phase diagram[151], but Ag itself is already quite inert and yields substantial H$_2$O$_2$[152]. We took the view that the main mechanism to enhance selectivity is to preferentially cover undercoordinated Ag sites, which should be more reactive and capable of breaking the O-O bond. DFT calculations show it is indeed energetically favorable for Hg to sit on the steps of Ag-Hg, and this is supported by ex-situ STM experiments[153]. However, an experimental definitive proof is not straightforward to obtain.

Samira Siahrostami and Mohammedreza Karamad calculated the OOH binding energy to the new Hg alloys, Pd-Hg, Ag-Hg and Cu-Hg. As activity spanned over three orders of magnitude I quantified it by taking the potential at which 1 mA/cm^2 of kinetic current to H$_2$O$_2$ is reached. The 1 mA/cm^2 limit is set by the reliability of the RRDE measurement; the current at the ring should be substantial and oxygen mass transport should not limit

the disk current. It is possible to make the same plot with different threshold values and the general view remains unchanged.

The data is plotted in Figure 4.7. The solid lines correspond to the theoretically calculated onset potential values from a thermodynamic analysis. Experimental points at the right leg of the volcano (the weak-binding side) follow closely theoretical predictions. The left leg, however, does not match very well the calculations. There are only two points; Cu-Hg and Pt, and they have substantially lower activity than predicted from the analysis. For Cu-Hg the reason might be that either the structure or the water layer are different than considered in the calculations; for Pt the explanation lies in its selectivity. Pt actually produces H_2O_2, but it is also a very good catalyst for reducing it further to H_2O. This means that even if Pt produces H_2O_2 at high rates, it also decomposes H_2O_2 preventing detection at the ring[154]. The decomposition is only avoided when the Pt surface is covered in hydrogen (in the H-upd region)[49, 89]. I find three observations from the volcano plot to be especially relevant:

- Volcano plots do not quantify selectivity, only activity. That is the underlying reason for the low Pt activity compared to theoretical calculations. More complex 3D plots can take selectivity into account, but straightforward conclusions are harder to derive[155].
- A good agreement between theoretical calculations and experiments is crucial to derive meaningful conclusions. The theoretical model seems to capture the overall trend in activity over three orders of magnitude.
- This is the first experimental proof of a volcano-type relationship for electrochemical H_2O_2 production where all the data points are derived from a single set of experiments.
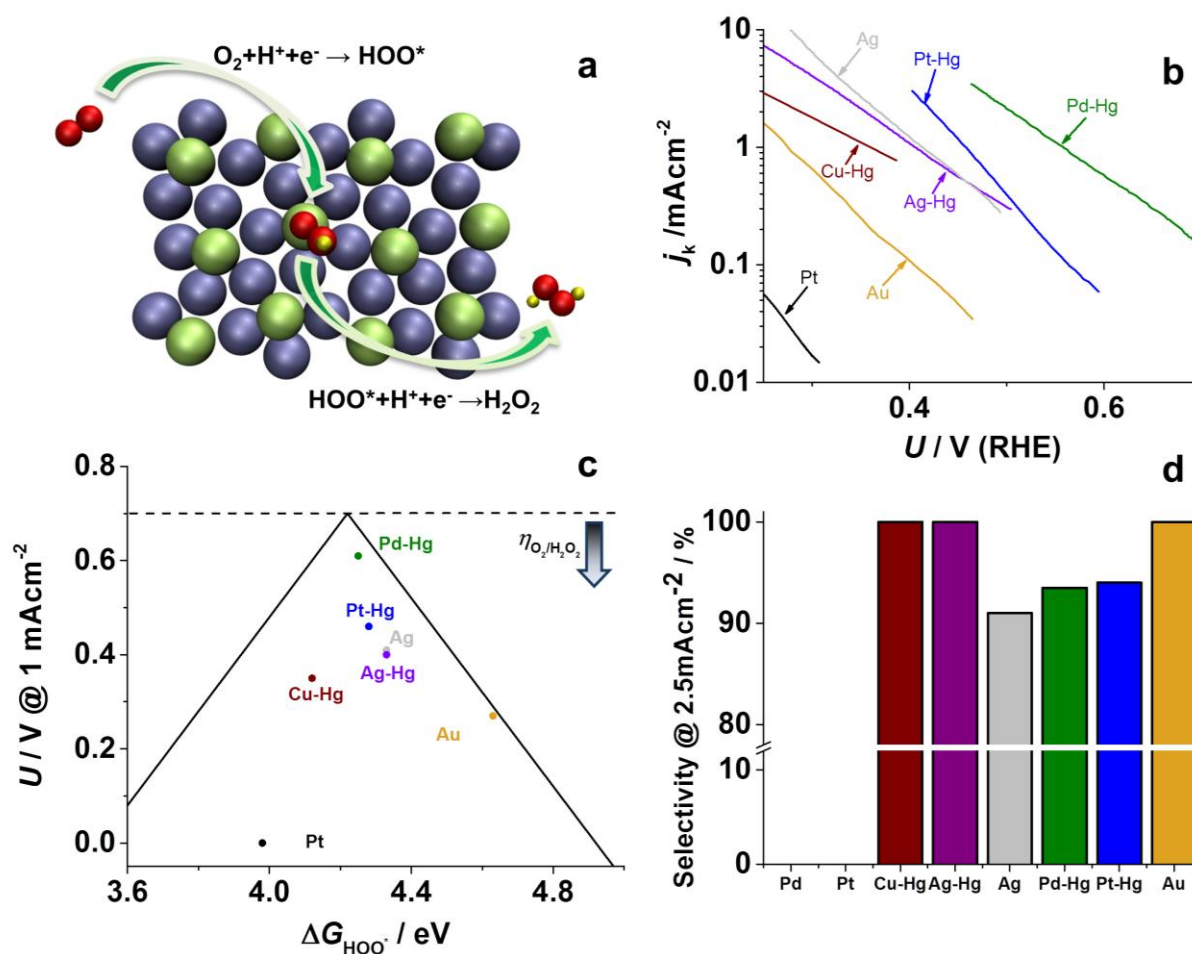
Figure 14: Trends in activity and selectivity for H_2O_2 production. a) Schematic representation of oxygen reduction to H_2O_2 on a model $Pd_2Hg_5(001)$ surface. Palladium atoms are represented in green, mercury in blue, oxygen in red and hydrogen in yellow. b) Partial kinetic current density to H_2O_2 as a function of the applied potential, corrected for mass transport losses. c) Potential required to reach 1 mA/cm² of kinetic current density to H_2O_2 on polycrystalline catalysts as a function of the calculated HOO* binding energy. The solid lines represent the theoretical Sabatier volcano[146]. The dotted line represents the thermodynamic potential for oxygen reduction to H_2O_2. d) H_2O_2 selectivity for different catalysts at 2.5 mA/cm² of total current density. For this figure, data for Cu-Hg was extrapolated for ~100 mV as it is unstable above 0.25 V[143]. Data for Au adapted from Jirkovsky et al [140]. All electrochemical experiments were performed at 50 mV/s and 1600 rpm in O_2-saturated 0.1 M $HClO_4$ at room temperature. The surface area was normalized to the geometrical value.

From the volcano it seemed logical to test Pd-Hg/C nanoparticles to see if they would mimic the performance of extended surfaces. The answer turned out positive, with Pd-Hg/C being five times more active than Pt-Hg/C and 100 times more than Au/C in terms of mass activity per amount of precious metal, as shown in Figure 4.8.
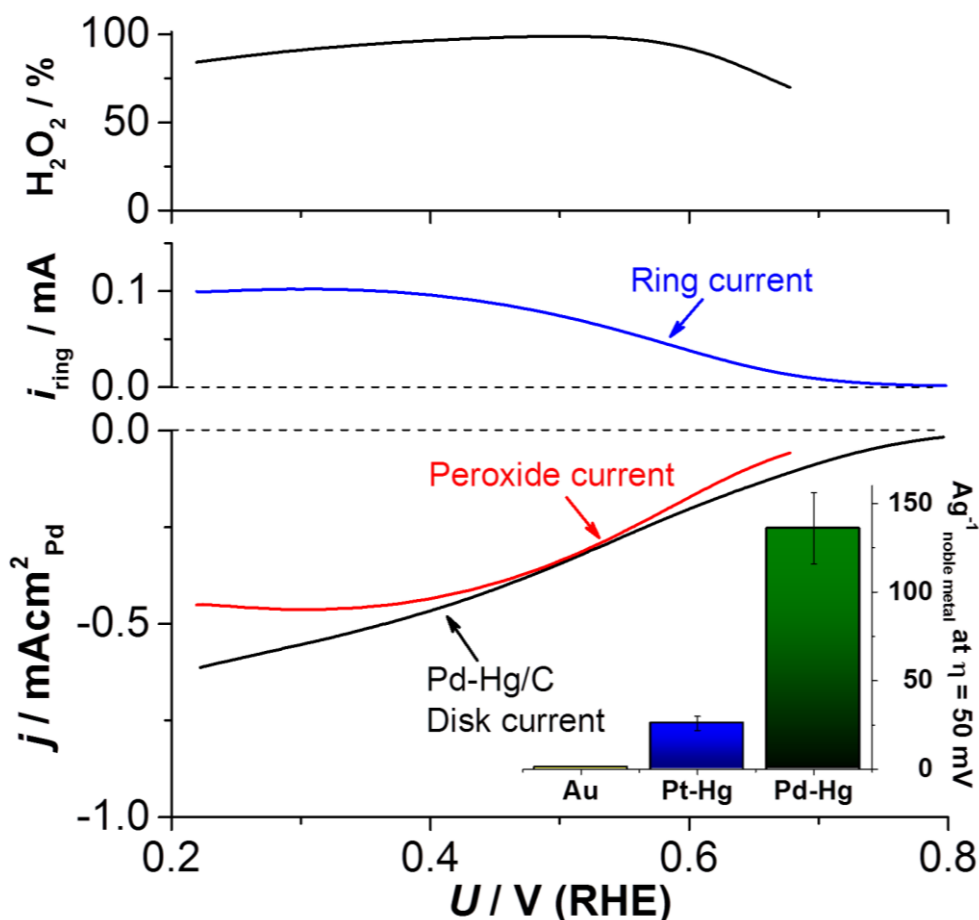
Figure 15: Oxygen reduction on Pd-Hg/C nanoparticles. The main plot shows H_2O_2 selectivity and RRDE data as a function of potential, with disk current normalized to Pd surface area estimated from the oxide reduction peak. Inset: Mass activity per amount of precious metal of Au/C, Pt-Hg/C and Pd-Hg/C for H_2O_2 production at 0.65 V.

Davide Deiana performed TEM on the nanoparticles. Given the very different atomic numbers of Pd and Hg (46 and 80 respectively) it was possible to distinguish columns of atoms on TEM due to the very different absorbance, which depends on the atomic number. In particular, Hg has higher absorbance and looks brighter than Pd. The images revealed a core-shell structure with an inhomogeneous thickness of Pd-Hg alloy at the shell and Pd at the core. This was further confirmed by STEM-EDS, which permitted determination of the elemental composition. In Figure 4.9, Hg is represented in orange and Pd in blue. In several cases zooming in permitted identification of the structure at the shell. This is crystalline and ordered, and the stoichiometry turned out to be a Pd-Hg alloy with a 1:1 proportion. This is in contrast with the structure considered in the theoretical model, Pd_2Hg_5. Even so, it is worth pointing out that the very topmost layer may contain more Hg thank the deeper layers, which would not be appreciable in TEM. A 1:1 composition would not contain isolated Pd atoms, to our understanding critical to

achieve high selectivity to H$_2$O$_2$. More detailed studies, for instance via EXAFS or infrared spectroscopy, are needed to confirm the structure of the outer layer.
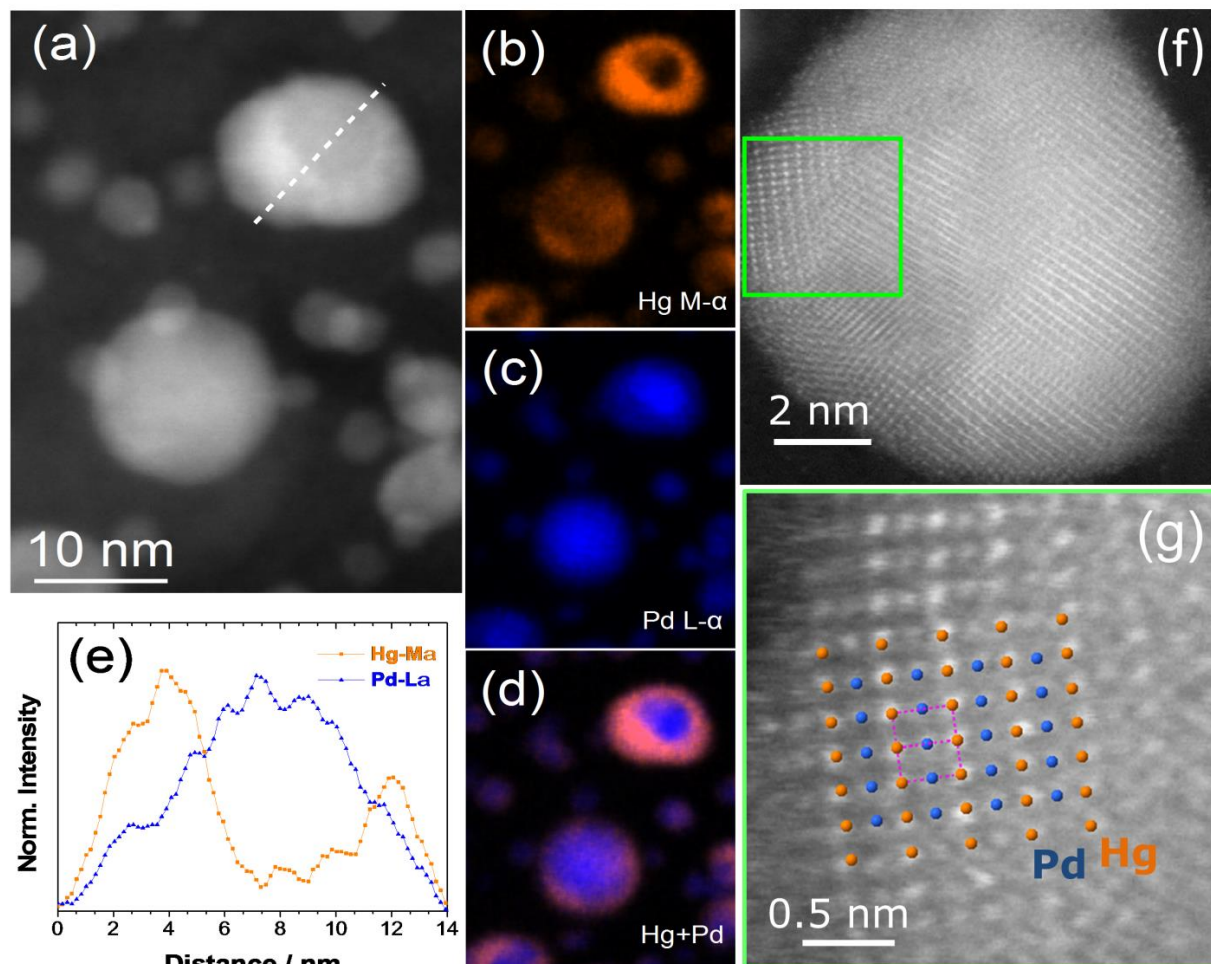
Figure 16: Electron microscopy characterization of Pd-Hg nanoparticles. a) HAADF-STEM image of Pd-Hg nanoparticles and respective Hg, Pd and Hg+Pd STEM-EDS elemental maps (b-d). e) Normalized EDS Hg-Mα (orange) and Pd-Lα (blue) intensity line profiles extracted from the spectrum image data cube along with the white dashed line drawn on (a). f) Fourier-filtered HAADF-STEM image of a Pd-Hg nanoparticle, showing a visible core-shell structure. g) High magnification HAADF-STEM image of the region enclosed in the green square in (f); superimposed to the image there are the atoms corresponding to a 1:1 Pd-Hg alloy, obtained from its known structure[103]. TEM measurements performed by Davide Deiana.

4.5 Oxygen reduction on single site catalysts in alkaline environment

Following the experiments in acid electrolyte I wanted to see how the Hg catalysts would behave in alkaline environment. Many electrochemical reactions present differences in selectivity or activity depending on pH. Examples include oxygen reduction[156], hydrogen

evolution and oxidation[157, 158] and formic acid oxidation[159]. The mechanisms behind performance changes are to date poorly understood. In the reaction studied here, oxygen reduction, a paradigmatic example occurs in Ag electrodes, which in acid show a remarkable selectivity to H_2O_2 but in alkaline become almost as active as pure Pt to produce H_2O[152]. From an application point of view, the development of new electrocatalysts in alkaline environment is of secondary importance. Carbon is well known to produce H_2O_2 at high yields[160], and commercialization has been achieved for niche uses[161, 162]. What limits the widespread production of hydrogen peroxide in alkaline is the lack of high performance stable membranes[67]. In fact, synthesis has to be carried out in NaOH solutions, which makes separation of H_2O_2 hard and limits its applicability. Nevertheless, it would be interesting to confirm that isolated sites can also change selectivity in alkaline environment and it would add to the ongoing academic discussion on pH effects in oxygen reduction[163, 164]. Notably, in alkaline environment H_2O_2 suffers a deprotonation to HO_2^- (pK_a=11.7). This changes the oxygen reduction balance, but according to the literature the reversible potential for the reaction remains the same[165].

$$O_2 + H_2O + 2e^- \rightarrow HO_2^- + OH^- \qquad\qquad U^0_{O_2/HO_2^-} = 0.7\ V$$

I started by testing Pt-Hg. I followed the exact same electrodeposition method as before to prepare the electrodes, but now I carried out the measurements in KOH solution instead of $HClO_4$. Figure 4.10 presents a typical oxygen reduction voltammogram on Pt-Hg in 0.1 M KOH. Even at 0.7 V the disk current is very high, and it actually decreases as overpotential increases. This seems counterintuitive, but can be rationalized by looking at the ring profile. As overpotential increases there is more H_2O_2 produced. Disk current is mass transport limited, and a decrease in the number of electrons transferred towards two explains the decreased overall disk current. However, selectivity is poor, never being above 75 %.
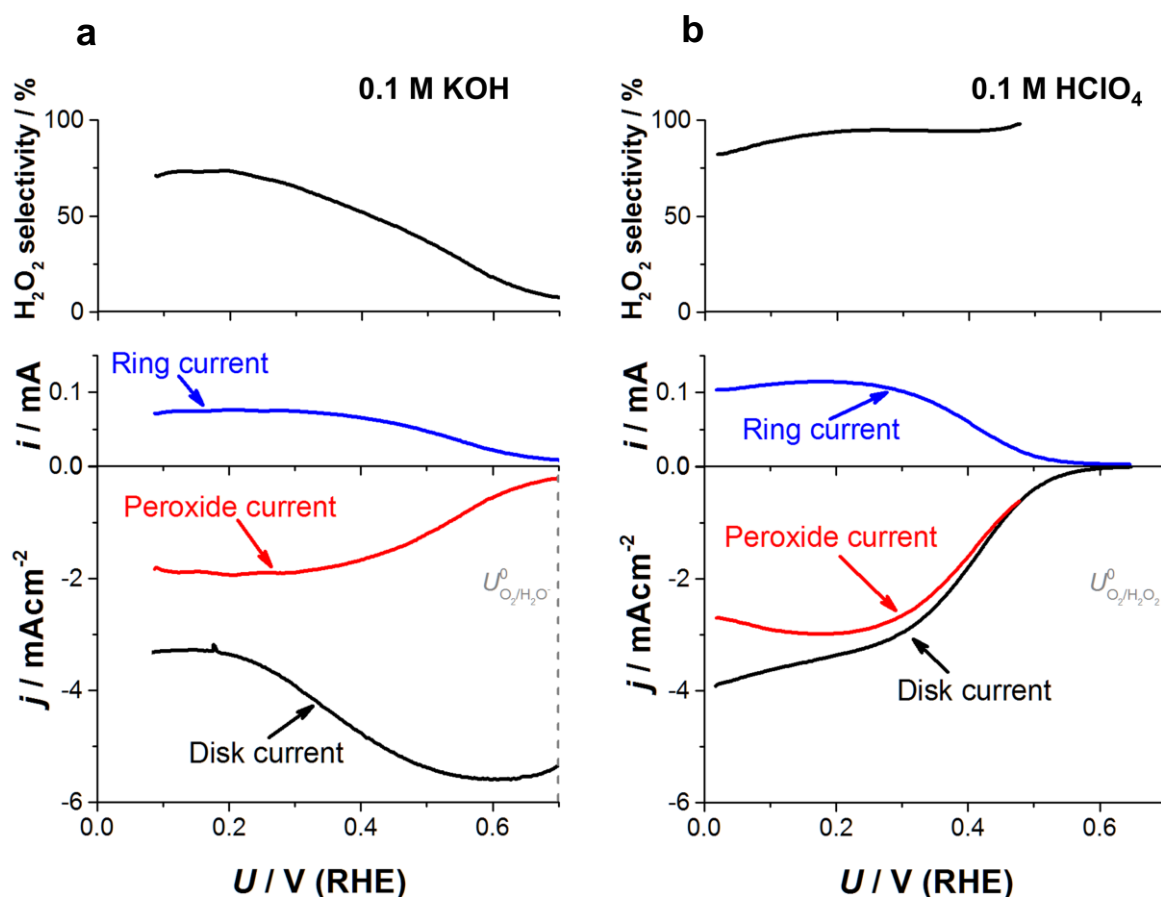
Figure 17: pH effects on Pt-Hg electrodes for oxygen reduction. a) RRDE measurements in 0.1 M KOH (pH 13). b) RRDE measurements in 0.1 M HClO₄ (pH 1). In both cases, from top to bottom, H₂O₂ selectivity, ring currents and disk currents are shown. Peroxide currents are derived from the ring current. Measurements taken at 1600 rpm and 50 mV/s in O₂-saturated electrolyte.

Similar results were obtained for Pd-Hg and Ag-Hg. Surprisingly the results were different for Cu-Hg. It was selective to H_2O_2 and the activity was close to that of glassy carbon in alkaline, as shown in Figure 4.11. This could suggest the reaction mechanism is different than in the other alloys, either because the structure is different than anticipated or due to water layer effects. Both the Cu-Hg data and that on other alloys remain a highly speculative topic at the point of writing this thesis. In the case of Ag-Hg, where we consider Hg covers only the steps, a shift in selectivity would be expected. That is because pure Ag already changes selectivity to water from acid to alkaline, and covering the steps with Hg should not influence it. There are a few hypotheses which could explain why Pt-Hg and Pd-Hg shift selectivity in alkaline.

- pH dependent reaction mechanism. This could include outer-sphere reactions in alkaline[166] which do not occur in acid environment.
- Different water layer orientation in alkaline than in acid. Rossmeisl and coworkers proposed that the orientation of water in the double layer changes with pH[167].

This could shit the binding energies of reaction intermediates, and change barriers for proton transfer.

Testing these ideas experimentally is particularly challenging, requiring methods still under development such as free electron lasers[168]. Nevertheless, this data highlights the importance of pH in controlling selectivity and the need to develop a solid model to understand the key factors influencing it.
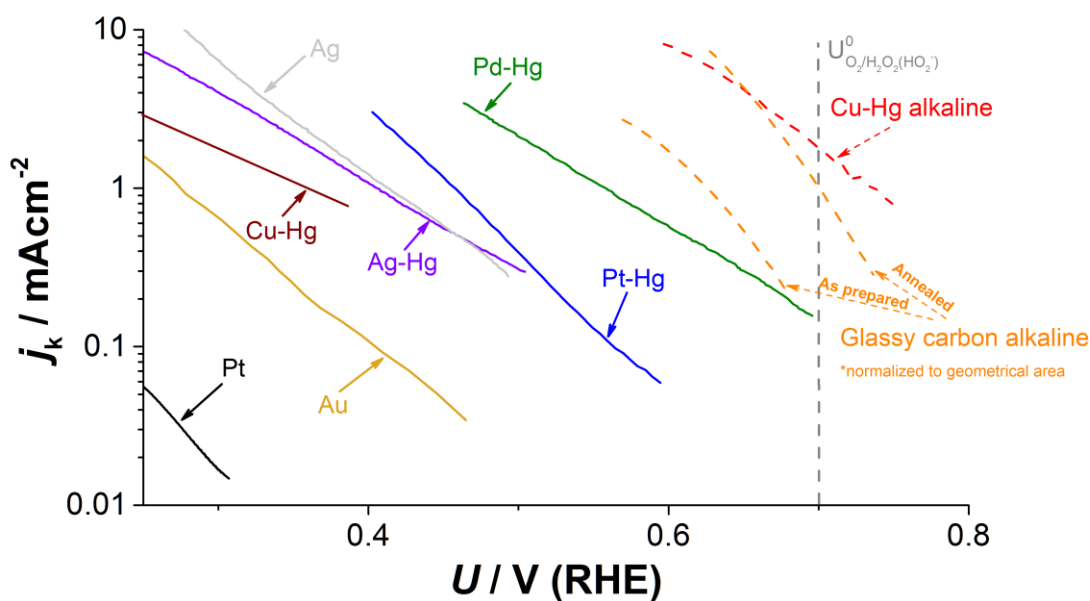
Figure 18: Comparison of measurements for oxygen reduction to H_2O_2/HO_2^- in acid and alkaline for polycrystalline electrodes. Solid lines are values in 0.1 M $HClO_4$ (pH 1), while dashed lines are in 0.1 M KOH (pH 13)**.** The vertical dashed line represents the reversible potential for the reaction, at 0.7 V. All currents normalized to geometrical area.

4.6 Outlook

A new set of catalysts for electrochemical H_2O_2 production based on Hg alloys has been the main output of this research. On the basis of single crystal studies on Hg modified Pt(111), we conjecture that these alloys have a particular structure containing isolated sites of the non-Hg metal surrounded by Hg, which prevent O-O bond breaking during oxygen reduction. In acid environment, Pd-Hg nanoparticles are two orders of magnitude more active (in terms of mass activity) for H_2O_2 synthesis over previously known Au-based catalysts. It remains to be seen whether these materials will be implemented

commercially –given they consist of noble metals and mercury, a combination of two a priori undesirable elements (for cost and toxicity reasons respectively).

By studying the trends in activity for different catalysts it has been possible to demonstrate the existence of a volcano-type relationship between binding energy and activity for H$_2$O$_2$ synthesis. Such trends, however, do not hold in alkaline environment. The reason for that remains elusive, and major breakthroughs are required for a solid fundamental understanding of this phenomenon.

There are three aspects that I would like to stress based on my research:

- While activity of the catalysts is important, stopping H$_2$O$_2$ decomposition is even more critical. This can be achieved by boosting selectivity, and isolated sites have proven highly effective for that. It would be interesting to find alternative structures with isolated sites formed by non-mercury, non-noble metal catalysts. Opportunities include oxide and sulfide surfaces[169].
- For certain applications, mainly those using H$_2$O$_2$ as a chemical feedstock, established processes require concentrated H$_2$O$_2$ (normally 30 % by weight). To the best of my knowledge such concentrations have not been achieved by a purely electrochemical method. First applications of electrochemical methods are occurring in areas where low concentrations are desired and on-site production can be leveraged. One excellent example is wastewater treatment, but also mining and dairy applications are of interest.
- It would be of fundamental interest to understand how pH impacts on an electrochemical reaction. This would be a step forward for electrochemistry as a whole since many reactions are affected by pH.

5 Nanostructured Cu surfaces for CO$_{(2)}$ electroreduction

5.1 Introduction

Energy security, climate change concerns and the increased adoption of variable enegy sources such as wind or solar press for the development of new technologies capable of storing and releasing energy at need and reducing greenhouse gas emissions. An attractive possibility would be the conversion of CO_2 into alcohols and/or hydrocarbons. Nature achieves that in plants, which use the photosynthesis process to capture CO_2 from the atmosphere and convert it into reduced products with sunlight as the energy input. This takes place through an enzyme named d-ribulose-1,5-bisphosphate carboxylase/oxygenase, which converts CO_2 into hydrocarbons[170]. As a curiosity, it turns out this is one of the least efficient enzymes in nature (high CO_2 concentrations in the atmosphere of primitive Earth did not make efficiency of such enzyme an evolution priority[170, 171]).

It is possible to convert CO_2 to valuable chemicals electrochemically. This can be achieved through electroreduction of CO_2, either on solid oxide electrolyzers[172] or at low temperature[51]. While solid oxide technology is mature enough for implementation – mainly for the conversion of CO_2 into synthesis gas–, low temperature electrolysis is not that advanced and there is need for fundamental research to discover low overpotential catalysts capable of driving the reaction selectively.

Here I would like to point out the economics of such a reaction, which are often disregarded by researchers in the field. In Figure 5.1 I show in light blue current market prices for three widely produced chemicals; hydrogen, ethanol and methanol. In dark blue I show the cost to make these chemicals electrochemically, assuming that the only contribution to cost is electricity for electrolysis (at a price of 0.085 \$/kWh). I have also considered that the electrochemical device runs at no overpotential with oxygen evolution at the anode (at 1.23 V). Therefore, these calculations represent a best-case scenario accounting only for thermodynamics. In reality there would be major costs associated to building and operating a plant, transport of products etc.
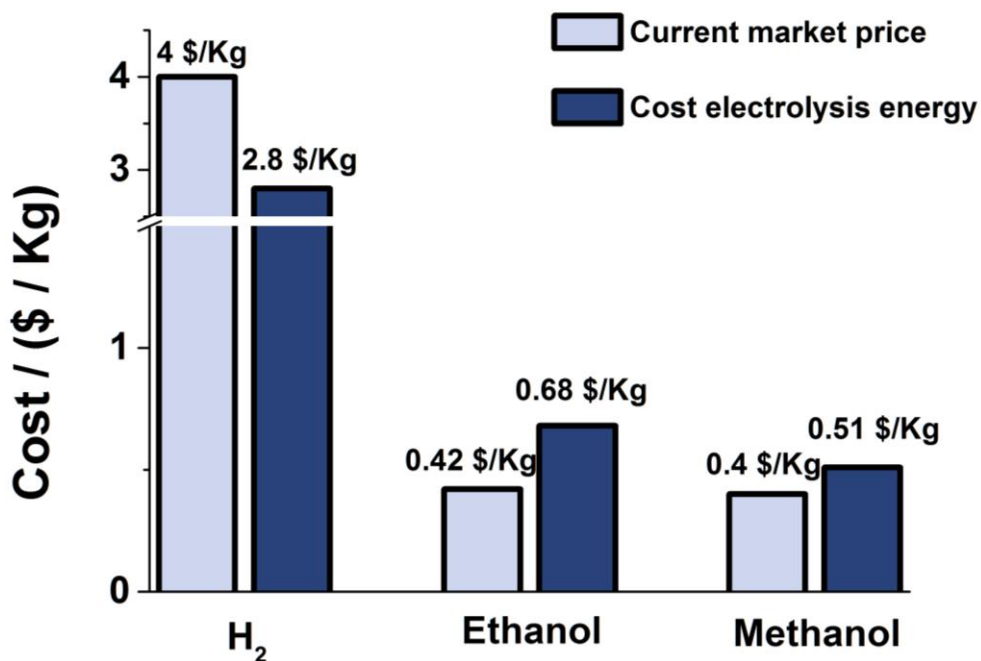
Figure 5.1: Cost comparison for current market prices and electrochemical costs for different chemicals. Current market prices are in light blue, obtained from NASDAQ[106]; in dark blue, corresponding electrolysis energy price using the respective thermodynamic reversible potentials, oxygen evolution at 1.23 V and electricity prices of 0.085 $/kWh. Note the break in the y-axis.

From an economical point of view, hydrogen is the only of these products which would make sense to produce electrochemically. Both ethanol and methanol have an electrolysis cost significantly higher than current market prices. From this data, it looks like electrochemical reduction of CO$_2$ to alcohols faces major challenges to become competitive. There are a few situations which can vary this:

1. Demand could go up for these chemicals, which in occasions results in as much as doubling of the price reported here[106].

2. The reaction considered at the anode is oxygen evolution. Lower costs could be achieved by changing the anode reaction to produce more valuable products than oxygen and/or with a lower energy cost (chlorine or hydrogen peroxide evolution would be good examples).

3. Electricity prices can vary by up to a 30 % depending on supply and demand, which would impact electrolysis cost. Note also that significant differences exist between countries; in Denmark industrial electricity price is ~0.12 $/kWh, in Norway ~0.06 $/kWh[173].

The latter point has broader implications when transitioning to a renewable energy infrastructure. Renewable sources of energy, such as wind or solar, are variable in nature. In days when wind is blowing strongly or the Sun is shining, there would be an

oversupply to a limited demand. As supply increases, prices go down. In this event, it could be favorable to store energy when prices are low and release it at a later point when prices are high again (i.e. wind is not blowing or demand picks up). I illustrate this in Figure 5.2, which shows electricity consumption as well as contributions of wind and conventional energy to the supply in western Denmark. Some days wind energy produces more electricity than that required for consumption, and some days it produces no electricity at all. A method to balance supply is necessary to gain energy independence. This can be achieved by different means; to name a few, batteries, supercapacitors and synthesis of fuels[174]. That way, batteries would be charged or fuels synthesized when electricity supply is high, and energy would be released when supply is low. At present, it is unknown which solution or combination of solutions will be used and research is very intense in the field.
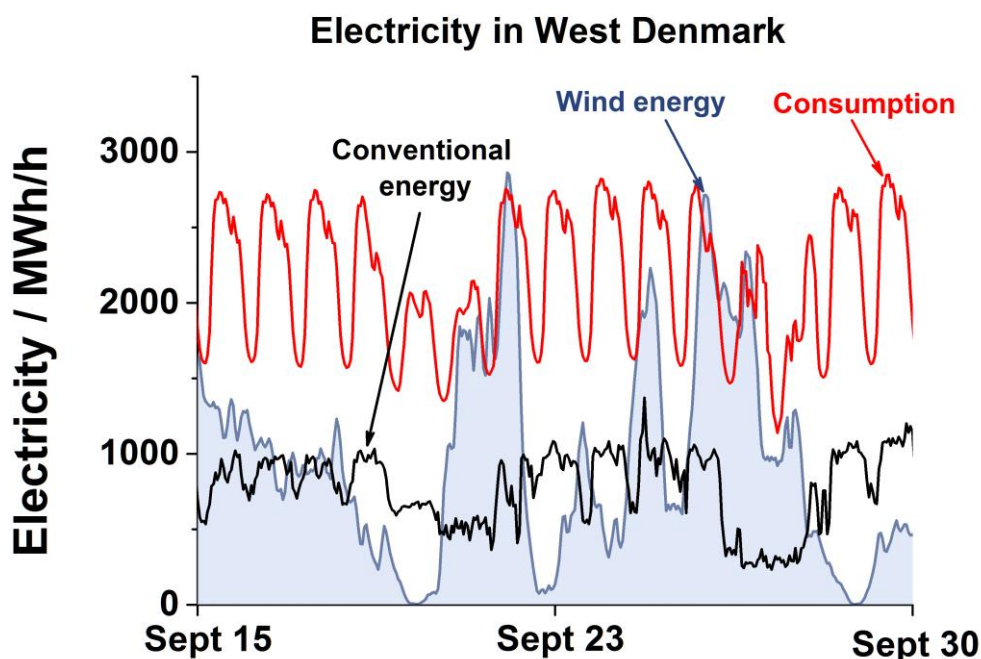
Figure 5.2: Electricity supply by source in West Denmark during the second half of September 2014. Data adapted from energinet.dk [175].

Liquid fuels such as ethanol or methanol are easier to store than hydrogen and a valid energy source for transportation; thus the interest to use electricity surplus for their synthesis. An attractive way to achieve that is to use CO_2 directly as the raw material. This would enable recycling of fuels and a decentralized infrastructure. Critical to that goal is a technology capable of converting CO_2 into fuels. Electrochemical methods are promising in that regards owing to their easy start-up-stop and little plant requirements.

To date, however, no catalyst can reduce CO_2 to valuable products in an efficient and selective way.

Extensive work was done by Professor Hori and coworkers from Chiba University (Japan) in the 1990s. From their research, catalyst can be classified into four main categories depending on their selectivity[36, 43, 51]:

- Formate: Very inert elements such as Sn, Hg, Bi produce formate selectively, albeit at a very high overpotential.
- CO: Noble metals (Au, Ag and Pd) are some examples of materials producing mainly CO selectively.
- Hydrocarbons: Copper stands out as the only pure element capable of reducing CO_2 into a variety of chemicals, probably because of its intermediate binding strength to reactants[36, 176].
- H$_2$: More reactive metals such as Pt, Ni and Fe yield mainly hydrogen as a result of water reduction occurring simultaneously to CO_2 reduction.

Most of the attempts to improve current catalysts have been oriented at increasing electrochemical activity, mainly through surface nanostructuring. Notable examples include Au[177, 178, 179, 180, 181], Bi[182, 183], Ag[184, 185], Sn[186, 187] and Cu[45, 188, 189, 190, 191]. However, changes in selectivity are typically minimal. This implies that there are highly active and selective materials to produce CO (Au) or formate (Bi, Sn), but they fail to reduce the products further. Cu is the only exception where more than two electrons are transferred during the reaction, but selectivity remains poor in most cases and overpotentials high. This has motivated researchers to think of a two-step process where CO_2 is initially reduced to CO, and CO is reduced further in a second step. CO reduction yields products on Cu electrodes, but both activity and selectivity are far from optimal[192]. A major breakthrough occurred in the Kanan laboratory at Stanford, where they showed that oxidizing and reducing the Cu surface resulted in a very high surface area material producing ethanol and acetate during CO reduction[46]. In particular, Faradaic efficiency to CO reduction is higher than 50 % at -0.3 V (the remaining product being hydrogen). While there is room for improvement, this was the first result showing significant amounts of alcohols from electrochemical CO reduction. So far the mechanisms that make this form of Cu special are not well understood. Rather than diving into hypotheses, for now I will explain briefly how to prepare the samples and the electrochemical results, and discuss possible explanations in the results section.

5.2 Oxide-derived Cu

Figure 5.3 shows the typical preparation procedure of OD Cu. In short, a Cu foil is oxidized in air for 1 h at 500 ºC, and it is then reduced back to metallic Cu. This step can be done in-situ in the electrochemical cell, or ex-situ reducing it with hydrogen. From now on, I will focus on the thermally reduced sample since it is the only one clean enough for TPD experiments.
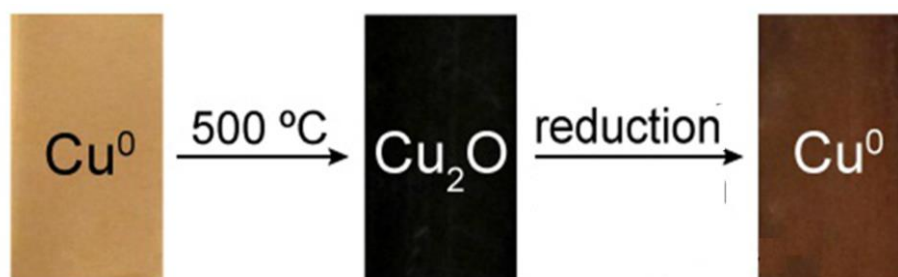
Figure 5.3: OD Cu preparation. A fresh Cu foil is oxidized at 500 ºC in air for 1 h, which results in a black surface. Then it is reduced (either electrochemically or thermally in a H_2 atmosphere) which gives a brownish color.

As presented in Figure 5.4, CO reduction on OD Cu yields a variety of products. Notably, liquid oxygenates such as acetate, ethanol and propanol are present, with a combined Faradaic efficiency higher than 40 %. C_2H_4 is also present with a 4 % Faradaic efficiency. The remaining ~55 % of efficiency is attributed to hydrogen evolution. As a comparison, Cu nanoparticles tested under the same conditions have an efficiency of 6 % to ethanol and acetate combined. In addition, when normalizing CO reduction current to Cu surface area (estimated from capacitance measurements), OD Cu has an activity 25 times greater than nanoparticles[46].

It also turns out that annealing OD Cu after reduction greatly diminishes its capacity to reduce CO. As seen in Figure 5.4, both activity and selectivity are negligible after annealing at 350 ºC. Annealing at an intermediate temperature of 200 ºC results in an intermediate performance. The oxidation conditions also play a role, as exemplified by data on a sample oxidized at 300 ºC (instead of 500 ºC), which also has intermediate performance. Interestingly, activity for hydrogen evolution is comparable for all samples at ~0.008mA/cm^2, and mainly changes in CO reduction activity modulate efficiency.
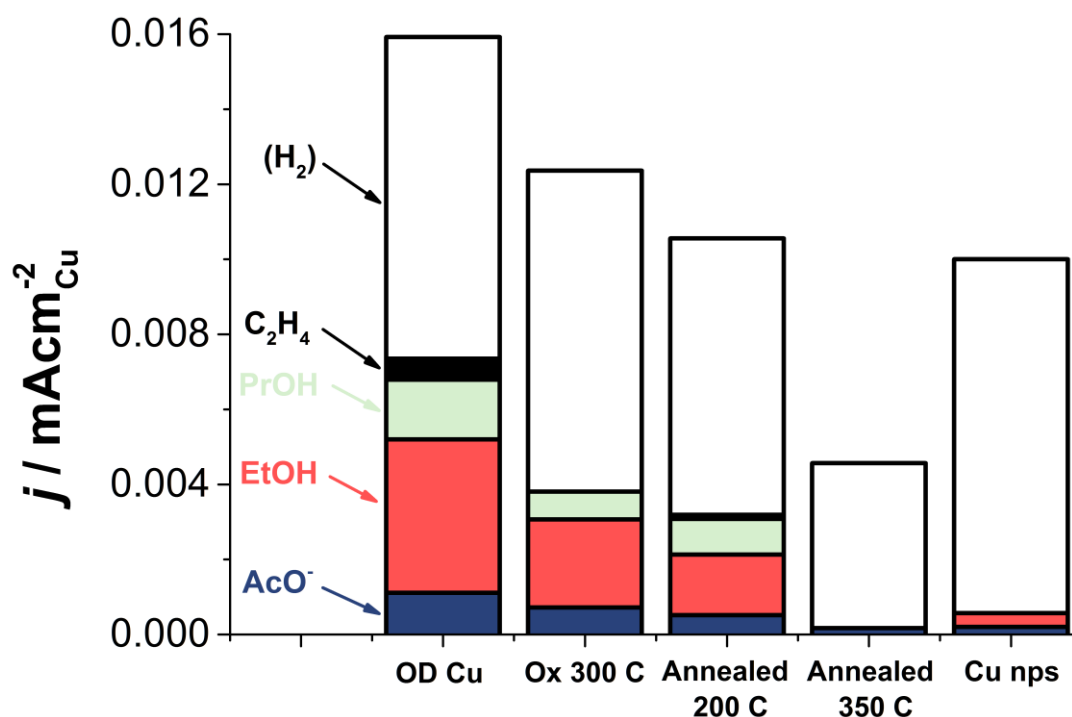
Figure 5.4: CO reduction activity on OD Cu samples and Cu nanoparticles. The y-axis represents absolute value of current density normalized to surface area of Cu, estimated from capacitance measurements. The white background is total current density, mostly corresponding to H$_2$, and the colored bars represent current densities to acetate (blue), ethanol (red), propanol (green) and ethylene (black). Measurements performed by Christina Li at Stanford University.

Most samples are porous and have high surface area, as confirmed by both SEM and electrochemical measurements (Figure 5.5). OD Cu has a roughness factor of 50, and the roughness factor drops to 24 when annealing at 200 ºC, and further to 14 when annealing at 350 ºC. When oxidizing the sample at 300 ºC roughness factor is the lowest, at a value of 6. From this data it is clear that surface area alone cannot be the decisive factor in determining CO reduction activity. For instance, the sample oxidized at 300 ºC has an activity much higher than the sample annealed at 350 ºC. The surface area of the former is lower than that of the latter, which implies that larger surface area does not necessarily translate into activity improvements.
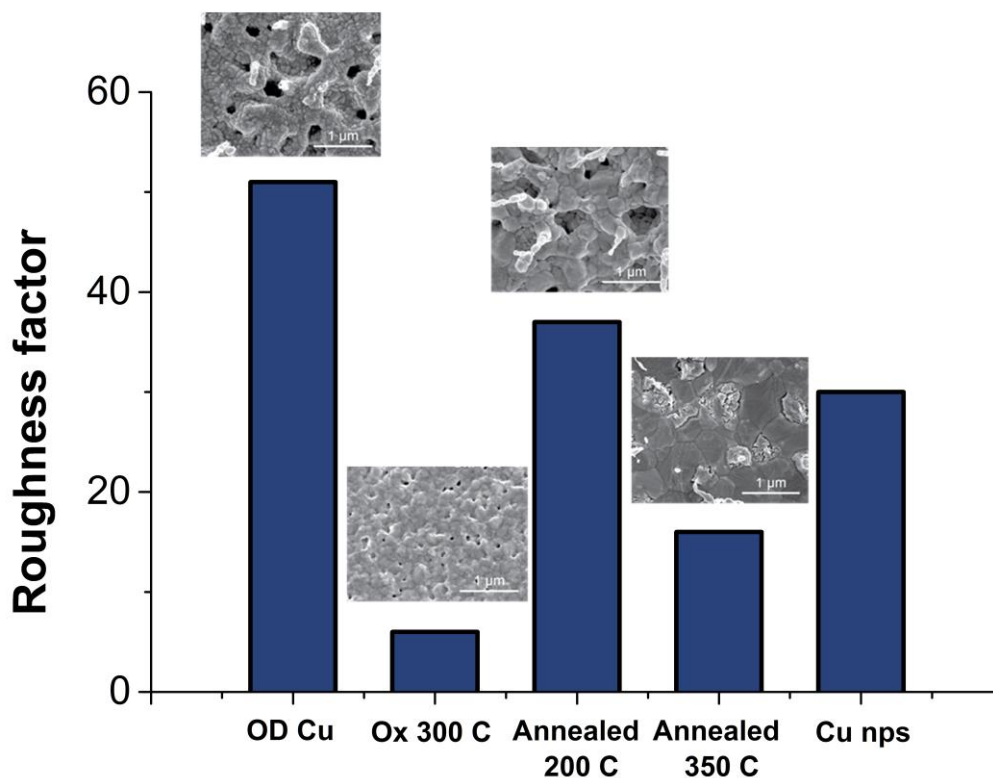
Figure 5.5: Roughness factors and SEM images for various Cu samples. Roughness factor is derived from capacitance data, and it is relative to an electropolished polycrystalline Cu sample measured under the same conditions. Measurements performed by Christina Li at Stanford University.

The intrinsic complexity of the samples implies that understanding their activity is challenging. Early attempts at the Kanan laboratory probed hypotheses such as microstrain or grain boundary density, but structural characterization via XRD and TEM did not report any evident factors. Several other hypotheses have been suggested, but a definitive proof has remained elusive. Three main lines of thought are discussed in the literature:

- Koper and coworkers attribute the high activity to Cu(100) facets, which they report to be favorable for CO reduction to C_2 products and minimize hydrogen evolution[189, 193, 194]. In these experiments products are not quantified, and recent in-situ STM reports show Cu single crystals severely reconstruct under reaction conditions[195].

- On the basis of theoretical calculations, Nørskov and coworkers propose that undercoordinated sites are responsible for the activity[196, 197].

- Kanan et al observe a high density of grain boundaries in OD Cu, and suggest they can influence electrochemical activity[46], either directly or by inducing defects at the surface.

To test these hypotheses I thought it would be useful to understand which facets are present at the surface. Potentially, that could reveal the existence of an unusual distribution of sites. Temperature programmed desorption can be employed for that purpose, although in the past it has seldom been used in connection to electrochemical measurements[84, 198].

As a benchmark, we reproduced TPD data from the literature on polycrystalline Cu[199]. The TPD profile is shown in Figure 5.6. Clearly, there are two distinct features; one centered at 170 K, associated to low index facets, and one centered at 220 K, attributed to step sites. We then prepared OD Cu for the TPD measurements by oxidizing a Cu foil outside the chamber and reducing it in the chamber at 130 ºC under a flow of H$_2$. This ensured that the sample was clean after reduction, as confirmed by XPS. Figure 5.6 shows the resulting TPD profile, markedly different from polycrystalline Cu. Firstly, as a result of the higher surface area of OD Cu the absolute signal was three times higher than for polycrystalline Cu. The second difference in the TPD of OD Cu is the shift of the signal to higher temperatures. In UHV experiments this shift has not been reported on single crystals, and for that reason I treated it independently from the rest in the deconvolution.

I deconvoluted the TPD in three peaks: one centered at 170 K attributed to low-index facets; one centered at 220 K arising from stepped sites, and a high temperature peak at 270 K indicating some very strongly bound CO molecules. I used Gaussians for the fits as suggested in the literature[84], and the peak positions of low index facets and stepped sites were fixed ±10 K from the polycrystalline Cu value. The high temperature peak was left unconstrained, but always came to ~270 K. The dark red area in Figure 5.6 cannot be accounted for by sites existent in polycrystalline Cu, and we attributed it to grain boundaries and defects at the surface. These highly undercoordinated configurations of atoms would be very reactive and bind CO very strongly.
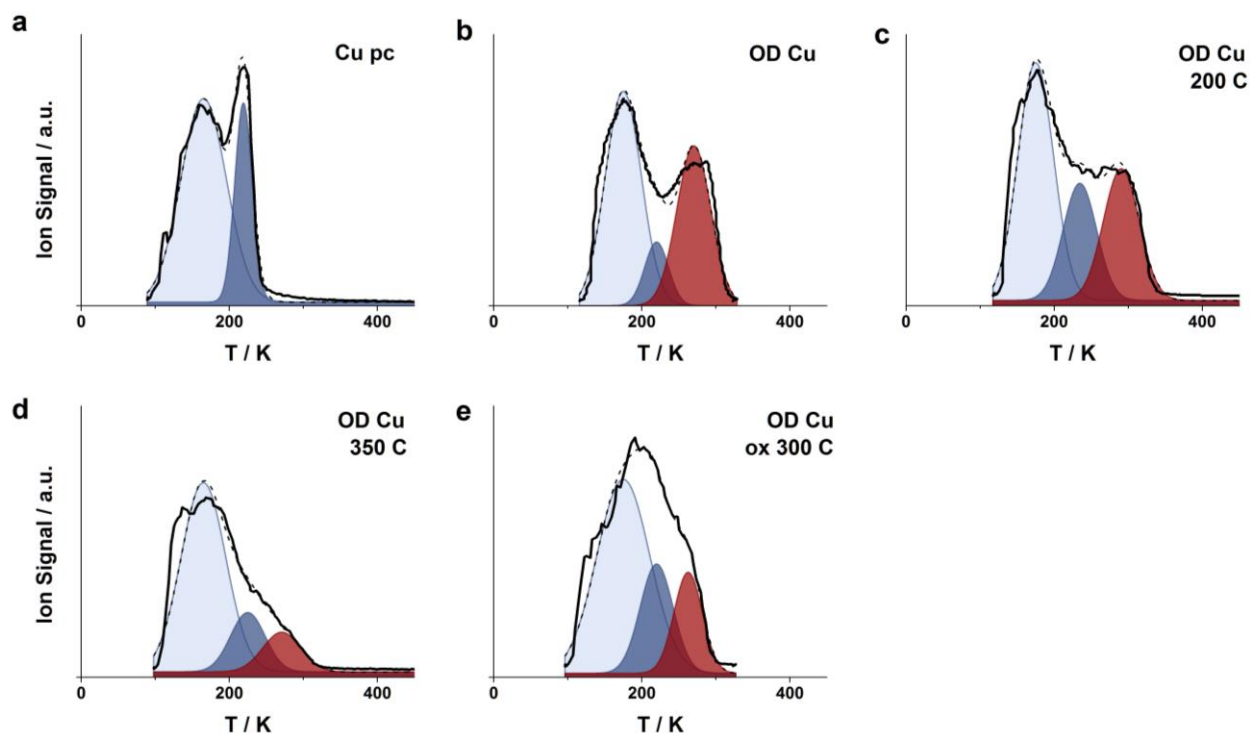
Figure 5.6: TPD profiles for various Cu samples and corresponding deconvolution of the features. Low index facets are highlighted in light blue, undercoordinated sites in dark blue and strong binding sites in red. a) Polycrystalline copper. b) Oxide-derived copper. c) Oxide-derived copper annealed at 200 ºC. d) Oxide-derived copper annealed at 350 ºC. e) Oxide-derived copper oxidized at 300 ºC. In all measurements the ramp rate was 2 K/s and CO dosage was 200 L (L=Langmuir, unit of dosage equivalent to 10^{-6} torr for one second). Measurements performed by Tobias Johansson.

An alternative, but to my mind less probable explanation for the high temperature feature would be that it arises from readsorption of CO in the pores. Similar high temperature features have been observed on commercial $Cu/ZnO/Al_2O_3$ catalysts for methanol synthesis, but using a tubular setup where samples are very prone to readsorption of CO[200, 201]. Readsorption does not occur so easily in UHV, especially at the low coverages used in these experiments. From the absolute area under the TPD it is possible to estimate the amount of CO adsorbed, and therefore the coverage. The raw data is shown in Figure 5.7. Polycrystalline Cu was dosed 200 L, which should completely cover the surface with CO[199]. OD Cu has a factor of 50 times that area, and for the same 200 L dosage the signal is three times higher than on polycrystalline Cu. Increasing the dosage to 12.000 L gives 40 times higher signal. From this data, CO coverage of OD Cu on the 200 L experiments is less than 10 %, which should not induce a significant shift in desorption temperatures. Further insights could be gained by modelling TPD experiments in porous samples[200]. For the time being, the most plausible explanation for the strongly bound CO under UHV is the existence of very undercoordinated and reactive sites at the surface of OD Cu. The high density of grain boundaries in these samples may induce the

presence of these sites at the surface[46], which would be kinetically trapped in the reduction process.
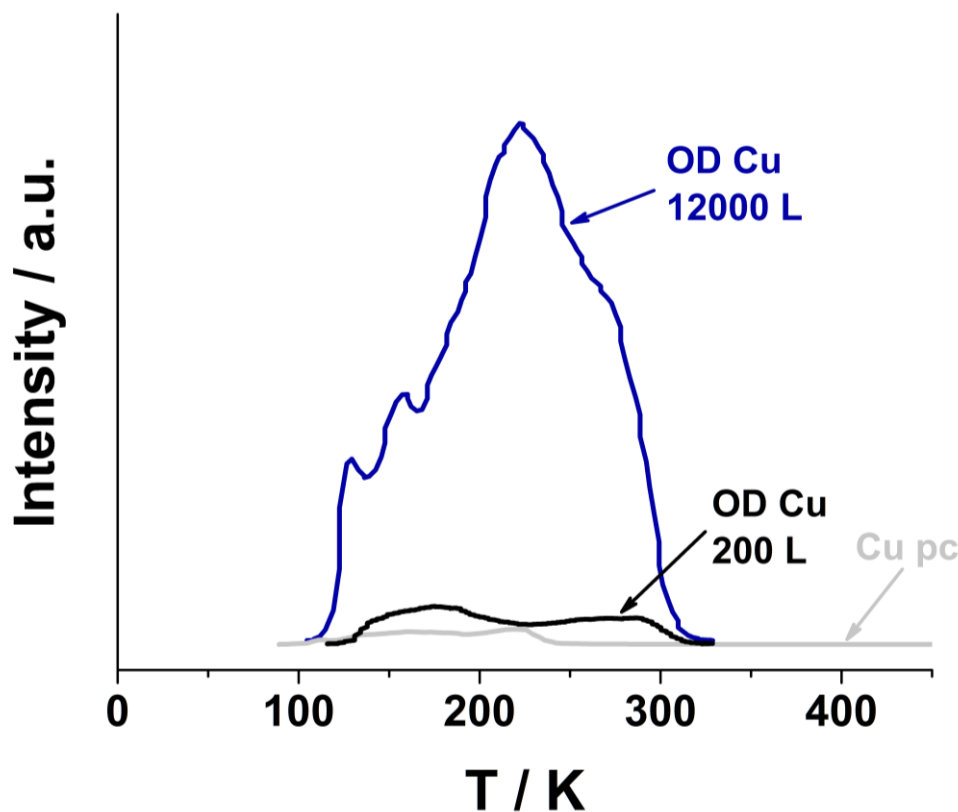
Figure 5.7: Comparison of TPD profiles for Cu pc (200 L) and OD Cu at two different CO doses (200 and 12000 L). In all measurements the ramp rate was 2 K/s. The ripples at ~150 K are caused by small oscillations in sample temperature in the beginning of the experiment. Measurements performed by Tobias Johansson.

Annealing the samples removes these sites by bringing the surface to a more stable configuration. Samples with intermediate activity, prepared either by posterior annealing or by lower oxidation temperature, show a decreased strong binding site feature. After annealing the sample in UHV (at 350 ºC for 2 h) the resulting TPD showed a drastically reduced proportion of strongly bound CO molecules (Figure 5.6). In contrast, the decrease in both activity and high temperature feature was milder when post-annealing the sample at only 200 ºC. This pointed towards a dependency between the very strongly bound CO and the CO reduction activity, which was further confirmed by the TPD on the sample oxidized at 300 ºC instead of 500 ºC. The qualitative correlation between electrochemical CO reduction activity and high temperature TPD feature is evident, although it is hard to establish a more quantitative relation.

Other hypotheses for the high activity of OD Cu are immediately discarded based on this data. In particular, surface area does not seem to be a crucial factor, given that a) high surface area samples can be inactive (i.e. OD Cu post-annealed); b) low surface area samples can be active (i.e. sample oxidized at 300 ºC).

5.3 Enhancing thermal stability of OD Cu

One of the problems associated with OD Cu is its thermal stability. At high temperatures the nanostructure tends to collapse, which results in decreased surface area, increase in hydrogen evolution activity and decrease in $CO_{(2)}$ reduction current. This would limit applicability of similar nanostructured materials at higher temperatures, which is desirable because high temperatures facilitate C-O bond cleavage[202]. One hypothesis is that at high temperature the surface would restructure to the lowest energy configuration, resulting in decreased number of grain boundaries. This would lead to a lowered catalytic activity[46]. It turns out that the materials science community has been studying grain boundaries on copper as their existence results in metal embrittlement and easier fracture[203, 204]. One of the leading causes for grain boundary appearance is the presence of other elements, particularly post-transition metals (such as Sn, Bi or Sb). In this case, a higher density of grain boundaries leads to easier fracture and for that reason impurities are removed from the Cu lattice. Kanan and coworkers propose that during $CO_{(2)}$ reduction grain boundaries can enhance activity and selectivity[46], and it might be possible to stabilize them by adding small amounts of dopants. This was the main hypothesis I probed at Matt Kanan's laboratories at Stanford. I mainly studied CO_2 reduction, but all data correlates well for CO reduction too.

It was important to first reproduce data on OD Cu. In Figure 5.8 I show my results at -0.5 V, very similar to those previously reported by Christina on the same samples[45]. The current is equally parts between H_2, CO and formate. In the same figure I also show what happens to a sample annealed at 200 ºC for 2 h under N_2 atmosphere. The overall current is higher and the selectivity shifts completely to H_2.

I tried a few different strategies to dope Cu with Bi: co-electrodeposition of Cu and Bi, deposition of Bi on the reduced samples and Bi deposition on Cu before oxidation treatment. The first two strategies yielded inconsistent amounts of Bi and the electrochemical activity was not affected. By far the most reproducible and promising strategy was to electrodeposit Bi on a Cu foil followed by oxidation at 500 ºC in air and reduction by annealing at 130 ºC under H_2 atmosphere. XPS confirmed Bi presence both after electrodeposition and after the reduction step. In addition, the amount of Bi could be controlled by the deposition time. However, Bi turned out not to improve selectivity of

the annealed samples. While total current decreased, the only product was still hydrogen. One explanation could be that Bi moves to grain boundaries and stabilizes them, but in doing so it blocks the surface sites which reduce CO.
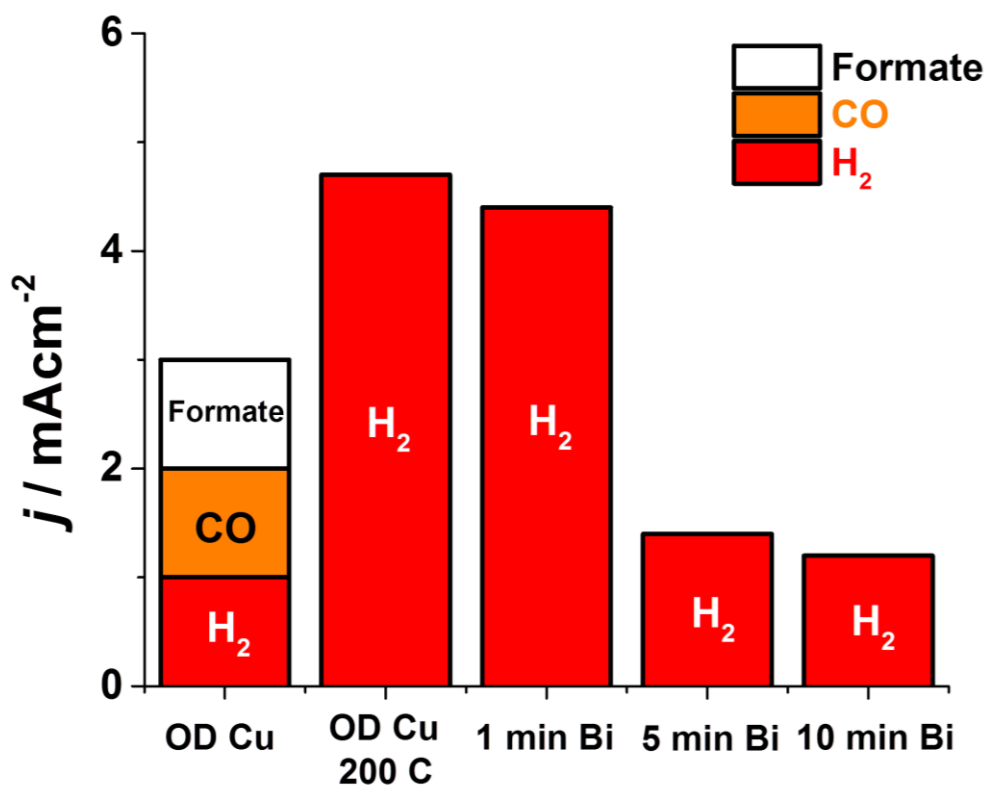
Figure 5.8: CO$_2$ electroreduction on OD Cu, OD Cu annealed and OD Cu annealed and doped with Bi. All Bi-doped samples have been annealed at 200 ºC. The y-axis is current density normalized to geometrical surface area. Experiments carried out at -0.5 V in CO$_2$-saturated 0.5 M NaHCO$_3$.

I also tried other materials such as Sb or Sn, which should have similar effects than Bi[205], but the end result was very similar. More structural analysis (SEM, TEM) would be needed to formulate a more definitive explanation, but given the results were not very promising I did not pursue this further. The method I used to prepare these materials, i.e. electrodeposition and subsequent oxidation treatment could also be adapted further; for instance OD Cu could be improved by producing alloys via this method.

5.4 Outlook

OD Cu represents the first proof of principle that CO reduction to valuable oxygenates is possible. Development of catalysts is still in the very early stages and there is plenty of room for improvement. This opens up very interesting avenues, going from ionic liquid

coatings to nanostructured alloys. Improvements will be accelerated by a fundamental understanding on the high activity of OD Cu. I have tried to contribute to that by exploring the active sites on this surface. Of the several hypotheses proposed, TPD data suggests strong binding energy sites are responsible for the electrochemical activity. Such sites are inexistent in other inactive forms of Cu, and their presence scales with activity for CO reduction products. A valid hypothesis is that such sites are kinetically trapped defects formed during the reduction process, which disappear upon annealing of the samples. It would be interesting to increase density of strong binding sites to further improve activity, as well as modify the surface slightly by alloying to suppress hydrogen evolution further.

Another important hurdle that needs to be solved before implementation is the thermal stability of nanostructured surfaces. Bi-doping seemed a promising pathway to stabilize grain boundaries, but results showed this was insufficient to keep CO_2 reduction activity. Alloying Cu –rather than just doping it– with heat-resistant materials might be an easier strategy to enhance thermal stability.

In spite of the progress achieved, the very basic cost analysis presented in the introduction places serious doubts into large scale feasibility of CO_2 reduction even under best case scenarios. Very niche applications in cost insensitive industries like submarines or space shuttles will likely be the first to implement such devices. Whether other uses will become a reality remains an open question.

6 Conclusions

In this thesis I have given some examples on how fundamental understanding of electrocatalytic reactions can lead to improvements in activity, selectivity and stability of catalysts.

Building upon years of research, a new set of materials based on alloys of Pt and rare earths have been reported for oxygen reduction to water. These alloys have an activity as much as five times higher than pure Pt, and are stable upon extended cycling. Under reaction conditions a Pt overlayer is formed, whose degree of compression seems to determine activity and is highly dependent on the underlying crystal structure.

A combination of theoretical calculations and experiments led to the discovery of new catalysts for hydrogen peroxide synthesis. As much as a 100-fold improvement over state-of-the-art in mass activity was demonstrated, as well as selectivity approaching 100 %. More importantly, the single site concept was demonstrated as a way to tune selectivity in electrochemical reactions.

Finally, investigations on OD Cu samples shed some light into the reasons for their unprecedented activity for CO reduction. Metastable highly reactive sites at the surface are responsible for alcohol production from CO. Positively identifying these sites is the first step in further activity and selectivity improvements.

Bibliography

1.   OECD. Population Growth Rate Factbook; 2013.

2.   Wikipedia. 2014 Available from: http://en.wikipedia.org/wiki/Global_hectare

3.   Global Footprint Network; 2010.

4.   Duro JA, Teixidó-Figueras J. Ecological footprint inequality across countries: The role of environment intensity, income and interaction effects. *Ecological Economics* 2013, **93**(0)**:** 34-41.

5.   Mackenzie H, Messinger H, Smith R. Canada's Ecological Footprint by Income; 2008.

6.   GDP and its breakdown at current prices in US Dollars. *United Nations Statistics Division* 2013.

7.   How to feed the world 2050. *Food and Agricultural Organization of the United Nations* 2009.

8.   GSMA. Smartphone forecasts and assumptions, 2007-2020; 2014.

9.   United Nations Water. 2013 Available from: http://www.unwater.org/water-cooperation-2013/water-cooperation/facts-and-figures/en/

10.   World Bank Gross Domestic Product 2010; 2010.

11.   World Energy Expenditures. 2014 Available from: http://www.leonardo-energy.org/world-energy-expenditures

12.   Cayuela R. *The Future of the Chemical Industry by 2050*. John Wiley & Sons, 2013.

13.   Ullman's Encyclopedia of Industrial Chemistry. *Ullman's Encyclopedia of Industrial Chemistry, Wiley, 1999-2013*.

14.   Electrocatalysis. Available from: http://www.nature.com/subjects/electrocatalysis

15.   Norskov JK, Bligaard T, Hvolbaek B, Abild-Pedersen F, Chorkendorff I, Christensen CH. The nature of the active site in heterogeneous metal catalysis. *Chemical Society Reviews* 2008, **37**(10)**:** 2163-2171.

16.   Norskov JK, Bligaard T, Rossmeisl J, Christensen CH. Towards the computational design of solid catalysts. *Nat Chem* 2009, **1**(1)**:** 37-46.

17.   Zheng Y, Jiao Y, Jaroniec M, Qiao SZ. Advancing the Electrochemistry of the Hydrogen-Evolution Reaction through Combining Experiment and Theory. *Angewandte Chemie International Edition* 2015, **54**(1)**:** 52-65.

18.   Calle-Vallejo F, Martínez JI, García-Lastra JM, Rossmeisl J, Koper MTM. Physical and Chemical Nature of the Scaling Relations between Adsorption Energies of Atoms on Metal Surfaces. *Physical Review Letters* 2012, **108**(11)**:** 116103.

19.   Medford AJ, Wellendorff J, Vojvodic A, Studt F, Abild-Pedersen F, Jacobsen KW, Bligaard T, Nørskov JK. Assessing the reliability of calculated catalytic ammonia synthesis rates. *Science* 2014, **345**(6193)**:** 197-200.

20.   Stephens IEL, Bondarenko AS, Gronbjerg U, Rossmeisl J, Chorkendorff I. Understanding the electrocatalysis of oxygen reduction on platinum and its alloys. *Energy & Environmental Science* 2012.

21.   Parsons R. The rate of electrolytic hydrogen evolution and the heat of adsorption of hydrogen. *Transactions of the Faraday Society* 1958, **54**(0)**:** 1053-1063.

22.   Jaegermann W, Tributsch H. Interfacial properties of semiconducting transition metal chalcogenides. *Progress in Surface Science* 1988, **29**(1–2)**:** 1-167.

23.   Hinnemann B, Moses PG, Bonde J, Jørgensen KP, Nielsen JH, Horch S, Chorkendorff I, Nørskov JK. Biomimetic Hydrogen Evolution: MoS2 Nanoparticles as Catalyst for Hydrogen Evolution. *J Am Chem Soc* 2005, **127**(15)**:** 5308-5309.

24.   Jaramillo TF, Jørgensen KP, Bonde J, Nielsen JH, Horch S, Chorkendorff I. Identification of Active Edge Sites for Electrochemical H2 Evolution from MoS2 Nanocatalysts. *Science* 2007, **317**(5834)**:** 100-102.

25.   Laursen AB, Kegnaes S, Dahl S, Chorkendorff I. Molybdenum sulfides-efficient and viable materials for electro - and photoelectrocatalytic hydrogen evolution. *Energy & Environmental Science* 2012, **5**(2)**:** 5577-5591.

26.   Kibsgaard J, Chen Z, Reinecke BN, Jaramillo TF. Engineering the surface structure of MoS2 to preferentially expose active edge sites for electrocatalysis. *Nat Mater* 2012, **11**(11)**:** 963-969.

27.   Kibsgaard J, Jaramillo TF, Besenbacher F. Building an appropriate active-site motif into a hydrogen-evolution catalyst with thiomolybdate [Mo3S13]2− clusters. *Nat Chem* 2014, **6**(3)**:** 248-253.

28.   Greeley J, Jaramillo TF, Bonde J, Chorkendorff I, Norskov JK. Computational high-throughput screening of electrocatalytic materials for hydrogen evolution. *Nat Mater* 2006, **5**(11)**:** 909-913.

29.   Trasatti S. Electrocatalysis in the anodic evolution of oxygen and chlorine. *Electrochim Acta* 1984, **29**(11)**:** 1503-1512.

30. Suntivich J, May KJ, Gasteiger HA, Goodenough JB, Shao-Horn Y. A Perovskite Oxide Optimized for Oxygen Evolution Catalysis from Molecular Orbital Principles. *Science* 2011, **334**(6061)**:** 1383-1385.

31. Stamenkovic V, Mun BS, Mayrhofer KJJ, Ross PN, Markovic NM, Rossmeisl J, Greeley J, Nørskov JK. Changing the Activity of Electrocatalysts for Oxygen Reduction by Tuning the Surface Electronic Structure. *Angewandte Chemie International Edition* 2006, **45**(18)**:** 2897-2901.

32. Stamenkovic VR, Mun BS, Arenz M, Mayrhofer KJJ, Lucas CA, Wang G, Ross PN, Markovic NM. Trends in electrocatalysis on extended and nanoscale Pt-bimetallic alloy surfaces. *Nat Mater* 2007, **6**(3)**:** 241-247.

33. GreeleyJ, Stephens IEL, Bondarenko AS, Johansson TP, Hansen HA, Jaramillo TF, RossmeislJ, ChorkendorffI, Nørskov JK. Alloys of platinum and early transition metals as oxygen reduction electrocatalysts. *Nat Chem* 2009, **1**(7)**:** 552-556.

34. Stephens IEL, Bondarenko AS, Perez-Alonso FJ, Calle-Vallejo F, Bech L, Johansson TP, Jepsen AK, Frydendal R, Knudsen BP, Rossmeisl J, Chorkendorff I. Tuning the Activity of Pt(111) for Oxygen Electroreduction by Subsurface Alloying. *J Am Chem Soc* 2011, **133**(14)**:** 5485-5491.

35. Suntivich J, Gasteiger HA, Yabuuchi N, Nakanishi H, Goodenough JB, Shao-Horn Y. Design principles for oxygen-reduction activity on perovskite oxide catalysts for fuel cells and metal-air batteries. *Nat Chem* 2011, **3**(8)**:** 647-647.

36. Kuhl KP, Hatsukade T, Cave ER, Abram DN, Kibsgaard J, Jaramillo TF. Electrocatalytic Conversion of Carbon Dioxide to Methane and Methanol on Transition Metal Surfaces. *J Am Chem Soc* 2014, **136**(40)**:** 14107-14113.

37. Koper MTM. Thermodynamic theory of multi-electron transfer reactions: Implications for electrocatalysis. *Journal of Electroanalytical Chemistry* 2011, **660**(2)**:** 254-260.

38. Koper MTM. Theory of multiple proton-electron transfer reactions and its implications for electrocatalysis. *Chemical Science* 2013, **4**(7)**:** 2710-2723.

39. Bard AJ, Faulkner LR. *Electrochemical Methods: Fundamentals and Applications*. Wiley-VCH, 2001.

40. Three electrode setup. 2015 Available from: http://ralphgroup.lassp.cornell.edu/projects/graphene_electrochemistry/

41. Gileadi E. *Physical Electrochemistry*. Wiley-VCH, 2011.

42. Kibler LA. Preparation and characterization of noble metal single crystal electrode surfaces; 2003.

43. Kuhl KP, Cave ER, Abram DN, Jaramillo TF. New insights into the electrochemical reduction of carbon dioxide on metallic copper surfaces. *Energy & Environmental Science* 2012, **5**(5)**:** 7050-7059.

44. Wu HL, Yau S, Zei MS. Crystalline alloys produced by mercury electrodeposition on Pt(111) electrode at room temperature. *Electrochim Acta* 2008, **53**(20)**:** 5961-5967.

45. Li CW, Kanan MW. CO2 Reduction at Low Overpotential on Cu Electrodes Resulting from the Reduction of Thick Cu2O Films. *J Am Chem Soc* 2012, **134**(17)**:** 7231-7234.

46. Li CW, Ciston J, Kanan MW. Electroreduction of carbon monoxide to liquid fuel on oxide-derived nanocrystalline copper. *Nature* 2014, **508**(7497)**:** 504-507.

47. Gasteiger HA, Kocha SS, Sompalli B, Wagner FT. Activity benchmarks and requirements for Pt, Pt-alloy, and non-Pt oxygen reduction catalysts for PEMFCs. *Appl Catal B-Environ* 2005, **56**(1-2)**:** 9-35.

48. Hernandez-Fernandez P. Ph.D. thesis. Universidad Autónoma de Madrid, 2009.

49. Paulus UA, Schmidt TJ, Gasteiger HA, Behm RJ. Oxygen reduction on a high-surface area Pt/Vulcan carbon catalyst: a thin-film rotating ring-disk electrode study. *Journal of Electroanalytical Chemistry* 2001, **495**(2)**:** 134-145.

50. Malacrida P. Ph.D. thesis. Technical University of Denmark, 2014.

51. Hori Y. Electrochemical CO2 Reduction on Metal Electrodes. In: Vayenas C, White R, Gamboa-Aldeco M (eds). *Modern Aspects of Electrochemistry*, vol. 42. Springer New York, 2008, pp 89-189.

52. Huckaba CE, Keyes FG. THE ACCURACY OF ESTIMATION OF HYDROGEN PEROXIDE BY POTASSIUM PERMANGANATE TITRATION. *J Am Chem Soc* 1948, **70**(4)**:** 1640-1644.

53. Hong J, Zhang W, Ren J, Xu R. Photocatalytic reduction of CO2: a brief review on product analysis and systematic methods. *Analytical Methods* 2013, **5**(5)**:** 1086-1097.

54. Jovanov Z. Ph.D. thesis. Technical University of Denmark, 2014.

55. Biegler T, Rand DAJ, Woods R. Limiting oxygen coverage on platinized platinum; Relevance to determination of real platinum area by hydrogen adsorption. *Journal of Electroanalytical Chemistry and Interfacial Electrochemistry* 1971, **29**(2)**:** 269-277.

56. van der Vliet DF, Wang C, Li D, Paulikas AP, Greeley J, Rankin RB, Strmcnik D, Tripkovic D, Markovic NM, Stamenkovic VR. Unique Electrochemical Adsorption Properties of Pt-Skin Surfaces. *Angewandte Chemie International Edition* 2012, **51**(13)**:** 3139-3142.

57. Grdeń M, Łukaszewski M, Jerkiewicz G, Czerwiński A. Electrochemical behaviour of palladium electrode: Oxidation, electrodissolution and ionic adsorption. *Electrochim Acta* 2008, **53**(26)**:** 7583-7598.

58. Weaver MJ, Chang SC, Leung LWH, Jiang X, Rubel M, Szklarczyk M, Zurawski D, Wieckowski A. Evaluation of absolute saturation coverages of carbon monoxide on ordered low-index platinum and rhodium electrodes. *Journal of Electroanalytical Chemistry* 1992, **327**(1–2)**:** 247-260.

59.   Herrero E, Buller LJ, Abruña HD. Underpotential Deposition at Single Crystal Surfaces of Au, Pt, Ag and Other Materials. *Chemical Reviews* 2001, **101**(7)**:** 1897-1930.

60.   Green CL, Kucernak A. Determination of the Platinum and Ruthenium Surface Areas in Platinum−Ruthenium Alloy Electrocatalysts by Underpotential Deposition of Copper. I. Unsupported Catalysts. *The Journal of Physical Chemistry B* 2002, **106**(5)**:** 1036-1047.

61.   Chorkendorff I, Niemantsverdriet, J. W. . *Concepts of Modern Catalysis and Kinetics*. Wiley-VCH, 2007.

62.   . 2014 Available from: http://mini.physics.sunysb.edu/~marivi/TEACHING-OLD/PHY313/doku.php?id=lectures:8

63.   Häglund J, Fernández Guillermet A, Grimvall G, Körling M. Theory of bonding in transition-metal carbides and nitrides. *Physical Review B* 1993, **48**(16)**:** 11685-11691.

64.   Deiana D. Ph.D. thesis. Technical University of Denmark, 2014.

65.   Gasteiger HA, Garche J. Fuel Cells. *Handbook of Heterogeneous Catalysis*. Wiley-VCH Verlag GmbH & Co. KGaA, 2008.

66.   Wachsman ED, Lee KT. Lowering the Temperature of Solid Oxide Fuel Cells. *Science* 2011, **334**(6058)**:** 935-939.

67.   Varcoe JR, Atanassov P, Dekel DR, Herring AM, Hickner MA, Kohl PA, Kucernak AR, Mustain WE, Nijmeijer K, Scott K, Xu T, Zhuang L. Anion-exchange membranes in electrochemical energy systems. *Energy & Environmental Science* 2014, **7**(10)**:** 3135-3191.

68.   Toyota. 2015 Available from: http://www.toyota-global.com/innovation/environmental_technology/fuelcell_vehicle/

69.   Vesborg PCK, Jaramillo TF. Addressing the terawatt challenge: scalability in the supply of chemical elements for renewable energy. *RSC Advances* 2012, **2**(21)**:** 7933-7947.

70.   . Available from: https://www.mercedes-benz.com/en/

71.   Tesla Motors. 2015 Available from: http://www.teslamotors.com/

72.   Spendelow J, Marcinkoski J. DOE Fuel Cell Technologies Office Record; 2013.

73.   Wesselmark M, Wickman B, Lagergren C, Lindbergh G. Hydrogen oxidation reaction on thin platinum electrodes in the polymer electrolyte fuel cell. *Electrochemistry Communications* 2010, **12**(11)**:** 1585-1588.

74.   Bashyam R, Zelenay P. A class of non-precious metal composite catalysts for fuel cells. *Nature* 2006, **443**(7107)**:** 63-66.

75.   Lefevre M, Proietti E, Jaouen F, Dodelet J-P. Iron-Based Catalysts with Improved Oxygen Reduction Activity in Polymer Electrolyte Fuel Cells. *Science* 2009, **324**(5923)**:** 71-74.

76.   Jaouen F, Proietti E, Lefevre M, Chenitz R, Dodelet J-P, Wu G, Chung HT, Johnston CM, Zelenay P. Recent advances in non-precious metal catalysis for oxygen-reduction reaction in polymer electrolyte fuel cells. *Energy & Environmental Science* 2011, **4**(1)**:** 114-130.

77.   Hartl K, Hanzlik M, Arenz M. IL-TEM investigations on the degradation mechanism of Pt/C electrocatalysts with different carbon supports. *Energy & Environmental Science* 2011, **4**(1)**:** 234-238.

78.   Guo S, Sun S. FePt Nanoparticles Assembled on Graphene as Enhanced Catalyst for Oxygen Reduction Reaction. *J Am Chem Soc* 2012, **134**(5)**:** 2492-2495.

79.   Kibsgaard J, Gorlin Y, Chen Z, Jaramillo TF. Meso-Structured Platinum Thin Films: Active and Stable Electrocatalysts for the Oxygen Reduction Reaction. *J Am Chem Soc* 2012, **134**(18)**:** 7758-7765.

80.   Galeano C, Meier JC, Peinecke V, Bongard H, Katsounaros I, Topalov AA, Lu A, Mayrhofer KJJ, Schüth F. Toward Highly Stable Electrocatalysts via Nanoparticle Pore Confinement. *J Am Chem Soc* 2012, **134**(50)**:** 20457-20465.

81.   Baldizzone C, Mezzavilla S, Carvalho HWP, Meier JC, Schuppert AK, Heggen M, Galeano C, Grunwaldt J-D, Schüth F, Mayrhofer KJJ. Confined-Space Alloying of Nanoparticles for the Synthesis of Efficient PtNi Fuel-Cell Catalysts. *Angewandte Chemie International Edition* 2014, **53**(51)**:** 14250-14254.

82.   Li D, Wang C, Strmcnik DS, Tripkovic DV, Sun X, Kang Y, Chi M, Snyder JD, van der Vliet D, Tsai Y, Stamenkovic VR, Sun S, Markovic NM. Functional links between Pt single crystal morphology and nanoparticles with different size and shape: the oxygen reduction reaction case. *Energy & Environmental Science* 2014.

83.   Nesselberger M, Ashton S, Meier JC, Katsounaros I, Mayrhofer KJJ, Arenz M. The Particle Size Effect on the Oxygen Reduction Reaction Activity of Pt Catalysts: Influence of Electrolyte and Relation to Single Crystal Models. *J Am Chem Soc* 2011, **133**(43)**:** 17428-17433.

84.   Perez-Alonso FJ, McCarthy DN, Nierhoff A, Hernandez-Fernandez P, Strebel C, Stephens IEL, Nielsen JH, Chorkendorff I. The Effect of Size on the Oxygen Electroreduction Activity of Mass-Selected Platinum Nanoparticles. *Angewandte Chemie International Edition* 2012**:** n/a-n/a.

85.   Shao M, Peles A, Shoemaker K. Electrocatalysis on Platinum Nanoparticles: Particle Size Effect on Oxygen Reduction Reaction Activity. *Nano Letters* 2011, **11**(9)**:** 3714-3719.

86.   Chen C, Kang Y, Huo Z, Zhu Z, Huang W, Xin HL, Snyder JD, Li D, Herron JA, Mavrikakis M, Chi M, More KL, Li Y, Markovic NM, Somorjai GA*, et al.* Highly Crystalline Multimetallic Nanoframes with Three-Dimensional Electrocatalytic Surfaces. *Science* 2014, **343**(6177)**:** 1339-1343.

87.   Cui C, Gan L, Heggen M, Rudi S, Strasser P. Compositional segregation in shaped Pt alloy nanoparticles and their structural behaviour during electrocatalysis. *Nat Mater* 2013, **12**(8)**:** 765-771.

88.   Zhang J, Sasaki K, Sutter E, Adzic RR. Stabilization of Platinum Oxygen-Reduction Electrocatalysts Using Gold Clusters. *Science* 2007, **315**(5809)**:** 220-222.

89.   Stamenkovic VR, Fowler B, Mun BS, Wang G, Ross PN, Lucas CA, Markovic NM. Improved Oxygen Reduction Activity on Pt3Ni(111) via Increased Surface Site Availability. *Science* 2007, **315**(5811)**:** 493-497.

90.   Strasser P, Koh S, Anniyev T, Greeley J, More K, Yu C, Liu Z, Kaya S, Nordlund D, Ogasawara H, Toney MF, Nilsson A. Lattice-strain control of the activity in dealloyed core–shell fuel cell catalysts. *Nat Chem* 2010, **2**(6)**:** 454-460.

91.   Appleby AJ. *Electrocatalysis and fuel cells*. Taylor & Francis, 1971.

92.   Mayrhofer KJJ, Meier JC, Ashton SJ, Wiberg GKH, Kraus F, Hanzlik M, Arenz M. Fuel cell catalyst degradation on the nanoscale. *Electrochemistry Communications* 2008, **10**(8)**:** 1144-1147.

93.   Mayrhofer KJJ, Hartl K, Juhart V, Arenz M. Degradation of Carbon-Supported Pt Bimetallic Nanoparticles by Surface Segregation. *J Am Chem Soc* 2009, **131**(45)**:** 16348-16349.

94.   Chen S, Gasteiger HA, Hayakawa K, Tada T, Shao-Horn Y. Platinum-Alloy Cathode Catalyst Degradation in Proton Exchange Membrane Fuel Cells: Nanometer-Scale Compositional and Morphological Changes. *J Electrochem Soc* 2010, **157**(1)**:** A82-A97.

95.   Dubau L, Lopez-Haro M, Castanheira L, Durst J, Chatenet M, Bayle-Guillemaud P, Guétaz L, Caqué N, Rossinot E, Maillard F. Probing the structure, the composition and the ORR activity of Pt3Co/C nanocrystallites during a 3422 h PEMFC ageing test. *Applied Catalysis B: Environmental* 2013, **142–143**(0)**:** 801-808.

96.   Wang C, Chi M, Li D, Strmcnik D, van der Vliet D, Wang G, Komanicky V, Chang K-C, Paulikas AP, Tripkovic D, Pearson J, More KL, Markovic NM, Stamenkovic VR. Design and Synthesis of Bimetallic Electrocatalyst with Multilayered Pt-Skin Surfaces. *J Am Chem Soc* 2011, **133**(36)**:** 14396-14403.

97.   Wang D, Xin HL, Hovden R, Wang H, Yu Y, Muller DA, DiSalvo FJ, Abruña HD. Structurally ordered intermetallic platinum–cobalt core–shell nanoparticles with enhanced activity and stability as oxygen reduction electrocatalysts. *Nat Mater* 2013, **12**(1)**:** 81-87.

98.   Kang Y, Snyder J, Chi M, Li D, More KL, Markovic NM, Stamenkovic VR. Multimetallic Core/Interlayer/Shell Nanostructures as Advanced Electrocatalysts. *Nano Letters* 2014, **14**(11)**:** 6361-6367.

99.   Stephens IEL, Bondarenko AS, Bech L, Chorkendorff I. Oxygen Electroreduction Activity and X-Ray Photoelectron Spectroscopy of Platinum and Early Transition Metal Alloys. *ChemCatChem* 2012, **4**(3)**:** 341-349.

100. Hernandez-Fernandez P, Masini F, McCarthy DN, Strebel CE, Friebel D, Deiana D, Malacrida P, Nierhoff A, Bodin A, Wise AM, Nielsen JH, Hansen TW, Nilsson A, StephensIfan EL, Chorkendorff I. Mass-selected nanoparticles of PtxY as model catalysts for oxygen electroreduction. *Nat Chem* 2014, **6**(8)**:** 732-738.

101. Bandarenka AS, Hansen HA, Rossmeisl J, Stephens IEL. Elucidating the activity of stepped Pt single crystals for oxygen reduction. *Physical Chemistry Chemical Physics* 2014, **16**(27)**:** 13625-13629.

102. Abild-Pedersen F, Greeley J, Studt F, Rossmeisl J, Munter TR, Moses PG, Skúlason E, Bligaard T, Nørskov JK. Scaling Properties of Adsorption Energies for Hydrogen-Containing Molecules on Transition-Metal Surfaces. *Physical Review Letters* 2007, **99**(1)**:** 016105.

103. Guminski C. The Hg-Pd (Mercury-Palladium) system. *Bulletin of Alloy Phase Diagrams* 1990, **11**(1)**:** 22-26.

104. Jacob KT, Waseda Y. Gibbs energies of formation of rare earth MPt5 compounds. *Thermochimica Acta* 1990, **165**(2)**:** 223-233.

105. Escudero-Escribano M, Verdaguer-Casadevall A, Malacrida P, Grønbjerg U, Knudsen BP, Jepsen AK, Rossmeisl J, Stephens IEL, Chorkendorff I. Pt5Gd as a Highly Active and Stable Catalyst for Oxygen Electroreduction. *J Am Chem Soc* 2012, **134**(40)**:** 16476-16479.

106. NASDAQ. December 2014 Available from: http://www.nasdaq.com/

107. Walker RA, Darby Jr JB. Thermodynamic properties of solid nickel-platinum alloys. *Acta Metallurgica* 1970, **18**(12)**:** 1261-1266.

108. Pretorius R, Marais TK, Theron CC. Thin film compound phase formation sequence: An effective heat of formation model. *Materials Science Reports* 1993, **10**(1–2)**:** 1-83.

109. Hultgren RR. *Selected Values of the Thermodynamic Properties of Binary Alloys*, 1973.

110. Kleykamp H. Thermodynamics of the systems of the platinum metals with other transition metals: I. Integral data. *Journal of Nuclear Materials* 1993, **201**(0)**:** 193-217.

111. Mavrikakis M, Hammer B, Nørskov JK. Effect of Strain on the Reactivity of Metal Surfaces. *Physical Review Letters* 1998, **81**(13)**:** 2819-2822.

112. Gomez-Marin AMa, Rizo R, Feliu JM. Oxygen reduction reaction at Pt single crystals: a critical overview. *Catalysis Science & Technology* 2014, **4**(6)**:** 1685-1698.

113. Yoo SJ, Hwang SJ, Lee J-G, Lee S-C, Lim T-H, Sung Y-E, Wieckowski A, Kim S-K. Promoting effects of La for improved oxygen reduction activity and high stability of Pt on Pt-La alloy electrodes. *Energy & Environmental Science* 2012, **5**(6)**:** 7521-7525.

114. Bronger W. Preparation and X-ray investigation of platinum alloys with the rare-earth metals (Pt5Ln and Pt3Ln phases). *Journal of the Less Common Metals* 1967, **12**(1)**:** 63-68.

115. Tao F, Grass ME, Zhang Y, Butcher DR, Renzas JR, Liu Z, Chung JY, Mun BS, Salmeron M, Somorjai GA. Reaction-Driven Restructuring of Rh-Pd and Pt-Pd Core-Shell Nanoparticles. *Science* 2008, **322**(5903)**:** 932-934.

116. Vendelbo SB, Elkjær CF, Falsig H, Puspitasari I, Dona P, Mele L, Morana B, Nelissen BJ, van Rijn R, Creemer JF, Kooyman PJ, Helveg S. Visualization of oscillatory behaviour of Pt nanoparticles catalysing CO oxidation. *Nat Mater* 2014, **13**(9)**:** 884-890.

117. Snyder J, Fujita T, Chen MW, Erlebacher J. Oxygen reduction in nanoporous metal–ionic liquid composite electrocatalysts. *Nat Mater* 2010, **9**(11)**:** 904-907.

118. Frydendal R, Busch M, Halck NB, Paoli EA, Krtil P, Chorkendorff I, Rossmeisl J. Enhancing Activity for the Oxygen Evolution Reaction: The Beneficial Interaction of Gold with Manganese and Cobalt Oxides. *ChemCatChem* 2014**:** n/a-n/a.

119. Campos-Martin JM, Blanco-Brieva G, Fierro JLG. Hydrogen Peroxide Synthesis: An Outlook beyond the Anthraquinone Process. *Angewandte Chemie International Edition* 2006, **45**(42)**:** 6962-6984.

120. Thénard JL. Observations sur des nouvelles combinaisons entre l'oxigène et divers acides. *Annales de chimie et de physique* 1818, **8:** 306-312.

121. ICIS. 2015 Available from: http://www.icis.com/chemicals/channel-info-chemicals-a-z/

122. Wikipedia. 2015 Available from: http://en.wikipedia.org/wiki/Anthraquinone

123. Hâncu D, Green J, Beckman EJ. H_2O_2 in CO_2/H_2O Biphasic Systems: Green Synthesis and Epoxidation Reactions. *Industrial & Engineering Chemistry Research* 2002, **41**(18)**:** 4466-4474.

124. Samanta C. Direct synthesis of hydrogen peroxide from hydrogen and oxygen: An overview of recent developments in the process. *Applied Catalysis A: General* 2008, **350**(2)**:** 133-149.

125. Rostrup-Nielsen J. Presentation, XVII Sympósio Iberoamericano de Catálisis. 2000.

126. Edwards JK, Hutchings GJ. Palladium and Gold–Palladium Catalysts for the Direct Synthesis of Hydrogen Peroxide. *Angewandte Chemie International Edition* 2008, **47**(48)**:** 9192-9198.

127. Edwards JK, Solsona B, N EN, Carley AF, Herzing AA, Kiely CJ, Hutchings GJ. Switching Off Hydrogen Peroxide Hydrogenation in the Direct Synthesis Process. *Science* 2009, **323**(5917)**:** 1037-1041.

128. Edwards JK, Pritchard J, Lu L, Piccinini M, Shaw G, Carley AF, Morgan DJ, Kiely CJ, Hutchings GJ. The Direct Synthesis of Hydrogen Peroxide Using Platinum-Promoted Gold–Palladium Catalysts. *Angewandte Chemie International Edition* 2014, **53**(9)**:** 2381-2384.

129. BusinessWire. Degussa/Headwaters Pilot Plant Validates New Technology. 2005 Available from: http://www.businesswire.com/news/home/20050309005685/en/DegussaHeadwaters-Pilot-Plant-Validates-Technology#.VKWaJnsYmao

130.   Paoli EA, Masini F, Frydendal R, Deiana D, Schlaup C, Malizia M, Hansen TW, Horch S, Stephens IEL, Chorkendorff I. Oxygen evolution on well-characterized mass-selected Ru and RuO2 nanoparticles. *Chemical Science* 2015, **6**(1)**:** 190-196.

131.   Katsounaros I, Cherevko S, Zeradjanin AR, Mayrhofer KJJ. Oxygen Electrochemistry as a Cornerstone for Sustainable Energy Conversion. *Angewandte Chemie International Edition* 2014, **53**(1)**:** 102-121.

132.   Izgorodin A, Izgorodina E, MacFarlane DR. Low overpotential water oxidation to hydrogen peroxide on a MnOx catalyst. *Energy & Environmental Science* 2012, **5**(11)**:** 9496-9501.

133.   Fukuzumi S, Yamada Y, Karlin KD. Hydrogen peroxide as a sustainable energy carrier: Electrocatalytic production of hydrogen peroxide and the fuel cell. *Electrochim Acta* 2012, **82**(0)**:** 493-511.

134.   Kato S, Jung J, Suenobu T, Fukuzumi S. Production of hydrogen peroxide as a sustainable solar fuel from water and dioxygen. *Energy & Environmental Science* 2013, **6**(12)**:** 3756-3764.

135.   Yamanaka I, Onizawa T, Takenaka S, Otsuka K. Direct and Continuous Production of Hydrogen Peroxide with 93 % Selectivity Using a Fuel-Cell System. *Angewandte Chemie* 2003, **115**(31)**:** 3781-3783.

136.   Yamanaka I, Murayama T. Neutral H2O2 Synthesis by Electrolysis of Water and O2. *Angewandte Chemie International Edition* 2008, **47**(10)**:** 1900-1902.

137.   Yamanaka I, Onisawa T, Hashimoto T, Murayama T. A Fuel-Cell Reactor for the Direct Synthesis of Hydrogen Peroxide Alkaline Solutions from H2 and O2. *ChemSusChem* 2011, **4**(4)**:** 494-501.

138.   Lobyntseva E, Kallio T, Alexeyeva N, Tammeveski K, Kontturi K. Electrochemical synthesis of hydrogen peroxide: Rotating disk electrode and fuel cell studies. *Electrochim Acta* 2007, **52**(25)**:** 7262-7269.

139.   Kinumoto T, Inaba M, Nakayama Y, Ogata K, Umebayashi R, Tasaka A, Iriyama Y, Abe T, Ogumi Z. Durability of perfluorinated ionomer membrane against hydrogen peroxide. *J Power Sources* 2006, **158**(2)**:** 1222-1228.

140.   Jirkovsky JS, Halasa M, Schiffrin DJ. Kinetics of electrocatalytic reduction of oxygen and hydrogen peroxide on dispersed gold nanoparticles. *Physical Chemistry Chemical Physics* 2010, **12**(28)**:** 8042-8053.

141.   Jirkovský JS, Panas I, Ahlberg E, Halasa M, Romani S, Schiffrin DJ. Single Atom Hot-Spots at Au–Pd Nanoalloys for Electrocatalytic H2O2 Production. *J Am Chem Soc* 2011, **133**(48)**:** 19432-19441.

142.   Fellinger T-P, Hasché F, Strasser P, Antonietti M. Mesoporous Nitrogen-Doped Carbon for the Electrocatalytic Synthesis of Hydrogen Peroxide. *J Am Chem Soc* 2012, **134**(9)**:** 4072-4075.

143. Pourbaix M. Atlas of electrochemical equilibria in aqueous solutions. 1974.

144. Topalov AA, Katsounaros I, Auinger M, Cherevko S, Meier JC, Klemm SO, Mayrhofer KJJ. Dissolution of Platinum: Limits for the Deployment of Electrochemical Energy Conversion? *Angewandte Chemie International Edition* 2012, **51**(50)**:** 12613-12615.

145. Norskov JK, Rossmeisl J, Logadottir A, Lindqvist L, Kitchin JR, Bligaard T, Jonsson H. Origin of the overpotential for oxygen reduction at a fuel-cell cathode. *Journal of Physical Chemistry B* 2004, **108**(46)**:** 17886-17892.

146. Viswanathan V, Hansen HA, Rossmeisl J, Nørskov JK. Unifying the 2e– and 4e– Reduction of Oxygen on Metal Surfaces. *The Journal of Physical Chemistry Letters* 2012, **3**(20)**:** 2948-2951.

147. Maroun F, Ozanam F, Magnussen OM, Behm RJ. The Role of Atomic Ensembles in the Reactivity of Bimetallic Electrocatalysts. *Science* 2001, **293**(5536)**:** 1811-1814.

148. Sheng WC, Gasteiger HA, Shao-Horn Y. Hydrogen Oxidation and Evolution Reaction Kinetics on Platinum: Acid vs Alkaline Electrolytes. *J Electrochem Soc* 2010, **157**(11)**:** B1529-B1536.

149. Wu H, Yau S, Vogel W, Zei M, Yang LYO, Itaya K. In situ scanning tunneling microscopy imaging of mercury film electrodeposited on Ir(111). *Electrochemistry Communications* 2009, **11**(2)**:** 454-456.

150. Russell AS, Kennedy TR, Howitt J, Lyons HAM. Intermetallic compounds formed in mercury Part IV Summary of work on the Sn-Cu, Sn-Fe, Zn-Cu, Zn-Fe, Cd-Cu, Hg-Cu, Mn-Cu, and Zn-Mn systems. *Journal of the Chemical Society* 1932**:** 2340-2342.

151. Baren MR. The Ag-Hg (silver-mercury) system. *J Phase Equilib* 1996, **17**(2)**:** 122-128.

152. Blizanac BB, Ross PN, Markovic NM. Oxygen electroreduction on Ag(111): The pH effect. *Electrochim Acta* 2007, **52**(6)**:** 2264-2271.

153. Levlin M, Ikävalko E, Laitinen T. Adsorption of mercury on gold and silver surfaces. *Fresenius J Anal Chem* 1999, **365**(7)**:** 577-586.

154. Gómez-Marín AM, Schouten KJP, Koper MTM, Feliu JM. Interaction of hydrogen peroxide with a Pt(111) electrode. *Electrochemistry Communications* 2012, **22**(0)**:** 153-156.

155. Medford A, Lausche A, Abild-Pedersen F, Temel B, Schjødt N, Nørskov J, Studt F. Activity and Selectivity Trends in Synthesis Gas Conversion to Higher Alcohols. *Top Catal* 2014, **57**(1-4)**:** 135-142.

156. Strmcnik D, Escudero-Escribano M, Kodama K, Stamenkovic VR, Cuesta A, Markovic NM. Enhanced electrocatalysis of the oxygen reduction reaction based on patterning of platinum surfaces with cyanide. *Nat Chem* 2010, **2**(10)**:** 880-885.

157. Subbaraman R, Tripkovic D, Strmcnik D, Chang K-C, Uchimura M, Paulikas AP, Stamenkovic V, Markovic NM. Enhancing Hydrogen Evolution Activity in Water Splitting by Tailoring Li+-Ni(OH)2-Pt Interfaces. *Science* 2011, **334**(6060)**:** 1256-1260.

158. Strmcnik D, Uchimura M, Wang C, Subbaraman R, Danilovic N, van der V, Paulikas AP, Stamenkovic VR, Markovic NM. Improving the hydrogen oxidation reaction rate by promotion of hydroxyl adsorption. *Nat Chem* 2013, **5**(4)**:** 300-306.

159. Joo J, Uchida T, Cuesta A, Koper MTM, Osawa M. Importance of Acid–Base Equilibrium in Electrocatalytic Oxidation of Formic Acid on Platinum. *J Am Chem Soc* 2013, **135**(27)**:** 9991-9994.

160. Gorlin Y, Chung C-J, Nordlund D, Clemens BM, Jaramillo TF. Mn3O4 Supported on Glassy Carbon: An Active Non-Precious Metal Catalyst for the Oxygen Reduction Reaction. *ACS Catalysis* 2012, **2**(12)**:** 2687-2694.

161. Xogen Inc. 2015 Available from: http://xogen.ca/

162. Giner Inc. 2015 Available from: http://www.ginerinc.com/technologies.php?a=EL

163. Strbac S. The effect of pH on oxygen and hydrogen peroxide reduction on polycrystalline Pt electrode. *Electrochim Acta* 2011, **56**(3)**:** 1597-1604.

164. Ramaswamy N, Tylus U, Jia Q, Mukerjee S. Activity Descriptor Identification for Oxygen Reduction on Nonprecious Electrocatalysts: Linking Surface Science to Coordination Chemistry. *J Am Chem Soc* 2013, **135**(41)**:** 15443-15449.

165. *CRC Handbook of Chemistry and Physics*. CRC Press, 2014-2015.

166. Ramaswamy N, Mukerjee S. Influence of Inner- and Outer-Sphere Electron Transfer Mechanisms during Electrocatalysis of Oxygen Reduction in Alkaline Media. *The Journal of Physical Chemistry C* 2011, **115**(36)**:** 18015-18026.

167. Rossmeisl J, Chan K, Ahmed R, Tripkovic V, Bjorketun ME. pH in atomic scale simulations of electrochemical interfaces. *Physical Chemistry Chemical Physics* 2013, **15**(25)**:** 10321-10325.

168. Dell'Angela M, Anniyev T, Beye M, Coffee R, Föhlisch A, Gladh J, Katayama T, Kaya S, Krupin O, LaRue J, Møgelhøj A, Nordlund D, Nørskov JK, Öberg H, Ogasawara H*, et al.* Real-Time Observation of Surface Bond Breaking with an X-ray Laser. *Science* 2013, **339**(6125)**:** 1302-1305.

169. Jirkovský JS, Björling A, Ahlberg E. Reduction of Oxygen on Dispersed Nanocrystalline CoS2. *The Journal of Physical Chemistry C* 2012, **116**(46)**:** 24436-24444.

170. Ellis RJ. Biochemistry: Tackling unintelligent design. *Nature* 2010, **463**(7278)**:** 164-165.

171. Lin MT, Occhialini A, Andralojc PJ, Parry MAJ, Hanson MR. A faster Rubisco with potential to increase photosynthesis in crops. *Nature* 2014, **513**(7519)**:** 547-550.

172. Ebbesen SD, Mogensen M. Electrolysis of carbon dioxide in Solid Oxide Electrolysis Cells. *J Power Sources* 2009, **193**(1)**:** 349-358.

173.   IEA. 2014 Available from:
http://www.iea.org/publications/freepublications/publication/KeyWorld2014.pdf

174.   Arico AS, Bruce P, Scrosati B, Tarascon J-M, van Schalkwijk W. Nanostructured materials for advanced energy conversion and storage devices. *Nat Mater* 2005, **4**(5)**:** 366-377.

175.   Energinet. 2014 Available from: http://energinet.dk/EN/El/Engrosmarked/Udtraek-af-markedsdata/Sider/default.aspx

176.   Peterson AA, Abild-Pedersen F, Studt F, Rossmeisl J, Norskov JK. How copper catalyzes the electroreduction of carbon dioxide into hydrocarbon fuels. *Energy & Environmental Science* 2010, **3**(9)**:** 1311-1315.

177.   Chen Y, Li CW, Kanan MW. Aqueous CO2 Reduction at Very Low Overpotential on Oxide-Derived Au Nanoparticles. *J Am Chem Soc* 2012, **134**(49)**:** 19969-19972.

178.   Kauffman DR, Alfonso D, Matranga C, Qian H, Jin R. Experimental and Computational Investigation of Au25 Clusters and CO2: A Unique Interaction and Enhanced Electrocatalytic Activity. *J Am Chem Soc* 2012, **134**(24)**:** 10237-10243.

179.   Zhu W, Michalsky R, Metin Ö, Lv H, Guo S, Wright CJ, Sun X, Peterson AA, Sun S. Monodisperse Au Nanoparticles for Selective Electrocatalytic Reduction of CO2 to CO. *J Am Chem Soc* 2013, **135**(45)**:** 16833-16836.

180.   Manthiram K, Surendranath Y, Alivisatos AP. Dendritic Assembly of Gold Nanoparticles during Fuel-Forming Electrocatalysis. *J Am Chem Soc* 2014, **136**(20)**:** 7237-7240.

181.   Mistry H, Reske R, Zeng Z, Zhao Z-J, Greeley J, Strasser P, Cuenya BR. Exceptional Size-Dependent Activity Enhancement in the Electroreduction of CO2 over Au Nanoparticles. *J Am Chem Soc* 2014, **136**(47)**:** 16473-16476.

182.   DiMeglio JL, Rosenthal J. Selective Conversion of CO2 to CO with High Efficiency Using an Inexpensive Bismuth-Based Electrocatalyst. *J Am Chem Soc* 2013, **135**(24)**:** 8798-8801.

183.   Medina-Ramos J, DiMeglio JL, Rosenthal J. Efficient Reduction of CO2 to CO with High Current Density Using in Situ or ex Situ Prepared Bi-Based Materials. *J Am Chem Soc* 2014, **136**(23)**:** 8361-8367.

184.   Rosen BA, Salehi-Khojin A, Thorson MR, Zhu W, Whipple DT, Kenis PJA, Masel RI. Ionic Liquid–Mediated Selective Conversion of CO2 to CO at Low Overpotentials. *Science* 2011, **334**(6056)**:** 643-644.

185.   Lu Q, Rosen J, Zhou Y, Hutchings GS, Kimmel YC, Chen JG, Jiao F. A selective and efficient electrocatalyst for carbon dioxide reduction. *Nat Commun* 2014, **5**.

186.   Chen Y, Kanan MW. Tin Oxide Dependence of the CO2 Reduction Efficiency on Tin Electrodes and Enhanced Activity for Tin/Tin Oxide Thin-Film Catalysts. *J Am Chem Soc* 2012, **134**(4)**:** 1986-1989.

187.   Zhang S, Kang P, Meyer TJ. Nanostructured Tin Catalysts for Selective Electrochemical Reduction of Carbon Dioxide to Formate. *J Am Chem Soc* 2014, **136**(5)**:** 1734-1737.

188.   Tang W, Peterson AA, Varela AS, Jovanov ZP, Bech L, Durand WJ, Dahl S, Norskov JK, Chorkendorff I. The importance of surface morphology in controlling the selectivity of polycrystalline copper for CO2 electroreduction. *Physical Chemistry Chemical Physics* 2012, **14**(1)**:** 76-81.

189.   Schouten KJP, Qin Z, Gallent EP, Koper MTM. Two Pathways for the Formation of Ethylene in CO Reduction on Single-Crystal Copper Electrodes. *J Am Chem Soc* 2012, **134**(24)**:** 9864-9867.

190.   Reske R, Mistry H, Behafarid F, Roldan Cuenya B, Strasser P. Particle Size Effects in the Catalytic Electroreduction of CO2 on Cu Nanoparticles. *J Am Chem Soc* 2014, **136**(19)**:** 6978-6986.

191.   Manthiram K, Beberwyck BJ, Alivisatos AP. Enhanced Electrochemical Methanation of Carbon Dioxide with a Dispersible Nanoscale Copper Catalyst. *J Am Chem Soc* 2014, **136**(38)**:** 13319-13325.

192.   Hori Y, Takahashi R, Yoshinami Y, Murata A. Electrochemical Reduction of CO at a Copper Electrode. *The Journal of Physical Chemistry B* 1997, **101**(36)**:** 7075-7081.

193.   Calle-Vallejo F, Koper MTM. Theoretical Considerations on the Electroreduction of CO to C2 Species on Cu(100) Electrodes. *Angewandte Chemie International Edition* 2013, **52**(28)**:** 7282-7285.

194.   Schouten KJP, Calle-Vallejo F, Koper MTM. A Step Closer to the Electrochemical Production of Liquid Fuels. *Angewandte Chemie International Edition* 2014, **53**(41)**:** 10858-10860.

195.   Kim Y-G, Baricuatro JH, Javier A, Gregoire JM, Soriaga MP. The Evolution of the Polycrystalline Copper Surface, First to Cu(111) and Then to Cu(100), at a Fixed CO2RR Potential: A Study by Operando EC-STM. *Langmuir* 2014, **30**(50)**:** 15053-15056.

196.   Durand WJ, Peterson AA, Studt F, Abild-Pedersen F, Nørskov JK. Structure effects on the energetics of the electrochemical reduction of CO2 by copper surfaces. *Surface Science* 2011, **605**(15–16)**:** 1354-1359.

197.   Peterson AA, Nørskov JK. Activity Descriptors for CO2 Electroreduction to Methane on Transition-Metal Catalysts. *The Journal of Physical Chemistry Letters* 2012, **3**(2)**:** 251-258.

198.   van der Niet MJTC, den Dunnen A, Juurlink LBF, Koper MTM. Co-adsorption of O and H2O on Nanostructured Platinum Surfaces: Does OH Form at Steps? *Angewandte Chemie* 2010, **122**(37)**:** 6722-6725.

199.   Vollmer S, Witte G, Wöll C. Determination of Site Specific Adsorption Energies of CO on Copper. *Catal Lett* 2001, **77**(1-3)**:** 97-101.

200.   Strunk J, Naumann d'Alnoncourt R, Bergmann M, Litvinov S, Xia X, Hinrichsen O, Muhler M. Microkinetic modeling of CO TPD spectra using coverage dependent microcalorimetric heats of adsorption. *Physical Chemistry Chemical Physics* 2006, **8**(13)**:** 1556-1565.

201.   Sandoval MJ, Bell AT. Temperature-Programmed Desorption Studies of the Interactions of H2, CO, and CO2 with Cu/SiO2. *Journal of Catalysis* 1993, **144**(1)**:** 227-237.

202.   Whipple DT, Kenis PJA. Prospects of CO2 Utilization via Direct Heterogeneous Electrochemical Reduction. *The Journal of Physical Chemistry Letters* 2010, **1**(24)**:** 3451-3458.

203.   Duscher G, Chisholm MF, Alber U, Ruhle M. Bismuth-induced embrittlement of copper grain boundaries. *Nat Mater* 2004, **3**(9)**:** 621-626.

204.   Alber U, Müllejans H, Rühle M. Bismuth segregation at copper grain boundaries. *Acta Materialia* 1999, **47**(15–16)**:** 4047-4060.

205.   Bokstein BS, Smirnov AN. Grain boundary segregation in Cu–Sb alloys. *Materials Letters* 2003, **57**(29)**:** 4501-4504.

Pt5Gd as a Highly Active and Stable Catalyst for Oxygen Electroreduction

María Escudero-Escribano,[†] Arnau Verdaguer-Casadevall,[†] Paolo Malacrida,[†] Ulrik Grønbjerg,[†,‡]
Brian P. Knudsen,[†] Anders K. Jepsen,[†] Jan Rossmeisl,[‡] Ifan E. L. Stephens,[†] and Ib Chorkendorff*,[†]

[†]Center for Individual Nanoparticle Functionality, Department of Physics, Building 312, Technical University of Denmark (DTU),
DK-2800 Lyngby, Denmark

[‡]Center for Atomic-Scale Materials Design, Department of Physics, Building 307, Technical University of Denmark (DTU), DK-2800
Lyngby, Denmark

Ⓢ Supporting Information

ABSTRACT: The activity and stability of Pt_5Gd for the
oxygen reduction reaction (ORR) have been studied, using
a combination of electrochemical measurements, angle-
resolved X-ray photoelectron spectroscopy (AR-XPS), and
density functional theory calculations. Sputter-cleaned,
polycrystalline Pt_5Gd shows a 5-fold increase in ORR
activity, relative to pure Pt at 0.9 V, approaching the most
active in the literature for catalysts prepared in this way.
AR-XPS profiles after electrochemical measurements in 0.1
M $HClO_4$ show the formation of a thick Pt overlayer on
the bulk Pt_5Gd, and the enhanced ORR activity can be
explained by means of compressive strain effects.
Furthermore, these novel bimetallic electrocatalysts are
highly stable, which, in combination with their enhanced
activity, makes them very promising for the development
of new cathode catalysts for fuel cells.

Proton exchange membrane fuel cells (PEMFCs) are a
potentially zero emission source of power, which are
expected to play a key role in a future society based on
sustainable energy. The main obstacle to the development of
PEMFCs as a commercially competitive reality is the high
overpotential required for the oxygen reduction reaction
(ORR) to proceed at an adequate rate. Due to this fact, the
ORR has been the most intensively studied fuel-cell reaction
over the past decade.[1−7] The most active electrocatalysts
known for the ORR are based upon Pt. However, high loadings
of Pt are necessary at the cathode in order to achieve acceptable
power densities.[1] In order to reduce the Pt loading, there is a
need to develop novel catalysts with enhanced activity and
long-term stability under operating conditions.[1,2]

The activity of Pt toward the ORR can be improved by
slightly weakening its binding to the O-containing reaction
intermediates, O, OH, and OOH. The optimal catalyst should
have an OH binding energy ≈0.1 eV weaker than pure Pt.[4a]
The most widely used approach to achieve this goal is to alloy
Pt with other metals, such as Co, Ni, Fe, Cu, hence improving
its ORR activity.[1,3−5,8] The more reactive solute metal, e.g. Co,
Ni, Fe, Cu, will tend to dissolve in the acidic electrolyte of a
PEMFC, leaving behind a Pt overlayer. Unless the catalyst has
been pre-annealed,[3b,c,5b] this overlayer is typically several
monolayers thick.[5a,8] On the acid leached catalysts, the

weakening of the binding to OH occurs as a result of the
compressive strain imposed onto the Pt-overlayer by the alloy
bulk.

It is crucial to improve not only the fuel-cell cathode catalyst
activity but also its durability. Alloys of Pt and late transition
metals generally degrade by dealloying.[1b,4a,9] This involves the
segregation of the solute metal to the surface[9a,c] and its
subsequent dissolution. The susceptibility of Pt alloys with late
transition metals, such as Fe, Co, Ni and Cu toward dealloying
can be understood on the basis of their negligible heat of
formation.

Recently, Pt_3Y was identified on the basis of density
functional theory (DFT) calculations as being a catalyst that
should be both active and stable for the ORR.[4a] Experiments
confirmed that the catalyst exhibited the highest ORR activity
ever measured for a polycrystalline surface.[1b,4] Alloys of Pt with
early transition metals or rare earths, such as Y, Gd, or La, have
exceptionally negative heats of formation;[1b,10,11] this should
provide them with the kinetic stability to prevent dealloying
under fuel cell reaction conditions, unlike alloys of Pt and late
transition metals. This is because the kinetic barrier for solute
metal diffusion through the alloy core and the thick Pt overlayer
should be at least partially determined by the heat of formation.
Moreover, despite their denomination, rare earths are more
abundant, produced on a larger scale, and less expensive than
Pt.[12] Very recent studies on Pt_xLa[1b,13] have demonstrated that
these alloys present enhanced activity compared to pure Pt[1b] as
well as high stability.[13] To the best of our knowledge, no other
studies concerning the activity and/or the stability of Pt and
rare earth metal alloys have been reported so far. Pt_5Gd is a
very stable alloy, with a formation energy of −3.9 eV/formula
unit,[11] similar to that of Pt_3Y[4a] and Pt_5La.[1b]

In this communication, we present, for the first time,
experimental and theoretical studies concerning the activity and
stability of Pt_5Gd for the ORR. The bulk, polycrystalline
electrode was sputter cleaned in an ultrahigh-vacuum chamber,
before being transferred to a rotating ring disk electrode
(RRDE) assembly to conduct electrochemical measurements in
0.1 M $HClO_4$. Full experimental details can be found in the
Supporting Information (SI).

The activity of the catalyst toward the ORR was evaluated in an O_2-saturated 0.1 M $HClO_4$ solution, using cyclic voltammetry. Typical cyclic voltammograms (CVs) on sputter-cleaned Pt_5Gd and Pt polycrystalline electrodes in oxygen-saturated perchloric acid solutions are shown in Figure 1a. The ORR was measured once a stable CV was obtained in a
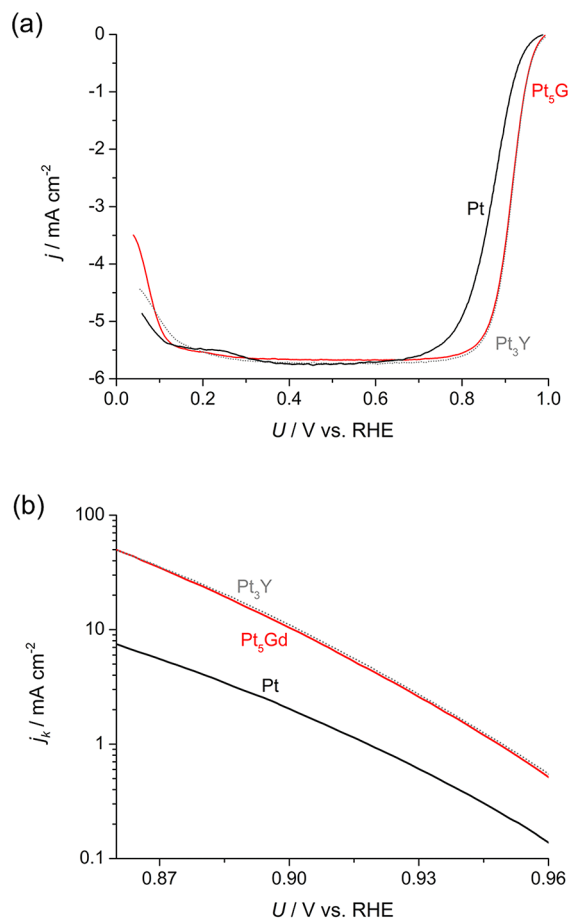

Figure 1. (a) RRDE polarization curves at 1600 rpm and 50 mV s^{-1} for the ORR on Pt_5Gd (red curve), Pt (black curve), and Pt_3Y (dotted gray curve) polycrystalline electrodes in O_2-saturated 0.1 M $HClO_4$. (b) Tafel plots showing the kinetic current density (j_k) of Pt_5Gd, Pt, and Pt_3Y as a function of the potential (U), based on data from (a).

nitrogen-saturated electrolyte (typically after ca. 100 cycles). On both electrodes, the onset for the ORR starts at ≈1 V, and the current increases exponentially with decreasing potential, characteristic of kinetic control. At more negative potentials, the current becomes increasingly controlled by mass transport, until it is completely transport limited, reaching the value of 5.7 mA cm^{-2}. We assume that the roughness factor was 1 cm^2/cm^2, as found for other Pt alloys tested for the ORR.[4] In the potential region of mixed kinetic transport, there is a considerable positive shift for Pt_5Gd, relative to Pt. This represents a substantial decrease in the overpotential for the alloy surface. Moreover, Figure 1 also shows that the ORR activity on Pt_5Gd is essentially the same as that of polycrystalline Pt_3Y (see gray dotted curve).[4] In the Tafel plot shown in Figure 1b, the kinetic current density, j_k, i.e., the current density in the absence of any mass-transfer effects, is represented as a function of the potential, U. Pt_5Gd exhibits a kinetic current density, at 0.90 V, $j_k = (10.4 \pm 0.2)$ mA cm^{-2}, which means that

Pt_5Gd exhibits a 5-fold improvement over Pt. A similar enhancement was obtained on polycrystalline Pt_3Y (see gray dotted curve in Figure 1b).[4] Previous results on sputter-cleaned polycrystalline Pt_3M (M = Ni, Co, Fe) alloys by Stamenkovic et al.[3] showed up to 2-fold improvements in activity over pure Pt. However, our results show that Pt_5Gd and Pt_3Y[1b,4] present the highest activities for sputter-cleaned (Pt-skeleton)[3b] structures reported in the literature so far. According to these results, the ranking of ORR activity for the most active polycrystalline Pt alloys is in ascending order: Pt ≪ Pt_5La ≈ Pt_3Y < Pt_3Y ≈ Pt_5Gd.[1b]

In order to investigate the chemical composition of the active phase of the Pt_5Gd electrocatalyst, angle-resolved XPS (AR-XPS) experiments were carried out before and after the electrochemical measurements. After sputter cleaning the sample (before electrochemistry, see Figure 2a), the Pt to Gd
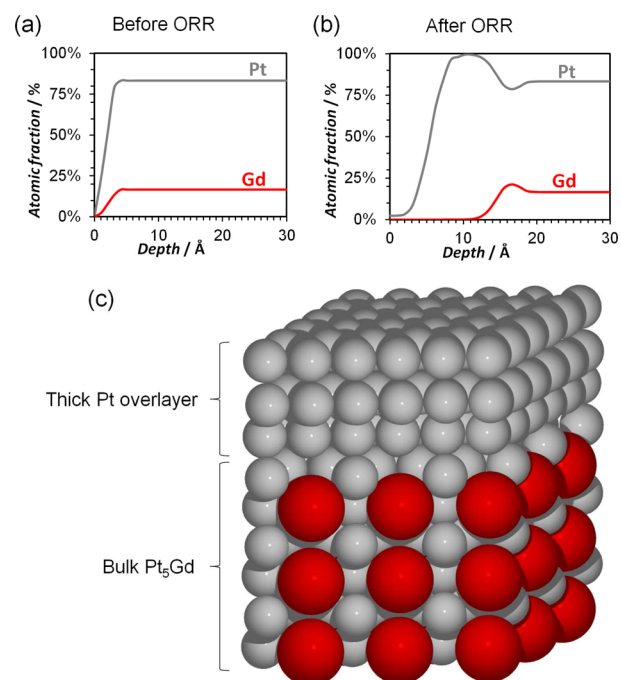

Figure 2. Nondestructive AR-XPS profiles of polycrystalline, sputter cleaned, Pt_5Gd before (a) and after (b) the ORR measurements. The adventitious C and O traces have been omitted for clarity; these are presumably accumulated during the transfer. The sputter cleaned sample exhibited a small submonolayer coverage of C and O, associated with the high sticking coefficient of any residual molecules on Gd, which is very reactive. (c) Schematic three-dimensional view of the structure shown in (b), consisting of a Pt (gray balls) overlayer, covering a bulk Pt_5Gd alloy (the large red balls are Gd atoms). In this case, the thickness of the Pt overlayer, at three monolayers, is arbitrary.

ratio was 5.0 ± 0.2, as estimated from three different measurements at 21° emission angle from the normal to the surface. At this angle, the surface sensitivity is lower, and the effects of possible differential sputtering are minimized. However, these do not seem to play an important role on the surface composition, as the Pt to Gd ratio does not change significantly with the emission angle (see Figure S8). Following the ORR experiments, the sample was transferred to the UHV chamber, and Pt to Gd ratio of 9.1 ± 0.9 was measured. This suggests that Gd is partially dissolved in the acidic electrolyte. Figure 2 shows the typical depth profiles of Pt_5Gd before (a) and after (b) ORR. Evidently a Pt overlayer with a thickness of

few Pt layers was formed. This is consistent with other acid leached Pt-skeleton alloys, including Pt_5La, Pt_5Y, and Pt_3Y.[1,4,14] Further investigations are underway to quantify the exact thickness of the Pt overlayer. Accordingly, the effect of alloying Pt is to impose strain onto the Pt overlayer. In the absence of Gd in the first three atomic layers, there would be no "ligand effect".[1b,15]

It must be noted that under the acidic and oxidizing operating conditions of a PEMFC, there would be a strong thermodynamic force toward the dissolution of Gd from Pt_5Gd: the standard dissolution potential, U_0, for Gd to Gd^{3+} is −2.40 V vs the normal hydrogen electrode (NHE)[16] (which means that the standard Gibbs free energy for the dissolution of Gd to Gd^{3+} is −7.20 eV), and the alloying energy of Pt_5Gd stabilizes each Gd atom by 3.9 eV.[11] Then, the standard Gibbs free energy for the dissolution of Gd to Gd^{3+} will be −3.30 eV, and the corresponding standard reduction potential is −1.10 V vs NHE. Hence, despite the stabilization of Gd atoms in the Pt_5Gd alloy by 3.9 eV, at 1 V vs NHE we are 2.1 V above the standard reduction potential, i.e., there is a driving force of −6.3 eV for the dissolution of each Gd atom. A similar driving force exists for the dissolution of other rare earths or early transition metals when alloyed with Pt, including Pt_3Y and Pt_5La, explaining why the solute metal will dissolve from these surfaces.[1b] However, this is inconsistent with reports that metallic La or Y could be present at the surface Pt_3La or Pt_3Y electrodes under ORR conditions.[13,17] Despite the thermodynamic driving force, the Pt overlayer provides kinetic stability against Gd dissolution from the alloy bulk.

DFT calculations were performed in order to understand the high ORR activity of Pt_5Gd. The Pt_5Gd structure was modeled following the same procedure as for Pt_5La,[1b] as a strained close-packed pure Pt overlayer. The surface strain was estimated on the basis that the Pt−Pt interatomic distance would be set by the bulk lattice parameter of Pt_5Gd, $a = 0.522$ nm (based on XRD measurements described in the SI). A schematic representation of the structure is shown in Figure 2c. This would lead to a Pt overlayer that is compressed by 6% relative to Pt(111). Our DFT calculations suggest that this strain would result in an excessive weakening of the OH binding energy, relative to Pt(111), of ≈0.3 eV. The compressive strain that would provide the optimal OH binding energy ≈0.1 eV weaker than Pt(111) would be 2%.[5a] On the basis of the DFT model, we would expect the perfect, defect-free surface to have a lower activity than pure Pt, in contradiction to our experiments.[7,18] However, we expect that on the experimentally tested phase of Pt_5Gd, the strain at the surface would be significantly lower than the 6% we estimate for a "perfect" overlayer on Pt_5Gd, due to relaxation effects.[5a,19]

In order to study the stability of polycrystalline Pt_5Gd electrodes in acidic solutions, we first performed an accelerated stability test (test I) consisting of continuous cycles from 0.6 to 1.0 V vs RHE in an oxygen-saturated 0.1 M $HClO_4$ electrolyte at 100 mV s^{-1} and 23 °C. The CVs in an O_2-saturated 0.1 M $HClO_4$ solution before and after 10 000 cycles (after around 20 h of experiments) between 0.6 and 1.0 V are shown in Figure S4. Figure 3a shows the Tafel plots for the ORR on Pt_5Gd before (red curve) and after (orange dotted curve) 10 000 cycles in the conditions described above. Interestingly, these results show that the percentage of activity loss after 10 000 cycles is 14%, most of this loss occurring in the first 2000 cycles. For comparison, when subject to the same treatment, polycrystalline Pt loses 5% of its initial activity after 10 000
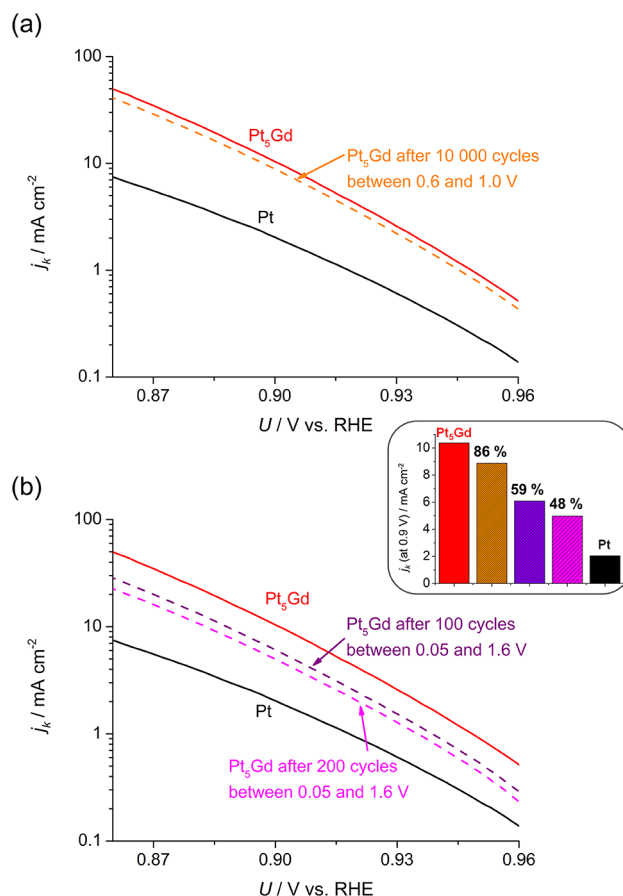

Figure 3. Tafel plots showing the stability of Pt_5Gd after: (a) 10 000 cycles between 0.6 and 1.0 V vs RHE at 100 mV s^{-1} (test I) and (b) 100 (purple curve) and 200 (magenta curve) cycles between 0.05 and 1.6 V vs RHE at 50 mV s^{-1} in O_2-saturated 0.1 M $HClO_4$ (test II). The inset shows the kinetic current density at 0.9 V of Pt_5Gd: sputter cleaned (red), after test I (orange), and after 100 (purple) and 200 (magenta) cycles of test II. For comparison, the kinetic current density of Pt is represented in black.

cycles. Presumably, this loss in activity can be explained by residual contamination from the electrolyte. The CV in N_2-saturated 0.1 M $HClO_4$ taken immediately before the ORR measurements was completely recovered after stability test I (not shown). This <15% deactivation seems to be related to a slight decrease in Gd from the near-surface region: the Pt:Gd XPS ratio at 21° to the sample normal increased from 9.1 (after ORR) to 12.3 (after stability test I, see Figure S5).

Following stability test I, we exposed it to a more aggressive experiment, by cycling it between 0.05 and 1.6 V (i.e., very strong corrosive conditions) at 50 mV s^{-1} in O_2-saturated solutions (test II). After 10 cycles, we did not observe any additional loss in activity in the ORR. However, after 50 cycles between 0.05 and 1.6 V the ORR polarization curve (after stability test I) could not be recovered. As shown in Figure 3b, the sample retains 59% of its initial activity after 100 cycles and 48% after 200 cycles (after ca. 30 h of experiments). Despite these very promising results, the stability of the catalyst will ultimately need to be tested in nanoparticulate form in a PEMFC.

In summary, we present a novel highly active and stable electrocatalyst for the ORR. The activity of Pt_5Gd is similar to that obtained on Pt_3Y in previous studies, which was identified as the most active Pt-based polycrystalline alloy for the ORR.

Moreover, polycrystalline Pt_5Gd electrodes are extremely stable, resistant to cycling to potentials as positive as 1.6 V. For all these reasons, we expect that alloying Pt with Gd and other rare earths will be a fruitful strategy toward the development of highly active and durable cathodes for PEMFCs.

ASSOCIATED CONTENT

Supporting Information

Experimental procedures, computational details, and additional figures. This material is available free of charge via the Internet at http://pubs.acs.org.

AUTHOR INFORMATION

Corresponding Author
ibchork@fysik.dtu.dk

Notes
The authors declare no competing financial interests.

ACKNOWLEDGMENTS

REFERENCES

(1) (a) Gasteiger, H. A.; Kocha, S. S.; Sompalli, B.; Wagner, F. T. *Appl. Catal., B* **2005**, *56*, 9. (b) Stephens, I. E.L.; Bondarenko, A. S.; Grønbjerg, U.; Rossmeisl, J.; Chorkendorff, I. *Energy Environ. Sci.* **2012**, *5*, 6744.

(2) (a) Adzic, R. R.; Zhang, J.; Sasaki, K.; Vukmirovic, J. X.; Shao, M.; Wang, J. X.; Nikelar, A. U.; Mavrikakis, M.; Valerio, J. A.; Uribe, F. *Top. Catal.* **2007**, *46*, 249. (b) Bing, Y.; Liu, H.; Zhang, L.; Ghosh., D.; Zhang, J. *Chem. Soc. Rev.* **2010**, *39*, 2184. (c) Wang, C.; van der Vliet, D.; More, K. L.; Zaluzec, N. J.; Peng, S.; Sun, S.; Daimon, H.; Wang, G.; Greeley, J.; Pearson, J.; Paulikas, A. P.; Karapetrov, G.; Strmcnik, D.; Markovic, N. M.; Stamenkovic, V. R. *Nano Lett.* **2011**, *11*, 919. (d) Rabis, A; Rodriguez, P.; Schmidt, T. J. *ACS Catal.* **2012**, *2*, 864.

(3) (a) Stamenkovic, V.; Mun, B. S.; Mayrhofer, K. J. J.; Ross, P. N.; Markovic, N. M.; Rossmeisl, J.; Greeley, J.; Nørskov, J. K. *Angew. Chem., Int. Ed.* **2006**, *45*, 2897. (b) Stamenkovic, V. R.; Mun, B. S.; Mayrhofer, K. J.J.; Ross, P. N.; Markovic, N. M. *J. Am. Chem. Soc.* **2006**, *128*, 8813. (c) Stamenkovic, V. R.; Fowler, B.; Mun, B. S.; Wang, G. F.; Ross, P. N.; Lucas, C. A.; Markovic, N. M. *Science* **2007**, *315*, 493. (d) Stamenkovic, V. R.; Mun, B. S.; Arenz, M.; Mayrhofer, K. J. J.; Lucas, C. A.; Wang, G. F.; Ross, P. N.; Markovic, N. M. *Nat. Mater.* **2007**, *6*, 241.

(4) (a) Greeley, J.; Stephens, I. E.L.; Bondarenko, A. S.; Johansson, T. P.; Hansen, H. A.; Jaramillo, T. F.; Rossmeisl, J.; Chorkendorff, I.; Nørskov, J. K. *Nat. Chem.* **2009**, *1*, 552. (b) Stephens, I. E.L.; Bondarenko, A. S.; Bech, L.; Chorkendorff, I. *ChemCatChem* **2012**, *4*, 341.

(5) (a) Strasser, P.; Koh, S.; Anniyev, T.; Greeley, J.; More, K.; Yu, C.; Liu, Z.; Kaya, S.; Nordlund, D.; Ogasawara, H.; Toney, M. F.; Nilsson, A. *Nat. Chem.* **2010**, *2*, 454. (b) Stephens, I. E.L.; Bondarenko, A. S.; Perez-Alonso, F. J.; Calle-Vallejo, F.; Jepsen, A. K.; Frydendal, R.; Knudsen, B. P.; Rossmeisl, J.; Chorkendorff, I. *J. Am. Chem. Soc.* **2011**, *133*, 5485.

(6) Strmcnik, D.; Escudero-Escribano, M.; Kodama, K.; Stamenkovic, V. R.; Cuesta, A.; Markovic, N. M. *Nat. Chem.* **2010**, *2*, 880.

(7) Nørskov, J. K.; Rossmeisl, J; Logadottir, A.; Lindqvist, L.; Kitchin, J. R.; Bligaard, T.; Jónsson, H. *J. Phys. Chem. B* **2004**, *108*, 17886.

(8) Toda, T.; Igarashi, H.; Uchida, H.; Watanabe, M. *J. Electrochem. Soc.* **1999**, *146*, 3750.

(9) (a) Mayrhofer, K. J. J.; Hartl, K.; Juhart, V.; Arenz, M. *J. Am. Chem. Soc.* **2009**, *131*, 16348. (b) Chen, S.; Gasteiger, H. A.; Hayakawa, K.; Tada, T.; Shao-Horn, Y. *J. Electrochem. Soc.* **2010**, *157*, A82. (c) Xin, H. L. L.; Mundy, J. A.; Liu, Z.; Cabezas, R.; Hovden, R.; Kourkoutis, L. F.; Zhang, J.; Subramanian, N. P.; Makharia, R.; Wagner, F. T.; Muller, D. A. *Nano Lett.* **2012**, *12*, 490.

(10) (a) Johannesson, G. H.; Bligaard, T.; Ruban, A. V.; Skriver, H. L.; Jacobsen, W.; Nørskov, J. K. *Phys. Rev. Lett.* **2002**, *88*, 255506. (b) Bligaard, T.; Johannesson, G. H.; Ruban, A. V.; Skriver, H. L.; Jacobsen, W.; Nørskov, J. K. *Appl. Phys. Lett.* **2003**, *83*, 4527.

(11) Jakob, K. T.; Waseda, Y. *Mater. Trans., JIM* **1990**, *31*, 135.

(12) Vesborg, P. C.K.; Jaramillo, T. F. *RSC Adv.* **2012**, *2*, 7933.

(13) Yoo, S. J.; Hwang, S. J.; Lee, J.-G.; Lee, S.-C.; Lim, T.-H.; Sung, Y.-E.; Wieckowski, A.; Kim, S.-K. *Energy Environ. Sci.* **2012**, *5*, 7521.

(14) Johansson, T. P. Ph.D. Thesis, Technical University of Denmark: Lyngby, Denmark, 2012.

(15) Kitchin, J. R.; Nørskov, J. K.; Barteau, M. A.; Chen, J. G. *J. Chem. Phys.* **2004**, *120*, 10240.

(16) Pourbaix, M. *Atlas of Electrochemical Equilibria in Aqueous Solutions*; National Association of Corrosion Engineers: Houston, TX, 1974.

(17) Yoo, S. J.; Kim, S.-K.; Jeon, T.-Y.; Hwang, S. J.; Lee, J.-G.; Lee, K.-S.; Cho, Y.-H.; Sung, Y.-E.; Lim, T.-H. *J Chem. Commun.* **2011**, *47*, 11414.

(18) Rossmeisl, J.; Karlberg, G. S.; Jaramillo, T. F.; Nørskov, J. K. *Faraday Discuss.* **2008**, *140*, 337.

(19) Yang, R.; Strasser, P.; Toney, M. F. *J. Phys. Chem. C* **2011**, *115*, 9074.

PAPER

Enhanced activity and stability of Pt–La and Pt–Ce alloys for oxygen electroreduction: the elucidation of the active surface phase†

Paolo Malacrida, María Escudero-Escribano, Arnau Verdaguer-Casadevall, Ifan E. L. Stephens and Ib Chorkendorff*

Three different Pt–lanthanide metal alloys (Pt_5La, Pt_5Ce and Pt_3La) have been studied as oxygen reduction reaction (ORR) electrocatalysts. Sputter-cleaned polycrystalline Pt_5La and Pt_5Ce exhibit more than a 3-fold activity enhancement compared to polycrystalline Pt at 0.9 V, while Pt_3La heavily corrodes in 0.1 M $HClO_4$ electrolyte. Angle Resolved X-ray Photoelectron Spectroscopy (AR-XPS) and Low Energy Ion Scattering (LEIS) have been extensively combined with electrochemical techniques to follow the chemical and structural changes at the surface. The highly reactive lanthanide atoms are not stable in the presence of oxygen and readily oxidize. The surface oxides are completely dissolved in the electrolyte. In Pt_5La and Pt_5Ce the so formed Pt overlayer provides kinetic stability against the further oxidation and dissolution. At the same time, it ensures a very high stability during ORR potential cycling, suggesting that these alloys hold promise as cathode catalysts in Proton Exchange Membrane Fuel Cells (PEMFCs).

1. Introduction

Proton Exchange Membrane Fuel Cells (PEMFCs) represent one of the most promising alternatives to traditional power sources in a future sustainable society, especially for transportation applications. Using hydrogen as a fuel, they could provide an efficient and clean alternative to engines based on fossil fuels.[1,2] However, the commercialisation of PEMFCs is still inhibited by their relatively low performances and high production costs. This is, to a large part, due to the slow kinetics of the oxygen reduction reaction (ORR) at the cathode and the copious amounts of Pt used to catalyse this reaction.[2,3] Although Pt-based materials are the most active ORR catalysts, they still exhibit rather high overpotentials. For this reason, in order to ensure high power densities, for instance in automotive vehicles, high Pt loadings are needed. Consequently, there has been much interest during the past few decades in developing new ORR catalysts. They should both be highly active and stable under the acidic oxidising conditions of a PEMFC cathode.[2–7] Since Pt is both expensive and scarce, it is necessary to decrease the amount of Pt required to catalyse the ORR, in favour of cheaper and more abundant materials. To date, the most successful catalysts which reach this aim are alloys of Pt and other transition metals.

Alloys of Pt and late transition metals such as Fe, Co, Ni, and Cu have been studied extensively, leading to strongly enhanced ORR activities.[2,3,7–12] Nonetheless, these alloys are thermodynamically unstable under fuel-cell conditions; the transition metal tends to dissolve into the electrolyte *via* a process known as dealloying.[5,11,13] The resulting surface composition is Pt enriched. However, a precise description of the structure is challenging, the level of enrichment and the thickness of the dealloyed region varying for different alloys, preparation techniques and electrochemical treatments. Generally the dissolution proceeds until a several layer-thick Pt overlayer is formed,[14] denoted by Stamenkovic *et al.* as a "Pt skeleton" structure.[7,8,10] Although this Pt overlayer might provide temporary kinetic stability against further dissolution, further dealloying is considered as the main cause of deactivation for these catalysts.[15]

A single Pt monolayer on the surface of the alloy can be stabilised by vacuum annealing. This structure was denoted by Stamenkovic *et al.* as a "Pt-skin" structure.[8,10] Such surfaces have exhibited the highest ORR activities ever reported.[9,16–18] However, it may be challenging to synthesise a supported Pt-skin catalyst in large amounts and stabilise it over the long time periods and many potential cycles required for a PEMFC cathode.[19]

The above considerations led to the search for new Pt-alloy catalysts. A theoretical screening based on Density Functional Theory (DFT) calculations was set out to identify alloys that were both active and stable.[20] The activity of the catalyst was predicted on the notion that the optimal metal catalyst for the ORR should bind O (or OH) slightly more weakly than pure Pt.[21,22]

Center for Individual Nanoparticle Functionality, Department of Physics, Technical University of Denmark (DTU), Building 312, 2800 Lyngby, Denmark. E-mail: ibchork@fysik.dtu.dk

The key descriptor for stability was that the catalysts have as negative an alloying energy, or heat of formation, as possible. The calculations predicted that Pt_3Y and Pt_3Sc fulfilled these criteria. Indeed experiments confirmed an activity enhancement relative to polycrystalline Pt for both Pt_3Y and Pt_3Sc:[20,23] Pt_3Y in particular exhibiting the highest activity ever reported for a Pt-skeleton structure.

A negative heat of formation may stabilise a Pt alloy catalyst against degradation *via* dealloying. This is because the kinetic barrier for metal diffusion through the alloy should, to a large part, be dictated by the alloying energy. The exceptionally negative heat of formation of Pt_3Y, $\Delta H_{f(alloy)} \sim -4$ eV, is characteristic of several other alloys of Pt with early transition metals or lanthanides, such as Pt_5Gd, Pt_5La and Pt_5Ce as shown in Fig. 1.[24–29] This is because the d-band of these alloys is half filled, meaning that all the bonding states are full, and antibonding states are empty.[3,20,30,31] On the other hand, Fig. 1 also shows that alloys of Pt and late transition metals, such as Pt_3Co and Pt_3Ni, have much less negative alloying energies. Very recently, we also discovered that alloys of Pt_5La and Pt_5Gd are very promising catalysts for the ORR,[3,32,33] with Pt_5Gd, together with Pt_3Y, being the most active catalyst amongst polycrystalline Pt-skeleton structures. In addition to its high activity, the percentage of activity loss after 10 000 cycles between 0.6 and 1 V for Pt_5Gd is less than 15%. We note that despite their denomination as "rare earths", they are much more inexpensive and much more abundant than Pt.[34]

In order to elucidate the active phase of Pt_5Y, Pt_3Y, Pt_5Gd and Pt_5La, we employed angle resolved X-ray photoelectron spectroscopy. Our measurements suggested that in each case, the surface comprised of a thick Pt overlayer, to the order of 1 nm in depth. This is easily understood on the basis that there is a strong driving force for the dissolution of the metal from the surface layer. Moreover, oxides of Y, La and Gd are all unstable in acid solution.[35] In the absence of any solute metal in the near-surface region, we proposed that the activity of these catalysts was due to a compressive strain induced by the alloy bulk on the Pt overlayer, weakening the binding of surface adsorbates such as OH or O.
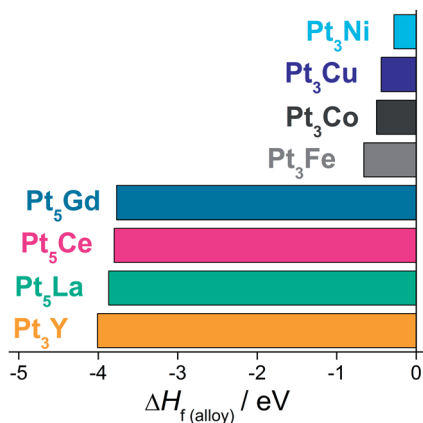
Recent studies by Kim and coworkers have also focused on alloys of Pt and early transition metals and lanthanides as ORR catalysts.[36–38] Their Pt_3La sample exhibited a similar activity to that of the Pt_5La we reported,[3,32] although their interpretation of its activity was somewhat different. On the basis of their AR-XPS measurements, they report that the surface composition is essentially unchanged before and after the reaction. Using DFT calculations on a closely packed structure of Pt_3La, they show that La will have a tendency to segregate towards the surface, in vacuum. They also suggest that the negative alloying energy is sufficient to ensure that the alloy is *thermodynamically* stable against oxidation or dissolution. This discrepancy between their interpretation and our own led us to revisit the issue of the surface composition of alloys of Pt and La. Moreover, there is a broader debate about the possible stabilisation of more reactive metals at the surface of Pt and Pd alloys, even for more extensively studied alloys, such as Pt–Ni and Pt–Co.[8,13,39,40] This possibility would be of fundamental relevance, since their enhanced activity could be also explained in terms of bifunctional effects: with both metals providing active sites during ORR, the more reactive atoms facilitating the O_2 dissociation or the removal of OH radicals from the more noble Pt sites.[41,42]

This article, for the first time, investigates the electrochemical behaviour of Pt_5Ce, demonstrating its very high activity and stability towards the ORR. Ce, together with La, is the most abundant, most largely produced and cheapest element among the rare earths.[34] Moreover, by comparing Pt_5Ce with Pt_5La and Pt_3La, we can elucidate the origin of the enhancement of the activity and stability for these alloys, which is still controversial. Furthermore, we use these catalysts to provide evidence for the intrinsic instability of Ce and La on the surface.

2. Experimental

Polycrystalline alloys (5 mm in diameter disks) of Pt_5La, Pt_3La and Pt_5Ce were supplied by Mateck GmbH, Germany. The crystal structures of the alloys were investigated by X-ray diffraction (XRD) and are in agreement with that reported in the literature. XRD measurements and full experimental details are described in the ESI.† The surface stoichiometry and the absence of impurities were checked by X-ray photoelectron spectroscopy (XPS). Before all electrochemical measurements the samples were cleaned under Ultra High Vacuum (UHV) conditions by Ar sputtering, until no C contaminations were observed. The ion energy was set to 0.5 keV and a beam current of 1 µA over a 7×7 mm^2 area was used to homogenously sputter the active surface.

2.1 Electrochemical characterization

The electrochemical experiments were performed with a VMP2 potentiostat (Bio-Logic Instruments), controlled by a computer. The rotating ring-disk electrode (RRDE) assemblies were provided by Pine Instruments Corporation. A standard two-compartment glass cell was used, which was equipped with a water jacket attached to a hot water bath to control the

Fig. 1 Experimental enthalpies of formation specified per formula unit. Values for the different Pt alloys are respectively taken from: Pt_3Ni,[24] Pt_3Cu,[25] Pt_3Co,[26] Pt_3Fe,[26] Pt_5Gd,[27] Pt_5Ce,[27,28] Pt_5La[27,28] and Pt_3Y.[27]

temperature. All the electrochemical experiments were carried out at 23 °C. The electrolyte, 0.1 M $HClO_4$ (Merck Suprapur), was prepared with Millipore (Milli-Q, 18.2 $M\Omega$ cm^{-1}) water. The counter electrode was a Pt wire and the reference was an Hg/Hg_2SO_4 electrode, separated from the working electrode compartment using ceramic frits. All the potentials in the text are referred to the reversible hydrogen electrode (RHE), and are corrected for ohmic losses. The polycrystalline alloys, inserted into the arbor of a RRDE, were immersed into the electrochemical cell under potential control of 0.1 V *vs.* RHE into a N_2 (N5, Air Products) saturated electrolyte. The electrodes were cycled until stable cyclic voltammograms (CVs) were obtained. The ORR activity measurements were conducted in an electrolyte saturated with O_2 (N55, Air Products).

2.2 Physical characterization

Angle Resolved X-ray Photoelectron Spectroscopy (AR-XPS) was used as a non-destructive technique to investigate the chemical state of the alloys and their surface morphology. Measurements were performed on a Thermo Scientific Theta Probe instrument with a base pressure of 5×10^{-10} mbar. The X-ray source is monochromatised Al Kα (1486.7 eV), giving a resolution better than 1.0 eV at the employed pass energy of 100 eV. The analyser has an acceptance angle of 60°, between 20° and 80° to the surface normal; for the angle resolved profiles, 16 different channels were analysed in parallel corresponding to 3.75° wide angle intervals. Angle resolved data were processed using the simulation tool, ARProcess (Thermo Avantage software), which uses a maximum entropy method combined with a genetic algorithm to define the depth profiles: angles over 65° were omitted to minimize the effects of elastic scattering. Further technical details are provided in the ESI.†

AR-XPS was initially carried out during sputter-cleaning starting 20 minutes after the beginning of the cleaning procedure. Sputtering was not stopped during these measurements in order to avoid sub-monolayer amounts of O to be adsorbed on the sample due to the expected high reactivity and high sticking coefficients of O on La and Ce (see ESI†).[43,44] This procedure did not induce any significant changes in the Ce 3d, La 3d and Pt 4f peak shape but prevented the presence of C and O contaminations: lower than 1% in all cases. Subsequently, samples were transferred to a fast-entry air lock, vented in dry nitrogen up to atmospheric pressure and readily protected by a drop of H_2-saturated Milli-Q water for transfer to a rotating ring disk electrode assembly. AR-XPS measurements were repeated after ORR testing and after stability tests in order to evaluate the active structure of the alloy and its stability. In order to investigate the stability of the alloys in the presence of oxygen, identical measurements were also taken after exposure of the sputtered-cleaned surfaces to air for 1 hour.

Low Energy Ion Scattering (LEIS) was used to probe the composition of the outmost layer of Pt_5Ce after electrochemical measurements. LEIS spectra were acquired with Ne^+ ions at 1 keV energy. A residual Ne pressure of 5×10^{-9} mbar gave sample currents between 10 and 16 nA. The beam was rastered over a large sample area, approximately 4 mm × 4 mm, in order

to minimize the destructive effects induced by ion sputtering. The average scattering angle was 125°, and the incidence angle was 45°. Initially, a few scans were repeated in order to clean the tested alloys from the organic impurities collected during the transfer and the electrochemical measurements. Each scan took approximately 2 minutes. This cleaning phase took 10 to 15 minutes, until the Pt signal started appearing. For comparison, LEIS spectra were also taken using the same parameters on the sputter-cleaned alloy.

3. Results

3.1 Crystal structure

The structure of the alloys was investigated by XRD as reported in the ESI.† No closed-packed structure is observed for either Pt_5La or Pt_5Ce, they instead exhibited a hexagonal structure with a lattice parameter of $a = 5.39$ Å and $a = 5.38$ Å respectively, in good agreement with the values reported previously.[45] The polycrystalline sample with nominal composition of Pt_3La was, as a matter of fact, composed of a mixture of two phases: Pt_2La and Pt_5La. This is consistent with the Pt–La phase diagrams in the literature, which do not show the existence of a stable Pt_3La phase.[46–48]

3.2 Electrochemical characterisation and ORR activity

Fig. S2† shows the stable CVs in N_2-saturated 0.1 M $HClO_4$ solutions on sputter-cleaned Pt_5Ce and Pt_5La, as compared to the base CV on polycrystalline Pt. The ORR activities of the electrocatalysts were evaluated in oxygen-saturated solutions after stable CVs in N_2 were obtained (typically after *ca.* 100 cycles). Fig. S6† shows typical CVs on sputter-cleaned Pt_5Ce, Pt_5La and Pt polycrystalline electrodes in O_2-saturated perchloric acid solutions. We assume that the roughness factor was 1 cm^2/cm^2, as we found to be the case for other Pt alloys, prepared in the same manner.[20,49] We have also performed CO-stripping measurements on Pt_5La and Pt_5Ce (all the results are explained and discussed in the ESI†). As the CO-stripping charges were similar or slightly lower for Pt_5La and Pt_5Ce alloys than for pure Pt, all currents were normalised by the geometric surface area, consistent with our previous studies.[3,20,23,33,49] Given that the electrodes consist of planar surfaces, with a surface composition of pure Pt, we consider the geometric surface area to be a more reliable and more conservative estimate of the microscopic surface area (single crystal studies have shown that the saturation coverages of CO and H on Pt overlayers can be highly sensitive to alloying).[50] The kinetic current density, j_k, *i.e.* the current density in the absence of any mass-transfer effects, was calculated by the equation $[(j_d j)/(j_d - j)]$, where j_d is the limited current density and j the measured current density. Fig. 2 shows the Tafel plot (j_k as a function of the potential, U) for sputter-cleaned Pt_5Ce, Pt_5La, Pt_3La and Pt polycrystalline electrodes in O_2-saturated 0.1 M $HClO_4$. It must be noted that the reported activity for the Pt polycrystalline sample agrees well, or is slightly higher, than recent experiments conducted by reputable groups under nominally the same conditions.[10,51,52] Pt_5Gd (which is, together with P_3Y, the
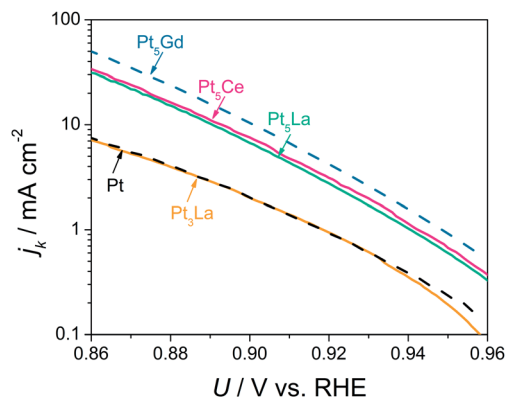
4236 | *J. Mater. Chem. A*, 2014, **2**, 4234–4243

This journal is © The Royal Society of Chemistry 2014

Fig. 2 Tafel plots showing the kinetic current density (j_k) normalized per geometric surface area of Pt_5Ce, Pt_5La, Pt_3La, Pt and Pt_5Gd[33] as a function of the potential (U).

most active polycrystalline Pt-alloy reported in the literature so far)[20,33] is also represented for comparison. As can be observed in Fig. 2, the kinetic current densities for Pt_5Ce and Pt_5La, at 0.90 V *vs.* RHE, are (7.4 ± 0.4) mA cm^{-2} and (6.8 ± 0.3) mA cm^{-2}, respectively. This means that the ORR activity enhancements for Pt_5Ce and Pt_5La are 3.7 and 3.4, respectively. This enhancement in activity is considerably higher than that exhibited by Pt_3Fe, Pt_3Co and Pt_3Ni catalysts prepared under similar conditions, which revealed about a factor of 2 enhancement compared to polycrystalline Pt.[8,53] According to our previous results, Pt_5Ce is the most active polycrystalline catalyst for the ORR after Pt_3Y[20] and Pt_5Gd.[33]

In contrast, the ORR activity on Pt_3La is very similar to that on pure Pt. It must be noted that, as discussed in the ESI and shown in Fig. S5,† CVs in N$_2$-saturated solutions present remarkable changes during cycling, indicating that the polycrystalline Pt_3La sample is corroded. This was confirmed by Inductively Coupled Plasma Mass Spectrometry (ICP-MS) measurements of equal volumes of electrolyte taken after measurements of the Pt_5La and Pt_3La ORR activity (Fig. S7†) and compared to a clean as-prepared electrolyte. In the case of Pt_3La, a substantial increase of the La signal was found indicating a strong La dissolution and a possible reason for such low activity, similar to Pt. In contrast, Yoo *et al.*[37] reported an appreciable enhancement in activity for the Pt_3La alloy over that of pure Pt, as well as high stability. Pt_3La results, together with a comparison between the behaviour of Pt_3La and the Pt_5La samples, and a discussion about the stability of these catalytic surfaces will be assessed below.

3.3 Active chemical state and surface stability

In order to follow the chemical state of the catalytic surfaces, AR-XPS was performed before and after all the preparation and testing steps of this study. The shapes of the La 3d and Ce 3d peaks in particular provide useful diagnostic information, despite the high level of complexity which is typical of the lanthanide metals. The presence of localized electrons in the 5d or 4f shells generates intense shake-up satellites in the 3d region of the La and Ce spectrum; their relative intensity and

energy position are strongly dependent on the chemical state.[54] The origin of such behaviour has been addressed by various studies and can be well described by the Schönhammer–Gunnarsson treatment.[55] The La and Ce initial state as well as the final state, excited by photoelectron emission, cannot be described with a single electron approximation and a many-body description is required. Both systems are described as the linear combination of different f^n states, where n is the electron occupancy of the 4f shell. These valence orbitals and in particular the 4f orbitals affect the level of screening of the core-hole and, as a result, the observed energy position of the 3d lines. A higher number of electrons in this 4f shell better screens the photoemitted electron from the core hole, resulting in a higher kinetic energy. In the spectra shown in Fig. 3 the La 3d and Ce 3d signals were fitted according to the assignment of f^n states reported in the literature.[44,56,57] Defining f^n as the predominant component of each lanthanide in the ground state, elemental La (valence electron configuration $5d_16s_2$) is predominantly composed of the $n = 0$ state, while for Ce ($4f_15d_16s_2$) the one electron occupancy of the 4f shell gives $n = 1$. For the interest of this study, it should be noted that these main peaks are the most intense in the metallic state and in intermetallic compounds; weaker satellites arise from the f^1 state in the case of La and from the f^0 and f^2 states in the case of Ce.[57] The charge transfer occurring during oxidation shifts the position of these states and, remarkably, results in a strong intensification of the f^0 satellite for La, and of the f^1 and f^2 satellites for Ce providing a clear diagnostic tool.[43,44,54]

Fig. 3a and b shows the La 3d and Ce 3d XPS peaks measured during sputtering of Pt_5La and Pt_5Ce respectively. Analogous results were obtained for Pt_3La and are presented in Fig. S11† together with the details of the fitting parameters (see ESI†). The shape of the 3d peaks is metallic; the f^n peak accounts for most of the intensity with distinctive visible f^{n+1} satellites at lower binding energies. The overall spectra resemble those measured on similar compounds, such as Pd_3La, Ni_5La, Pd_3Ce, Pd_5Ce and Ni_5Ce.[57–60] The well screened f^{n+1} satellites are strengthened compared to pure La or pure Ce as typical for such alloys.

It turns out that the chemical state of such reactive metals cannot be maintained while transferring the electrodes from UHV to air and to the acidic electrolyte for the electrochemical measurements. As shown in Fig. 3c and d, the La 3d and Ce 3d peaks drastically vary as a consequence of one hour long air exposure. Despite the very negative heat of alloy formation, there is an even stronger driving force towards the surface oxidation.[3] As described in the literature,[44,61] all peaks shift to higher binding energies and the satellite peaks grow in intensity: in some cases becoming even more intense than the principal ones. Similar effects were also measured after few seconds of air exposure, indicating that the surface is always oxidized before introduction into the electrolyte, even if protected by a drop of Milli-Q water.

Concerning Pt_5Ce, the fit of the Ce oxide phase is in general complicated by the presence of trivalent Ce from Ce_2O_3 and tetravalent Ce from CeO_2 overlapping to the metallic peaks. The intense f^0 components, which is absent for trivalent Ce,[44,62] suggest CeO_2 as the main oxidized phase. Therefore, for
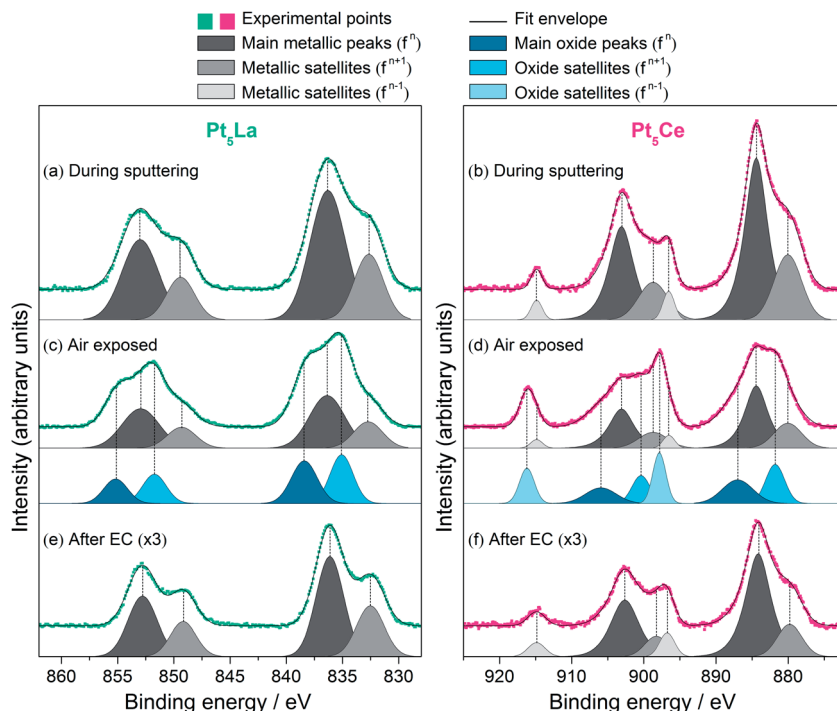
Fig. 3 XPS spectra of Pt$_5$La (left) and Pt$_5$Ce (right) at an average emission angle of 45°. For each alloy the spectra were acquired under three different conditions: during sputter-cleaning (a and b), after one hour long air exposure (c and d), and after electrochemical measurements (e and f). The measurements after electrochemical measurements were magnified three times due to the lower signal intensity. Fitted spectra of the metallic peaks (grey) and of the oxidized peaks (blue) appear under the experimental points. Details of the peak positions and relative intensities are found in Table S2.†

simplicity, in the fit of Fig. 3d only the CeO$_2$ phase was considered. This gave an oxide spectrum similar to the one of previously reported fits[44,56] and a sufficiently good agreement with the experimental data. A full quantification of the oxide components is complicated by the possible presence of sub-oxides and is beyond the interest of this study. Table S2† summarizes the intensity ratios of the main peaks and satellites. Remarkably the amount of oxidized La relative to the total La signal is similar for both Pt$_3$La and Pt$_5$La, indicating a similar level of surface oxidation.

AR-XPS spectra were taken after electrochemical measurements. Due to the mentioned surface instability of the alloyed lanthanides, only the spectra of Fig. 3e and f can provide direct information on the chemical state and structure of the active catalysts. In this case the La 3d and Ce 3d spectra are completely metallic, similar to those measured during sputtering. The disappearance of the oxide peaks suggests that any oxide phase is unstable under ORR conditions and dissolves in the acidic electrolyte. At the same time, the conservation of the metallic peaks during the air-exposure between the EC cell and the XPS setup indicates the presence of a protective layer, preventing the lanthanides from air contact and oxidation. The Pt enriched surface resulting from the dissolution of the oxides is expected to provide this kind of protection. A careful comparison with the XPS on sputter cleaned samples provides further information; despite the overall similarities the intensity ratios between the main peaks and the satellites show a slight intensification of the

f^{n+1} satellites for La and of the f^{n-1} satellites for Ce (see Fig. 3e and f and S11†); since this intensification is typical of La and Ce alloys,[57,59] it could be associated with the removal of surface La (or Ce) atoms which would be under-coordinated to Pt atoms. For all these considerations no metallic La or Ce should be expected on the surface of these electrochemically tested alloys.

By discerning the XPS spectra at different emission angles, AR-XPS is a powerful technique for reconstructing the surface structure of these catalysts. Fig. 4a and b shows how the catalyst composition changes as a function of the analyser acceptance angle. The presence of a Pt overlayer explains the increase in the Pt to La and Pt to Ce ratios, from the initial values measured during sputtering. This is particularly evident for higher angles due to the higher surface sensitivity. Fig. 4c and d represents the correspondent calculated depth profiles of Pt$_5$La and Pt$_5$Ce after electrochemistry. Both catalysts exhibit the formation of a thick Pt overlayer, which has been already described for other de-alloyed surfaces,[7,8,14,33,49] including Pt$_3$Co, Pt$_3$Ni, Pt$_3$Y, Pt$_5$Y and Pt$_5$Gd. The formation of this structure from the initial sputter-cleaned surface is illustrated in Fig. 4e for Pt$_5$Ce.

It should be noted that AR-XPS profiles represent an average over a 400 μm wide region of the crystals and over a depth of a few electron mean free paths ($\lambda \approx 10$ Å).[63] Therefore the presence of surface La or Ce atoms on some parts of the samples, which might be inhomogeneous due to their polycrystalline nature, cannot be excluded. In contrast LEIS only probes the outmost layer composition, hence allowing us to rule out this
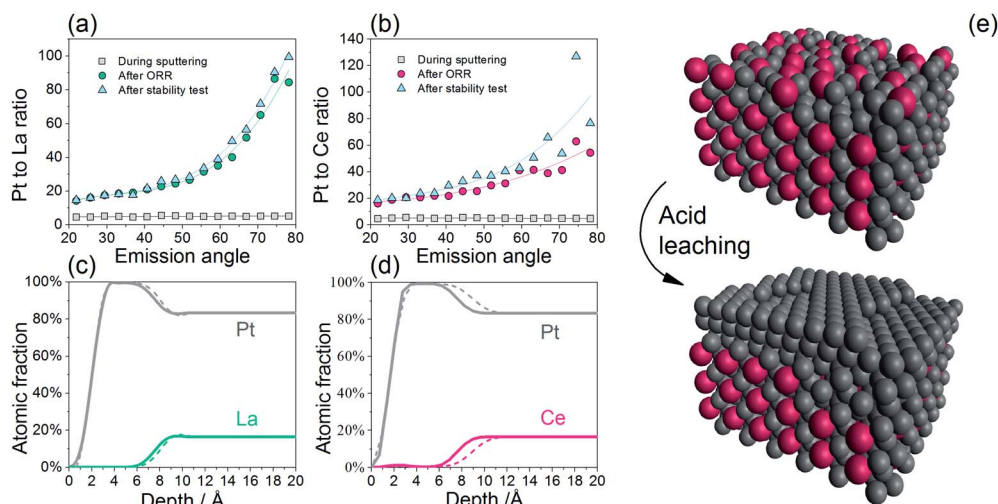
Fig. 4 Pt to lanthanide atomic ratios in Pt$_5$La (a) and Pt$_5$Ce (b) from AR-XPS under three different conditions: during sputter-cleaning (□), after electrochemical ORR testing (○) and after stability test (△). Corresponding AR-XPS depth profiles of Pt$_5$La (c) and Pt$_5$Ce (d), after the ORR activity test (solid line) and after the stability test (dashed line). An illustrative three-dimensional view of the Pt$_5$Ce structure after sputter-cleaning (e) and after ORR activity test with the formation of a Pt overlayer on top of the Pt$_5$Ce bulk alloy (f). Grey and red spheres represent Pt and Ce atoms respectively.

possibility. Fig. 5 shows the LEIS spectra acquired on Pt$_5$Ce after electrochemical ORR testing at different times. The spectrum of the sputter-cleaned surface is also reported for comparison, showing the typical energy positions of the ions backscattered from Pt ($E_K \approx 680$ eV) or from Ce ($E_K \approx 580$ eV). The very first scans (not shown) are dominated by the background originating from adventitious O and C surface contamination accumulated between the electrochemical measurements and the transfer to UHV. The progressive cleaning of the surface induced by the

Ne$^+$ ions allows to clearly see the Pt peak after 18 minutes. At this time no Ce peaks can be seen. At increasing times and higher levels of ion sputtering on the surface, weak peaks from Ce start arising and the ratio of the peak areas progressively approaches the one measured on sputter-cleaned samples which is similar to the stoichiometric ratio. A plot of the esti-mated areas as a function of the sputtering time is shown in Fig. S12.† These observations prove the existence of a complete Pt overlayer, for which bifunctional effects are unlikely.
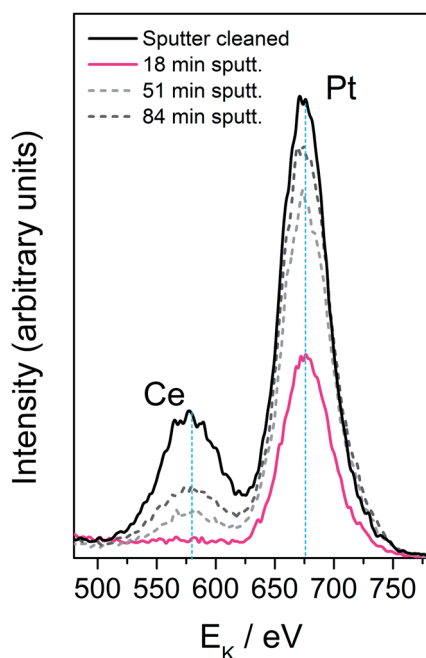
3.4 Stability

The stability of the alloys under ORR conditions was tested by applying 10 000 consecutive cycles from 0.6 to 1.0 V *vs.* RHE in an O$_2$-saturated 0.1 M HClO$_4$ electrolyte at 100 mV s^{-1} and 23 °C. The choice of this standard accelerated stability test was based on the protocols of the U.S. Department Of Energy[64] and of the Fuel Cell Commercialization Conference of Japan.[19] CVs from 0.6 to 1.0 V *vs.* RHE in an O$_2$-saturated 0.1 M HClO$_4$ electrolyte at 50 mV s^{-1} were taken before and after this procedure in order to compare the ORR activity (not shown). Both for Pt$_5$La and Pt$_5$Ce the losses in kinetic activities are remarkably low: around 8% for Pt$_5$La and 10% for Pt$_5$Ce, respectively. This is a further proof of the long-term stability of alloys of Pt with lanthanide metals, as shown recently for Pt$_5$Gd.[33] Fig. 6 shows the total activity enhancement for Pt$_5$La and Pt$_5$Ce, as compared to polycrystalline Pt and Pt$_5$Gd,[33] before and after the stability test, measured under the same condi-tions. As can be seen, after 10 000 potential cycles under the above described conditions, for both catalysts the final specific activity is still more than 3 times higher than for pure Pt. Very recently, Todoroki *et al.* studied the stability of Pt-enriched Ni/Pt(111) catalysts. Interestingly, although their ORR activity was 8 times higher than that of pure Pt(111), after only

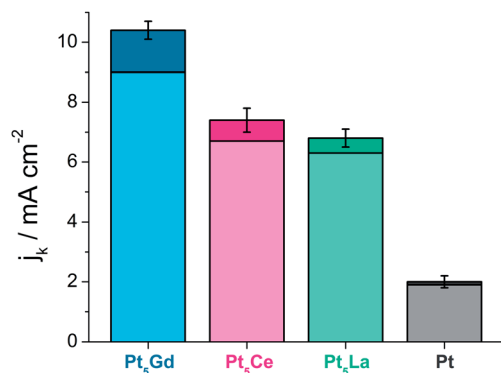**Fig. 5** LEIS spectra of Pt$_5$Ce after ORR testing for different sputtering times and comparison with the sputter-cleaned reference surface.

This journal is © The Royal Society of Chemistry 2014

J. Mater. Chem. A, 2014, **2**, 4234–4243 | **4239**

Fig. 6 Kinetic current density (per geometric surface area) measured at 0.9 V of Pt_5Gd,[33] Pt_5Ce, Pt_5La and Pt before and after a stability test consisting of 10 000 cycles between 0.6 and 1.0 V vs. RHE in an O_2-saturated 0.1 M $HClO_4$ electrolyte at 100 mV s^{-1}.

1000 potential cycles between 0.6 and 1.0 V they lost the 75% of their initial activity.[65] Previous studies on state-of-the-art Pt_3Co cathode catalysts for PEMFCs also show a substantial degradation of these catalysts under fuel-cell reaction conditions, mainly due to the dealloying of the Pt_3Co particles at the cathode.[15,66] The enhancement in activity and stability for both Pt_5Ce and Pt_5La as compared to pure Pt show that these alloys are very promising as cathode catalysts for PEMFCs. However, it should be anticipated that the chemical synthesis of Pt–La or Pt–Ce alloys in the nanoparticulate form, more suitable for their application in PEMFCs, will be technologically challenging, due to the high reactivity of lanthanide metals and the difficulties of reducing them by chemical-electrochemical techniques.

New AR-XPS measurements were acquired after the stability test. The comparison with the spectra achieved just after the ORR measurements provides useful information regarding the changes in the structure and composition which might occur during cycling. The aspect of the La 3d and Ce 3d peaks is very similar to the one observed in Fig. 3 after EC measurements. This indicates that no big changes in the chemical state of these reactive metals occur, as shown in Table S2.† The Pt overlayer still provides kinetic stability against their dissolution. Fig. 4a and b shows further changes on the catalyst composition after stability tests. By comparing the concentration ratios after ORR testing and after the stability test it is possible to notice a further increase, indicating a slight thickening of the Pt overlayer. AR-XPS depth profiles of Pt_5La and Pt_5Ce (Fig. 4c and d) accordingly exhibit small increments in the Pt overlayer thicknesses. For both alloys, and in particular for Pt_5La, these changes are very modest, demonstrating the high structural stability of these alloys.

4. Discussion

4.1 Surface stability and active chemical state

The XPS spectra of Fig. 3 have clearly demonstrated the inherent surface instability of Pt–La and Pt–Ce alloys under air exposure. The tendency towards the surface oxidation of La and Ce prevails; this is despite the very negative heat of formation of

such compounds stabilised by the high alloying temperatures. The metallic components of the La 3d and Ce 3d still account for most of the XPS signal (see Table S2†) indicating that the presence of the alloy introduces kinetic barriers against deep oxidation, while pure La or Ce would quickly form a thick oxide layer.[67,68]

Our evidence clearly differs from the recent results and conclusions of Yoo et al. on Pt_3La.[37] They claim that La atoms are stable on the surface of Pt_3La under reaction conditions. However, the peak shape and position of their La 3d peaks resemble those of the La oxide peaks shown in Fig. 3c and S11,† with absent or negligible metallic components. It turns out that these spectra are characteristic of compounds where La is in an oxidized state, with f^{n+1} satellite components almost as intense as the main La 3d peaks.[43,61,69] This consideration, as well as the fact that no explicit details about the purity of the synthesized alloys or any surface cleaning procedures are given in their work[37] suggest the presence of oxygen on the surface and the formation of a rather thick La oxide layer. It is also worth noting that the XRD trace that Yoo et al. report suggests that their Pt_3La phase is a solid solution with the same crystal structure as Pt, albeit with some lattice strain.[70,71] In a Pt_3La solid solution, although the bulk composition may be constant, there would be random substitution of Pt and La at any given atomic coordinate. A stable solid solution typically forms in metal compounds where there are weak interactions between the different constituent atoms. However, the strong interaction between Pt and La would provide a significant driving force to form an ordered intermetallic compound; in such a compound the number of La–La nearest neighbours would be minimised and the number of Pt–La nearest neighbours would be maximised. Notably, the phase diagrams of Pt–La intermetallic compounds found in the literature do not report the existence of a stable Pt_3La phase.[46–48] This is in agreement with our XRD measurements on Pt_3La (Fig. S1†), composed of a mixture of two phases: Pt_2La and Pt_5La. In our view, the reason for which a meta-stable solid solution was formed under Yoo et al.'s experimental conditions is that they prepared their compounds by magnetron sputtering at room temperature, without any additional heat treatment. On this basis, the low stability of Yoo et al.'s Pt_3La solid solution towards air oxidation is unsurprising.

According to the XPS data (Fig. 3e and f, 4c and d and S11†), both the La oxide and metallic La are dissolved from the near-surface region under ORR conditions. Simple thermodynamic considerations provide an intuitive explanation for this phenomenon. First focusing on Pt_5La, the instability of the oxide layer is trivial to explain: La_2O_3 is thermodynamically unstable against dissolution to La^{3+} at pH 0.[35] Moreover, metallic La is also unstable under these conditions. The standard dissolution potential of a La atom to La^{3+} is −2.38 V vs. the standard hydrogen electrode (SHE).[72] Accounting for the three electrons involved in the reaction, the resulting standard Gibbs free energy of dissolution of a La atom would be around −7.1 eV at 0 V SHE. The standard Gibbs free energy of formation ($\Delta G_{Pt_5La} = -3.8$ eV)[28] partially stabilizes the La atoms, lowering the standard Gibbs free energy of dissolution to −3.3 eV. The

4240 | J. Mater. Chem. A, 2014, 2, 4234–4243

This journal is © The Royal Society of Chemistry 2014

corresponding standard reduction potential is still −1.1 V *vs.* SHE. For Pt$_5$Ce a similar analysis results in a standard reduction potential of Ce^{3+} to Ce of −1.1 V, essentially the same as for Pt$_5$La. These values are 2.1 V lower than the potential a fuel cell cathode may reach during shut down. At that potential, there is a strong driving force of about −6.3 eV for the dissolution of La and Ce, despite the very negative heat of alloy formation. Hence no La and Ce atoms should be present on the surface of these catalysts. Despite the different preparation technique described by Yoo *et al.*[37] for Pt$_3$La, it is very unlikely that any kind of pure Pt–La phase could overcome this huge driving force towards dissolution of the La atoms from the surface; a tendency that seems to be independent of the bulk structure. This is even more unlikely in the absence of any stabilising heat treatment.

On the other hand, the Pt overlayer, formed by the dissolution of the lanthanide metals from the first few monolayers of the alloy, provides kinetic stability to the catalyst. The diffusion of La or Ce would be very slow through the overlayer, due to the strong Pt–La and Pt–Ce interactions. On the other hand, Pt$_3$La continuously corrodes. We ascribe this difference to the presence of multiple phases in the XRD pattern of Pt$_3$La. We previously demonstrated the influence of stoichiometry on the stability of Pt$_x$Y phases:[49] Pt$_2$Y and PtY, in particular, heavily corroded. We anticipate a similar behaviour for the Pt$_2$La phase. Others have made similar observations for alloys of Pt and late transition metals, when the concentration of the less noble metal is relatively high.[73,74] The high activity and stability of Pt$_5$La and Pt$_5$Ce, in comparison to Pt$_3$La, outlines the importance of comprehensive physical characterization to identify the most active and stable phases.

4.2 Mechanism of activity enhancement

An approximate thickness of the Pt overlayer of around 6–7 Å can be gauged from the angle-resolved depth profiles of Fig. 4c and d, on both Pt$_5$La and Pt$_5$Ce, respectively. This would correspond to approximately 3 Pt monolayers. Assuming that the overlayer thickness is uniform, ligand effects would be negligible.[75] It should be noted, however, that the XPS technique averages over a large area, whose homogeneity is not certain. Furthermore, the algorithms analysing the AR-XPS data are rather sensitive to uncertainties on the sensitivity factors of the peaks used for quantification. Therefore, our data cannot provide a more precise estimation of the Pt overlayer thickness.

The thick Pt overlayers shown in Fig. 4c and d suggest that the high ORR activity is due to strain effects. This notion is supported by the data shown in Fig. 7, which shows that the ORR activity of Pt$_5$La, Pt$_5$Ce and Pt$_5$Gd is correlated with the lattice parameter *a*. We recently proposed that the structure of the overlayer would resemble closely packed Pt, as suggested by our DFT calculations on Pt$_5$La.[3] A similar behaviour has been experimentally observed on single crystal Pt$_5$Y that, in a vacuum, forms a compressed Pt overlayer on top of the alloy.[76] In acid electrolyte, *in situ* STM studies on Pt–Fe alloys have also shown the formation of a closely packed Pt overlayer, resembling Pt(111).[77] For this kind of structure the Pt–Pt distance in the overlayer would be correlated with the distance of the
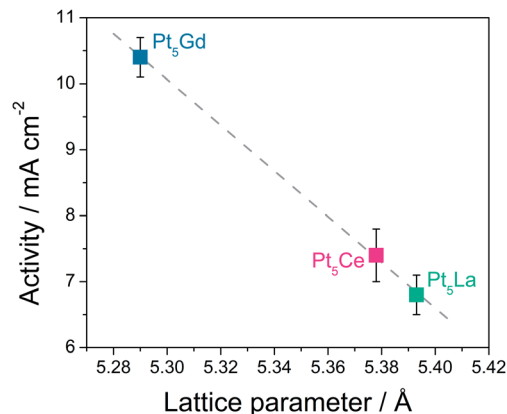

Fig. 7 Experimental ORR activity (kinetic current density per geometric surface area at 0.9 V *vs.* RHE) of polycrystalline Pt$_5$La, Pt$_5$Ce, Pt$_5$Gd[33] *versus* the lattice parameter *a* of the alloys as determined from XRD measurements. The dotted line is a linear fit of the points.

closest Pt nearest neighbours in the bulk, d_{Pt-Pt}.[3,33] In the case of Pt$_5$La, Pt$_5$Ce and Pt$_5$Gd it turns out that $d_{Pt-Pt} = a/2$. Consequently, a lower value of *a* suggests increased compressive strain to the surface and higher ORR activity. We note that in a thick Pt overlayer, the strain may relax somewhat, relative to the bulk.[13,78] In the future, we will aim to more accurately quantify the actual strain in the surface overlayer.

5. Conclusions

This study addresses the electrochemical properties of three ORR catalysts: Pt$_5$La, Pt$_3$La and Pt$_5$Ce, the latter being reported here, for the first time, as a highly active ORR catalyst. Both Pt$_5$La and Pt$_5$Ce exhibited a more than 3-fold activity improvement, relative to Pt, with only minor losses after accelerated stability tests. This suggests that they are promising materials for future implementation in PEMFCs. In contrast, we found that the catalyst with a nominal composition of Pt$_3$La tended to corrode.

Despite the strong tendency towards the oxidation of lanthanide metals, AR-XPS shows that in the active phase of the catalyst, La and Ce exist in the metallic form. This powerful technique also showed the formation of a ∼3 monolayer thick Pt overlayer, which stabilizes Pt$_5$La and Pt$_5$Ce and prevents the further oxidation and dissolution in an electrochemical environment. This evidence is inconsistent with the recent reports by Yoo *et al.* for Pt–La compounds, where La appears in an oxidized state and is also present on the surface of the catalyst.[37] AR-XPS and LEIS experiments, as well as simple thermodynamic considerations rationalise our own results. In the presence of the thick Pt overlayer reported here, only strain effects can explain the enhanced activity of Pt$_5$La and Pt$_5$Ce.

Acknowledgements

References

1 U. Eberle, B. Müller and R. von Helmolt, *Energy Environ. Sci.*, 2012, **5**, 8780–8798.

2 H. A. Gasteiger, S. S. Kocha, B. Sompalli and F. T. Wagner, *Appl. Catal., B*, 2005, **56**, 9–35.

3 I. E. L. Stephens, A. S. Bondarenko, U. Grønbjerg, J. Rossmeisl and I. Chorkendorff, *Energy Environ. Sci.*, 2012, **5**, 6744–6762.

4 R. R. Adzic, J. Zhang, K. Sasaki, M. B. Vukmirovic, M. Shao, J. X. Wang, A. U. Nilekar, M. Mavrikakis, J. A. Valerio and F. Uribe, *Top. Catal.*, 2007, **46**, 249–262.

5 J. Zhang, M. B. Vukmirovic, Y. Xu, M. Mavrikakis and R. R. Adzic, *Angew. Chem., Int. Ed.*, 2005, **44**, 2132–2135.

6 F. T. Wagner, B. Lakshmanan and M. F. Mathias, *J. Phys. Chem. Lett.*, 2010, **1**, 2204–2219.

7 V. Stamenkovic, B. S. Mun, K. J. J. Mayrhofer, P. N. Ross, N. M. Markovic, J. Rossmeisl, J. Greeley and J. K. Nørskov, *Angew. Chem.*, 2006, **118**, 2963–2967.

8 V. R. Stamenkovic, B. S. Mun, K. J. J. Mayrhofer, P. N. Ross and N. M. Markovic, *J. Am. Chem. Soc.*, 2006, **128**, 8813–8819.

9 V. R. Stamenkovic, B. Fowler, B. S. Mun, G. Wang, P. N. Ross, C. A. Lucas and N. M. Marković, *Science*, 2007, **315**, 493–497.

10 V. R. Stamenkovic, B. S. Mun, M. Arenz, K. J. J. Mayrhofer, C. A. Lucas, G. Wang, P. N. Ross and N. M. Markovic, *Nat. Mater.*, 2007, **6**, 241–247.

11 K. J. J. Mayrhofer, K. Hartl, V. Juhart and M. Arenz, *J. Am. Chem. Soc.*, 2009, **131**, 16348–16349.

12 L. Gan, R. Yu, J. Luo, Z. Cheng and J. Zhu, *J. Phys. Chem. Lett.*, 2012, **3**, 934–938.

13 H. L. Xin, J. A. Mundy, Z. Liu, R. Cabezas, R. Hovden, L. F. Kourkoutis, J. Zhang, N. P. Subramanian, R. Makharia, F. T. Wagner and D. A. Muller, *Nano Lett.*, 2012, **12**, 490–497.

14 M. Watanabe, K. Tsurumi, T. Mizukami, T. Nakamura and P. Stonehart, *J. Electrochem. Soc.*, 1994, **141**, 2659–2668.

15 S. Chen, H. A. Gasteiger, K. Hayakawa, T. Tada and Y. Shao-Horn, *J. Electrochem. Soc.*, 2010, **157**, A82–A97.

16 D. F. van der Vliet, C. Wang, D. Tripkovic, D. Strmcnik, X. F. Zhang, M. K. Debe, R. T. Atanasoski, N. M. Markovic and V. R. Stamenkovic, *Nat. Mater.*, 2012, **11**, 1051–1058.

17 I. E. L. Stephens, A. S. Bondarenko, F. J. Perez-Alonso, F. Calle-Vallejo, L. Bech, T. P. Johansson, A. K. Jepsen, R. Frydendal, B. P. Knudsen, J. Rossmeisl and I. Chorkendorff, *J. Am. Chem. Soc.*, 2011, **133**, 5485–5491.

18 C. Wang, M. Chi, D. Li, D. Strmcnik, D. van der Vliet, G. Wang, V. Komanicky, K.-C. Chang, A. P. Paulikas, D. Tripkovic, J. Pearson, K. L. More, N. M. Markovic and V. R. Stamenkovic, *J. Am. Chem. Soc.*, 2011, **133**, 14396–14403.

19 A. Ohma, K. Shinohara, A. Iiyama, T. Yoshida and A. Daimaru, *ECS Trans.*, 2011, **41**, 775–784.

20 J. Greeley, I. E. L. Stephens, A. S. Bondarenko, T. P. Johansson, H. A. Hansen, T. F. Jaramillo, J. Rossmeisl, I. Chorkendorff and J. K. Nørskov, *Nat. Chem.*, 2009, **1**, 552–556.

21 J. K. Nørskov, J. Rossmeisl, A. Logadottir, L. Lindqvist, J. R. Kitchin, T. Bligaard and H. Jónsson, *J. Phys. Chem. B*, 2004, **108**, 17886–17892.

22 J. Rossmeisl, G. S. Karlberg, T. Jaramillo and J. K. Nørskov, *Faraday Discuss.*, 2009, **140**, 337.

23 T. P. Johansson, E. T. Ulrikkeholm, P. Hernandez-Fernandez, P. Malacrida, H. A. Hansen, A. S. Bandarenka, J. K. Nørskov, J. Rossmeisl, I. E. L. Stephens and I. Chorkendorff, *Top. Catal.*, 2013, 1–10.

24 R. A. Walker and J. B. Darby Jr, *Acta Metall.*, 1970, **18**, 1261–1266.

25 R. Pretorius, T. K. Marais and C. C. Theron, *Mater. Sci. Rep.*, 1993, **10**, 1–83.

26 R. Hultgren, P. D. Desai, D. T. Hawkins, M. Gleiser and K. K. Kelley, *Selected Values of the Thermodynamic Properties of Binary Alloys*, 1973.

27 H. Kleykamp, *J. Nucl. Mater.*, 1993, **201**, 193–217.

28 K. T. Jacob and Y. Waseda, *Thermochim. Acta*, 1990, **165**, 223–233.

29 K. T. Jacob and Y. Waseda, *Bull. Mater. Sci.*, 1990, **13**, 235–244.

30 G. H. Jóhannesson, T. Bligaard, A. V. Ruban, H. L. Skriver, K. W. Jacobsen and J. K. Nørskov, *Phys. Rev. Lett.*, 2002, **88**, 255506.

31 T. Bligaard, G. H. Jóhannesson, A. V. Ruban, H. L. Skriver, K. W. Jacobsen and J. K. Nørskov, *Appl. Phys. Lett.*, 2003, **83**, 4527–4529.

32 J. Nørskov, J. Greeley, I. Stephens, A. S. Bondarenko, T. Johansson, H. A. Hansen, T. Jaramillo, J. Rossmeisl and I. Chorkendorff, Platinum and Palladium Alloys Suitable as Fuel Cell Electrodes, *U.S. Patent* No. 20,120,214,083, 2012.

33 M. Escudero-Escribano, A. Verdaguer-Casadevall, P. Malacrida, U. Grønbjerg, B. P. Knudsen, A. K. Jepsen, J. Rossmeisl, I. E. L. Stephens and I. Chorkendorff, *J. Am. Chem. Soc.*, 2012, **134**, 16476–16479.

34 P. C. K. Vesborg and T. F. Jaramillo, *RSC Adv.*, 2012, **2**, 7933–7947.

35 M. Pourbaix, *Atlas of electrochemical equilibria in aqueous solutions*, Nat'L Assoc. Of Corrosion, [S.l.], 1974.

36 S. J. Yoo, K.-S. Lee, S. J. Hwang, Y.-H. Cho, S.-K. Kim, J. W. Yun, Y.-E. Sung and T.-H. Lim, *Int. J. Hydrogen Energy*, 2012, **37**, 9758–9765.

37 S. J. Yoo, S. J. Hwang, J.-G. Lee, S.-C. Lee, T.-H. Lim, Y.-E. Sung, A. Wieckowski and S.-K. Kim, *Energy Environ. Sci.*, 2012, **5**, 7521–7525.

38 S. J. Hwang, S.-K. Kim, J.-G. Lee, S.-C. Lee, J. H. Jang, P. Kim, T.-H. Lim, Y.-E. Sung and S. J. Yoo, *J. Am. Chem. Soc.*, 2012, **134**, 19508–19511.

39 A. S. Bandarenka, A. S. Varela, M. Karamad, F. Calle-Vallejo, L. Bech, F. J. Perez-Alonso, J. Rossmeisl, I. E. L. Stephens and I. Chorkendorff, *Angew. Chem., Int. Ed.*, 2012, **51**, 11845–11848.

4242 | *J. Mater. Chem. A*, 2014, **2**, 4234–4243

This journal is © The Royal Society of Chemistry 2014

40 M. Teliska, V. S. Murthi, S. Mukerjee and D. E. Ramaker, *J. Electrochem. Soc.*, 2005, **152**, A2159–A2169.

41 P. B. Balbuena, D. Altomare, N. Vadlamani, S. Bingi, L. A. Agapito and J. M. Seminario, *J. Phys. Chem. A*, 2004, **108**, 6378–6384.

42 Y. Xu, A. V. Ruban and M. Mavrikakis, *J. Am. Chem. Soc.*, 2004, **126**, 4717–4725.

43 A. M. de Asha and R. M. Nix, *Surf. Sci.*, 1995, **322**, 41–50.

44 M. Juel, S. Martinsen and S. Raaen, *Thin Solid Films*, 2008, **517**, 805–810.

45 W. Bronger, *J. Less-Common Met.*, 1967, **12**, 63–68.

46 T. B. Massalski, J. L. Murray, L. H. Bennett and H. Baker, *Binary alloy phase diagrams*, American Society for Metals, 1986.

47 S. Reimann and H.-J. Schaller, *J. Alloys Compd.*, 2006, **419**, 133–139.

48 H. Okamoto, *J. Phase Equilib. Diffus.*, 2008, **29**, 122.

49 I. E. L. Stephens, A. S. Bondarenko, L. Bech and I. Chorkendorff, *ChemCatChem*, 2012, **4**, 341–349.

50 D. F. van der Vliet, C. Wang, D. Li, A. P. Paulikas, J. Greeley, R. B. Rankin, D. Strmcnik, D. Tripkovic, N. M. Markovic and V. R. Stamenkovic, *Angew. Chem.*, 2012, **124**, 3193–3196.

51 K. J. J. Mayrhofer, D. Strmcnik, B. B. Blizanac, V. Stamenkovic, M. Arenz and N. M. Markovic, *Electrochim. Acta*, 2008, **53**, 3181–3188.

52 M. Nesselberger, S. Ashton, J. C. Meier, I. Katsounaros, K. J. J. Mayrhofer and M. Arenz, *J. Am. Chem. Soc.*, 2011, **133**, 17428–17433.

53 U. A. Paulus, A. Wokaun, G. G. Scherer, T. J. Schmidt, V. Stamenkovic, N. M. Markovic and P. N. Ross, *Electrochim. Acta*, 2002, **47**, 3787–3798.

54 J. C. Fuggle, M. Campagna, Z. Zolnierek, R. Lässer and A. Platau, *Phys. Rev. Lett.*, 1980, **45**, 1597–1600.

55 J. W. Allen, S. J. Oh, O. Gunnarsson, K. Schönhammer, M. B. Maple, M. S. Torikachvili and I. Lindau, *Adv. Phys.*, 1986, **35**, 275–316.

56 F. Zhang, P. Wang, J. Koberstein, S. Khalid and S.-W. Chan, *Surf. Sci.*, 2004, **563**, 74–82.

57 J. C. Fuggle, *J. Less-Common Met.*, 1983, **93**, 159–169.

58 L. Schlapbach, *Solid State Commun.*, 1981, **38**, 117–123.

59 J. C. Fuggle, F. U. Hillebrecht, Z. Zołnierek, R. Lässer, C. Freiburg, O. Gunnarsson and K. Schönhammer, *Phys. Rev. B: Condens. Matter Mater. Phys.*, 1983, **27**, 7330–7341.

60 F. U. Hillebrecht and J. C. Fuggle, *Phys. Rev. B: Condens. Matter Mater. Phys.*, 1982, **25**, 3550–3556.

61 W.-D. Schneider, B. Delley, E. Wuilloud, J.-M. Imer and Y. Baer, *Phys. Rev. B: Condens. Matter Mater. Phys.*, 1985, **32**, 6819–6831.

62 A. Pfau and K. D. Schierbaum, *Surf. Sci.*, 1994, **321**, 71–80.

63 S. Tanuma, C. J. Powell and D. R. Penn, *Surf. Interface Anal.*, 1991, **17**, 911–926.

64 The US Department of Energy (DOE), *Energy Efficiency and Renewable Energy* http://www.eere.energy.gov/hydrogenandfuelcells/mypp/pdfs/fuel_cells.pdf *and the US DRIVE Fuel Cell Technical Team Technology Roadmap* http://www.uscar.org/guest/teams/17/Fuel-Cell-Tech-Team, 2013.

65 N. Todoroki, Y. Iijima, R. Takahashi, Y. Asakimori and T. Wadayama, *J. Electrochem. Soc.*, 2013, **160**, F591–F596.

66 F. Maillard, L. Dubau, J. Durst, M. Chatenet, J. André and E. Rossinot, *Electrochem. Commun.*, 2010, **12**, 1161–1164.

67 G. Praline, B. E. Koel, R. L. Hance, H.-I. Lee and J. M. White, *J. Electron Spectrosc. Relat. Phenom.*, 1980, **21**, 17–30.

68 T. L. Barr, *J. Phys. Chem.*, 1978, **82**, 1801–1810.

69 D. D. Sarma, M. S. Hegde and C. N. R. Rao, *J. Chem. Soc., Faraday Trans. 2*, 1981, **77**, 1509–1520.

70 B. C. Beard and P. N. Ross, *J. Electrochem. Soc.*, 1990, **137**, 3368–3374.

71 H. Abe, F. Matsumoto, L. R. Alden, S. C. Warren, H. D. Abruña and F. J. DiSalvo, *J. Am. Chem. Soc.*, 2008, **130**, 5452–5458.

72 *CRC Handbook of Chemistry and Physics*, ed. W. M. Haynes, CRC Press, 93rd edn, 2012.

73 A. Bonakdarpour, J. Wenzel, D. A. Stevens, S. Sheng, T. L. Monchesky, R. Löbel, R. T. Atanasoski, A. K. Schmoeckel, G. D. Vernstrom, M. K. Debe and J. R. Dahn, *J. Electrochem. Soc.*, 2005, **152**, A61–A72.

74 C. Wang, M. Chi, G. Wang, D. van der Vliet, D. Li, K. More, H.-H. Wang, J. A. Schlueter, N. M. Markovic and V. R. Stamenkovic, *Adv. Funct. Mater.*, 2011, **21**, 147–152.

75 J. R. Kitchin, J. K. Nørskov, M. A. Barteau and J. G. Chen, *J. Chem. Phys.*, 2004, **120**, 10240–10246.

76 T. P. Johansson, New Materials for Oxygen Reduction Electrodes, PhD thesis, Department of Physics, Technical University of Denmark, 2012.

77 L.-J. Wan, T. Moriyama, M. Ito, H. Uchida and M. Watanabe, *Chem. Commun.*, 2002, 58–59.

78 P. Strasser, S. Koh, T. Anniyev, J. Greeley, K. More, C. Yu, Z. Liu, S. Kaya, D. Nordlund, H. Ogasawara, M. F. Toney and A. Nilsson, *Nat. Chem.*, 2010, **2**, 454–460.

Enabling direct H₂O₂ production through rational electrocatalyst design

Samira Siahrostami[1†], Arnau Verdaguer-Casadevall[2†], Mohammadreza Karamad[1], Davide Deiana[3], Paolo Malacrida[2], Björn Wickman[2,4], María Escudero-Escribano[2], Elisa A. Paoli[2], Rasmus Frydendal[2], Thomas W. Hansen[3], Ib Chorkendorff[2], Ifan E. L. Stephens[2]★ and Jan Rossmeisl[1]★

Future generations require more efficient and localized processes for energy conversion and chemical synthesis. The continuous on-site production of hydrogen peroxide would provide an attractive alternative to the present state-of-the-art, which is based on the complex anthraquinone process. The electrochemical reduction of oxygen to hydrogen peroxide is a particularly promising means of achieving this aim. However, it would require active, selective and stable materials to catalyse the reaction. Although progress has been made in this respect, further improvements through the development of new electrocatalysts are needed. Using density functional theory calculations, we identify Pt–Hg as a promising candidate. Electrochemical measurements on Pt–Hg nanoparticles show more than an order of magnitude improvement in mass activity, that is, A g⁻¹ precious metal, for H₂O₂ production, over the best performing catalysts in the literature.

At present, the most commonly produced chemicals, such as ammonia, hydrogen, methanol and hydrogen peroxide are produced in centralized reactors on a very large scale. There is a general call[1,2] for a more decentralized infrastructure where both energy conversion and chemical synthesis are conducted closer to the point of consumption. Electrochemical devices are set to play an increasingly important role in reaching this goal; they can be operated under ambient conditions, at variable rates and require little auxiliary plant[3]. They can also be coupled with intermittent renewable power sources, such as solar or wind, providing a means to store electricity and level out demand. Herein, we focus on the electrochemical production of hydrogen peroxide.

Copious amounts of H_2O_2 are produced globally; its annual production exceeds 3 million tons (ref. 4). It is both an environmentally benign chemical oxidant, used for chemical synthesis, the pulp and paper industry and in water treatment[5,6], and a potential energy carrier[7]. When produced from H_2 and O_2, H_2O_2 production is exergonic, with a standard Gibbs free energy of formation, $\Delta G_f^0 = -120\,kJ\,mol^{-1}$. At present, H_2O_2 is produced using the anthraquinone process, a batch method conducted in large-scale facilities, with an average yield of 50 thousand tons per year per plant[4]. It involves the sequential hydrogenation and oxidation of anthraquinone molecules, and it is energy intensive[8].

The inherent complexity of the anthraquinone process has motivated many researchers towards developing a direct synthesis of H_2O_2 from its elements[9,10], aiming at: small-scale, continuous production through a catalytic process[6]. Pd-modified Au nanoparticles (henceforth denoted as Pd/Au) are the most active catalysts for this process[9]. The electroreduction of oxygen to H_2O_2 in a fuel cell or electrolyser holds significant advantages over the above processes. It would enable on-site production of hydrogen peroxide, and unlike the direct synthesis route, it would not be constrained by the need to maintain the hydrogen and oxygen

outside the explosive regime. Moreover, when produced in a fuel cell, it should, in principle, be possible to recover most of the ΔG_f^0, 120 kJ mol⁻¹, as electrical energy. Alternatively, one could do away with H_2 altogether, and synthesize H_2O_2 at the cathode of an electrolyser; with oxygen evolution occurring at its anode, the energy input would be ∼200 kJ mol⁻¹ (see Supplementary Information). Nonetheless, industrially viable, electrochemical production of H_2O_2 requires a catalyst that is stable, active and selective for the electroreduction of oxygen[6,11–14].

The most active and selective catalysts found for this reaction, thus far, are based on porphyrins containing $3d$ transition metals such as Co (ref. 15). However, the nitrogen ligands of these catalysts degrade in the presence of H_2O_2, resulting in rapid performance losses[16,17]. On the other hand, catalysts based on noble metals provide adequate stability under the harsh reaction conditions. Au nanoparticles have a modest activity for H_2O_2 production, ∼1 mA at 0.4 V overpotential, but with a selectivity of only ∼80%. On the other hand, Pd/Au nanoparticles show similar activity to Au and up to ∼90% selectivity[13]. An overview of different electrocatalysts for H_2O_2 production is shown in Fig. 1, compiled from the literature.

Here, our goal is to discover new alloys for the electrochemical generation of H_2O_2, exhibiting an unprecedented combination of activity, selectivity and stability. We specifically focus our attention on catalysts that function under ambient conditions, containing elements that are stable in acidic, rather than basic electrolytes. This is because H_2O_2 decomposes at high temperatures or alkaline conditions[6], and devices based on hydroxide-conducting polymeric electrolytes exhibit low membrane stability, poor water management and low hydrogen oxidation activity[18,19].

We identify the catalysts using density functional theory (DFT) calculations, synthesize and test them electrochemically and characterize their composition and structure *ex situ*.
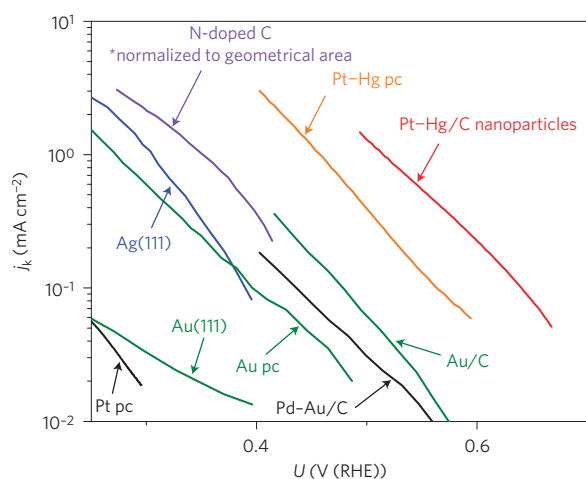
Figure 1 | Overview of different electrocatalysts for H_2O_2 production from the literature and from the present work. For the comparison, the kinetic current has been derived by correcting the partial current density for H_2O_2 production for mass transport limitations. Further details are available in the Methods and in the Supplementary Information. Data adapted from: ref. 46 for Pt polycrystalline (pc); ref. 47 for Au(111); ref. 48 for Au pc; ref. 49 for Ag(111); ref. 14 for N-doped C; ref. 13 for Pd–Au/C and Au/C. Data for Pt–Hg pc and Pt–Hg/C is from the present study.

Computational screening

The electroreduction of O_2 to H_2O_2 involves two coupled electron and proton transfers[20]:

$$O_2 + {}^* + (H^+ + e^-) \rightarrow HOO^* \qquad (1)$$

$$HOO^* + (H^+ + e^-) \rightarrow H_2O_2 + {}^* \qquad (2)$$
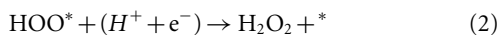
where $*$ denotes an unoccupied active site, and HOO^* denotes the single adsorbed intermediate for the reaction. The catalyst provides high activity, by minimizing kinetic barriers for (1) and (2), and selectivity, by maximizing the barrier for HOO^* reduction or dissociation to O^* and OH^*, the intermediates of the four-electron reduction of O_2 to H_2O.

The catalytic activity and selectivity, in turn, are determined by an interplay between two effects: ensemble effects and electronic effects. The binding of the reaction intermediates is controlled by electronic effects[21,22]. Varying the catalyst material allows one to tune the binding of HOO^* to the surface. This means that the key parameter, or descriptor, in controlling the catalyst activity is the HOO^* binding energy, ΔG_{HOO^*}. As the binding energy of HOO^* scales linearly with that of HO^*, ΔG_{HO^*} by a constant amount of 3.2 ± 0.2 eV (ref. 23), ΔG_{HO^*} can also be used as a descriptor. In Fig. 2e, the thermodynamic limiting potential, U_T, which is the most positive potential at which both (1) and (2) are downhill in free energy, is plotted, in blue, as a function of ΔG_{HO^*}; the HOO^* binding energy is also shown on the upper horizontal axis for comparison. The thermodynamic overpotential for the two-electron reaction, η_{O_2/H_2O_2}, is denoted by the blue arrow, and is defined as the distance from the Nernstian potential for H_2O_2 production, $U^0_{O_2/H_2O_2} = 0.7$ V, to the U_T. Applying a bias equivalent to η_{O_2/H_2O_2} would allow the catalyst to sustain appreciable kinetic rates for H_2O_2 production, due to low charge transfer barriers[24–26].

Figure 2e establishes that there is a volcano-type relationship between η_{O_2/H_2O_2} (and hence the catalytic activity), and ΔG_{HO^*}. Catalysts on the right-hand side of the volcano are limited by HOO^* formation. For Au(211) it is 0.41 eV uphill to form HOO^* at $U^0_{O_2/H_2O_2}$, as shown in the free-energy diagram in Fig. 2b. Accordingly, a thermodynamic overpotential of 0.41 V is required to drive the reaction. Catalysts on the left-hand side, such as Pt or Pd,

bind HOO^* too strongly, and the overpotential for the two-electron pathway is due to the reduction of HOO^* to H_2O_2. The ideal catalyst, at the peak of the volcano, has a $\Delta G_{HOO^*} \sim 4.2 \pm 0.2$ eV and $\eta_{O_2/H_2O_2} = 0$; its free-energy diagram is flat at the equilibrium potential, as shown in Fig. 2b. This means that the ideal catalyst would exhibit high current densities at negligible overpotentials.

In Fig. 2e, the U_T for the four-electron reduction of O_2 to H_2O is also plotted, in red, as a function of ΔG_{HO^*} and ΔG_{HOO^*}. In this case, there is an extra step contributing to the overpotential for the reaction, HO^* reduction (where HO^* is an adsorbed hydroxyl group, formed from the dissociation or reduction of HOO^*; ref. 27):

$$HO^* + (H^+ + e^-) \rightarrow H_2O + {}^* \qquad (3)$$
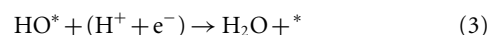
The thermodynamic overpotential for equation (3), H_2O formation, η_{O_2/H_2O}, is indicated by the red arrow. Strikingly, in contrast to the two-electron volcano, even on the optimal catalyst, a minimum η_{O_2/H_2O} of ~ 0.4 V is required to drive H_2O formation.

The high value of η_{O_2/H_2O} is typical for reactions involving more than two electrons[20,22,23,26,28,29]; this is to overcome the large difference in adsorption energies between the intermediates, HO^* and HOO^*, whose binding energies scale linearly with each other[26]. On the other hand, the negligible overpotential required to drive O_2 reduction to H_2O_2 is characteristic of two-electron reactions, where the criterion for finding the ideal catalyst is relatively trivial: the adsorption of the sole reaction intermediate should be thermoneutral at the equilibrium potential[30].

The selectivity towards H_2O_2 or H_2O is determined by its propensity to break the O–O bond. This is, in turn, set by the binding strengths of the intermediates of the four-electron pathway, O^* and HO^*. To the left side of the peak (strong HO^* binding) of both the four- and two-electron volcanoes (Fig. 2e), it is more downhill in free energy to form H_2O from HO^*; this means the selectivity towards the four-electron pathway will dominate over the two-electron pathway, as is the case for Pt and Pd. The right side (weak HO^* binding) of both two- and four-electron volcanoes overlap each other. In other words, at the peak of the two-electron volcano, there is a high activity for both H_2O_2 and H_2O formation, and both pathways will occur in tandem. Moving further right, beyond the peak of the two-electron volcano, towards Au it becomes more difficult to break the O–O bond and form HO^* and O^*, either through the chemical dissociation of HOO^* or its electrochemical reduction. In summary, moving rightwards from the peak of the two-electron volcano weakens the interaction with O^* and HO^*, increasing the selectivity, but lowering the activity.

Apart from electronic effects, selectivity can also be controlled by geometric (or ensemble) effects; these are associated with the geometric arrangement of atoms on the catalyst surface[31,32]. On a selective catalyst, both the chemical dissociation to HO^* and O^* and the electrochemical reduction of HOO^* to $O^* + H_2O$ should be avoided. Therefore, destabilizing O^*, relative to HOO^*, improves the selectivity. This can be achieved by controlling the geometry of the binding site: HOO^* normally binds onto atop sites whereas O^* binds onto hollow sites[33]. Eliminating hollow sites will specifically destabilize O^*, without necessarily changing the activity. Catalysts such as Co-porphyrins[34] lack hollow sites whereas catalysts such as Pd/Au (ref. 13) contain hollow sites that interact weakly with oxygen; their active sites consist of single atoms, isolated by elements, such as Au, N or C (see Supplementary Information). This explains why Pd/Au is also an effective catalyst for the direct gas-phase synthesis of H_2O_2 from H_2 and O_2 (ref. 9).

Taking into account the above trends, using DFT, we screened for new alloy catalysts for the electrochemical generation of H_2O_2, which had not previously been tested. Our main criteria are that: for optimal activity, $\Delta G_{HOO^*} \sim 4.2 \pm 0.2$ eV; each of the constituent

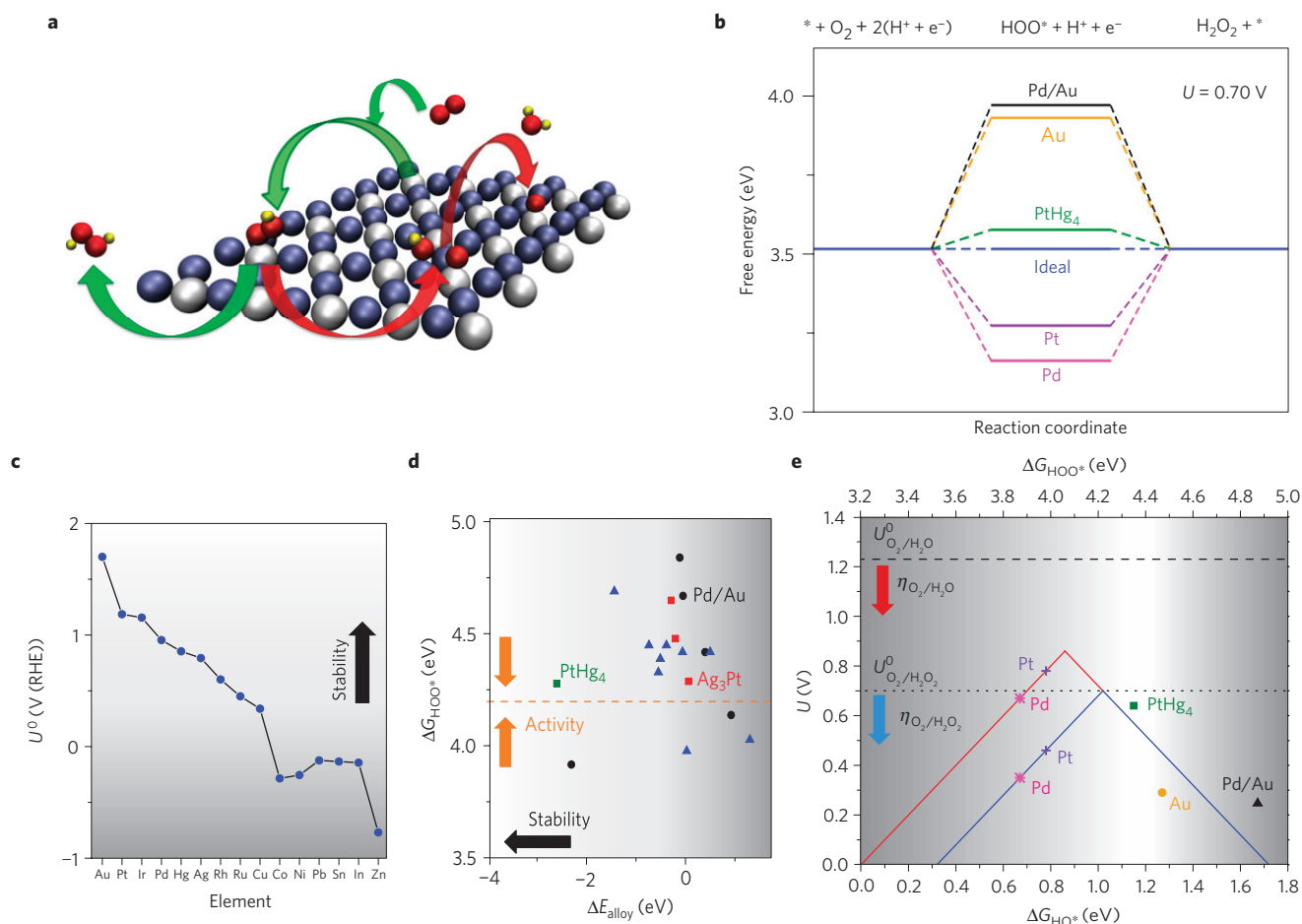**Figure 2 | Theoretical modelling of oxygen reduction to H_2O and H_2O_2. a**, Representation of the $PtHg_4$(110) surface, based on the investigation of Hg/Pt(111) in ref. 35. The green arrows represent the reaction path to H_2O_2, whereas the red arrows the path to H_2O. Mercury, blue; platinum, grey; oxygen, red; hydrogen, yellow. **b**, Free-energy diagram for oxygen reduction to H_2O_2. The ideal catalyst is compared with $PtHg_4$(110), Pd/Au and closely packed pure metals Pd(111) and Au(211), all calculated for this work, and Pt(111), adapted from ref. 27. **c**, Dissolution potential for various elements under standard conditions[50]. **d**, Formation energy (per formula unit) ΔE_{alloy}, as a function of ΔG_{HOO*}. The optimal value for HOO binding is plotted as the orange dashed line. Bulk alloys are shown by red and green squares, surface alloys with a Au substrate are shown as black circles and surface alloys with non-Au substrate are shown by blue triangles. For **c,d** the colour gradient scales with stability, with the most stable areas highlighted in white. **e**, Theoretically calculated oxygen reduction volcano plot for the two-electron (blue) and four-electron (red) reduction of O_2, with the limiting potential plotted as a function of ΔG_{HO*} (lower horizontal axis) and ΔG_{HOO*} (upper horizontal axis). The equilibrium potential for the two-electron pathway, $U^0_{O_2/H_2O_2}$, is shown as the dotted line, and the equilibrium potential for the four-electron pathway, $U^0_{O_2/H_2O}$, is shown as the dashed line. The range of interesting HO* free energy for high selectivity and activity is highlighted with the greyscale gradient at its edges, recognizing limitations to the accuracy of DFT. Extensive details of the alloys included in the DFT screening are included in the Supplementary Information.

elements should be stable against dissolution or oxidation under reaction conditions; and the alloy should have as negative a heat of formation as possible (this provides a driving force to form the required monatomic ensembles). Each of the alloys has an active site where isolated atoms of the reactive metal, for example Pt, Pd, Rh or Ir, are surrounded by more inert elements, such as Au and Hg. A total number of 30 alloys were screened. An outline for the screening process is given in Fig. 2, (further details are available in the Supplementary Information).

Our attention was focused on the use of Hg as a means of forming the isolated reactive atoms. Hg is catalytically inactive. It is stable against dissolution up to 0.80 V at pH 0 (at standard conditions), and according to both our calculations (see Supplementary Information) and experiments[35] it forms stable alloys. The negative enthalpy of formation of the formed phase, $PtHg_4$, will stabilize the Hg, relative to pure Hg, meaning that it will be stable against dissolution. Hg can be easily electrodeposited onto Pt (ref. 36); on Pt(111) it forms a self-organized surface structure at room

temperature[35]; each Pt atom is surrounded by Hg, as shown in Fig. 2a, thus forming the monatomic ensembles required for high selectivity. Figure 2b also shows that $PtHg_4$ has a close to optimal binding energy, with a thermodynamic overpotential smaller than 0.1 V. Alloying evidently induces electronic effects, as the binding of HOO* is ~0.37 eV weaker than pure Pt. Indeed, we emphasize that $PtHg_4$ is the only catalyst identified in the screening that fulfils all of our criteria for activity, selectivity and stability.

Although Hg is toxic, only monolayer quantities of Hg would be required to produce the required atomic ensembles; its present industrial applications, for example, lighting or the cathode for chlorine synthesis, require much larger amounts[4]. In the following we show that $PtHg_4$ is indeed highly selective and active for the two-electron pathway.

Experimental results

To synthesize $PtHg_4$, we modified a polycrystalline Pt disc following the procedure of ref. 35 for Hg/Pt(111). About 10 monolayers
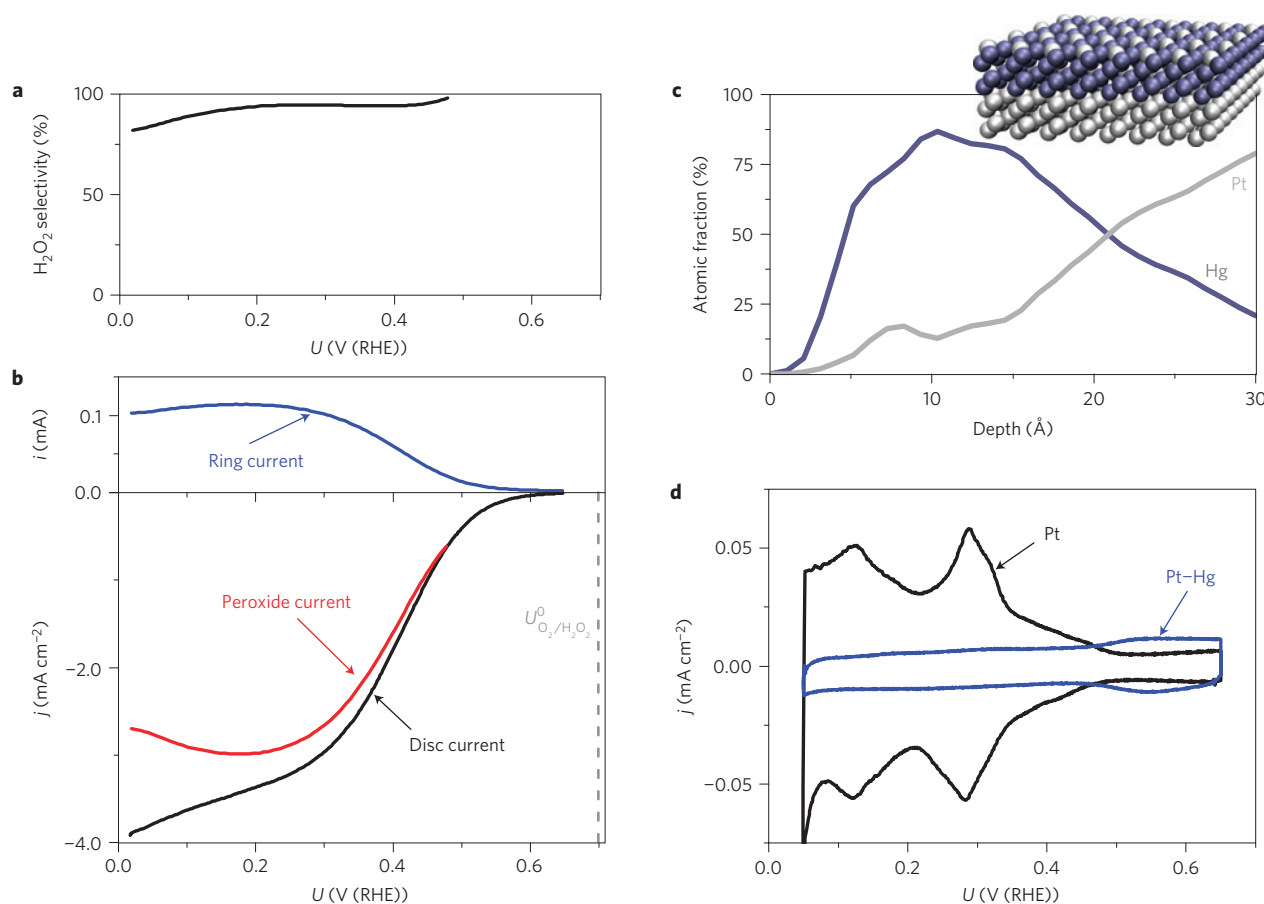
Figure 3 | Experimental characterization of Pt–Hg on extended surfaces. a, H_2O_2 selectivity as a function of the applied potential. **b**, RRDE voltammograms at 1,600 r.p.m. in O_2-saturated electrolyte with the disc current, ring current and current corresponding to hydrogen peroxide obtained from the ring current (only the anodic cycle is shown). **c**, Angle-resolved XPS depth profile of Pt–Hg. The adventitious C and O traces have been omitted for clarity. The inset shows a schematic representation of the structure revealed by the angle-resolved depth profile, with a Pt–Hg alloy above a Pt substrate. **d**, Voltammograms in N_2-saturated electrolyte of Pt and Pt–Hg. All electrochemical measurements were taken in 0.1 M $HClO_4$ and at 50 mV s^{-1} at room temperature.

of Hg were electrodeposited from $HgClO_4$. *Ex situ* angle-resolved X-ray photoelectron spectroscopy (XPS) of the sample at this stage revealed that the surface is composed of $\sim$20% Pt and $\sim$80% Hg, in agreement with a $PtHg_4$ structure (Fig. 3c). Figure 3d shows a cyclic voltammogram in N_2-saturated solution for Pt and Hg-modified Pt. The voltammogram for Pt shows the typical hydrogen adsorption/desorption peaks at 0.05–0.5 V, whereas Pt–Hg has a flat profile, suggesting a negligible amount of hydrogen adsorption. This is consistent with our DFT calculations (see Supplementary Information), which show that H is destabilized on $PtHg_4$(110), relative to Pt(111). Moreover, isolated Pd atoms on Au exhibit similar voltammograms[13]. We understand this phenomenon on the basis that on pure Pt and Pd, H usually adsorbs at hollow sites, with three Pt or Pd nearest neighbours[37]; isolated Pt or Pd atoms would lack such sites. The negative alloying energy of $PtHg_4$ provides a driving force to maximize the coordination of Hg to Pt and minimize the number of Pt–Pt nearest neighbours. Further evidence for the surface composition can be found in the Supplementary Information. In summary, our observations support the notion that isolated Pt atoms are formed at the surface of Pt–Hg, consistent with earlier experiments on Hg/Pt(111) (ref. 35).

We measure the electrochemical activity for oxygen reduction to hydrogen peroxide, using the rotating ring disc electrode (RRDE) technique[38]. Figure 3b shows the voltammograms in oxygen for Pt–Hg. The disc current increases exponentially with a decrease

in potential from $\sim$0.6 V, as kinetic barriers are lowered. To quantify the amount of hydrogen peroxide formed, the ring was potentiostated at 1.2 V, where the oxygen reduction current is negligible and H_2O_2 oxidation is mass transport limited. This gives rise to a positive current at the ring as hydrogen peroxide is produced at the disc (Fig. 3b). The onset potential at the ring and the disc coincide at $\sim$0.6 V, corresponding to an overpotential of $\sim$0.1 V. Such low overpotential is in agreement with our theoretical predictions. As the overpotential increases, most of the current in the disc can be accounted for by the amount of H_2O_2 detected at the ring; the efficiency of hydrogen peroxide production is as high as 96% in the region between 0.2 and 0.4 V (Fig. 3a). Within these potential limits, the hydrogen peroxide current density is 3 mA cm^{-2}, the theoretical mass transport limit for the two-electron reduction of oxygen. It is only at potentials below 0.2 V that both selectivity and hydrogen peroxide current start to decrease, implying that water formation is favoured.

To validate the stability criteria for our computational screening (Fig. 2), we also tested Pt–Sn and Ag_3Pt as catalysts for H_2O_2 production. As described in the Supplementary Information, we predict that both of these catalysts would, in principle, have optimal H_2O_2 activity. However, they fail to meet our stability criteria. Consequently, the less noble component, Sn or Ag, dissolved under reaction conditions. These examples illustrate the importance of stability in the corrosive electrochemical environment, which is both acidic and oxidizing.
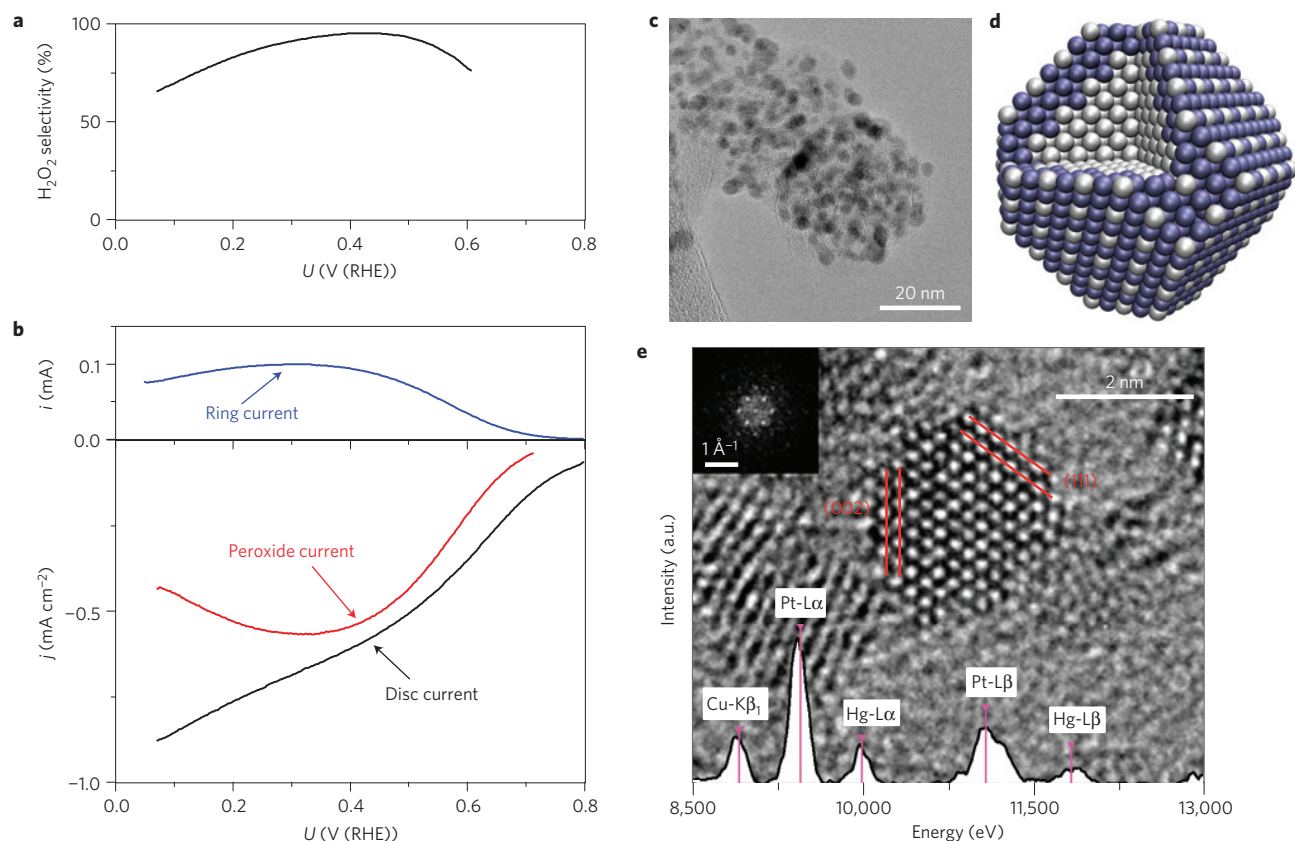
Figure 4 | Experimental characterization of Pt–Hg/C nanoparticles. a, H_2O_2 selectivity as a function of the applied potential. **b**, RRDE voltammograms at 1,600 r.p.m. in O_2-saturated electrolyte with the disc current, ring current and current corresponding to hydrogen peroxide obtained from the ring current (only the anodic cycle is shown). All electrochemical measurements were taken in 0.1 M $HClO_4$ and at 50 mV s^{-1} at room temperature. The disc current is normalized to the surface area of Pt nanoparticles (from H-upd) before deposition of Hg. **c**, TEM image of Pt–Hg/C nanoparticles. **d**, Schematic representation of a Pt–Hg/C nanoparticle. Mercury, blue; platinum, grey. **e**, HRTEM image of a single Pt–Hg nanoparticle, with the corresponding EDS spectrum of the particle superimposed on top, with peaks corresponding to Pt and Hg from the nanoparticle, and Cu, from the TEM grid; the {111} and {002} planes are shown in red; the corresponding diffractogram is shown in the inset.

Ultimately, should electrochemical hydrogen peroxide synthesis make a technological impact, it will require high-surface-area catalysts or thin films[26,39]. It turns out that Pt–Hg/C nanoparticles are even more active than the extended surfaces.

An ink was prepared from commercial Pt/C and drop-cast on a glassy carbon electrode (details in the Supplementary Information). To prepare the Pt–Hg alloy we followed the same electrodeposition procedure as for the polycrystalline surface. The features of the base voltammograms were similar to those of polycrystalline Pt–Hg (see Supplementary Information).

Transmission electron microscopy (TEM) analysis showed well-distributed nanoparticles on the carbon support (Fig. 4c). A high-resolution TEM (HRTEM) image of a single nanoparticle and its Fourier transform are shown in Fig. 4e. By positioning the scanning TEM probe on an individual nanoparticle, an energy-dispersive X-ray spectroscopy (EDS) spectrum as shown in Fig. 4e was acquired. Both Pt and Hg peaks are present in the spectrum. XPS analysis, which is sensitive to the first few atomic layers, confirmed the presence of both elements. However, the lattice parameters from the HRTEM are consistent with the structure of Pt. Together, the HRTEM and XPS data suggest a core of Pt and a shell of Pt–Hg (see Supplementary Information).

We then evaluated oxygen reduction on Hg-modified Pt nanoparticles (Fig. 4b), where we observed a similar current profile to the polycrystalline surfaces. The ring current proved that a high yield of hydrogen peroxide was achieved, with over 90% selectivity between 0.3 and 0.5 V (Fig. 4a). The catalyst is highly stable

under reaction conditions. When cycling the potential between 0.05 and 0.8 V for 8,000 cycles in an O_2-saturated electrolyte, there were no measurable losses in H_2O_2 production activity (see Supplementary Information).

The viability of an electrochemical device producing H_2O_2 will require it to be efficient, safe and that the cost of its constituent materials is minimal. Given that the most viable catalysts for H_2O_2 production are based on precious metals, it is essential that the loading of these metals is minimized, that is, that the current density per gram of precious metal is maximized.

State-of-the-art fuel cells and electrolysers are engineered to avoid losses due to the transport of oxygen. Thus, to yield a quantitative comparison of catalyst performance, we have corrected the data in Figs 3 and 4 for mass transport losses. The results are shown in Fig. 1. In terms of specific activity (normalized to the surface area of Pt), nanoparticulate Pt–Hg/C exhibits 4–5 times the activity of polycrystalline Pt–Hg. The higher activity of the nanoparticles compared with extended surfaces indicates that undercoordinated sites, which are more prevalent on nanoparticulate surfaces[40], could play an important role in the reaction. Notably, Pt–Hg/C shows more than one order of magnitude improvement in mass activity over previously reported Pd–Au/C or Au/C (ref. 13). To the best of our knowledge, Pt–Hg nanoparticles present the best activity reported in the literature for hydrogen peroxide synthesis on a metallic catalyst, with a selectivity of up to 96% and a mass activity of 26 ± 4 A g$^{-1}_{\text{noble metal}}$ at 50 mV overpotential.

In this work, we have taken advantage of the isolated active site concept to tune the activity and selectivity for oxygen reduction. Our theoretical model successfully predicted Pt–Hg as an active, selective and stable catalyst for hydrogen peroxide synthesis.

Comparing the activity reported here with that reported for other two-electron reactions, we anticipate that it should be possible to discover even more active catalysts for electrochemical H_2O_2 production[23,30,37,41,42]. Nonetheless, as our theoretical model shows, improved activity may come at the cost of selectivity. The rational approach used here to tune activity and selectivity can be extended to other, more complex reactions for sustainable energy conversion, in particular the electroreduction of CO_2 and N_2 (refs 28,29).

Methods

Computational details. The computational analysis was carried out using grid-based projector-augmented wave (GPAW) method, a DFT code based on a projected augmented wave (all-electron frozen core approximation) method integrated with the atomic simulation environment[43,44]. The revised Perdew–Burke–Ernzerhof functional was used as an exchange correlation functional[45]. An eight-layer 2×2 slab with 17.5 Å vacuum between successive slabs was used to model the $PtHg_4(110)$ surface. Monkhorst–Pack grids with dimensions of $4 \times 4 \times 1$ were used to sample the Brillouin zone. The bottom four layers were fixed in the bulk structure whereas the upper layers and adsorbates were allowed to relax in all directions until residual forces were less than 0.05 eV Å⁻¹. Further details on DFT calculations are provided in the Supplementary Information.

Extended surface electrode preparation. A platinum polycrystalline electrode was mirror polished to <0.25 μm before every experiment and prepared by flame annealing as previously reported[46]. Several voltammograms in nitrogen-saturated 0.1 M $HClO_4$ were recorded to ensure a reproducible surface, and then the electrode was moved to an electrodeposition cell containing 0.1 M $HClO_4$ + 1 mM $HgClO_4$. The potential was swept from open circuit (about 1 V) at 50 mV s⁻¹ to 0.2 V, where the potential was stopped for 2 min to electrodeposit mercury following the procedure detailed in ref. 35. The potential was scanned to 0.65 V at 50 mV s⁻¹ and stopped there while removing the electrode from the cell. We immediately moved the Hg-modified Pt electrode back into the RRDE cell, where it was inserted under potential control of about 0.1 V in N_2-saturated 0.1 M $HClO_4$. Then the potential was swept between 0.05 and 0.65 V until a stable cyclic voltammogram was obtained. As we observed mercury traces at the ring, we cleaned it electrochemically by cycling it between 0.05 and 1.6 V while rotating the electrode to avoid mercury redeposition. Once the ring and disc voltammetries became stable, we saturated the cell with O_2 to record voltammetries at the disc while keeping the ring at 1.2 V to detect H_2O_2.

High-surface-area catalysts. To prepare the Pt/C nanoparticles, a simple synthesis method was employed. First, 5.75 mg of 60% wt Pt supported on C was mixed with 9.5 ml of Millipore water, 3 ml of isopropanol and 50 μl of 1:100 Nafion. To facilitate dispersion of the nanoparticles, 20 μl of 2% wt solution of polyvinylpyrrolidone was used. The nanoparticles had a nominal size of 3 nm. The mixture was sonicated for 20 min at about 25 °C and 10 μl of it was drop-casted on top of a glassy carbon disc of 0.196 cm². The sample was then left to dry before embedding into a RRDE set-up. To ensure a good dispersion of the film, oxygen reduction was carried out on the Pt/C nanoparticles (see Supplementary Information). The same procedure adopted for the polycrystalline sample was followed to electrodeposit mercury. All data relative to nanoparticles were normalized to the underpotential deposition of hydrogen (H-upd; that is, assuming that the voltammetric charge between 0.5 and 0.05 V is equivalent to 210 μC cm⁻² of Pt surface area[18]) before Hg deposition, and the corresponding capacitance was subtracted from all oxygen reduction measurements.

Chemicals. Concentrated $HClO_4$ was obtained from Merck and diluted to 0.1 M. $HgClO_4$ was obtained from Sigma Aldrich and diluted in 0.1 M $HClO_4$ to reach 1 mM $HgClO_4$. All gases were of 5N5 quality and purchased from AGA.

Electrochemical measurements. A typical three-electrode cell was used for the RRDE experiments. Another three-electrode cell was used to electrodeposit mercury. In both cells the counter electrodes were Pt wires and Hg/Hg_2SO_4 electrodes were used as a reference, separated from the working electrode compartment using a ceramic frit. All potentials are quoted with respect to the reversible hydrogen electrode, and are corrected for ohmic losses. All experiments were performed using a Bio-Logic Instruments' VMP2 potentiostat, controlled by a computer. The RRDE assembly was provided by Pine Instruments Corporation. The ring was made of platinum and its collection efficiency, N, was of 20±1%. To compute H_2O_2 selectivity, η, we made use of the following equation[38]: $\eta = 2(I_r/N/I_d + I_r/N)$, where I_r and I_d are ring and disc currents, respectively. H_2O_2 selectivity is not calculated below ~0.2 mA of disc current, owing to a poorer signal to background ratio at low currents.

To correct the current for mass transport losses, the equation $1/j = 1/j_d + 1/j_k$ was used, where j is the total current, j_d is the mass-transport-limited current to hydrogen peroxide (obtained from the ring), and j_k is the kinetic current to hydrogen peroxide. Further details are given in the Supplementary Information.

References

1. Perlo, P. *et al. Catalysis for Sustainable Energy Production* 89–105 (Wiley, 2009).
2. Armaroli, N. & Balzani, V. The future of energy supply: challenges and opportunities. *Angew. Chem. Int. Ed.* **46,** 52–66 (2007).
3. Kotrel, S. & Brauninger, S. in *Handbook of Heterogeneous Catalysis* 2nd edn (eds Ertl, G., Knoezinger, H., Schueth, F. & Weitkamp, J.) 1963 (Wiley, 2008).
4. *Ullmann's Encyclopedia of Industrial Chemistry* (Wiley, 1999–2013).
5. Samanta, C. Direct synthesis of hydrogen peroxide from hydrogen and oxygen: An overview of recent developments in the process. *Appl. Catal. A* **350,** 133–149 (2008).
6. Campos-Martin, J. M., Blanco-Brieva, G. & Fierro, J. L. G. Hydrogen peroxide synthesis: An outlook beyond the anthraquinone process. *Angew. Chem. Int. Ed.* **45,** 6962–6984 (2006).
7. Fukuzumi, S., Yamada, Y. & Karlin, K. D. Hydrogen peroxide as a sustainable energy carrier: Electrocatalytic production of hydrogen peroxide and the fuel cell. *Electrochim. Acta* **82,** 493–511 (2012).
8. Hâncu, D., Green, J. & Beckman, E. J. H_2O_2 in CO_2/H_2O biphasic systems: Green synthesis and epoxidation reactions. *Ind. Eng. Chem. Res.* **41,** 4466–4474 (2002).
9. Edwards, J. K. *et al.* Switching off hydrogen peroxide hydrogenation in the direct synthesis process. *Science* **323,** 1037–1041 (2009).
10. Ford, D. C., Nilekar, A. U., Xu, Y. & Mavrikakis, M. Partial and complete reduction of O_2 by hydrogen on transition metal surfaces. *Surf. Sci.* **604,** 1565–1575 (2010).
11. Yamanaka, I., Hashimoto, T., Ichihashi, R. & Otsuka, K. Direct synthesis of H_2O_2 acid solutions on carbon cathode prepared from activated carbon and vapor-growing-carbon-fiber by a H_2/O_2 fuel cell. *Electrochim. Acta* **53,** 4824–4832 (2008).
12. Lobyntseva, E., Kallio, T., Alexeyeva, N., Tammeveski, K. & Kontturi, K. Electrochemical synthesis of hydrogen peroxide: Rotating disk electrode and fuel cell studies. *Electrochim. Acta* **52,** 7262–7269 (2007).
13. Jirkovský, J. S. *et al.* Single atom hot-spots at Au–Pd nanoalloys for electrocatalytic H_2O_2 Production. *J. Am. Chem. Soc.* **133,** 19432–19441 (2011).
14. Fellinger, T-P., Hasché, F., Strasser, P. & Antonietti, M. Mesoporous nitrogen-doped carbon for the electrocatalytic synthesis of hydrogen peroxide. *J. Am. Chem. Soc.* **134,** 4072–4075 (2012).
15. Gouérec, P. & Savy, M. Oxygen reduction electrocatalysis: Ageing of pyrolyzed cobalt macrocycles dispersed on an active carbon. *Electrochim. Acta* **44,** 2653–2661 (1999).
16. Bezerra, C. W. B. *et al.* A review of Fe–N/C and Co–N/C catalysts for the oxygen reduction reaction. *Electrochim. Acta* **53,** 4937–4951 (2008).
17. Schulenburg, H. *et al.* Catalysts for the oxygen reduction from heat-treated iron(III) tetramethoxyphenylporphyrin chloride: Structure and stability of active sites. *J. Phys. Chem. B* **107,** 9034–9041 (2003).
18. Sheng, W., Gasteiger, H. A. & Shao-Horn, Y. Hydrogen oxidation and evolution reaction kinetics on platinum: Acid vs alkaline electrolytes. *J. Electrochem. Soc.* **157,** B1529–B1536 (2010).
19. Ayers, K. E., Dalton, L. T. & Anderson, E. B. Efficient generation of high energy density fuel from water. *ECS Trans.* **41,** 27–38 (2012).
20. Viswanathan, V., Hansen, H. A., Rossmeisl, J. & Nørskov, J. K. Unifying the 2e– and 4e– reduction of oxygen on metal surfaces. *J. Phys. Chem. Lett.* **3,** 2948–2951 (2012).
21. Norskov, J. K., Bligaard, T., Rossmeisl, J. & Christensen, C. H. Towards the computational design of solid catalysts. *Nature Chem.* **1,** 37–46 (2009).
22. Greeley, J. *et al.* Alloys of platinum and early transition metals as oxygen reduction electrocatalysts. *Nature Chem.* **1,** 552–556 (2009).
23. Koper, M. T. M. Thermodynamic theory of multi-electron transfer reactions: Implications for electrocatalysis. *J. Electroanal. Chem.* **660,** 254–260 (2011).
24. Janik, M. J., Taylor, C. D. & Neurock, M. First-principles analysis of the initial electroreduction steps of oxygen over Pt(111). *J. Electrochem. Soc.* **156,** B126–B135 (2009) doi:10.1149/1.3008005.
25. Tripković, V., Skúlason, E., Siahrostami, S., Nørskov, J. K. & Rossmeisl, J. The oxygen reduction reaction mechanism on Pt(111) from density functional theory calculations. *Electrochim. Acta* **55,** 7975–7981 (2010).
26. Stephens, I. E. L., Bondarenko, A. S., Gronbjerg, U., Rossmeisl, J. & Chorkendorff, I. Understanding the electrocatalysis of oxygen reduction on platinum and its alloys. *Energy Environ. Sci.* **5,** 6744–6762 (2012).
27. Rossmeisl, J., Karlberg, G. S., Jaramillo, T. & Norskov, J. K. Steady state oxygen reduction and cyclic voltammetry. *Faraday Discuss.* **140,** 337–346 (2009).

28. Peterson, A. A. & Nørskov, J. K. Activity descriptors for CO_2 electroreduction to methane on transition-metal catalysts. *J. Phys. Chem. Lett.* **3,** 251–258 (2012).
29. Skulason, E. *et al.* A theoretical evaluation of possible transition metal electro-catalysts for N_2 reduction. *Phys. Chem. Chem. Phys.* **14,** 1235–1245 (2012).
30. Hansen, H. A. *et al.* Electrochemical chlorine evolution at rutile oxide (110) surfaces. *Phys. Chem. Chem. Phys.* **12,** 283–290 (2010).
31. Maroun, F., Ozanam, F., Magnussen, O. M. & Behm, R. J. The role of atomic ensembles in the reactivity of bimetallic electrocatalysts. *Science* **293,** 1811–1814 (2001).
32. Strmcnik, D. *et al.* Enhanced electrocatalysis of the oxygen reduction reaction based on patterning of platinum surfaces with cyanide. *Nature Chem.* **2,** 880–885 (2010).
33. Viswanathan, V. *et al.* Simulating linear sweep voltammetry from first-principles: Application to electrochemical oxidation of water on Pt(111) and Pt3Ni(111). *J. Phys. Chem. C* **116,** 4698–4704 (2012).
34. Siahrostami, S., Bjorketun, M. E., Strasser, P., Greeley, J. & Rossmeisl, J. Tandem cathode for proton exchange membrane fuel cells. *Phys. Chem. Chem. Phys.* **15,** 9326–9334 (2013).
35. Wu, H. L., Yau, S. & Zei, M. S. Crystalline alloys produced by mercury electrodeposition on Pt(111) electrode at room temperature. *Electrochim. Acta* **53,** 5961–5967 (2008).
36. Angerstein-Kozlowska, H., MacDougall, B. & Conway, B. E. Origin of activation effects of acetonitrile and mercury in electrocatalytic oxidation of formic acid. *J. Electrochem. Soc.* **120,** 756–766 (1973).
37. Skuílason, E. *et al.* Modeling the electrochemical hydrogen oxidation and evolution reactions on the basis of density functional theory calculations. *J. Phys. Chem. C* **114,** 18182–18197 (2010).
38. Paulus, U. A., Schmidt, T. J., Gasteiger, H. A. & Behm, R. J. Oxygen reduction on a high-surface area Pt/Vulcan carbon catalyst: A thin-film rotating ring-disk electrode study. *J. Electroanal. Chem.* **495,** 134–145 (2001).
39. Van der Vliet, D. F. *et al.* Mesostructured thin films as electrocatalysts with tunable composition and surface morphology. *Nature Mater.* **11,** 1051–1058 (2012).
40. Perez-Alonso, F. J. *et al.* The effect of size on the oxygen electroreduction activity of mass-selected platinum nanoparticles. *Angew. Chem. Intl Ed.* **51,** 4641–4643 (2012).
41. Wesselmark, M., Wickman, B., Lagergren, C. & Lindbergh, G. Hydrogen oxidation reaction on thin platinum electrodes in the polymer electrolyte fuel cell. *Electrochem. Commun.* **12,** 1585–1588 (2010).
42. Wolfschmidt, H., Weingarth, D. & Stimming, U. Enhanced reactivity for hydrogen reactions at Pt nanoislands on Au(111). *ChemPhysChem* **11,** 1533–1541 (2010).
43. Mortensen, J. J., Hansen, L. B. & Jacobsen, K. W. Real-space grid implementation of the projector augmented wave method. *Phys. Rev. B* **71,** 035109 (2005).
44. Atomic Simulation Environment (ASE), available at https://wiki.fysik.dtu.dk/ase, Center for Atomic Scale Material Design (CAMD), Technical University of Denmark, Lyngby.
45. Hammer, B., Hansen, L. B. & Nørskov, J. K. Improved adsorption energetics within density-functional theory using revised Perdew-Burke-Ernzerhof functionals. *Phys. Rev. B* **59,** 7413–7421 (1999).
46. Verdaguer-Casadevall, A., Hernandez-Fernandez, P., Stephens, I. E. L., Chorkendorff, I. & Dahl, S. The effect of ammonia upon the electrocatalysis of hydrogen oxidation and oxygen reduction on polycrystalline platinum. *J. Power Sources* **220,** 205–210 (2012).
47. Alvarez-Rizatti, M. & Jüttner, K. Electrocatalysis of oxygen reduction by UPD of lead on gold single-crystal surfaces. *J. Electroanal. Chem. Interfacial Electrochem.* **144,** 351–363 (1983).
48. Jirkovsky, J. S., Halasa, M. & Schiffrin, D. J. Kinetics of electrocatalytic reduction of oxygen and hydrogen peroxide on dispersed gold nanoparticles. *Phys. Chem. Chem. Phys.* **12,** 8042–8053 (2010).
49. Blizanac, B. B., Ross, P. N. & Markovic, N. M. Oxygen electroreduction on Ag(111): The pH effect. *Electrochim. Acta* **52,** 2264–2271 (2007).
50. *CRC Handbook of Chemistry and Physics* (CRC Press, 1996).

Author contributions

J.R. and S.S. conceived the DFT calculations. S.S. and M.K. performed the DFT calculations. A.V. and I.E.L.S. designed the experiments. A.V. performed the electrochemical experiments, D.D. the TEM, P.M. the XPS and B.W. the EQCM and SEM-EDS. E.A.P. and R.F. prepared the Ag₃Pt sample and performed its XRD. S.S., A.V. and I.E.L.S. co-wrote the first draft of the paper. A.V. designed the figures. All authors discussed the results and commented on the manuscript.

Additional information

Supplementary information is available in the online version of the paper. Reprints and permissions information is available online at www.nature.com/reprints. Correspondence and requests for materials should be addressed to I.E.L.S. or J.R.

Competing financial interests

Patent application EP 13165265.3 'Alloy catalyst material' has been filed.

Enabling direct H$_2$O$_2$ production through rational electrocatalyst design

Samira Siahrostami, Arnau Verdaguer-Casadevall, Mohammadreza Karamad, Davide Deiana, Paolo Malacrida, Björn Wickman, María Escudero-Escribano, Elisa A. Paoli, Rasmus Frydendal, Thomas W. Hansen, Ib Chorkendorff, Ifan E. L. Stephens and Jan Rossmeisl

Nature Materials **12**, 1137–1143 (2013); published online 17 November 2013; corrected after print 21 November 2013.

In the version of this Article originally published, the middle initials of the penultimate author were missing; the name should have read Ifan E. L. Stephens. In the Author contributions and Additional information sections 'I.S.' should have read 'I.E.L.S.' These errors have now been corrected in the online versions of the Article.

Enabling direct H$_2$O$_2$ production through rational electrocatalyst design

Samira Siahrostami, Arnau Verdaguer-Casadevall, Mohammadreza Karamad, Davide Deiana, Paolo Malacrida, Björn Wickman, María Escudero-Escribano, Elisa A. Paoli, Rasmus Frydendal, Thomas W. Hansen, Ib Chorkendorff, Ifan E. L. Stephens and Jan Rossmeisl

Nature Materials **12,** 1137–1143 (2013); published online 17 November 2013; corrected after print 21 November 2013 and 23 December 2013.

In the version of this Article originally published, in Fig. 1, the top two values on the *y* axis were switched. This error has now been corrected in the online versions of the Article.

Trends in the Electrochemical Synthesis of H_2O_2: Enhancing Activity and Selectivity by Electrocatalytic Site Engineering

Arnau Verdaguer-Casadevall,[†] Davide Deiana,[‡] Mohammadreza Karamad,[§] Samira Siahrostami,[§] Paolo Malacrida,[†] Thomas W. Hansen,[‡] Jan Rossmeisl,[§] Ib Chorkendorff,*[,†] and Ifan E. L. Stephens*[,†]

[†]Center for Individual Nanoparticle Functionality, Department of Physics, [‡]Center for Electron Nanoscopy, and [§]Center for Atomic-scale Materials Design, Department of Physics, Technical University of Denmark, DK-2800 Kongens Lyngby, Denmark

S *Supporting Information*

ABSTRACT: The direct electrochemical synthesis of hydrogen peroxide is a promising alternative to currently used batch synthesis methods. Its industrial viability is dependent on the effective catalysis of the reduction of oxygen at the cathode. Herein, we study the factors controlling activity and selectivity for H_2O_2 production on metal surfaces. Using this approach, we discover two new catalysts for the reaction, Ag–Hg and Pd–Hg, with unique electrocatalytic properties both of which exhibit performance that far exceeds the current state-of-the-art.

KEYWORDS: H_2O_2 production, catalysis, electrochemistry, oxygen reduction, nanoparticles
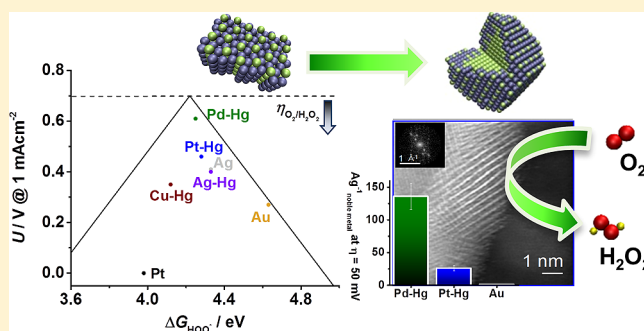
Economic development and a continued increase in global population place growing pressure on our energy resources. A significant fraction of the world's total energy consumption and raw materials are employed to produce chemicals. These chemicals are typically generated on a large scale in centralized locations.[1] However, localized chemical production, closer to the point of consumption, would present significant cost and energy savings. Electrochemical devices will play a major role in the transformation, as they can be operated at ambient temperatures and pressures in small plants and require minimal capital investment.[2]

Herein, we focus on the electrochemical oxygen reduction to hydrogen peroxide, a chemical whose electrochemical production is particularly appealing.[3] Currently, 3 M tons/year of H_2O_2 are being produced, mainly for use in the paper and chemical industry.[3] It is synthesized from hydrogen and oxygen by a complex batch method, the anthraquinone process, only suitable for large scale facilities.[4] The inherent disadvantages of batch synthesis methods and its energetic inefficiency have motivated industry and academia alike to develop an alternative. Consequently, the "direct catalytic" route to H_2O_2 synthesis has long been a dream reaction for the heterogeneous catalysis community; it involves the direct reaction of H_2 and O_2 in a liquid solvent on a Pd/Au catalyst.[5,6] Not only would the direct method enable production in a continuous mode, but it would also permit small scale, decentralized production. However, the direct route needs to handle potentially explosive mixtures of hydrogen and oxygen and does not make use of the embedded energy released upon reacting H_2.

A growing community of researchers are proposing an electrochemical route based on catalysts that selectively reduce oxygen to hydrogen peroxide.[7−9] That way, the danger of explosion is avoided by keeping hydrogen and oxygen separated. Moreover, producing H_2O_2 in a fuel cell would enable recovery of the energy released during the reaction. Alternatively, by producing it in an electrolyzer, one could avoid usage of H_2 altogether and use water as a source of protons.

Crucial to the performance of electrochemical devices for H_2O_2 production is the catalyst at the electrodes. A successful electrocatalyst should have (a) high activity, operating with high current densities as close as possible to the equilibrium potential, to optimize energy efficiency and catalyst loading; (b) high selectivity, ensuring high yields of H_2O_2; and (c) high stability, enabling long-term durability.

Significant efforts have been spent in the field of electrocatalysis to find descriptors for the trends in activity for electrochemical reactions. They all lead to a Sabatier volcano, where the highest activity is achieved on the surface with a moderate interaction with the reaction intermediates.[10−17] Most importantly, knowledge of this descriptor can lead to the discovery of new materials whose electrocatalytic performance exceeds the current state-of-the-art.[13,14,18,19]

The activity for H_2O_2 production is a function of the binding of the sole reaction intermediate, HOO* (Figure 1a).[20,21] For the ideal catalyst, the adsorption of HOO* should be thermoneutral at the equilibrium potential ($U^0_{O_2/H_2O_2}$ = 0.7 V),
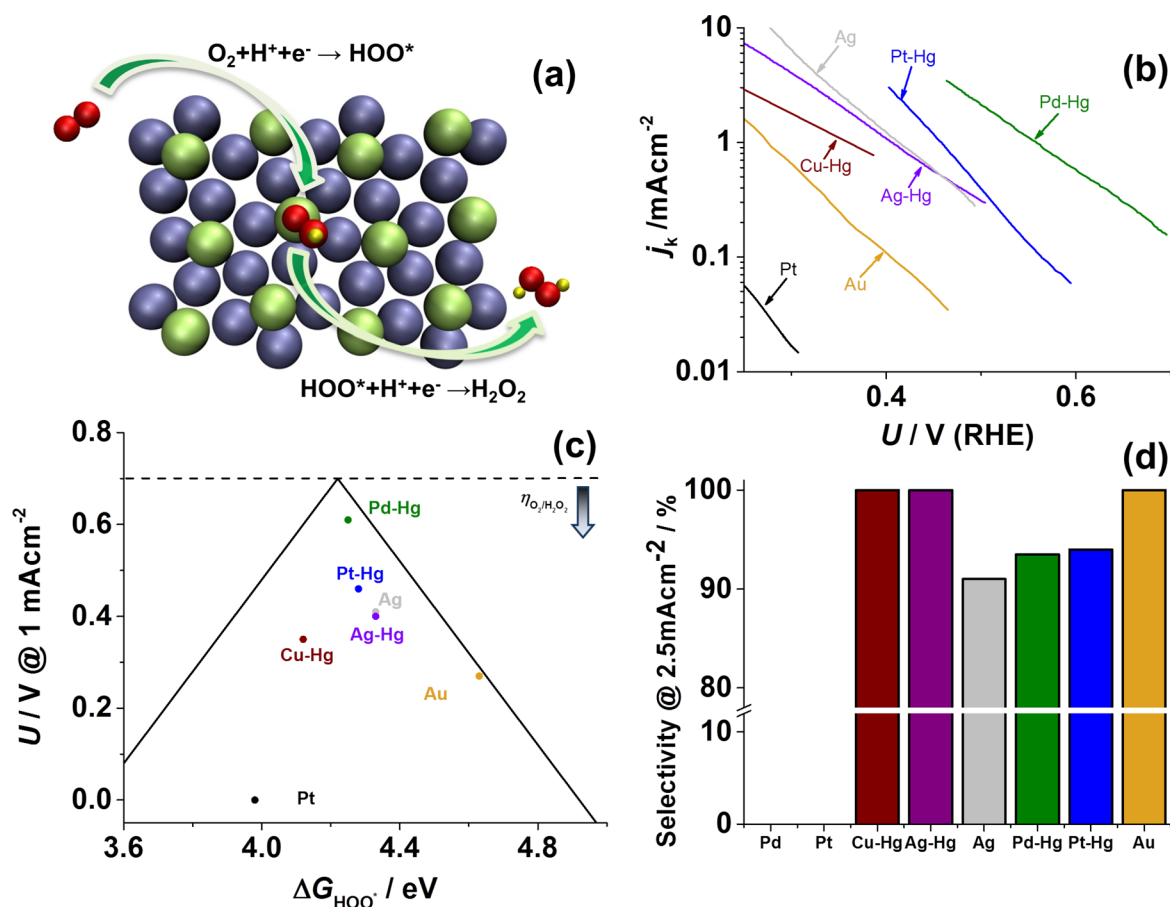
Figure 1. Trends in activity and selectivity for H_2O_2 production. (a) Schematic representation of oxygen reduction to H_2O_2 on a model Pd_2Hg_5 (001) surface. Palladium atoms are represented in green, mercury in blue, oxygen in red, and hydrogen in yellow. (b) Partial kinetic current density to H_2O_2 as a function of the applied potential, corrected for mass transport losses. (c) Potential required to reach 1 mAcm^{-2} of kinetic current density to H_2O_2 on polycrystalline catalysts as a function of the calculated HOO* binding energy. The solid lines represent the theoretical Sabatier volcano.[21] The dotted line represents the thermodynamic potential for oxygen reduction to H_2O_2. (d) H_2O_2 selectivity for different catalysts at 2.5 mAcm^{-2} of total current density. For this figure, data for Cu−Hg was extrapolated for ∼100 mV as it is unstable above 0.25 V.[27] Data for Au adapted from Jirkovsky et al.,[28] data for Pt from Verdaguer-Casadevall et al.,[48] and data for Pt−Hg from Siahrostami et al.[20] All electrochemical experiments were performed at 50 mV s^{-1} and 1600 rpm in O_2-saturated 0.1 M $HClO_4$ at room temperature with corrections for Ohmic drop. The surface area was normalized to the geometrical value.

so that the theoretical overpotential for the reaction, $\eta = 0$. Stronger or weaker binding to HOO* will introduce additional overpotential, or lower electrocatalytic activity. This means that the theoretical overpotential should show a Sabatier-volcano type dependence on the HOO* adsorption energy, ΔG_{HOO}.

Selectivity is determined by the ability of the catalyst to split the O−O bond during the oxygen reduction reaction, preventing water formation ($U^0_{O_2/H_2O} = 1.23$ V). The most successful catalysts in this respect include Co porphyrins[22] and Pd−Au.[7] They rely on the presence of isolated sites of a reactive atom, Co or Pd, surrounded by more inert atoms, N, C, and Au. Such sites are unable to break the O−O bond, ensuring a high selectivity to H_2O_2.

On the basis of the above ideas, we recently discovered a new catalyst for H_2O_2 production. Our density functional theory calculations identified Pt−Hg as a highly active and selective catalyst for the reaction. Our experiments confirmed the theoretical predictions, showing that both extended surfaces and nanoparticles of Pt−Hg are highly active and selective for oxygen reduction to H_2O_2.[20] In the current study, our goal is to systematically study trends for H_2O_2 production on both pure metals and alloy surfaces. We identify the most promising

catalysts using well-characterized extended surfaces. Density functional theory (DFT) calculations are used to rationalize the observed trends. We then apply this knowledge gained from the model surfaces to produce the catalyst in a technologically relevant form, that is, nanoparticles. This approach serves as a general example of how improved catalysts can be developed via a fundamental understanding of the factors controlling their performance in an electrochemical environment.

When Hg is electrodeposited on Pt, the two metals form an ordered intermetallic at room temperature where isolated Pt atoms are surrounded by Hg.[23] The same electrodeposition procedure can be performed to modify other metals in particular Cu, Pd, and Ag. We choose these metals as they all alloy with Hg[24−26] and they exhibit at least some stability against dissolution under the acidic conditions and potential range where O_2 reduction to H_2O_2 would take place (i.e., 0 to 0.7 V).[27] Further details regarding the preparation and characterization of these extended surfaces can be found in the Supporting Information.

On Figure 1b, we plot the partial current densities to hydrogen peroxide production, corrected for mass transport, on polycrystalline electrodes as a function of the applied potential.
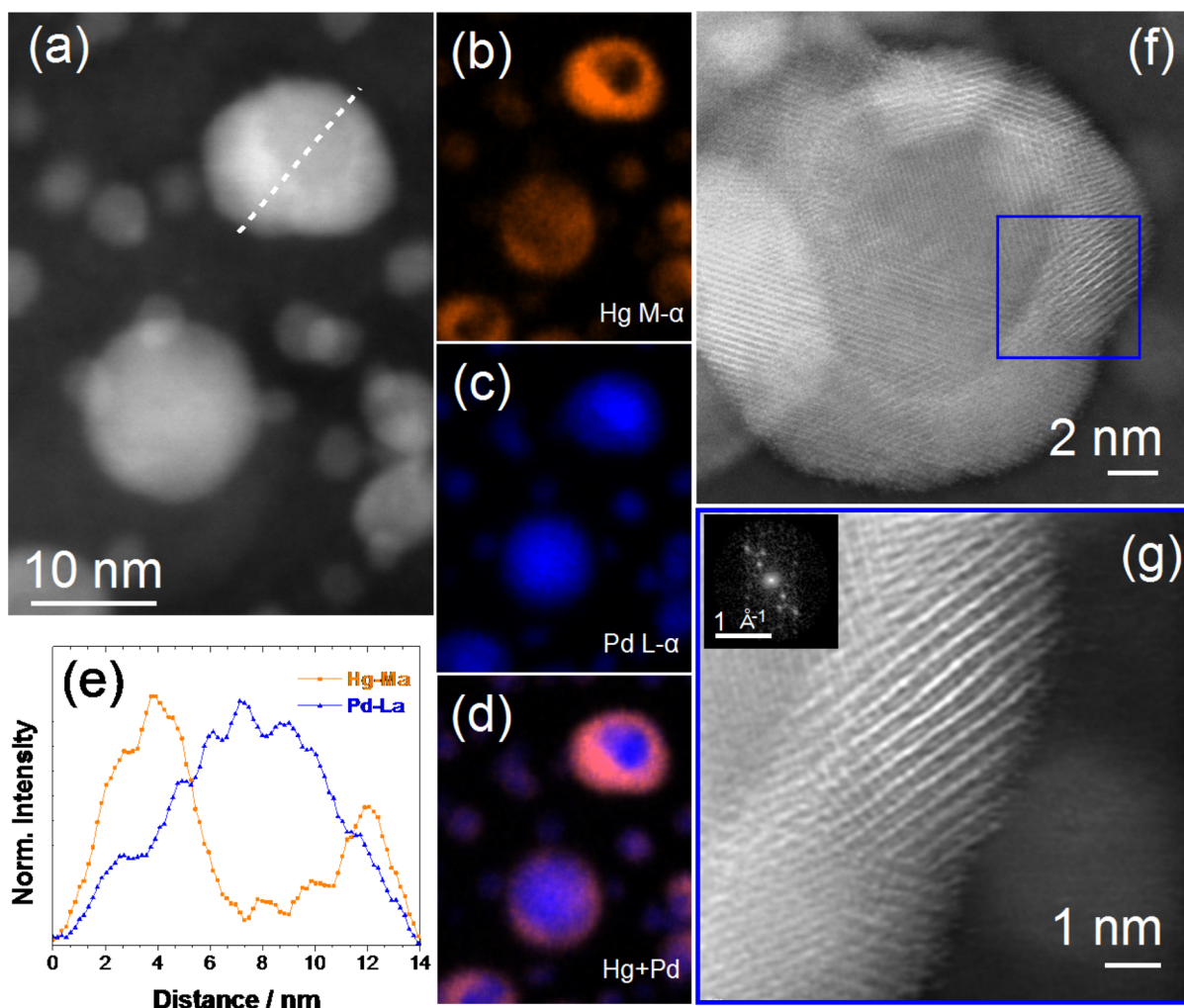
Figure 2. Electron microscopy characterization of Pd−Hg nanoparticles. (a) HAADF-STEM image of Pd−Hg nanoparticles and respective Hg, Pd, and Hg+Pd STEM-EDS elemental maps (b−d). (e) Normalized EDS Hg-Mα (orange) and Pd-Lα (blue) intensity line profiles extracted from the spectrum image data cube along with the white dashed line drawn on (a). (f) Fourier-filtered HAADF-STEM image of a Pd−Hg nanoparticle, showing a visible core−shell structure. (g) High-magnification HAADF-STEM image of the region enclosed in the blue square in (f); the inset shows the FFT of the bright fringes region.

Clearly, the electrode material has a decisive effect on the overpotential. In particular, the highest current at the lowest overpotential is obtained on Pd−Hg electrodes, while Pt−Hg, Ag−Hg, and Cu−Hg present increasing overpotentials. Notably, pure Ag has a high activity for this reaction, similar to that of Pt−Hg. All these materials are more active than Au-based catalysts, which have been extensively investigated in previous studies;[7,28,29] Pt−Hg, Ag, and Ag−Hg exhibit an order of magnitude improvement over Au, whereas the activity of Pd−Hg is 2 orders of magnitude higher.

To rationalize these findings, we used DFT to calculate $\Delta G_{HOO}*$ on the active sites for the reaction. Extensive details regarding the calculations are available in the Supporting Information. On Figure 1c, we plot the experimental overpotential required to reach 1 mAcm^{-2} of current to H$_2$O$_2$ for different catalysts, as a function of $\Delta G_{HOO}*$. In particular, Pd−Hg exhibits the lowest overpotential, or highest activity, because it lies closest to the peak of the volcano. Catalysts such as Au or Ag bind HOO* too weakly, which means that their overpotential is due to the lack of formation of HOO* from O$_2$. All these catalysts lie on the right leg of the volcano and their activity follows the HOO* binding energy. On the

other hand, the left leg of the volcano is somewhat steeper than the theoretical Sabatier volcano would suggest. The reason for this is selectivity: catalysts at the left leg will tend to favor water formation over H$_2$O$_2$.[20,21] Therefore, catalysts on the left leg will not typically produce any measurable amounts of H$_2$O$_2$. Nonetheless, H$_2$O$_2$ can be produced from such strong binding surfaces under conditions of accelerated mass transport.[30,31] Otherwise, should the catalysts on the left leg of the volcano lack the ensembles of atoms required to dissociate the O−O bond, they will also show some selectivity to H$_2$O$_2$; this is the case on pure Pt, below ∼0.3 V, where its surface is covered by adsorbed hydrogen,[19] or on Cu−Hg, where the Cu surface atoms are isolated from each other (see Supporting Information). Despite these limitations, the volcano captures the overall trends. Moreover, to the best of our knowledge this is the first time that these trends for H$_2$O$_2$ production are confirmed experimentally.

The selectivity to H$_2$O$_2$ is much higher on Hg-modified electrodes than on pure metal surfaces. In the case of Pd−Hg and Cu−Hg, we anticipate that the structure of the active site resembles that of Pt−Hg,[23] that is, single atoms of Pd or Cu, surrounded by Hg. At least two contiguous reactive atoms are

required to dissociate HOO*, break the O−O bond and form the intermediates of the 4-electron reduction reaction, O* and HO*.[7,32] Consequently, monatomic sites are unable to break the O−O bond, making them selective for H_2O_2 production.

In the case of Ag−Hg, the cause of its high selectivity at 100% over the entire potential range is subtly different. The alloy has only a slightly negative enthalpy of formation at −0.03 eV/atom[26] as described in the Supporting Information. For this reason, the compound forms a solid solution, rather than an ordered intermetallic. Within such a solid solution, there will be regions close to pure Ag and other regions close to pure Hg; this would explain why the activity is equal or slightly lower to that of pure Ag. We hypothesize that the reason for the very high selectivity of Ag−Hg is due to the preferential deposition of Hg on the steps of Ag.[33] DFT calculations show that the barrier for HOO* (or H_2O_2) dissociation is much higher on terrace sites than on step sites.[34] This means that steps should be inherently more selective toward the 4-electron reduction than terraces. Blocking them with Hg provides a means of ensuring high selectivity to H_2O_2 production.

The industrial implementation of electrochemical H_2O_2 production requires well dispersed catalysts with a high current density per unit mass in order to be economically competitive.[35,36] On the basis of the results obtained for extended surfaces, Pd−Hg has an intrinsically higher activity than any other catalyst reported thus far. Below, we translate this improvement into technologically relevant Pd−Hg/C nanoparticles.

Pd/C was prepared in an ink and drop cast on a glassy carbon electrode, using the thin film rotating disk electrode technique.[37] The oxygen reduction activity was measured on the pure Pd catalyst and found to agree closely with literature values,[38] validating our experimental procedure (see Supporting Information). Following this, we electrodeposited mercury onto the electrode.

The catalyst composition was verified by scanning transmission electron microscopy (STEM) and X-ray energy dispersive spectroscopy (EDS). Figure 2f shows the high-angle annular dark-field (HAADF)-STEM image of a Pd−Hg nanoparticle. A difference in contrast between the central and outer regions of the particle is clearly visible. The HAADF signal intensity has a strong dependence with the atomic number, hence the brighter regions around the central zone of the nanoparticle indicate an Hg-rich thick surface, suggesting a core−shell structure. A closer inspection of the shell region shown in Figure 2g reveals alternating high contrast lattice fringes with spacing of 2.9 ± 0.2 Å. This is consistent with the 3.0310 Å distance separating the (001) planes of the Pd_2Hg_5 alloy structure.[25] Furthermore, these planes contain only Hg atoms and consequently appear brighter in the HAADF image. In order to confirm the presence of the Hg-rich shell, STEM-EDS mapping was performed. The STEM image and the corresponding EDS elemental maps of a region with different nanoparticles are shown in Figure 2a−d. The combined Hg and Pd elemental maps unmistakably show that a core−shell structure is formed with an anisotropic thickness of the shell. This can be visualized even more clearly by the EDS intensity profile linescan in Figure 2e. The anisotropy in the shell thickness can be ascribed to the different reactivity of each facet on the nanoparticle. The alloying of Pd and Hg was also confirmed by X-ray photoelectron spectroscopy (see Supporting Information). Further proof of the structure is shown in the Supporting Information. Taken as a whole, the TEM images in

Figure 2 demonstrate that the nanoparticles form a core−shell structure at room temperature. The core is Pd, whereas the shell consists of an ordered intermetallic, likely Pd_2Hg_5. This is the same structure that was modeled in our DFT calculations, whose (001) facet we used to simulate the highly active and selective extended polycrystalline Pd−Hg surfaces described above.

Oxygen reduction on Pd−Hg/C nanoparticles shows a very similar behavior to polycrystalline Pd−Hg (Figure 3d). Upon saturation of the electrolyte with O_2, we observed a negative current corresponding to oxygen reduction. The ring current shows that a substantial amount of the disk current is due to
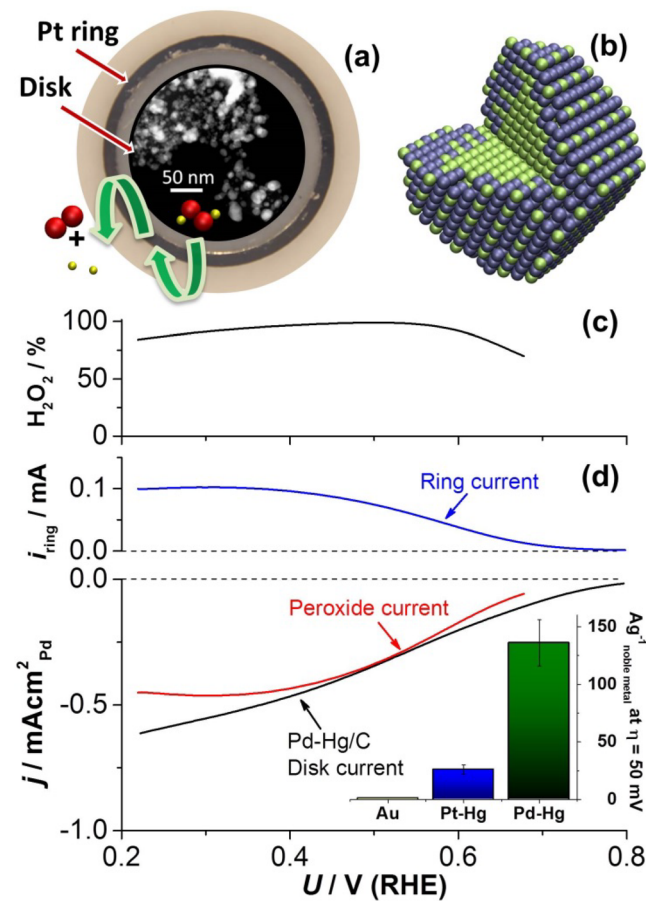

Figure 3. Electrochemical characterization of Pd−Hg/C nanoparticles. (a) Rotating ring-disk electrode with a schematic representation of H_2O_2 oxidation at the ring. The disk has been modified to show a HAADF-STEM overview of the Pd−Hg/C nanoparticles. (b) Schematic representation of a Pd−Hg nanoparticle with Pd colored in green and Hg in blue. (c) H_2O_2 selectivity as a function of the applied potential. (d) RRDE voltammograms at 1600 rpm in O_2-saturated electrolyte with the disk current (black), ring current (blue) and corresponding current to hydrogen peroxide (red) obtained from the ring current (only the anodic cycle is shown). The disk current is normalized to the surface area of Pd nanoparticles (estimated from the oxide reduction peak before deposition of Hg). The inset shows the mass activity (A per g of noble metal) at 50 mV of overpotential for nanoparticulate catalysts. Data for Pt−Hg adapted from Siahrostami et al.[20] All electrochemical experiments were performed at 50 mV s^{-1} and 1600 rpm in O_2 saturated 0.1 M $HClO_4$ at room temperature with corrections for Ohmic drop and capacitive currents.[49] Full details on the normalization procedure and mass activity calculations are available in the Supporting Information.

hydrogen peroxide production with a selectivity higher than 95% between 0.35 and 0.55 V (Figure 3c). At 50 mV overpotential, Pd—Hg/C presents an activity per mass of precious metal five times higher than Pt—Hg/C and more than 2 orders of magnitude higher than state-of-the-art Au/C (inset of Figure 3d). In addition, Pd—Hg/C is highly stable, displaying negligible losses after 8000 potential cycles between 0.2 and 0.7 V.

In summary, we have modified different metal surfaces with Hg, as a means to tune the oxygen reduction activity and selectivity of various electrodes toward H_2O_2 production. By using a combination of theory and experiments, we have verified that the activity can be described by the *HOO binding energy, via a Sabatier-volcano. Selectivity in turn is described by the geometric arrangement of the catalyst sites. This approach led to the discovery of both Ag—Hg and Pd—Hg as catalysts for H_2O_2 production. The deployment of either catalyst could bring about significant improvements to the efficiency, selectivity, and cost[39] of a H_2O_2 producing device, in comparison to the current state-of-the art.[7,20] Fine tuning the particle shape, size, and composition should lead to an even higher activity per mass of precious metal.[40−44] Nonetheless, future progress will be grounded on the basis of the active sites developed in this work. The concepts used here to tune oxygen reduction activity and selectivity can be extended to other reactions such as the reduction of CO_2[45,46] or the selective oxidation of hydrocarbons.[47]

ASSOCIATED CONTENT

ⓢ Supporting Information

Detailed description of experimental and theoretical methods, as well as additional voltammetric data, characterization results, and DFT calculations. This material is available free of charge via the Internet at http://pubs.acs.org.

AUTHOR INFORMATION

Corresponding Authors
*E-mail: (I.C.) ibchork@fysik.dtu.dk.
*E-mail: (I.E.L.S.) ifan@fysik.dtu.dk.

Author Contributions
A.V. and I.E.L.S. developed the idea and designed the experiments. A.V. performed the electrochemical experiments, D.D. performed the microscopy, and P.M. performed the XPS. M.K. and S.S. performed the theoretical calculations. A.V. and I.E.L.S. wrote the first draft of the paper. A.V. and D.D. designed the figures. All authors discussed the results and commented on the manuscript.

Notes
The authors declare the following competing financial interest(s): Some of the authors of this manuscript were inventors on patent application EP 13165265.3 Alloy catalyst material. This patent includes some of the catalyst materials described here within its scope..

ACKNOWLEDGMENTS

REFERENCES

(1) Chorkendorff, I.; Niemantsverdriet, J. W. *Concepts of Modern Catalysis and Kinetics*, student ed.; Wiley-VCH Verlag GmBH & Co. KGaA: Weinheim, 2003.

(2) Kotrel, S., Brauninger, S. *Handbook of Heterogeneous Catalysis*, 2nd ed.; Ertl, G., Knoezinger, H., Schueth, F., Weitkamp, J., Eds.; Wiley: New York, 2008.

(3) Campos-Martin, J. M.; Blanco-Brieva, G.; Fierro, J. L. G. *Angew. Chem., Int. Ed.* **2006**, *45* (42), 6962−6984.

(4) *Ullman's Encyclopedia of Industrial Chemistry*; Wiley: New York, 1999−2013.

(5) Edwards, J. K.; Solsona, B.; N, E. N.; Carley, A. F.; Herzing, A. A.; Kiely, C. J.; Hutchings, G. J. *Science* **2009**, *323* (5917), 1037−1041.

(6) Samanta, C. *Appl. Catal., A* **2008**, *350* (2), 133−149.

(7) Jirkovský, J. S.; Panas, I.; Ahlberg, E.; Halasa, M.; Romani, S.; Schiffrin, D. J. *J. Am. Chem. Soc.* **2011**, *133* (48), 19432−19441.

(8) Fellinger, T.-P.; Hasché, F.; Strasser, P.; Antonietti, M. *J. Am. Chem. Soc.* **2012**, *134* (9), 4072−4075.

(9) Yamanaka, I.; Onizawa, T.; Takenaka, S.; Otsuka, K. *Angew. Chem.* **2003**, *115* (31), 3781−3783.

(10) Parsons, R. *Trans. Faraday Soc.* **1958**, *54* (7), 1053−1063.

(11) Trasatti, S. *J. Electroanal. Chem.* **1972**, *39* (1), 163−&.

(12) Stamenkovic, V. R.; Mun, B. S.; Arenz, M.; Mayrhofer, K. J. J.; Lucas, C. A.; Wang, G.; Ross, P. N.; Markovic, N. M. *Nat. Mater.* **2007**, *6* (3), 241−247.

(13) Greeley, J.; Stephens, I. E. L.; Bondarenko, A. S.; Johansson, T. P.; Hansen, H. A.; Jaramillo, T. F.; Rossmeisl, J.; Chorkendorff, I.; Nørskov, J. K. *Nature Chem.* **2009**, *1* (7), 552−556.

(14) Suntivich, J.; May, K. J.; Gasteiger, H. A.; Goodenough, J. B.; Shao-Horn, Y. *Science* **2011**, *334* (6061), 1383−1385.

(15) Stephens, I. E. L.; Bondarenko, A. S.; Perez-Alonso, F. J.; Calle-Vallejo, F.; Bech, L.; Johansson, T. P.; Jepsen, A. K.; Frydendal, R.; Knudsen, B. P.; Rossmeisl, J.; Chorkendorff, I. *J. Am. Chem. Soc.* **2011**, *133* (14), 5485−5491.

(16) Subbaraman, R.; Tripkovic, D.; Chang, K.-C.; Strmcnik, D.; Paulikas, A. P.; Hirunsit, P.; Chan, M.; Greeley, J.; Stamenkovic, V.; Markovic, N. M. *Nat. Mater.* **2012**, *11* (6), 550−557.

(17) Bandarenka, A. S.; Varela, A. S.; Karamad, M.; Calle-Vallejo, F.; Bech, L.; Perez-Alonso, F. J.; Rossmeisl, J.; Stephens, I. E. L.; Chorkendorff, I. *Angew. Chem., Int. Ed.* **2012**, *51* (47), 11845−11848.

(18) Hinnemann, B.; Moses, P. G.; Bonde, J.; Jorgensen, K. P.; Nielsen, J. H.; Horch, S.; Chorkendorff, I.; Nørskov, J. K. *J. Am. Chem. Soc.* **2005**, *127* (15), 5308−5309.

(19) Stamenkovic, V. R.; Fowler, B.; Mun, B. S.; Wang, G.; Ross, P. N.; Lucas, C. A.; Marković, N. M. *Science* **2007**, *315* (5811), 493−497.

(20) Siahrostami, S.; Verdaguer-Casadevall, A.; Karamad, M.; Deiana, D.; Malacrida, P.; Wickman, B.; Escudero-Escribano, M.; Paoli, E. A.; Frydendal, R.; Hansen, T. W.; Chorkendorff, I.; Stephens, I. E. L.; Rossmeisl, J. *Nat. Mater.* **2013**, *12* (12), 1137−1143.

(21) Viswanathan, V.; Hansen, H. A.; Rossmeisl, J.; Nørskov, J. K. *J. Phys. Chem. Lett.* **2012**, *3* (20), 2948−2951.

(22) Jaouen, F.; Proietti, E.; Lefevre, M.; Chenitz, R.; Dodelet, J.-P.; Wu, G.; Chung, H. T.; Johnston, C. M.; Zelenay, P. *Energy Environ. Sci.* **2011**, *4* (1), 114−130.

(23) Wu, H. L.; Yau, S.; Zei, M. S. *Electrochim. Acta* **2008**, *53* (20), 5961−5967.

(24) Russell, A. S.; Kennedy, T. R.; Howitt, J.; Lyons, H. A. M. *J. Chem. Soc.* **1932**, 2340−2342.

(25) Guminski, C. *Bull. Alloy Phase Diagrams* **1990**, *11* (1), 22−26.

(26) Baren, M. R. *J. Phase Equilib.* **1996**, *17* (2), 122−128.

(27) Pourbaix, M. *Atlas of electrochemical equilibria in aqueous solutions*, National Association of Corrosion Engineers, **1974**.

(28) Jirkovsky, J. S.; Halasa, M.; Schiffrin, D. J. *Phys. Chem. Chem. Phys.* **2010**, *12* (28), 8042−8053.

(29) Erikson, H.; Jürmann, G.; Sarapuu, A.; Potter, R. J.; Tammeveski, K. *Electrochim. Acta* **2009**, *54* (28), 7483−7489.

(30) Chen, S.; Kucernak, A. *J. Phys. Chem. B* **2004**, *108* (10), 3262−3276.

(31) Schneider, A.; Colmenares, L.; Seidel, Y. E.; Jusys, Z.; Wickman, B.; Kasemo, B.; Behm, R. J. *Phys. Chem. Chem. Phys.* **2008**, *10* (14), 1931−1943.

(32) Siahrostami, S.; Bjorketun, M. E.; Strasser, P.; Greeley, J.; Rossmeisl, J. *Phys. Chem. Chem. Phys.* **2013**, *15* (23), 9326−9334.

(33) Levlin, M.; Ikävalko, E.; Laitinen, T. *Fresenius J. Anal. Chem.* **1999**, *365* (7), 577−586.

(34) Rankin, R. B.; Greeley, J. *ACS Catal.* **2012**, *2* (12), 2664−2672.

(35) Stephens, I. E. L.; Bondarenko, A. S.; Gronbjerg, U.; Rossmeisl, J.; Chorkendorff, I. *Energy Environ. Sci.* **2012**.

(36) Gasteiger, H. A.; Markovic, N. M. *Science* **2009**, *324* (5923), 48−49.

(37) Schmidt, T. J.; Gasteiger, H. A.; Stab, G. D.; Urban, P. M.; Kolb, D. M.; Behm, R. J. *J. Electrochem. Soc.* **1998**, *145* (7), 2354−2358.

(38) Shao, M.-H.; Sasaki, K.; Adzic, R. R. *J. Am. Chem. Soc.* **2006**, *128* (11), 3526−3527.

(39) Vesborg, P. C. K.; Jaramillo, T. F. *RSC Adv.* **2012**, *2* (21), 7933−7947.

(40) Sasaki, K.; Naohara, H.; Cai, Y.; Choi, Y. M.; Liu, P.; Vukmirovic, M. B.; Wang, J. X.; Adzic, R. R. *Angew. Chem., Int. Ed.* **2010**, *49* (46), 8602−8607.

(41) Guo, S.; Li, D.; Zhu, H.; Zhang, S.; Markovic, N. M.; Stamenkovic, V. R.; Sun, S. *Angew. Chem., Int. Ed.* **2013**, *52* (12), 3465−3468.

(42) Cui, C.; Gan, L.; Heggen, M.; Rudi, S.; Strasser, P. *Nat. Mater.* **2013**, *12* (8), 765−771.

(43) Mayrhofer, K. J. J.; Juhart, V.; Hartl, K.; Hanzlik, M.; Arenz, M. *Angew. Chem., Int. Ed.* **2009**, *48* (19), 3529−3531.

(44) Wang, D. L.; Xin, H. L. L.; Hovden, R.; Wang, H. S.; Yu, Y. C.; Muller, D. A.; DiSalvo, F. J.; Abruna, H. D. *Nat. Mater.* **2013**, *12* (1), 81−87.

(45) Kuhl, K. P.; Cave, E. R.; Abram, D. N.; Jaramillo, T. F. *Energy Environ. Sci.* **2012**, *5* (5), 7050−7059.

(46) Li, C. W.; Kanan, M. W. *J. Am. Chem. Soc.* **2012**, *134* (17), 7231−7234.

(47) Tomita, A.; Nakajima, J.; Hibino, T. *Angew. Chem., Int. Ed.* **2008**, *47* (8), 1462−1464.

(48) Verdaguer-Casadevall, A.; Hernandez-Fernandez, P.; Stephens, I. E. L.; Chorkendorff, I.; Dahl, S. *J. Power Sources* **2012**, *220* (0), 205−210.

(49) Nesselberger, M.; Ashton, S.; Meier, J. C.; Katsounaros, I.; Mayrhofer, K. J. J.; Arenz, M. *J. Am. Chem. Soc.* **2011**, *133* (43), 17428−17433.